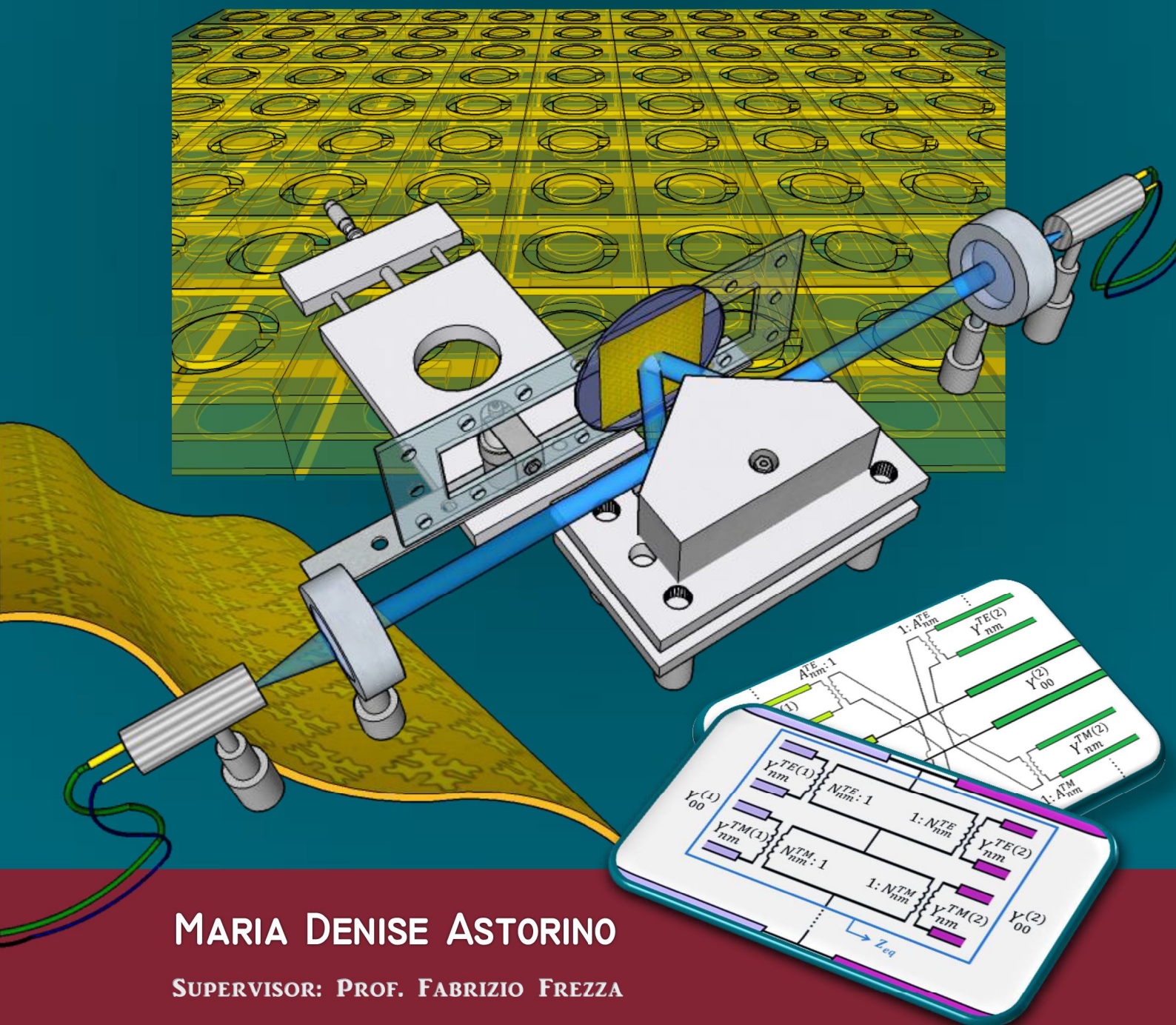




PHD DEGREE IN MATHEMATICAL MODELS FOR ENGINEERING,
ELECTROMAGNETICS AND NANOSCIENCES
XXXI CYCLE

WIDEBAND EQUIVALENT-CIRCUIT MODEL ANALYSIS,
REALIZATION AND TIME-DOMAIN SPECTROSCOPY CHARACTERIZATION
OF TERAHERTZ PERIODIC METAMATERIAL DEVICES



MARIA DENISE ASTORINO

SUPERVISOR: PROF. FABRIZIO FREZZA

The most important attitude that
can be formed is that of desire to
go on learning.

John Dewey
Experience and Education

*Ai miei genitori,
ai miei nonni.*

Contents

Index	5
1 Introduction	9
References	14
2 Fundamentals	17
2.1 Electromagnetic wave propagation	17
2.2 Fresnel equations	21
2.3 Floquet's theorem	22
2.3.1 Grating lobes	25
2.4 Metamaterials	26
2.5 Homogenization through Nicolson-Ross-Weir algorithm	28
2.6 Transmission line theory	30
2.7 Fabrication methods	32
2.8 Terahertz time-domain spectroscopy	37
2.9 Davidenko's method and validation by genetic algorithm	41
2.9.1 Transmission mode: parametric sweep on the slab thickness	46
2.9.2 Reflection mode: parametric sweep on the grounded slab thickness	47
2.9.3 Reflection mode: parametric sweep on the grounded slab permittivity	48
2.9.4 Reflection mode: parametric sweep on the grounded slab permittivity in oblique incidence	49
2.10 Polarizability	50
References	51
3 Fully Analytical and Semi-Analytical Equivalent Circuits	53
3.1 Introduction	53
3.2 Strip gratings	55
3.2.1 Numerical results for a strip grating printed on a grounded dielectric slab under TE incidence	61
3.3 Slit gratings	63
3.3.1 Numerical results for a slit grating printed on a grounded dielectric slab under TM incidence	67

3.4	Semi-analytical circuit model for a strip grating	69
3.5	Fully analytical EC for FSS of arbitrary geometry	70
3.5.1	Array of metallic patches	79
3.5.2	Array of 2D metallic crosses	83
3.6	Semi-analytical circuit model for arrays of 2D metallic FSSs . . .	87
3.6.1	Array of freestanding patches	87
3.6.2	Array of patches printed on a finite dielectric spacer	88
3.6.3	Array of crosses on a finite lossless dielectric slab	90
3.6.4	Array of rings on a finite lossless dielectric slab	91
3.6.5	Array of split ring resonators (SRRs) on a finite lossless dielectric slab	92
3.7	Fully analytical EC for complementary FSS of arbitrary geometry	93
3.7.1	Rectangular slot-based filters on a finite lossless silicon slab	99
3.8	Semi-analytical circuit model for complementary FSSs	100
3.8.1	Filters based on rectangular slots	100
3.8.2	Filters based on dogbone-shaped holes	101
3.8.3	Filters based on cross-shaped holes	102
3.9	Conclusions	103
	References	104
4	Equivalent-Circuit Model for Stacked Slot-based 2D Periodic Arrays of Arbitrary Geometry for Broadband Analysis	107
4.1	Introduction	107
4.2	Equivalent Π circuit topology for stacked slot-based 2D periodic arrays	109
4.3	Numerical results	114
4.4	Conclusions	121
	References	122
5	THz Metamaterial Absorbers	125
5.1	Introduction	125
5.2	Ultra-thin narrow-band MMA	127
5.3	Ultra-thin complementary narrow-band MMA	135
5.4	Ultra-thin dual-band MMA	137
5.5	Retrieval of effective electromagnetic parameters	141
5.6	Conclusions	144
	References	146
6	Broad-band Metamaterial Absorber	149
6.1	Introduction	149
6.2	Ultra-thin broad-band metamaterial absorber	150
6.2.1	Design and analysis at normal incidence	150

6.2.2	Analysis at oblique incidence for TE and TM polarizations	155
6.2.3	Absorption mechanism: dielectric and Ohmic losses	158
6.3	Effective-medium theory and interference theory	159
6.3.1	Retrieval of the effective electromagnetic parameters	159
6.3.2	Grounded-slab model	161
6.4	Conclusions	162
	References	163
7	Parametric Macromodels for Optimization of Metamaterial Devices	165
7.1	Introduction	165
7.2	Metamaterial absorber	167
7.3	Parametric macromodeling	169
7.3.1	Design space sampling and model cross-validation	171
7.4	Numerical results	172
7.5	Conclusions	176
	References	177
8	Polarization-Maintaining Reflection-mode THz-TDS of a Polyimide Based Ultra-Thin Narrow-Band MMA	181
8.1	Introduction	181
8.2	MMA description	184
8.3	Fabricated prototype	185
8.4	Experimental setup for polarization-maintaining reflection-mode THz-TDS	186
8.5	Simulation and experimental results	190
8.6	Conclusions	191
	References	193
9	Transmission and Reflection Modes THz-TDS Characterization of Polyimide-based Metamaterial Devices	197
9.1	Introduction	197
9.2	Transmission-mode THz-TDS for polyimide characterization	199
9.2.1	Polyimide film fabrication	202
9.3	Transmission-mode THz-TDS measurements for metasurface characterization	202
9.3.1	Metasurface fabrication	206
9.4	Reflection-mode THz-TDS measurements for oblique incidence characterization of the narrow-band MMA	207
9.5	Conclusions	209
	References	211

10 Finite Element Analysis of Scatterers with Discontinuous Impedance	
Boundary Conditions	213
10.1 Introduction	213
10.2 Impedance boundary conditions	215
10.2.1 IBC implemented in COMSOL Multiphysics	216
10.3 PEC-PMC sphere	216
10.3.1 IBC PEC-PMC sphere	220
10.4 2D axial symmetry electrostatic simulation for axial polarizability analysis	221
10.4.1 Axial polarizability of a PEC sphere	223
10.4.2 Axial polarizability of a PMC sphere	224
10.4.3 Axial polarizability of a PEC-PMC sphere	224
10.5 Alternative solution using infinite elements	225
10.6 Conclusions	227
References	228
11 Conclusions	229
11.1 Author's bibliography	234
Publications	234
Proceedings	234
Appendices	235
A Supplementary Information: Equivalent-Circuit Model	235
A.1 Equivalent circuit model for a single periodic slot-based FSS em- bedded within two arbitrary dielectric half-spaces	235
A.2 References	238
B Supplementary Information: Custom Reflection-Mode THz-TDS	239
B.1 Aluminum prism geometry	239
B.2 Experimental absorbance spectra under 16° oblique incidence in TE polarization as a function of the azimuthal angle φ	241
B.3 Effect of higher Ohmic losses of the metal layers at THz frequencies.	242
B.4 References	243
C Normalized Axial and Transversal Polarizabilities	245
C.1 Normalized polarizabilities of ellipsoids	245
C.1.1 PEC prolate spheroid	246
C.1.2 PEC oblate spheroid	248
C.2 Normalized polarizabilities of double sphere	249
C.2.1 Two touching PEC spheres	250
C.2.2 Two intersecting PEC spheres	251
C.3 References	253

CHAPTER 1

Introduction

Unprecedented in history, the era we are living in is experiencing an Information Technology revolution; in particular, processes such as the globalization of knowledge and the availability of real-time information have promoted a change of paradigm in multiple spheres of human activities. This is even more evident for the research community, which has profited from the increased volume of data and from the ever-improving computational resources; synergistic interactions between different fields have thus become customary, paving the way for research in relatively unexplored areas, such as the frequency spectrum called “THz gap” [1]. Unlike the well-established spectral bandwidths of microwaves and optics, the lack of materials with usable electric response in terahertz range, which lies between them, has limited its developments; in more recent years the perspectives of unique applications have caused several attempts to bridge this gap. These efforts have determined a broad impact into THz emerging technologies, fabrication techniques and design methods that to date are still being investigated, improved, and engineered.

At the border between electronics and photonics, the inception of terahertz research can be dated several decades ago, but it recently underwent a rapid growth, due to the combined improvement of multiple technological resources. Over the last years, we have witnessed an exponential development not only of Information Technology but also of micro/nano-fabrication, computational tools, and analytical/numerical methods; these, added to the introduction of new types of materials such as metamaterials, polymers, metal-oxides, have contributed to increase the line-of-sight and reach of research on terahertz spectrum. Terahertz, along with integrated optics, has profited from these advancements and is now expanding into multiple branches; various potentialities of scientific and industrial relevance have already been demonstrated.

Some non-linear phenomena have been observed in sensing and imaging ap-

plications [2, 3]. The capability to probe nanometer-sized structures [4] such as nanofibers and nanotubes, the ability to discern several spectroscopic fingerprints [5] and to observe THz-induced modifications in human gene [6] made THz technology a powerful tool for biosensing techniques. The low-interference, non-ionizing and non-invasive nature of THz radiation has phased in it into fields such as optoelectronics, medicine, defense, security (e.g. in airports) and communications (e.g. satellite to satellite THz communications guarantee higher data rates with respect to microwaves, especially when THz carrier waves do not cross the Earth's atmosphere [7]). Nowadays, the list of possible applications is still in expansion, also thanks to the exploration of promising experimental methods, artificial materials and THz hardware.

Since the emergence of THz Time-Domain Spectroscopy (THz-TDS) as an experimental technique, the generation and detection of broadband coherent terahertz radiation have provided wide accessibility to this frequency region and to its multifaceted possible evolutions [8]. This procedure has shown its versatility by enabling a plethora of innovative advances: since non-polar and non-metallic materials are transparent at THz frequencies due to the low photon energies, THz-TDS allows non-destructive characterization of biochemical elements [9], drugs [10], pharmaceutical products [11], explosives [12] and foods for quality control purposes [13]. Moreover, THz-TDS has proved to be a useful tool for the characterization of photonic crystals and metamaterials.

In this framework, metamaterials, a new class of artificial composites with non-naturally-occurring features [14–17], have been introduced inside THz regime for both the realization of advanced devices and the improvement of existing equipment. Metamaterials have already matured applications in microwaves and optics; indeed, being frequency scalable materials, many concepts initially developed for other spectral ranges can be adapted into terahertz frequencies. Research in metamaterials moves towards superlenses [18], cloaking elements [19], microfluidic sensors [20], biomedical sensors [21], antennas [22], and absorbers [23]. In particular, electromagnetic metamaterial absorbers are capable of controlling the losses, quantified by the imaginary parts of the complex effective parameters, with diversified applications in spectrally sensitive photo-detectors [24], imaging [25], thermal emitters [26], spatial light modulators [27], and wireless communications [28]. In order to engineer and properly manipulate the electromagnetic behavior of these complex systems, a key role is given to the analytical and computational aspects.

In this context, the continuous improvement of computational electromagnetics has enabled the progress of Equivalent-Circuit (EC) approach [29] and parametric macromodel analysis [30] as hybrid combinations of theoretical/numerical

techniques with partial results of full-wave simulations; this has allowed to significantly reduce CPU time and memory consumption, particularly useful at THz frequencies. The long-term goal of these methods is twofold: to gain a physical insight into the electromagnetic behavior of the devices under test and to optimize their performances through a feasibility study on manufacturing tolerances. Due to the high availability of computational resources of modern workstations, another option may be the direct use of numerical simulations with commercial general purpose electromagnetic software; however, this approach prevents from obtaining an appropriate and versatile topology for the circuit models and, in general, needs of higher computational costs, which made it sometimes prohibitive (especially for the investigation of multilayered structures, the required CPU time and memory consumption can be quite onerous, as demonstrated in this thesis). A critical evaluation between the computational resources at disposal and the efforts to develop equivalent models is necessary, but it is to be noted that the latter approach guarantees long-term benefits in terms of efficiency, repeatability, and flexibility, motivating and boosting the research activity in this direction.

In this PhD thesis, I have thoroughly researched THz periodic metamaterial devices by dealing with all the phases of their development: electromagnetic analysis, design, fabrication, characterization, and data post-processing. Overall, my work has involved both theoretical and practical aspects; initially, for the analysis and design phases, I have adopted an analytical/numerical perspective for the retrieval of the devised circuit topologies. In particular, I have developed and applied EC models and parametric macromodels for the physical investigation and optimization of the devices; these methods have been validated by proving their efficiency and effectiveness through the comparison with Finite-Element Method (FEM) based simulations. Also, they guarantee a wider range of applications in terms of frequency spectra, complexity of geometrical shapes, and material characteristics. For the realization phase, I have used a heuristic procedure of fabrication and after evaluating possible non-idealities, I have made tolerance studies in order to obtain a stable electromagnetic performance. For the characterization of the microfabricated devices, I have used custom THz-TDS setups for both reflection and transmission-modes; the resulting configurations have proved to be compact and interesting also for further integration in embedded measurement systems. For the data analysis phase, I have post-processed the acquired measurements by adopting retrieval procedures of the constitutive parameters of the samples. Other than topics specifically related to the THz field, I have developed some models of analytical/numerical character for the study of scatterers with discontinuous impedance boundary conditions.

The fulfillment of these goals has required multiple skills and facilities; this

allowed me to mature a multidisciplinary vision and to be able to handle measurements on the fabricated samples. To this end, I have operated with various Institutions for the practical realization and experimental validation of my projects:

- *Institute for Microelectronics and Microsystems* CNR-IMM of Rome for fabrication of polyimide-based samples;
- *Research Center for Nanotechnologies Applied to Engineering* (CNIS) for access to Atomic Force Microscopy (AFM);
- *Institute for Complex Systems* CNR-ISC and *Physics Department* (Sapienza) for THz-TDS measurements;
- *Department of Industrial and Information Engineering and Economics* (University of L'Aquila Electromagnetic Compatibility Research Laboratory, UAq EMC Laboratory), and *Microwave Department Institut Mines-Télécom Atlantique* (CNRS UMR 6285 Lab-STICC, Brest, France) for parametric macromodel development;
- *Department of Electronics and Nanoengineering*, Aalto University (School of Electrical Engineering, Espoo, Finland) for inclusion in the electromagnetic research group activities of Professor Ari Sihvola and for logistic support;
- *Department of Information Engineering, Electronics and Telecommunications* (DIET, Sapienza) and *Department of Basic and Applied Sciences for Engineering* (SBAI, Sapienza) for software licenses and doctoral funds.

This PhD thesis is composed of self-consistent Chapters (some are drawn from published papers, others present further works and advancements) that encompass a variety of topics and projects. In Chapter 2, I have presented the theoretical fundamentals, with particular regard for Floquet's theorem, metamaterials, homogenization technique, transmission line theory, fabrication methods, THz-TDS, Davidenko's method, and polarizability concept. In Chapter 3, I have expanded and reworked the theoretical analysis underlying the retrieval of equivalent-circuit networks capable of describing the electromagnetic behavior of one-dimensional and two-dimensional periodic arrays; I have validated the derived EC models through numerical comparisons with FEM-based simulations. Chapter 4 contains the improvement of EC models for layered apertures in thin metallic films and the related numerical results published as "Equivalent-circuit model for stacked slot-based 2D periodic arrays of arbitrary geometry for broadband analysis" in Ref. [31]. In Chapter 5, I have designed and analyzed the

electromagnetic behavior of THz metamaterial absorbers with various spectral responses, published as “Ultra-thin narrow-band, complementary narrow-band, and dual-band metamaterial absorbers for applications in the THz regime” in Ref. [32] (see also Refs. [33, 34] for intermediate studies). In Chapter 6, I have reported the development of a broadband THz metamaterial absorber and the analyses published as “Broad-band terahertz metamaterial absorber with stacked electric ring resonators” in Ref. [35]. Chapter 7 describes parametric macromodels for the optimization of metamaterial-based devices and the numerical validations published as “Efficient design of metamaterial absorbers using parametric macromodels” in Ref. [36]. In Chapter 8, a custom reflection-mode THz-TDS setup has been devised for oblique incidence characterization of the fabricated THz metamaterial absorber published as “Polarization-maintaining reflection-mode THz time-domain spectroscopy of a polyimide based ultra-thin narrow-band metamaterial absorber” in Ref. [37]. Chapter 9 collects some transmission/reflection mode THz-TDS experiments on polyimide samples as well as polyimide-based metamaterial devices. In Chapter 10, I have investigated scatterers with strongly discontinuous impedance boundary conditions through finite element analysis that have contributed to the conference paper published as “Analysis of scatterers with discontinuous impedance boundary condition using surface-integral equation method” in Ref. [38]. In Chapter 11, I have drawn the conclusions of this thesis. In Appendixes, I have added various insights to improve readability and integrate the contents of some Chapters: in Appendix A, I have described the equivalent circuit model for a single periodic slot-based frequency selective surface embedded within two arbitrary dielectric half-spaces used in Chapter 4; in Appendix B, I have presented the design of the prism component and some additional measurements related to Chapter 8; in Appendix C, I have tested the simulation domains proposed in Chapter 10 for the polarizability calculation of rotationally symmetric scatterers.

References

- [1] J. Chamberlain, “Where optics meets electronics: recent progress in decreasing the terahertz gap,” *Philosophical Transactions of the Royal Society of London A: Mathematical, Physical and Engineering Sciences*, vol. 362, no. 1815, pp. 199–213, 2004.
- [2] S. Savel’ev, V. Yampol’Skiĭ, A. Rakhmanov, and F. Nori, “Terahertz Josephson plasma waves in layered superconductors: spectrum, generation, nonlinear and quantum phenomena,” *Reports on Progress in Physics*, vol. 73, no. 2, p. 026501, 2010.
- [3] S. Tani, F. Blanchard, and K. Tanaka, “Ultrafast carrier dynamics in graphene under a high electric field,” *Physical Review Letters*, vol. 109, no. 16, p. 166603, 2012.
- [4] Y. Ohki, M. Okada, N. Fuse, K. Iwai, M. Mizuno, and K. Fukunaga, “Terahertz time-domain spectroscopic analysis of molecular behavior in polyamide nanocomposites,” *Applied Physics Express*, vol. 1, no. 12, p. 122401, 2008.
- [5] R. Ulbricht, E. Hendry, J. Shan, T. F. Heinz, and M. Bonn, “Carrier dynamics in semiconductors studied with time-resolved terahertz spectroscopy,” *Reviews of Modern Physics*, vol. 83, no. 2, p. 543, 2011.
- [6] L. V. Titova, A. K. Ayesheshim, A. Golubov, R. Rodriguez-Juarez, R. Woycicki, F. A. Hegmann, and O. Kovalchuk, “Intense THz pulses down-regulate genes associated with skin cancer and psoriasis: a new therapeutic avenue?,” *Scientific Reports*, vol. 3, p. 2363, 2013.
- [7] T. Kürner and S. Priebe, “Towards THz communications—status in research, standardization and regulation,” *Journal of Infrared, Millimeter, and Terahertz Waves*, vol. 35, no. 1, pp. 53–62, 2014.
- [8] S. Nishizawa, K. Sakai, M. Hangyo, T. Nagashima, M. W. Takeda, K. Tominaga, A. Oka, K. Tanaka, and O. Morikawa, “Terahertz time-domain spectroscopy,” in *Terahertz Optoelectronics*, pp. 203–270, Springer, 2005.
- [9] B. Fischer, M. Walther, and P. U. Jepsen, “Far-infrared vibrational modes of DNA components studied by terahertz time-domain spectroscopy,” *Physics in Medicine & Biology*, vol. 47, no. 21, p. 3807, 2002.
- [10] J. F. Federici, B. Schulkin, F. Huang, D. Gary, R. Barat, F. Oliveira, and D. Zimdars, “THz imaging and sensing for security applications—explosives, weapons and drugs,” *Semiconductor Science and Technology*, vol. 20, no. 7, p. S266, 2005.
- [11] P. F. Taday, “Applications of terahertz spectroscopy to pharmaceutical sciences,” *Philosophical Transactions of the Royal Society of London A: Mathematical, Physical and Engineering Sciences*, vol. 362, no. 1815, pp. 351–364, 2004.
- [12] A. G. Davies, A. D. Burnett, W. Fan, E. H. Linfield, and J. E. Cunningham, “Terahertz spectroscopy of explosives and drugs,” *Materials Today*, vol. 11, no. 3, pp. 18–26, 2008.
- [13] A. Gowen, C. O’Sullivan, and C. O’Donnell, “Terahertz time domain spectroscopy and imaging: Emerging techniques for food process monitoring and quality control,” *Trends in Food Science & Technology*, vol. 25, no. 1, pp. 40–46, 2012.
- [14] V. G. Veselago, “The electrodynamics of substances with simultaneously negative values of ϵ and μ ,” *Soviet Physics Uspekhi*, vol. 10, no. 4, p. 509, 1968.
- [15] N. Engheta and R. W. Ziolkowski, *Metamaterials: physics and engineering explorations*. John Wiley & Sons, 2006.
- [16] C. Caloz and T. Itoh, *Electromagnetic metamaterials: transmission line theory and microwave applications*. John Wiley & Sons, 2005.
- [17] A. Sihvola, “Metamaterials in electromagnetics,” *Metamaterials*, vol. 1, no. 1, pp. 2–11, 2007.
- [18] X. Zhang and Z. Liu, “Superlenses to overcome the diffraction limit,” *Nature Materials*, vol. 7, no. 6, p. 435, 2008.

-
- [19] W. Cai, U. K. Chettiar, A. V. Kildishev, and V. M. Shalaev, "Optical cloaking with metamaterials," *Nature Photonics*, vol. 1, no. 4, p. 224, 2007.
- [20] A. Ebrahimi, W. Withayachumnankul, S. Al-Sarawi, and D. Abbott, "High-sensitivity metamaterial-inspired sensor for microfluidic dielectric characterization," *IEEE Sensors Journal*, vol. 14, no. 5, pp. 1345–1351, 2014.
- [21] M. P. Vargas, *Planar Metamaterial Based Microwave Sensor Arrays for Biomedical Analysis and Treatment*. Springer Science & Business Media, 2014.
- [22] A. Erentok and R. W. Ziolkowski, "Metamaterial-inspired efficient electrically small antennas," *IEEE Transactions on Antennas and Propagation*, vol. 56, no. 3, pp. 691–707, 2008.
- [23] N. Landy, S. Sajuyigbe, J. Mock, D. Smith, and W. Padilla, "Perfect metamaterial absorber," *Physical Review Letters*, vol. 100, no. 20, p. 207402, 2008.
- [24] W. Li and J. Valentine, "Metamaterial perfect absorber based hot electron photodetection," *Nano Letters*, vol. 14, no. 6, pp. 3510–3514, 2014.
- [25] N. Landy, C. Bingham, T. Tyler, N. Jokerst, D. Smith, and W. Padilla, "Design, theory, and measurement of a polarization-insensitive absorber for terahertz imaging," *Physical Review B*, vol. 79, no. 12, p. 125104, 2009.
- [26] C. Wu, B. Neuner III, J. John, A. Milder, B. Zollars, S. Savoy, and G. Shvets, "Metamaterial-based integrated plasmonic absorber/emitter for solar thermophotovoltaic systems," *Journal of Optics*, vol. 14, no. 2, p. 024005, 2012.
- [27] S. Savo, D. Shrekenhamer, and W. J. Padilla, "Liquid crystal metamaterial absorber spatial light modulator for THz applications," *Advanced Optical Materials*, vol. 2, no. 3, pp. 275–279, 2014.
- [28] M. Karaaslan, M. Bağmanç, E. Ünal, O. Akgol, and C. Sabah, "Microwave energy harvesting based on metamaterial absorbers with multi-layered square split rings for wireless communications," *Optics Communications*, vol. 392, pp. 31–38, 2017.
- [29] F. Mesa, R. Rodriguez-Berral, and F. Medina, "Unlocking complexity using the ECA: The equivalent circuit model as an efficient and physically insightful tool for microwave engineering," *IEEE Microwave Magazine*, vol. 19, no. 4, pp. 44–65, 2018.
- [30] F. Ferranti, G. Antonini, T. Dhaene, and L. Knockaert, "Parametric macromodeling of lossy and dispersive multiconductor transmission lines," *IEEE Transactions on Advanced Packaging*, vol. 33, no. 2, pp. 481–491, 2010.
- [31] M. D. Astorino, F. Frezza, and N. Tedeschi, "Equivalent-circuit model for stacked slot-based 2D periodic arrays of arbitrary geometry for broadband analysis," *Journal of Applied Physics*, vol. 123, no. 10, p. 103106, 2018.
- [32] M. D. Astorino, F. Frezza, and N. Tedeschi, "Ultra-thin narrow-band, complementary narrow-band, and dual-band metamaterial absorbers for applications in the THz regime," *Journal of Applied Physics*, vol. 121, no. 6, p. 063103, 2017.
- [33] M. D. Astorino, F. Frezza, and N. Tedeschi, "Narrow-band and dual-band metamaterial absorbers in the THz regime," in *URSI International Symposium on Electromagnetic Theory (EMTS)*, pp. 34–37, IEEE, 2016.
- [34] M. D. Astorino and N. Tedeschi, "Design and analysis of an ultra-thin dual-band metamaterial absorber for THz applications," in *XXI Riunione Nazionale di Elettromagnetismo (RiNEm)*, 2016.
- [35] M. D. Astorino, F. Frezza, and N. Tedeschi, "Broad-band terahertz metamaterial absorber with stacked electric ring resonators," *Journal of Electromagnetic Waves and Applications*, vol. 31, no. 7, pp. 727–739, 2017.
- [36] G. Antonini, M. D. Astorino, F. Ferranti, F. Frezza, and N. Tedeschi, "Efficient design of metamaterial absorbers using parametric macromodels," *Applied Computational Electromagnetics Society Journal*, vol. 33, no. 7, pp. 772–780, 2018.

- [37] M. D. Astorino, R. Fastampa, F. Frezza, L. Maiolo, M. Marrani, M. Missori, M. Muzi, N. Tedeschi, and A. Veroli, “Polarization-maintaining reflection-mode THz time-domain spectroscopy of a polyimide based ultra-thin narrow-band metamaterial absorber,” *Scientific Reports*, vol. 8, no. 1, p. 1985, 2018.
- [38] B. B. Kong, P. Ylä-Oijala, M. D. Astorino, H. Wallén, and A. Sihvola, “Analysis of scatterers with discontinuous impedance boundary condition using surface-integral equation method,” in *12th International Congress on Artificial Materials for Novel Wave Phenomena - Metamaterials 2018*, pp. 225–227, IEEE, 2018.

CHAPTER 2

Fundamentals

This Chapter covers the fundamentals of electromagnetic theory applied in this thesis. In the first three sections, I have introduced some general concepts such as Maxwell's equations (Section 2.1), Fresnel's equations (Section 2.2) and Floquet's theorem (Section 2.3). In Section 2.4, I have presented the classification of metamaterials as well as the related modeling methods: Nicolson-Ross-Weir algorithm (Section 2.5) for homogenization and transmission lines (Section 2.6). Since part of my research activity included also the realization and experimental characterization of some metamaterial devices, I have described some well-established fabrication process flows (Section 2.7) and terahertz Time-Domain Spectroscopy (THz-TDS) measurements (Section 2.8); I have also described Davidenko's method (Section 2.9), which has been used to process the THz-TDS experimental data. Focusing the last part of my work on scattering problems, I defined also the concept of polarizability (Section 2.10).

2.1 Electromagnetic wave propagation

Electromagnetic field theory is at the basis of physics and electronic engineering, and it is essential to understand and design complex systems employing scattering, microwave and solid-state circuits, optical communications, quantum electronics, and so on. In particular, the design of circuit models is a practical application of electromagnetic theory, that it is used when the wavelength is bigger with respect to the physical circuit dimensions. But in these advanced circuit systems, the electromagnetic field interactions must be included properly through lumped and distributed elements.

The electromagnetic theory contains a series of theoretical concepts and laws developed by many nineteenth century's scientists that have been combined into a consistent set of vector equations, namely Maxwell's equations [1, 2].

Maxwell's equations govern the relations of the electric and magnetic fields,

charges and currents associated with electromagnetic waves.

We consider the differential form of Maxwell's equations that relates the fields, current and charge densities at any point in space at any time. These relations are properly assumed if the field vectors possess these characteristics: single-valued, bounded, continuous functions of position and time with continuous derivatives. However, in presence of abrupt changes in current and charge densities, for example at interfaces between different media, we have to recourse to the boundary conditions for a complete description of the electromagnetic interaction.

Maxwell's equations in differential form read:

$$\nabla \times \mathbf{E} = -\frac{\partial \mathbf{B}}{\partial t}, \quad (2.1)$$

$$\nabla \times \mathbf{H} = \mathbf{J}_i + \mathbf{J}_c + \frac{\partial \mathbf{D}}{\partial t}, \quad (2.2)$$

$$\nabla \cdot \mathbf{D} = q_{ev}, \quad (2.3)$$

$$\nabla \cdot \mathbf{B} = 0, \quad (2.4)$$

where all the field quantities are time-varying and function of the space coordinates and time:

- \mathbf{E} is the electric field intensity in V/m;
- \mathbf{H} is the magnetic field intensity in A/m;
- \mathbf{D} is the electric flux density in C/m²;
- \mathbf{B} is the magnetic flux density in Wb/m²;
- \mathbf{J}_i is the impressed electric current density in A/m²;
- \mathbf{J}_c is the conduction electric current density in A/m²;
- q_{ev} is the electric charge density in C/m³.

In addition to the four Maxwell's equations, we add the continuity equation that relates the variations of the total current density $J_{ic} = J_i + J_c$ and the charge density q_{ev} :

$$\nabla \cdot \mathbf{J}_{ic} = -\frac{\partial q_{ev}}{\partial t}. \quad (2.5)$$

Assuming then, an $e^{j\omega t}$ time dependence, we can replace the time derivatives in Maxwell's equations in differential form with $j\omega$, obtaining Maxwell's equations in phasor form.

On a macroscopic scale, we need to account for charged particles contained in materials that, interacting with the electromagnetic fields, change the wave

propagation. This can be done with three further constitutive relations:

$$\mathbf{D} = \varepsilon_0 \mathbf{E} + \mathbf{P}, \quad (2.6)$$

$$\mathbf{B} = \mu_0 \mathbf{H} + \mathbf{M}, \quad (2.7)$$

$$\mathbf{J}_c = \sigma \mathbf{E}, \quad (2.8)$$

where \mathbf{P} and \mathbf{M} are the polarization and magnetization, respectively, and for free space $\varepsilon_0 = 10^{-9}/(36\pi)$ F/m is the permittivity, $\mu_0 = 4\pi 10^{-7}$ H/m is the permeability, and $\sigma = 0$ S/m is the conductivity. In general, these constitutive parameters are functions of the applied field strength, its direction, position in the medium and working frequency.

The simplest medium, apart from the vacuum, is a linear, stationary, homogeneous, isotropic, non-dispersive in time and space medium, for which the following relationships are valid:

$$\mathbf{P} = \varepsilon_0 \chi \mathbf{E}, \quad (2.9)$$

$$\mathbf{M} = \mu_0 \chi_m \mathbf{H}, \quad (2.10)$$

where χ and χ_m are dimensionless quantities that are called, respectively, electric and magnetic susceptibility.

Introducing Eqs. (2.9)-(2.10) in Eqs. (2.6)-(2.7), we obtain:

$$\mathbf{D} = \varepsilon \mathbf{E}, \quad (2.11)$$

$$\mathbf{B} = \mu \mathbf{H}, \quad (2.12)$$

with

$$\varepsilon = \varepsilon_0(1 + \chi) = \varepsilon_0 \varepsilon_r, \quad (2.13)$$

$$\mu = \mu_0(1 + \chi_m) = \mu_0 \mu_r, \quad (2.14)$$

where ε_r is the relative permittivity better known as the dielectric constant, and μ_r is the relative permeability. In general, the permittivity and permeability may be complex valued function of the angular frequency ω and tensors. In that case, the imaginary parts of ε and μ account for loss in the medium due to damping of the vibrating dipole moments and damping forces.

At this point, it is useful to introduce the relation between optical and dielectric constants for dielectrics:

$$\varepsilon(\omega) = \hat{n}^2(\omega), \quad (2.15)$$

where the relative complex permittivity $\varepsilon(\omega)$ and the complex index of refraction

$\hat{n}(\omega)$, respectively, can be expanded as:

$$\varepsilon = \varepsilon' - j\varepsilon'', \quad (2.16)$$

$$\tilde{n} = n - j\kappa. \quad (2.17)$$

The dielectric constants can then be explicit in terms of the optical constants:

$$\varepsilon' = n^2 - \kappa^2, \quad (2.18)$$

$$\varepsilon'' = 2n\kappa, \quad (2.19)$$

and vice versa

$$n = \left(\frac{\sqrt{\varepsilon'^2 + \varepsilon''^2} + \varepsilon'}{2} \right)^{\frac{1}{2}}, \quad (2.20)$$

$$\kappa = \left(\frac{\sqrt{\varepsilon'^2 + \varepsilon''^2} - \varepsilon'}{2} \right)^{\frac{1}{2}}. \quad (2.21)$$

The extinction coefficient κ , which determines the optical absorption, is related to the absorption coefficient α , which indicates the amount of absorption loss when the wave propagates through the medium, by the following relation:

$$\alpha = 2\frac{\omega\kappa}{c}. \quad (2.22)$$

Therefore, the way a medium reacts to an external electromagnetic field is determined by dispersion $n(\omega)$ indicating the phase velocity, and absorption $\kappa(\omega) \geq 0$.

The loss tangent $\tan \delta$ is defined as the ratio between the imaginary and real parts of the permittivity:

$$\tan \delta = \frac{\varepsilon''}{\varepsilon'}. \quad (2.23)$$

Maxwell's equations and the constitutive relations can then be combined to give rise to decoupled 2nd-order vector differential equations for \mathbf{E} and \mathbf{H} . If we consider a linear, isotropic and passive medium in a source-free region, along with the relations $\nabla \cdot \varepsilon \mathbf{E} = 0$ and $\nabla \times \nabla \times \mathbf{E} = \nabla(\nabla \cdot \mathbf{E}) - \nabla^2 \mathbf{E}$, the Helmholtz wave equation in the Cartesian coordinate system reads:

$$(\nabla^2 + k^2)\mathbf{E} = 0, \quad (2.24)$$

with plane wave solutions of the form $E = E_0 e^{j(\mathbf{k} \cdot \mathbf{r} - \omega t)}$, where $\mathbf{r} = x\hat{\mathbf{x}} + y\hat{\mathbf{y}} + z\hat{\mathbf{z}}$ and $\mathbf{k} = k_x\hat{\mathbf{x}} + k_y\hat{\mathbf{y}} + k_z\hat{\mathbf{z}}$ are the position and wave vectors, respectively. The dispersion relation is obtained from $k = \sqrt{k_x^2 + k_y^2 + k_z^2} = nk_0 = \omega\sqrt{\mu\varepsilon}$ in which $k_0 = \omega/c$ is the angular wavenumber in vacuum and k is called the propagation constant (or phase constant, or wave number) of the medium.

In an analogous manner, it is possible to derive the wave equation or Helmholtz equation for \mathbf{H} , $(\nabla^2 + k^2)\mathbf{H} = 0$.

2.2 Fresnel equations

On a linear dielectric medium, the boundary conditions for the incident electric and magnetic fields, derived from Maxwell's equations, are:

$$E_{1,\parallel} = E_{2,\parallel}, \quad (2.25)$$

$$\varepsilon_1 E_{1,\perp} = \varepsilon_2 E_{2,\perp}, \quad (2.26)$$

$$\frac{1}{\mu_1} B_{1,\parallel} = \frac{1}{\mu_2} B_{2,\parallel}, \quad (2.27)$$

$$B_{1,\perp} = B_{2,\perp}, \quad (2.28)$$

where the subscripts 1 and 2 denote the two sides of the interface, and the subscripts symbols \parallel and \perp denote the parallel and perpendicular components of the fields at the boundary.

In Fig. 2.1(a), it is described the Transverse Electric (TE) polarization, where the electric field of the incident wave is perpendicular to the incidence plane (i.e. the plane which contains the surface normal and the propagation vector \mathbf{k} of the incident field), while in Fig. 2.1(b), it is treated the symmetric case of Transverse Magnetic (TM) polarization with the electric field parallel to the incidence plane. The angles θ_i , θ_r and θ_t are the angles between the propagation vectors for the incident, reflected and transmitted waves, and the surface normal, related by:

$$\theta_i = \theta_r, \quad (2.29)$$

and by the Snell's law:

$$n_i \sin \theta_i = n_t \sin \theta_t. \quad (2.30)$$

The ratios of the reflected and transmitted field amplitudes due to the boundary conditions are known as the Fresnel equations [1, 2]:

$$r_{TE} = \frac{E_{r,TE}}{E_{i,TE}} = \frac{n_i \cos \theta_i - n_t \cos \theta_t}{n_i \cos \theta_i + n_t \cos \theta_t}, \quad t_{TE} = \frac{E_{t,TE}}{E_{i,TE}} = \frac{2n_i \cos \theta_i}{n_i \cos \theta_i + n_t \cos \theta_t}, \quad (2.31)$$

$$r_{TM} = \frac{E_{r,TM}}{E_{i,TM}} = \frac{n_t \cos \theta_i - n_i \cos \theta_t}{n_t \cos \theta_i + n_i \cos \theta_t}, \quad t_{TM} = \frac{E_{t,TM}}{E_{i,TM}} = \frac{2n_i \cos \theta_i}{n_t \cos \theta_i + n_i \cos \theta_t}, \quad (2.32)$$

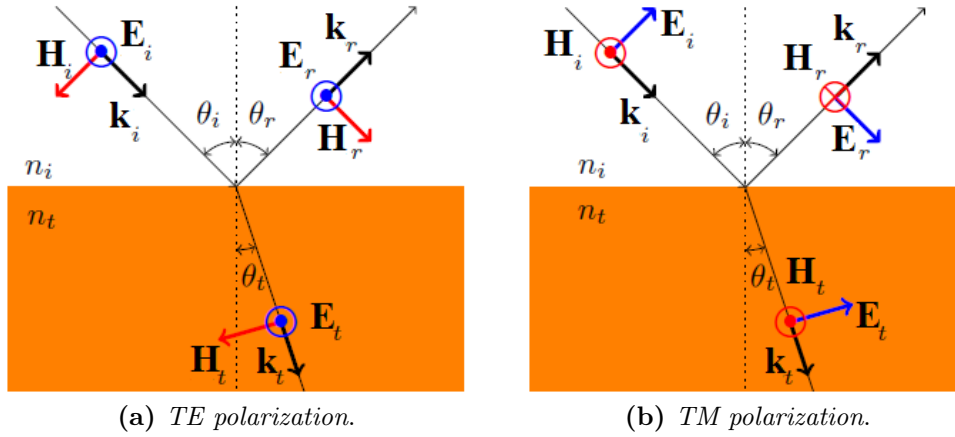


Figure 2.1: (a) The magnetic field lies in the plane of incidence for the transverse electric polarization; (b) the electric field lies in the plane of incidence for the transverse magnetic polarization.

from which reflectance and transmittance are defined as:

$$R = |r|^2 = |S_{11}|^2, \quad (2.33)$$

$$T = \frac{n_t \cos \theta_t}{n_i \cos \theta_i} |t|^2 = |S_{21}|^2, \quad (2.34)$$

where S_{11} and S_{21} are the scattering parameters computed by the numerical electromagnetic solver COMSOL Multiphysics.

2.3 Floquet's theorem

In this thesis, we will deal with 1D and 2D periodic structures, such as slit/strip gratings, frequency selective surfaces, and metamaterial devices. The solution of the wave equation in these periodic media can be derived using a form of Floquet's theorem [3, 4].

The field in an adjacent cell, considering propagating modes in a one-dimensional periodic dielectric structure of periodicity P , is related by a complex constant as follows:

$$E(x, y, z + P) = E(x, y, z)e^{-j\beta P}, \quad (2.35)$$

where $E(x, y, z)$ is a periodic function of z and β is the phase constant in the z -direction. If the propagating mode in the periodic structure has the form:

$$E(x, y, z) = E_p(x, y, z)e^{-j\beta z}, \quad (2.36)$$

where $E_p(x, y, z)$ is a periodic function of z with period P , then:

$$E(x, y, z + P) = E_p(x, y, z + P)e^{-j\beta(z+P)}. \quad (2.37)$$

Since $E_p(x, y, z)$ is periodic with period P :

$$E_p(x, y, z + P) = E_p(x, y, z). \quad (2.38)$$

Substituting Eq. (2.38) into Eq. (2.37) yields:

$$E(x, y, z + P) = E_p(x, y, z)e^{-j\beta(z+P)}, \quad (2.39)$$

and, using Eq. (2.36), we obtain:

$$E(x, y, z + P) = E(x, y, z)e^{-j\beta P}, \quad (2.40)$$

which is exactly Eq. (2.35), a statement of Floquet's theorem.

From the theory of Fourier series, the periodic electric field with period P can be expanded as a periodic function in z and phase constant β and is given by:

$$E(x, y, z) = \sum_n E_n(x, y)e^{-j\frac{2\pi n}{P}z}e^{-j\beta z} = \sum_n E_n(x, y)e^{-j\beta_n z}, \quad (2.41)$$

where the coefficients that serve to represent the dependence on x and y are:

$$E_n(x, y) = \frac{1}{P} \int_0^P E_n(x, y, z)e^{j\frac{2\pi n}{P}z} dz, \quad (2.42)$$

and the phase constant of the n th harmonic is:

$$\beta_n = \beta + \frac{2\pi n}{P}. \quad (2.43)$$

Thus, the field in a periodic structure can be expanded in an infinite set of harmonics through Floquet's theorem, each with frequency f and propagation constant β_n . The phase velocity ν_n of the n th harmonic is:

$$\nu_n = \frac{\omega}{\beta_n} = \frac{\omega}{\beta + \frac{2\pi n}{P}}. \quad (2.44)$$

For slow-wave structures, the phase velocity of the n th harmonic can be less than the free space velocity $\nu_n < c$, while the group velocity ν_g is independent of n :

$$\nu_g = \frac{1}{\frac{\partial \beta_n}{\partial \omega}} = \frac{1}{\frac{\partial(\beta + \frac{2\pi n}{P})}{\partial \omega}} = \frac{\partial \omega}{\partial \beta}. \quad (2.45)$$

In the case of two-dimensional periodic structures, the solution of the electromagnetic problem can be obtained through the use of a double Fourier series, as we will demonstrate in what follows.

Assuming a time dependence of the type $e^{j\omega t}$ and a propagation of the wave

along the z -axis, we have to solve the wave equation (see Eq. (2.24)):

$$(\nabla^2 + k^2)E(x, y, z) = 0, \quad (2.46)$$

where

$$E(x, y, z) = E_t(x, y)e^{-jk_z z}. \quad (2.47)$$

Since there is a periodicity both along the x -axis (P_x) and along the y -axis (P_y), one can write:

$$E(x + P_x, y + P_y, z) = E_t(x, y)e^{-j(k_x P_x + k_y P_y)}e^{-jk_z z}. \quad (2.48)$$

Therefore, on the surface of the two-dimensional periodic structure, the same field is present in each cell except for a phase shift and the analysis can be reduced to that of a single cell of the array.

The wave equation (2.46) can be solved by the method of separation of variables, a standard technique for treating such partial differential equations, by assuming that the solution can be written as a product of two functions for each of the two coordinates $E_t(x, y) = f(x)g(y)$, obtaining:

$$\left[\frac{\partial^2}{\partial x^2} + \frac{\partial^2}{\partial y^2} + (k^2 - k_z^2) \right] E_t(x, y) = 0, \quad (2.49)$$

and dividing by $f(x)g(y)$ gives:

$$\frac{1}{f} \frac{\partial^2 f}{\partial x^2} + \frac{1}{g} \frac{\partial^2 g}{\partial y^2} + (k^2 - k_z^2) = 0. \quad (2.50)$$

We can recognize that each of the terms in Eq. (2.50) must be equal to a constant because they are independent of each other. That is, $\frac{1}{f} \frac{\partial^2 f}{\partial x^2}$ is only a function of x , and the remaining terms in Eq. (2.50) do not depend on x , so $\frac{1}{f} \frac{\partial^2 f}{\partial x^2}$ must be a constant, and similarly for the other term depending on y . Thus, we define two separation constants, k_x and k_y , such that:

$$\frac{\partial^2 f}{\partial x^2} = -k_x^2 f, \quad (2.51)$$

$$\frac{\partial^2 g}{\partial y^2} = -k_y^2 g, \quad (2.52)$$

that combined with Eq. (2.50) give $k_t^2 = k^2 - k_z^2 = k_x^2 + k_y^2$. Therefore, the partial differential equation (2.49) has been reduced to two separate ordinary differential equations in Eqs. (2.51)-(2.52) with solutions $e^{\pm jk_x x}$ and $e^{\pm jk_y y}$.

Considering the only dependence on x , the function f has to assume the form:

$$f(x + P_x) = f(x)e^{-jk_x P_x}. \quad (2.53)$$

Taking the function F into consideration:

$$F(x) = f(x)e^{jk_x x}, \quad (2.54)$$

it results periodic of period P_x since:

$$F(x + P_x) = f(x + P_x)e^{jk_x(x+P_x)} = f(x)e^{-jk_x P_x} e^{jk_x x} e^{jk_x P_x} = F(x). \quad (2.55)$$

Therefore, Eq. (2.54) can be represented with a Fourier series as follows:

$$F(x) = \sum_{n=-\infty}^{+\infty} f_n e^{-j\frac{2\pi n x}{P_x}}, \quad (2.56)$$

from which

$$f(x) = \sum_{n=-\infty}^{+\infty} f_n e^{-j\frac{(2\pi n + k_x P_x)x}{P_x}} = \sum_{n=-\infty}^{+\infty} f_n e^{-jk_{xn}x}. \quad (2.57)$$

Since each term of the series must satisfy Eq. (2.51), we obtain $k_{xn} = \frac{2\pi n}{P_x} + k_x$, and similarly along the y -axis $k_{ym} = \frac{2\pi m}{P_y} + k_y$, where the indexes n, m represent the considered Floquet mode.

At this point, we can write any component of the electric and magnetic fields in terms of Fourier series of the form:

$$E_{nm}(x, y, z) = \sum_{n=-\infty}^{+\infty} \sum_{m=-\infty}^{+\infty} A_{nm} e^{-jk_{xn}x} e^{-jk_{ym}y} e^{-jk_z z}, \quad (2.58)$$

in which A_{nm} represents the modal amplitude. Equation (2.58) is the expansion of the various components of the field in Floquet modes that we were looking for.

2.3.1 Grating lobes

In the analysis of periodic surfaces, the physical understanding of grating lobes is essential [5]. To this purpose, I will provide a derivation for the one-dimensional case with interelement spacing P , as shown in Fig. 2.2. In general, the higher order constructive interference generates, at specific angles, secondary beams. This happens when the unit cell dimensions become electrically large. Defining with θ the incidence angle, each periodic element, with respect to its neighbor located to the left, will be delayed in phase by $\beta P \sin \theta$. Also, the phase in the forward and specular directions of the same element will be enhanced by $\beta P \sin \theta$; at a certain θ , all the wavelets will be in phase, and the total reflected/transmitted

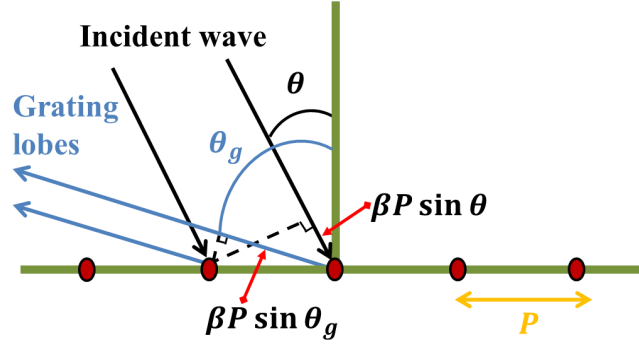


Figure 2.2: Propagation in direction θ_g is possible if $\beta P(\sin \theta + \sin \theta_g) = 2\pi n$.

field is obtained by the superposition of plane waves from the elements. However, propagation could take place also in other directions. As stated in Eq. (2.43), having each Floquet harmonic a different phase velocity, a higher order space harmonic can propagate when its transverse propagation constant $\beta_{n,t} = \beta \sin \theta + 2\pi n/P$ is smaller than that of free-space. If we denote with θ_g the grating lobe direction, grating lobes will appear when the phase delay equals a multiple of 2π , i.e. $\beta P(\sin \theta + \sin \theta_g) = 2\pi n$, and along θ_g direction all waves will be in phase, enabling propagation at the grating frequencies:

$$f_g = \frac{nc}{P(\sin \theta + \sin \theta_g)}. \quad (2.59)$$

2.4 Metamaterials

Starting from Maxwell's equations [1], it is possible to provide more exhaustive constitutive relations for the four field vectors \mathbf{E} , \mathbf{H} , \mathbf{D} , and \mathbf{B} :

$$\mathbf{D} = \bar{\bar{\epsilon}} \cdot \mathbf{E} + \bar{\bar{\xi}} \cdot \mathbf{H}, \quad (2.60)$$

$$\mathbf{B} = \bar{\bar{\mu}} \cdot \mathbf{H} + \bar{\bar{\zeta}} \cdot \mathbf{E}, \quad (2.61)$$

where $\bar{\bar{\epsilon}}$ and $\bar{\bar{\mu}}$ are the 2nd order permittivity and permeability tensors, and $\bar{\bar{\xi}}$ and $\bar{\bar{\zeta}}$ are the 2nd order magneto-electric tensors responsible for any cross-coupling between the electric and magnetic fields.

Along with the usual classification of electromagnetic materials in nonlinear, inhomogeneous and dispersive media, there exist further subclasses:

- *isotropic*: all tensors are scalars and $\bar{\bar{\xi}} = \bar{\bar{\zeta}} = 0$;
- *bi-isotropic*: all tensors are scalars with $\bar{\bar{\xi}} \neq 0$ and $\bar{\bar{\zeta}} \neq 0$;
- *anisotropic*: $\bar{\bar{\epsilon}}$ and $\bar{\bar{\mu}}$ are 2nd rank tensors and $\bar{\bar{\xi}} = \bar{\bar{\zeta}} = 0$;
- *bi-anisotropic*: $\bar{\bar{\epsilon}}$ and $\bar{\bar{\mu}}$ are 2nd rank tensors with $\bar{\bar{\xi}} \neq 0$ and $\bar{\bar{\zeta}} \neq 0$.

Moreover, depending on the four possible sign combinations of permittivity ε and permeability μ , the materials can be classified in the following categories [6], as illustrated in the ε - μ diagram of Fig. 2.3:

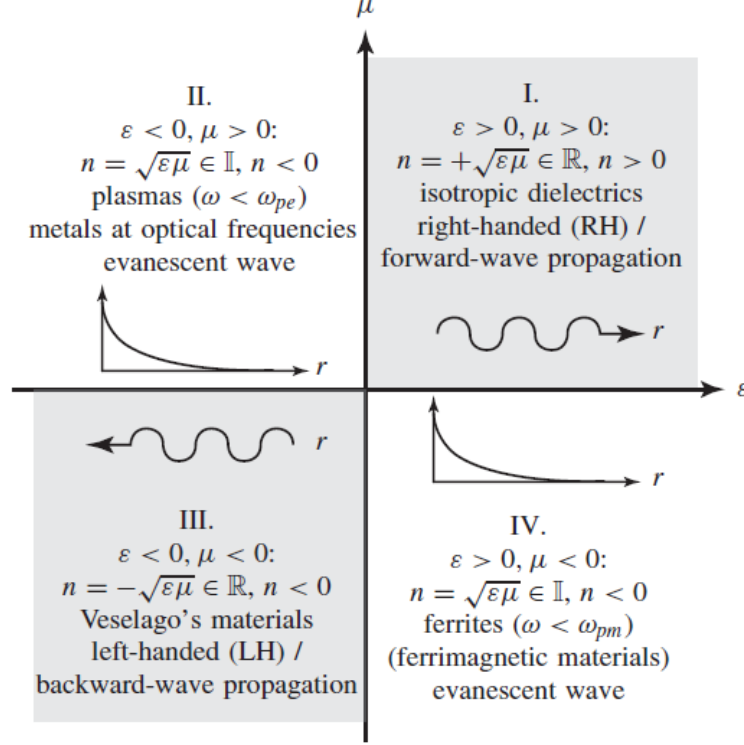


Figure 2.3: Permittivity-permeability and refractive index diagram, where the angular frequencies ω_{pe} and ω_{pm} represent the electric and magnetic plasma frequencies, respectively [6].

- I. *Double Positive (DPS) Material* with both permittivity and permeability greater than zero ($\varepsilon > 0, \mu > 0$), such as isotropic dielectrics;
- II. *Epsilon Negative (ENG) Material* which is a subclass of single negative material (SNG) for which the permittivity is less than zero and permeability greater than zero ($\varepsilon < 0, \mu > 0$), such as the metals at optical frequencies;
- III. *Double Negative (DNG) Material* with both permittivity and permeability less than zero ($\varepsilon < 0, \mu < 0$), such as the artificial Veselago's materials;
- IV. *Mu Negative (MNG) Material* which is a subclass of single negative material (SNG) for which the permittivity is greater than zero and permeability less than zero ($\varepsilon > 0, \mu < 0$), such as ferrites and some gyrotropic materials.

From this classification, we can see how the DNG materials represent a class of Left-Handed (LH) materials characterized by antiparallel phase and group velocities or Negative Refractive Index (NRI) due to the simultaneously negative

permittivity and permeability [7]. Other associated phenomena are the reversal of Doppler effect, of Vavilov-Cerenkov radiation, of the boundary conditions relating the normal components of the electric and magnetic fields at the interface between a conventional/Right-Handed (RH) medium and an LH medium, of Snell's law, plasmonic expressions of the constitutive parameters in resonant-type LH media and interchange of convergence and divergence effects in convex and concave lenses [6].

Thus, LH materials are known as metamaterials, being man-made artificial structures able to exhibit unusual properties. The term metamaterial, however, should not be confined only to the category of the LH structures, because it describes a wider variety of devices, for example, anisotropic metamaterials or structures engineered with proper nanotechnology and chemistry processes.

Now we can get to a broader definition of electromagnetic metamaterials: *artificially effectively homogeneous electromagnetic structures with unusual properties not readily available in nature* [6, 7]. In an effectively homogeneous structure, the structural average cell size p should be at least smaller than a quarter of the guided wavelength $p < \lambda_g/4$, known as the effective homogeneity limit. If this condition is satisfied, the refractive phenomena will dominate over scattering/diffraction phenomena, and the metamaterial structure is electromagnetically uniform along the direction of propagation and macroscopically described through the constitutive parameters (the permittivity ε and the permeability μ).

2.5 Homogenization through Nicolson-Ross-Weir algorithm

In order to derive the constitutive parameters of a d -thick material from the scattering coefficients S_{11} (reflection coefficient) and S_{21} (transmission coefficient), we have considered the transfer matrix T which relates the electric field and the reduced magnetic field ($\mathbf{H}_{red} = j\omega\mu_0\mathbf{H}$) at the two slab interfaces [8–14]:

$$T = \begin{pmatrix} T_{11} & T_{12} \\ T_{21} & T_{22} \end{pmatrix} = \begin{pmatrix} \cos(nk_0d) & -\frac{z}{k_0} \sin(nk_0d) \\ \frac{k_0}{z} \sin(nk_0d) & \cos(nk_0d) \end{pmatrix} \quad (2.62)$$

The scattering matrix elements can be obtained through the terms of the transfer matrix, according to the following relationships:

$$S_{11} = \frac{T_{11} - T_{22} + \left(jk_0T_{12} - \frac{T_{21}}{jk_0} \right)}{T_{11} + T_{22} + \left(jk_0T_{12} + \frac{T_{21}}{jk_0} \right)}, \quad (2.63)$$

$$S_{12} = \frac{2\det(T)}{T_{11} + T_{22} + \left(jk_0T_{12} + \frac{T_{21}}{jk_0}\right)}, \quad (2.64)$$

$$S_{21} = \frac{2}{T_{11} + T_{22} + \left(jk_0T_{12} + \frac{T_{21}}{jk_0}\right)}, \quad (2.65)$$

$$S_{22} = \frac{T_{22} - T_{11} + \left(jk_0T_{12} - \frac{T_{21}}{jk_0}\right)}{T_{11} + T_{22} + \left(jk_0T_{12} + \frac{T_{21}}{jk_0}\right)}. \quad (2.66)$$

If the slab is made of a homogeneous material, it results that $T_{11} = T_{22} = T_0$ and $\det(T) = 1$, from which the scattering matrix is symmetric:

$$S_{11} = S_{22} = \frac{\frac{1}{2}\left(jk_0T_{12} - \frac{T_{21}}{jk_0}\right)}{T_0 + \frac{1}{2}\left(jk_0T_{12} + \frac{T_{21}}{jk_0}\right)}, \quad (2.67)$$

$$S_{12} = S_{21} = \frac{1}{T_0 + \frac{1}{2}\left(jk_0T_{12} + \frac{T_{21}}{jk_0}\right)}. \quad (2.68)$$

By replacing the analytical expressions of the elements of the transfer matrix T in the Eqs. (2.67)-(2.68), the following scattering parameters are obtained at normal incidence at the interface of a homogeneous slab in vacuum:

$$S_{11} = S_{22} = \frac{j}{2}\left(\frac{1}{z} - z\right) \sin(nk_0d)S_{21}, \quad (2.69)$$

$$S_{12} = S_{21} = \frac{1}{\cos(nk_0d) - \frac{j}{2}\left(z + \frac{1}{z}\right) \sin(nk_0d)}. \quad (2.70)$$

The refractive index n and the wave impedance of the slab z can, therefore, be expressed in terms of the scattering parameters through the relations:

$$n = \pm \frac{1}{k_0d} \arccos\left[\frac{1}{2S_{21}}(1 - S_{11}^2 + S_{21}^2)\right], \quad (2.71)$$

$$z = \pm \sqrt{\frac{(1 + S_{11})^2 - S_{21}^2}{(1 - S_{11})^2 - S_{21}^2}}. \quad (2.72)$$

However, the expressions for n and Z are complex functions with multiple branches due to the arccosine that can generate ambiguity in determining ε_r and μ_r . These problems can be solved if the electromagnetic characteristics of the

material are known a priori. In the case of passive materials, in fact, the conditions $\text{Re}(Z) > 0$ and $\text{Im}(n) > 0$ must be respected leading to the expressions:

$$\text{Im}(n) = \pm \text{Im} \left(\frac{1}{k_0 d} \cos^{-1} \left[\frac{1}{2S_{21}} (1 - S_{11}^2 + S_{21}^2) \right] \right), \quad (2.73)$$

$$\text{Re}(n) = \pm \text{Re} \left(\frac{1}{k_0 d} \cos^{-1} \left[\frac{1}{2S_{21}} (1 - S_{11}^2 + S_{21}^2) \right] \right) + \frac{2\pi m}{k_0 d}, \quad (2.74)$$

where m is an integer.

The relative electric permittivity and magnetic permeability can subsequently be obtained through the relationships:

$$\varepsilon_r = \frac{n}{z}, \quad (2.75)$$

$$\mu_r = nz. \quad (2.76)$$

2.6 Transmission line theory

Transmission line theory is at the basis of circuit analysis when the physical dimensions of the network are of many wavelengths. Along a transmission line, the voltages and currents can vary in amplitude and phase, determining the distributed nature of the network parameters [1, 2, 6].

A schematic representation of an infinitesimal length Δz of transmission line is often constituted by two-wire line, as shown in Fig. 2.4(a). This section can be modeled as a lumped-element circuit whose per-unit-length parameters are the series resistance R in Ω/m , the series inductance L in H/m , the shunt conductance G in S/m , and the shunt capacitance C in F/m .

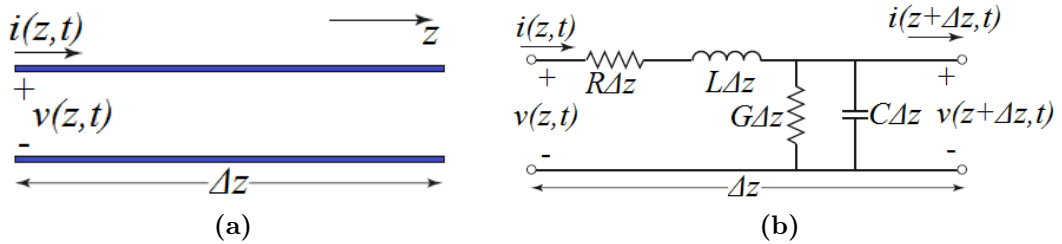


Figure 2.4: (a) An infinitesimal length Δz of transmission line with its voltage and current definitions, and (b) the lumped-element equivalent circuit.

By applying Kirchhoff's voltage and current laws to the circuit in Fig. 2.4(b) and taking the limit as $\Delta z \rightarrow 0$, the telegrapher equations with cosine-based phasors read:

$$\frac{dV(z)}{dz} = -(R + j\omega L)I(z), \quad (2.77)$$

$$\frac{dI(z)}{dz} = -(G + j\omega C)V(z). \quad (2.78)$$

These two equations can be solved simultaneously to provide wave equations for $V(z)$ and $I(z)$:

$$\frac{d^2V(z)}{dz^2} - \gamma^2V(z) = 0, \quad (2.79)$$

$$\frac{d^2I(z)}{dz^2} - \gamma^2I(z) = 0, \quad (2.80)$$

where the complex propagation constant is $\gamma = \alpha + j\beta = \sqrt{(R + j\omega L)(G + j\omega C)}$. From the traveling wave solutions $V(z) = V_0^+ e^{-\gamma z} + V_0^- e^{\gamma z}$ and $I(z) = I_0^+ e^{-\gamma z} + I_0^- e^{\gamma z}$, it is possible to introduce $Z_0 = \sqrt{(R + j\omega L)/(G + j\omega C)}$, namely the characteristic impedance.

If the transmission line, that we suppose lossless, is terminated at $z = 0$ in an arbitrary load impedance Z_L , this is related to the total voltage and current at the load by $Z_L = \frac{V_0^+ + V_0^-}{V_0^+ - V_0^-}$.

Therefore, we can introduce the voltage reflection coefficient $\Gamma(0)$ as the ratio between the amplitude of the reflected voltage wave and the amplitude of the incident voltage wave:

$$\Gamma(0) = \frac{V_0^-}{V_0^+} = \frac{Z_L - Z_0}{Z_L + Z_0}. \quad (2.81)$$

This reflection coefficient is defined at the load ($z = 0$), but this quantity can be generalized to any point $z = -l$ along the line as follows:

$$\Gamma(l) = \frac{V_0^- e^{-j\beta l}}{V_0^+ e^{j\beta l}} = \frac{Z_L - Z_0}{Z_L + Z_0} = \Gamma(0) e^{-2j\beta l}. \quad (2.82)$$

For a mismatched line, the voltage amplitude is oscillatory with position and also the impedance seen looking into the line must vary with position. The input impedance of a section of transmission line of length l and arbitrary load impedance Z_L is provided by the transmission line impedance equation:

$$Z_{in} = Z_0 \frac{Z_L \cos(\beta l) + jZ_0 \sin(\beta l)}{Z_0 \cos(\beta l) + jZ_L \sin(\beta l)}, \quad (2.83)$$

which can be specialized in a number of specific cases of lossless terminated transmission lines.

2.7 Fabrication methods

Fabrication methods are a key factor to take into account when designing THz devices, as these define the boundaries of the devices to realize: in particular, the materials that can be used and the possible non-idealities [15]. Since the dimensions of the THz wavelengths are between the 100 μm and 1 mm, and since we are going to develop metamaterials, which often require the cell elements to be much smaller than the wavelength, the expected sizes of our geometries are around the few of micrometers.

There are two possible approaches for micro/nano-fabrication: “bottom-up” or “top-down”. The first consists of the use of self-assembly, which involves mainly the control of various chemical processes; while this methodology has proven to be effective for some classes of devices (e.g. Quantum dots), mostly in terms of lower costs, its use is hindered by the high amount of time often required for some processes and/or by the stochastic nature of the results. On the other hand, a top-down approach involves the use of lithographic techniques for the patterning of the layers of materials, while other externally controlled tools are used to deposit or etch the materials; since this method allows to reliably obtain devices with a reasonable level of geometrical non-idealities, we have adopted it for our projects. Moreover, with this choice we managed to profit from the same fabrication procedures, instrumentation and infrastructure already set-up for integrated optical or microelectronics devices.

While the majority of micro/nano-fabrication processes operate at two-dimensional level on very thin films, there are also some three-dimensional processes, such as focused ion beam induced deposition [16]. As a general rule, we can state that 3D structures are definitely more difficult to produce in terms of time, costs, and complexity; most of the development in the field regards mainly the 2D manipulation of the structures, so micro/nano-fabrication are usually biased towards planar structures. It must be also underlined that many 3D structures can be realized by stacking multiple layers (which also increases costs).

Depending on the specific structure to realize, fabrication process flows are defined as a combination of the operations of Deposition, Lithography, and Etching. In what follows, I will list and describe briefly some of the most popular planar processes from each operation:

1. *Deposition*

- **Evaporation:** during this process, a hot source material (usually metal on pellets) evaporates from the bottom of a chamber (crucible) and then condenses on a surface placed at the top of the chamber (see Fig. 2.5(a)). The whole operation happens inside a low pressure environment, and in order to control the deposition rate the heating of the source is modulated. This

method allows to obtain very flat, pure and thin layers with high precision (less ± 1 nm of error on the thickness is reachable after some tests); a higher degree of repeatability is guaranteed compared to other methods; the deposition is anisotropic and “non-conformal”, which makes it good for “lift-off” processes (see later).

- **Sputtering:** in sputter deposition, also called Physical Vapor Deposition (PVD), some ionized inert gas (anode) is inserted into a chamber, and is attracted by an opposite charged sputtering target (cathode), which is the source of the metal/alloy that needs to be deposited; the collision between the gas (e.g. noble gases) and the target frees some material from the latter, which flows across the chamber to the desired substrate, where they are deposited (see Fig. 2.5(b)). The sputter yield depends on various factors, such as the energy of the incident ions, the masses of the ions and target atoms, the binding energy of atoms in the solid and the incident angle of ions; overall, the sputter machines can be smaller in volume occupation and less expensive than evaporation machines, but their process costs more. Although it requires to set up the parameters accordingly, this process allows to conformally deposit thin layers of a big variety of metals and alloys (see Fig. 2.5(c)); layer flatness and purity can be good, but not such as evaporation.
- **Spin-coating:** spin coaters deposit conformally viscous polymers on flat surfaces through the use of centrifugal force. This is done by dropping some of the liquid polymeric material on the substrate, which is held on the other side by the spinning machine (see Fig. 2.5(d)). Then the holder starts spinning; the concentration and viscosity of the polymer, the angular speed and time of the spinner, and adhesion of the polymer on the substrate are the main parameters used to control the results. Some post-processing is sometimes necessary: some polymers need to be developed (exposed to UV light), most need to be baked (on hotplates), some need time for the evaporation of volatile materials. This method is usually used to deposit layers of polymers with thicknesses between the hundreds of nm and the hundreds of μm ; the variability of the resulting thicknesses is usually relatively high, and it is often wise to expect it to be around 10-15%.

2. *Lithography*

- **Photolithography:** this is a sequence of other microprocesses (see Fig. 2.6) that allow to imprint the desired shapes on a photoresist by exposing it to UV light passing through specific masks. Photoresists may be either

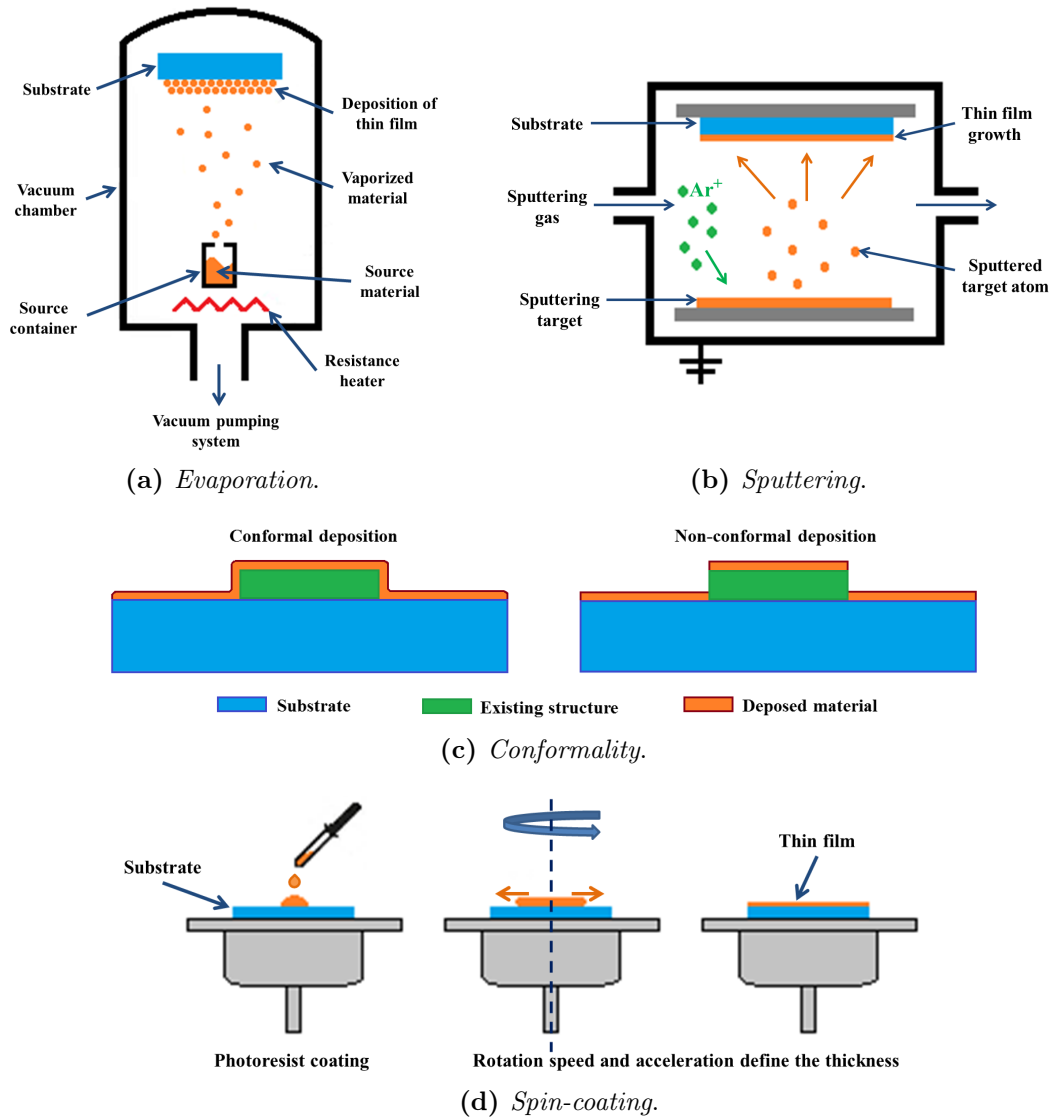


Figure 2.5: Examples of deposition.

negative or positive, which means that they may be hardened or not, respectively, after illumination. By first patterning the photoresist, it is later possible to pattern other materials with processes such as etching or deposition. The resolution of the output is strongly connected with the wavelength of the exposure light; “frontier devices” with a precision of few nanometers can be obtained by using far UV wavelength, in a process called “deep UV Lithography”. This method is favored by the industry, as it allows to produce devices on large areas, thus also on large scale; since it requires the creation of masks, which have non-negligible costs when it involves nanometric shapes, it may be unsuitable for the production of occasional samples.

- Electron Beam Lithography: this method consists in the illumination of the

photoresists by an electron beam, which turns on and off and impinges on every point of a desired area (see Fig. 2.6); depending on the type of photoresist, the illuminated area is developed positively or negatively. Once the pattern is defined in the machine, the beam will be directed through beam steering and micro-mechanical methods. The main parameter to control is the area dose, which is the amount of energy of the beam impinging on a surface and is equal to

$$\text{Area Dose} = \frac{\text{Beam Current} \times \text{Area Dwell Time}}{\text{Step Size} \times \text{Line Spacing}};$$

this is studied along with the possible scattering paths of the electrons. EBL allows to create patterns with the size of a few tens of nanometers without requiring masks; thus, it is a good instrument for the production of single samples. If the energy transported by the beam is weak, it is possible to reconstruct the nanometric image of a structure from the scattered signal, in “Scanning Electron Microscope” (SEM).

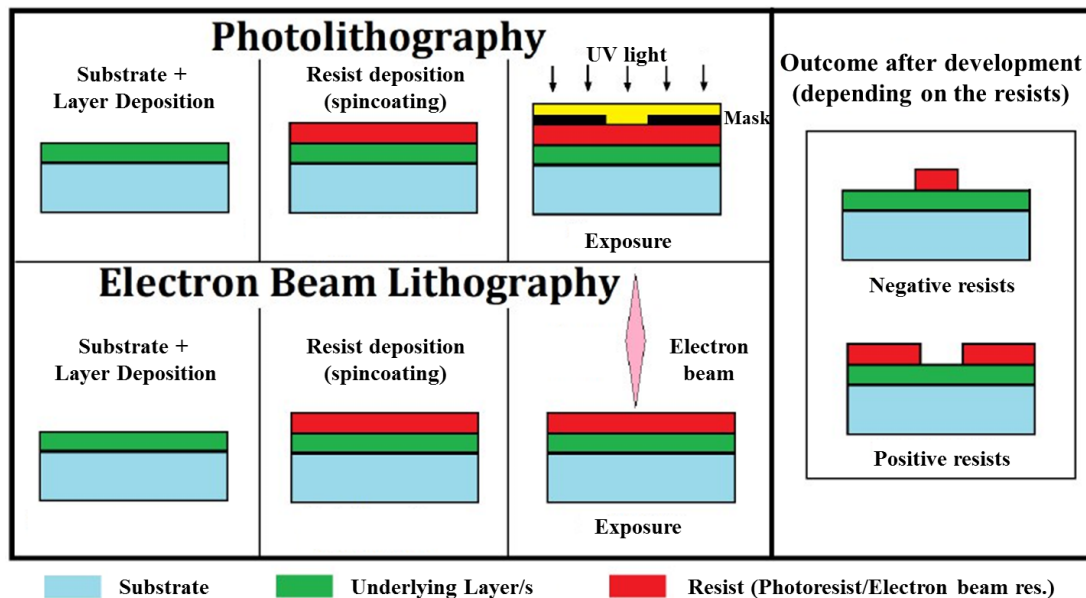


Figure 2.6: Photolithography and electron beam lithography process flows.

3. Etching

- **Wet Etching:** it involves the use of liquid solutions of chemicals in order to remove materials from the samples, usually after these have been patterned through lithography. Two things to keep in mind when using this method are that the removal acts isotropically (in all directions) and that it acts depending on application time; since this last parameter depends on human control, wet etching has a high variability in results if not handled correctly.

On the good side, this option is highly selective (because it regards specific chemical reaction) and cheaper.

- Dry Etching: called also “plasma etching”, it is the removal of material through the bombardment of the sample (after it has been lithographically patterned) by ions (usually a plasma of reactive gases). This type of removal is less selective, and removal rate needs to be weighted from material to material. This method is anisotropic, more repeatable, stable, which greatly counterbalance the increase in cost.

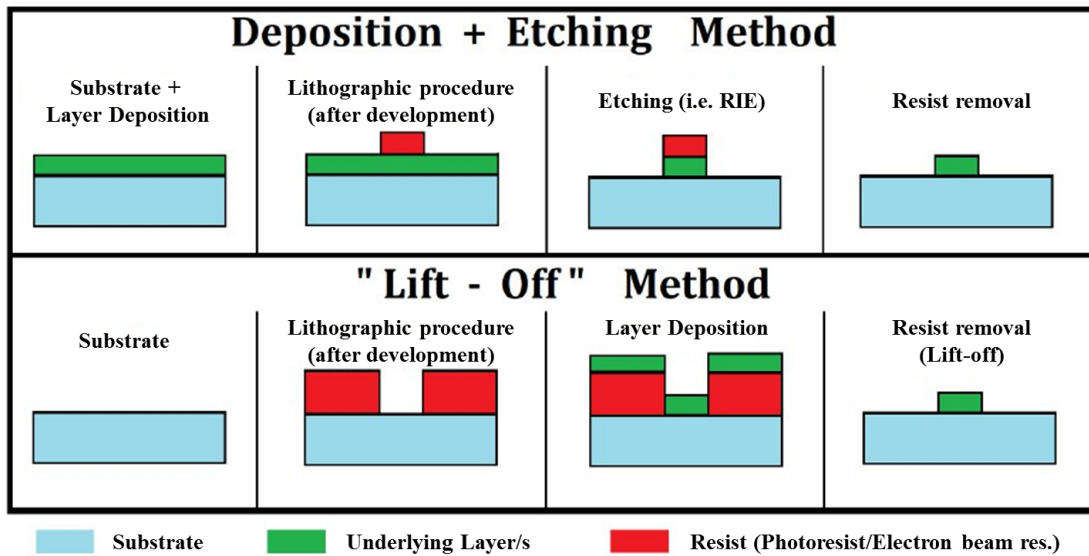


Figure 2.7: Deposition, etching, and lift-off methods.

Over the years the sequences of micro/nano-fabrication processes for the patterning of single planar layers have been standardized into two main ways: deposite-and-etch and lift-off (see Fig. 2.7). In order to produce more complex structures, multiple layers can be stacked; this requires a good control over the alignment between the layers, which is done through a correct use of markers.

Most of my devices were metamaterials, which are planar in nature, so standardized choices were also more effective. We opted mainly for lift-off processes because of the repeatability of the shapes and the low variability of the geometrical dimensions. Furthermore, we adapted our processes for THz devices from others already set up for microelectronics and integrated optics devices.

I had a heuristic approach to fabrication. We first defined the available processes that gave us more repeatable results, and the related range of variability of single geometrical parameters. I then calculated numerically geometries that would allow me to have stable performances even in the presence of non-idealities (we sometimes discarded high peak values, because of the volatility of the performances).

The projects I have presented in this thesis confirm the possibility to convert existing methods also for the fabrication of periodic planar THz metamaterials; more interestingly, the development of semi-analytical methods for the theoretical study of the devices helps greatly in the reduction of the workload for the “tolerance analysis”.

2.8 Terahertz time-domain spectroscopy

Terahertz (THz) radiation, also known as T-rays or far-infrared (FIR) radiation, encompasses electromagnetic frequencies in the range from 0.3 THz to 10 THz, between the infrared and microwave frequencies [17], as shown in Fig. 2.8. The two bordering spectra of THz regime have been extensively researched and have produced a wide variety of sources, detectors and devices: at lower frequencies, electronics has found applications in radio-communication technology, while at higher frequencies, laser technology and optical communication have found a fertile area of development. THz radiation is thus in between electronics and optics. Despite the intensive efforts of realizing efficient sources and detectors, THz spectrum has not been exploited for many decades due to technological difficulties, this is why it is also referred to as the “THz gap”.

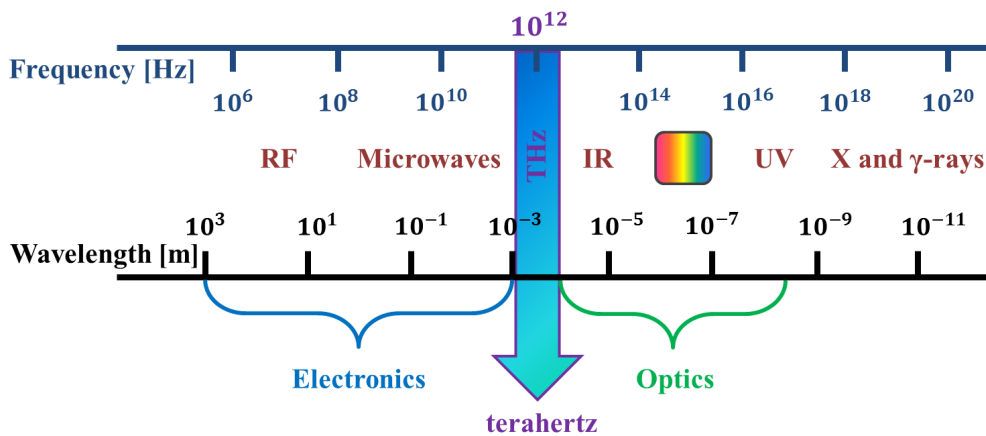


Figure 2.8: Spectrum of the electromagnetic radiation.

Recently, the advent of emerging technologies, such as terahertz Time-Domain Spectroscopy (THz-TDS), has enabled the generation and detection of broadband coherent T-ray radiation, by means of femtosecond mode-locked lasers [18, 19]. Unlike the incoherent-based Fourier Transform Infra-Red (FTIR) spectroscopy, the coherence of this method allows to maintain full amplitude and phase information of the signal and guarantees the insensitivity to thermal background noise.

THz-TDS can perform both transmission and reflection measurements, by adopting proper configurations of the optical elements along the THz path.

Reflection-mode THz spectroscopy is used in the analysis of optically dense sample, due to the high absorption and scattering suffered from the transmitted THz wave. Moreover, this configuration results particularly useful for investigating ground-backed devices, as we have demonstrated in Chapters 8-9 for the characterization of an ultra-thin narrow-band metamaterial absorber.

Transmission-mode THz spectroscopy is the most common and general setup, and its versatility has been exploited for the characterization of ultra-flexible polymers and metasurfaces, described in Chapter 9. A basic transmission-mode THz-TDS setup is sketched in Fig. 2.9.

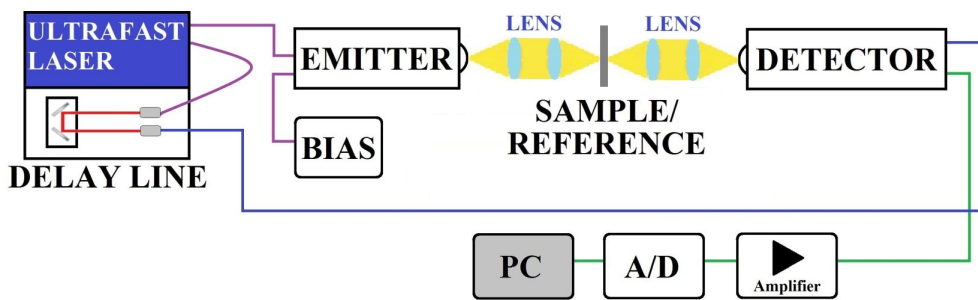


Figure 2.9: Schematic of a basic THz-TDS setup in transmission mode.

The ultrashort laser pulses, by interacting with a specific down-conversion component (such as Auston switch [20], Photo-Conductive Antenna PCA [18], nonlinear crystals [21], semiconductor quantum structures [22], etc.), generate subpicosecond pulses that span a frequency range comprised between few hundred gigahertz and few terahertz. The diverging THz beam is collimated and focused onto the sample/reference by a pair of plano-convex lenses; in some configurations, the guiding optics can be constituted of off-axis parabolic mirrors. The THz radiation can, therefore, be treated as a Gaussian laser beam being coherent, directional and polarized. The THz pulses, after passing through the sample/reference under test, are recollimated and focused by an identical set of lenses onto the detector where they induce a local change in the electric field. At the detector stage, a series of probe laser pulses, synchronized with the femtosecond laser pulses, coherently samples the THz waveform. A low-noise amplifier increases the output current from the detector and, through mechanical micromotions of the optical delay line, the temporal profile of the coherent time-resolved THz pulse is obtained with a high Signal to Noise Ratio (SNR). The delay line is capable of discrete spatial steps Δx , that correspond to discrete temporal steps $\Delta t = 2\Delta x/c$, where c is the speed of light. Therefore, the discrete signal $E(t)$ with $t = q\Delta t$ ($q = 1, 2, \dots, Q$) is obtained by sampling the data at each position of the delay line. The corresponding THz spectrum can be computed via a Fourier

transform:

$$E(\omega) = \frac{1}{2\pi} \int_{-\infty}^{+\infty} E(t)e^{-j\omega t} dt, \quad (2.84)$$

where $\omega = 2\pi f$ is the angular frequency. In order to increase the frequency resolution, the zero padding technique is usually applied by repeating the last value $E(Q\Delta t)$ to reach an array of 1024 or 2048 data points. The complex constitutive parameters of the sample can be extracted through a deconvolution of the reference from the sample measurements. More specifically, by performing two measurements with and without sample we can determine the experimental transfer function $\hat{T}_{exp}(\omega)$:

$$\hat{T}_{exp}(\omega) = T(\omega)e^{j\phi(\omega)} = \frac{E_{sample}(\omega)}{E_{ref}(\omega)}, \quad (2.85)$$

where E_{sample} and E_{ref} are the sample and reference spectra, respectively.

By solving the electromagnetic problem with and without sample we can determine the theoretical transfer function $\hat{T}_{theo}(\omega)$. At this point, by equating these two transfer functions we can extract the complex refractive index, by adopting some numerical resolution methods, such as Davidenko's method described in Section 2.9.

Since in our experiments (see Chapters 8-9) we used PCAs as conversion components for both the generation and detection of THz pulses via the photo-carrier transport process, the related physical mechanisms are described in detail in what follows. Figure 2.10 shows the H-shaped PCA [18], composed of two parallel coplanar transmission lines with protruding arms that act as a Hertzian dipole with a 5 μm wide photoconductive gap; these microstrip lines are built upon a photoconductive substrate. In order to allow beam focusing and to improve the coupling of T-rays through the index matching with the substrate, we used a silicon hyper-hemispherical lens in optical contact with the substrate.

In the generation phase, the ultrashort optical pulses of a mode-locked laser pump the photoconductive region, causing an increase of free carriers; these, before recombination, are accelerated across the dipole gap thanks to a biasing electric field (see Fig. 2.10(a)). The result is a transient photocurrent and a coherent broadband THz radiation from the dipole. A relation between the photocurrent density $J(t)$, the laser pump intensity $P(t)$, and the impulse response of the PCA $qn(t)v(t)$ is established through the convolution product [23]:

$$J(t) = P(t) * [qn(t)v(t)], \quad (2.86)$$

where q is the electron charge, $n(t)$ is the photocarrier density, and $v(t)$ is the photocarrier velocity. At the far-field, the coherent electric pulse is linearly po-

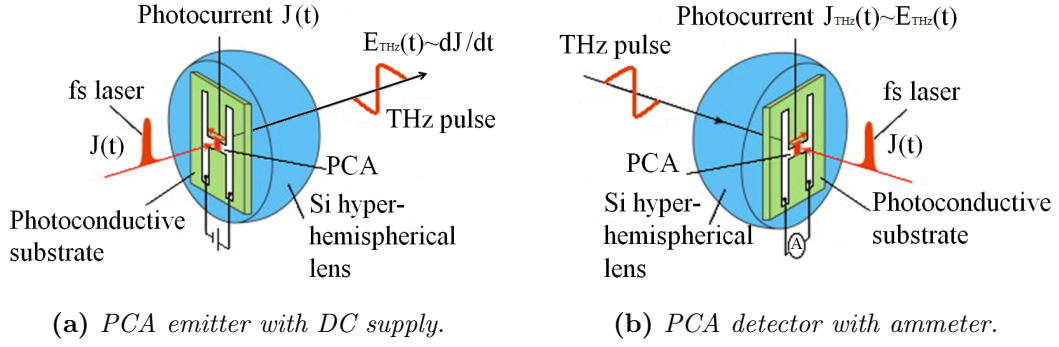


Figure 2.10: Photoconductive antenna details in (a) generation and (b) detection phases, where the red spots mark the laser focuses in the $5 \mu\text{m}$ -wide gap between the electrodes.

larized along the direction of the electric field and proportional to the first-order derivative of the photocurrent density:

$$E_{THz}(t) \propto \frac{dJ(t)}{dt}. \quad (2.87)$$

In the detection phase, when the active region is reached by a THz pulse with the polarization parallel to the dipole, the T-ray electric field induces a photocurrent by sweeping free carriers across the gap (see Fig. 2.10(b)). In this case, the photocarrier velocity in Eq. (2.86) is a function of the impinging THz field. In absence of THz pulse, free carriers recombine without generating a current flow; in fact, the mode-locked laser constantly produces optical probe pulses which excite the photoconductive gap of the PCA.

The results present in literature show the potentialities achieved in these last years by THz technology that has enabled a wide variety of applications: security screening [24], medical diagnostics [25], ultrafast spectroscopy [26], allowing to study the material responses and to detect anomalies through the interactions of THz waves with matter. THz-TDS makes possible investigating rotational transitions of molecules, lattice vibrations in solids, transitions in semiconductors and energy gaps in superconductors as well as allowing for the characterization of THz devices, especially of artificial materials such as engineered THz metamaterials; research in this field is currently very active and offers promising prospects for future developments.

2.9 Davidenko's method and validation by genetic algorithm

In order to determine the constitutive parameters of the sample, the experimental data obtained from THz-TDS need to be post-processed by equating the experimental and theoretical transfer functions ($\hat{T}_{exp}(\omega) = \hat{T}_{theo}(\omega)$, both described in Section 2.8) through Davidenko's method [27–30].

Davidenko's method is a reduction of Newton's method for the numerical solution of m -coupled nonlinear algebraic equations into m -coupled first-order differential equations in a dummy variable. Davidenko's method is a more efficient alternative and allows to relax the extent on the restrictions placed on the initial guess to be sufficiently close to the solution.

The basic idea is to reduce Newton's method for a system of m nonlinear algebraic equations in m unknowns to a set of m first-order Ordinary Differential Equations (ODEs) in a dummy variable ξ . In our case, Davidenko's method has been validated with $m = 2$, namely, in the case of a complex transcendental relation in a complex variable.

Let $f(x) = 0$ be a nonlinear algebraic equation in the variable x . It is possible to approach a root of the equation from an initial guess (i.e., the initial condition $x(0)$ of the differential equation $\frac{dx}{d\xi} = -\frac{f(x)}{df/dx}$) in infinitesimal steps of size dx corresponding to increments $d\xi$ of the dummy variable ξ , arriving at the root for $\xi \rightarrow \infty$. Thus, the original problem $f(x) = 0$ is a particular case of the differential equation for $\xi \rightarrow \infty$: the value of x which satisfies $f(x) = 0$ also satisfies the differential equation for $\xi \rightarrow \infty$, implying $f(x) = Ae^{-\xi}$, being A an integration constant.

In particular, the differential equation $\frac{dx}{d\xi} = -\frac{f(x)}{df/dx}$ can be extended to the m -dimensional case:

$$\frac{d\mathbf{x}}{d\xi} = -\mathbf{J}^{-1}\mathbf{f}(\mathbf{x}), \quad (2.88)$$

where \mathbf{J} is the Jacobian matrix for the m nonlinear algebraic set of equations in m unknowns, that in matrix form reads $\mathbf{f}(\mathbf{x}) = \mathbf{0}$, with $\mathbf{x} = (x_1, x_2, \dots, x_m)^T$, where T stands for transposed matrix.

Equation (2.88) is the basic form of Davidenko's method and can be considered as a system of m initial-value ODEs that can be integrated subjected to an initial condition $\mathbf{x}(0)$.

The asymptotic solutions at $\xi \rightarrow \infty$ could be found to the desired degree of precision by comparing the difference between the results of integrating up to two consecutive intervals; i.e., the quantity $|x(\xi + \Delta\xi) - x(\xi)| \leq \delta$, where δ represents the desired precision. It must be underlined that the algorithm has exponential

convergence with respect to the dummy variable ξ .

The complex transcendental equation with complex roots can be generally expressed as:

$$F(\omega, z) = 0, \quad (2.89)$$

with $z = x + jy$, where the unknowns are the real (x) and the imaginary (y) parts of the complex variable z , respectively. In this particular case, the complex unknown represents the refractive index $\hat{n} = n + j\kappa$, being n and κ the real and imaginary parts of \hat{n} , respectively.

In order to solve Eq. (2.89) for different values of the angular frequency ω , this equation can be treated as a set of two nonlinear algebraic equations in two unknowns by writing it as the set:

$$\text{Re}[F(\omega, \hat{n})] \equiv G(\omega, n, \kappa) = 0, \quad (2.90)$$

$$\text{Im}[F(\omega, \hat{n})] \equiv H(\omega, n, \kappa) = 0. \quad (2.91)$$

In this case, it is possible to express the Jacobian matrix of the system and its inverse in closed form, since the function $F(\omega, \hat{n})$ is an analytical complex function on the \hat{n} -plane except at a finite number of points. The Cauchy-Riemann relations are then satisfied: $G_n = H_\kappa$ and $G_\kappa = -H_n$, where $G_n \equiv \partial G/\partial n$, $G_\kappa \equiv \partial G/\partial \kappa$, and so on. The Jacobian matrix is:

$$J = \begin{bmatrix} G_n & G_\kappa \\ H_n & H_\kappa \end{bmatrix} = \begin{bmatrix} G_n & G_\kappa \\ -G_\kappa & G_n \end{bmatrix}$$

Then, using the properties of analytic functions, we have:

$$\frac{\partial F}{\partial \hat{n}} \equiv G_n + jH_n = G_n - jG_\kappa, \quad (2.92)$$

that is

$$G_n = \text{Re}[F_{\hat{n}}], \quad (2.93)$$

$$G_\kappa = -\text{Im}[F_{\hat{n}}]. \quad (2.94)$$

From the previous equations, the determinant of the Jacobian matrix is:

$$\det J = G_n^2 + G_\kappa^2 = |F_{\hat{n}}|^2, \quad (2.95)$$

from which the inverse Jacobian matrix is:

$$J^{-1} = \frac{1}{\det J} \begin{bmatrix} G_n & -G_\kappa \\ G_\kappa & G_n \end{bmatrix} = \frac{1}{|F_{\hat{n}}|^2} \begin{bmatrix} \text{Re}[F_{\hat{n}}] & \text{Im}[F_{\hat{n}}] \\ -\text{Im}[F_{\hat{n}}] & \text{Re}[F_{\hat{n}}] \end{bmatrix}$$

The formal expression of Davidenko's method with $\mathbf{x} = (n, \kappa)^T$ and $\mathbf{f} = (G, H)^T$ is:

$$\frac{d}{d\xi} \begin{bmatrix} n \\ \kappa \end{bmatrix} = -J^{-1} \begin{bmatrix} G \\ H \end{bmatrix}, \quad (2.96)$$

or, alternatively:

$$\begin{cases} \frac{dn}{d\xi} = -\frac{1}{|F_{\hat{n}}|^2} (\text{Re}[F] \text{Re}[F_{\hat{n}}] + \text{Im}[F] \text{Im}[F_{\hat{n}}]) \\ \frac{d\kappa}{d\xi} = +\frac{1}{|F_{\hat{n}}|^2} (\text{Re}[F] \text{Im}[F_{\hat{n}}] - \text{Im}[F] \text{Re}[F_{\hat{n}}]) \end{cases} \quad (2.97)$$

The system (2.97) of two coupled first-order ODEs represents the expression of the problem $F(\omega, \hat{n}) = 0$ in terms of Davidenko's algorithm. The solution of Eqs. (2.97) for $\xi \rightarrow \infty$ will give us n and κ for a given angular frequency ω to the desired precision δ .

In what follows, Davidenko's method has been applied to analyze dielectric slabs with finite thicknesses of arbitrary permittivity in transmission mode and grounded dielectric slabs in reflection mode under oblique incidence.

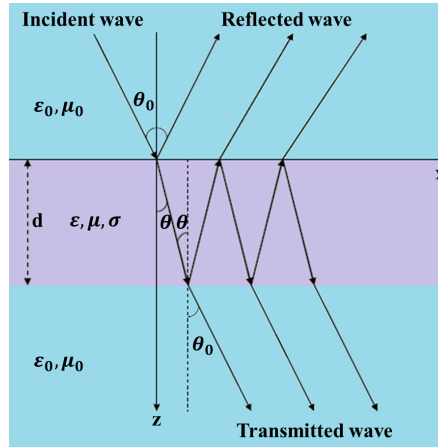


Figure 2.11: Wave propagation inside a dielectric slab of thickness d .

In order to determine the complex refractive index \hat{n} of a d -thick dielectric slab embedded between two air half-spaces (see Fig. 2.11), as a function of frequency, it is necessary to equate the transmission coefficient \hat{T}_{sim} simulated through a numerical solver (COMSOL Multiphysics) with the analytical expression of the transmission coefficient \hat{T}_{theo} , obtained considering the Fabry-Pérot (FP) effects:

$$\begin{aligned} \hat{T}_{theo} &= \frac{E_{sample}^t(\omega)}{E_{ref}^t(\omega)} = (TT'e^{-jk'_z d} + R'^2 TT'e^{-3jk'_z d} + R'^4 TT'e^{-5jk'_z d} + \dots)e^{j\omega d/c} \\ &= TT'e^{-jk'_z d} e^{j\omega d/c} \sum_{m=0}^{+\infty} (R'^2 e^{-2jk'_z d})^m = \frac{TT'e^{-jk'_z d} e^{j\omega d/c}}{1 - R'^2 e^{-2jk'_z d}}, \end{aligned} \quad (2.98)$$

with

$$R = \frac{1 - \hat{n}}{1 + \hat{n}}, \quad (2.99)$$

$$R' = -R, \quad (2.100)$$

$$T = \frac{2}{1 + \hat{n}}, \quad (2.101)$$

$$T' = \frac{2\hat{n}}{1 + \hat{n}}, \quad (2.102)$$

where R and T (R' and T') are the reflection and transmission coefficients at the air/slab (slab/air) interface in normal incidence, $k'_z = \hat{n}\omega/c$ is the z -component of propagation vector in the slab, and $E_{ref}^t(\omega) = e^{-j\omega d/c}$ is the reference field that has propagated the same distance d in vacuum.

The retrieved equation for the transmission mode can be numerically solved, upon substitution of Eqs. (2.99)-(2.102) in Eq. (2.98), defining the cost function:

$$F(\omega, \hat{n}) = \hat{T}_{sim} - \hat{T}_{theo} = \hat{T}_{sim}(\omega) - \frac{4\hat{n}}{(\hat{n} + 1)^2} \frac{e^{-j(\hat{n}-1)\omega d/c}}{1 - \left(\frac{\hat{n}-1}{\hat{n}+1}\right)^2 e^{-2j\hat{n}\omega d/c}}, \quad (2.103)$$

where we have to find \hat{n} complex root that satisfies for each ω the equation $F(\omega, \hat{n}) = 0$. Davidenko's method allows to find the roots of complex functions by the numerical solution of a differential equation in place of the original equation.

In the case of the reflection mode, the equation to solve results:

$$F(\omega, \hat{n}) = \hat{R}_{sim}(\omega) - \hat{R}_{theo}(\omega) = 0, \quad (2.104)$$

with $\hat{R}_{theo}(\omega) = \frac{E_{sample}^r(\omega)}{E_{ref}^r(\omega)}$ and

$$\begin{aligned} E_{sample}^r(\omega) &= R + R'TT'e^{-2jk'_z d} + R'^3TT'e^{-4jk'_z d} + R'^5TT'e^{-6jk'_z d} + \dots = \\ &= R + R'TT'e^{-2jk'_z d} \sum_{m=0}^{+\infty} (R'^2 e^{-2jk'_z d})^m = R + \frac{R'TT'e^{-2jk'_z d}}{1 - R'^2 e^{-2jk'_z d}}. \end{aligned} \quad (2.105)$$

In the proposed examples, I have analyzed the case of dielectric slabs backed by ground plane, whose reflection transfer function is:

$$\begin{aligned} \hat{R}_{theo} &= -(R - TT'e^{-2jk'_z d} + R'TT'e^{-4jk'_z d} - R'^2TT'e^{-6jk'_z d} + \dots) = \\ &= -R + TT'e^{-2jk'_z d} \sum_{m=0}^{\infty} (-R'e^{-2jk'_z d})^m = -R + \frac{TT'e^{-2j\hat{n}\omega d/c}}{1 + R'e^{-2j\hat{n}\omega d/c}}, \end{aligned} \quad (2.106)$$

being $E_{ref}^r(\omega) = -1$ the reference signal for a metallic surface.

In order to validate the results obtained with Davidenko's method, I will provide some numerical tests by using also the continuous genetic algorithm (GA) [31–33].

GA is an optimization technique that allows to find an optimal solution by minimizing the cost function (Eq. (2.103) for the transmission case and Eq. (2.104) for the reflection case).

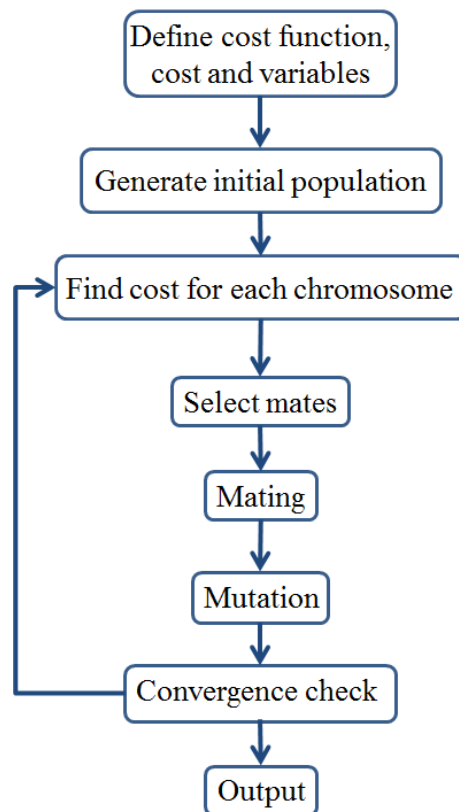


Figure 2.12: Flowchart of the continuous genetic algorithm.

As represented in the flowchart of Fig. 2.12, GA begins with the definition of the optimization variables, of the cost function and of the cost. Following the principles of genetics, in the algorithm, a chromosome is an array of variables that needs to be optimized. The initial population is composed of various chromosomes that, as in a natural selection process, evolve to the most fit members. These are kept for mating and for giving rise to the new offspring. However, GA could converge towards a local rather than a global minimum; in order to solve this inconvenience of fast convergence, some mutations are introduced in the variables by forcing the algorithm to search in other areas of the cost function. GA routine ends by testing for convergence.

2.9.1 Transmission mode: parametric sweep on the slab thickness

In order to check the validity of the two numerical approaches, a dielectric slab of finite variable thickness with a known homogeneous permittivity $\varepsilon_r = \varepsilon' + j\varepsilon'' = 2.9 - 0.25j$ has been analyzed under normal incidence in transmission mode. To this end, FEM-based simulations have been conducted to obtain the transmission scattering parameters, necessary to compute the cost function $\hat{T}_{sim} - \hat{T}_{theo} = 0$. In Fig. 2.13(a)-(b), Eq. (2.103) has been solved through Davidenko's method, while in Fig. 2.13(c)-(d) the same problem has been addressed in terms of continuous genetic algorithm. The extracted constitutive parameters are in good agreement with the expected values and, as shown in figure's insets, slightly decrease when increasing the slab thickness.

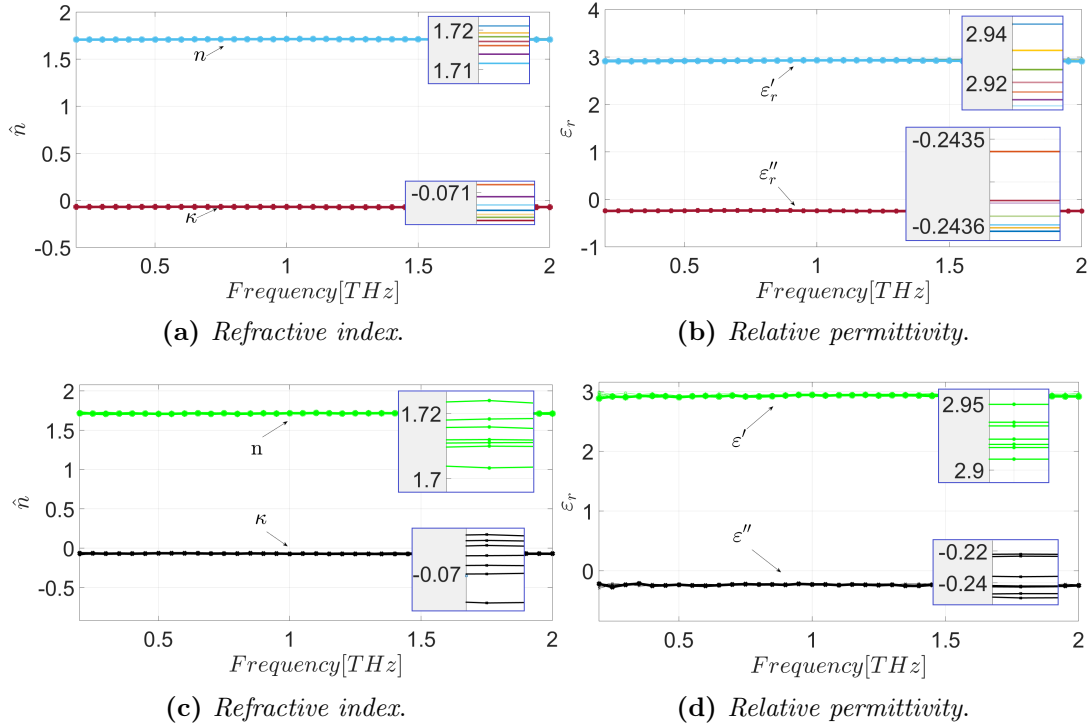


Figure 2.13: Application of (a)-(b) Davidenko's method and (c)-(d) genetic algorithm to a dielectric slab with permittivity $\varepsilon_r = 2.9 - 0.25j$ and different thicknesses between $20 \mu\text{m}$ and $50 \mu\text{m}$ with a $5 \mu\text{m}$ step in order to extract the real and imaginary parts of the refractive index and relative permittivity.

2.9.2 Reflection mode: parametric sweep on the grounded slab thickness

In Figs. 2.14-2.15, the cost function (2.104) has been solved assuming the transfer function in Eq. (2.106) for a grounded slab with thicknesses from $20 \mu\text{m}$ up to $95 \mu\text{m}$ and a fixed dielectric constant as in the previous transmission-mode examples.

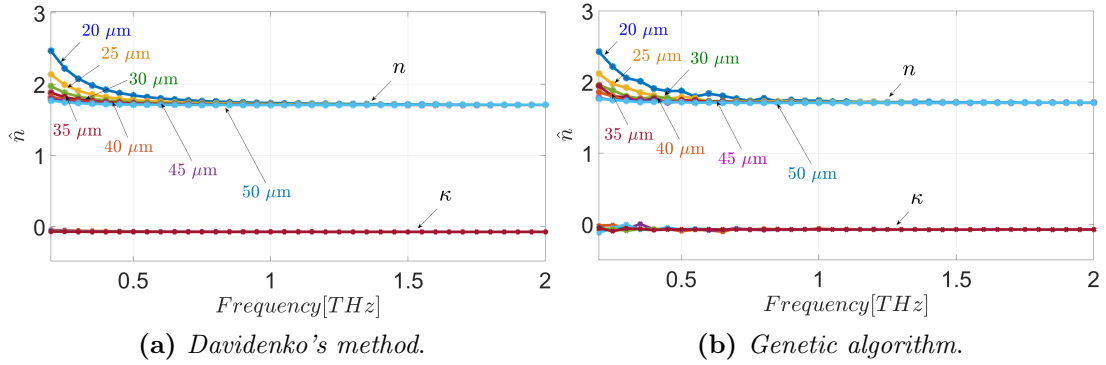


Figure 2.14: Reflection mode analysis for a grounded dielectric slab with permittivity $\varepsilon_r = 2.9 - 0.25j$ ($\hat{n} = 1.7 - 0.073j$) and different thicknesses between $20 \mu\text{m}$ and $50 \mu\text{m}$ with a step of $5 \mu\text{m}$.

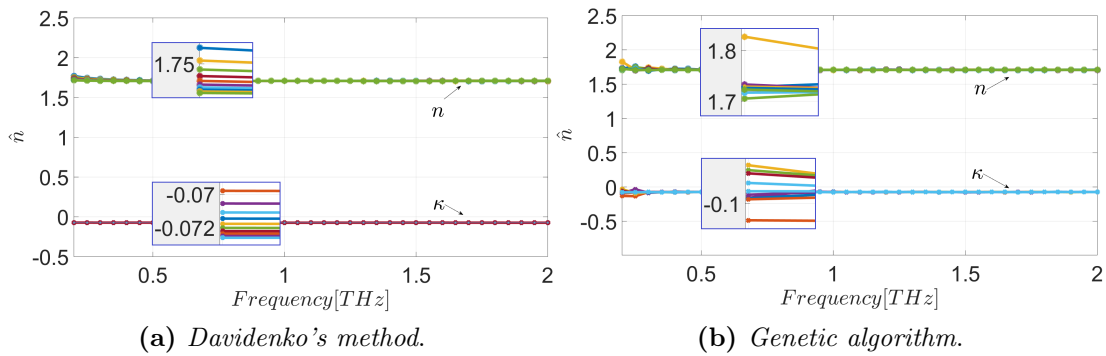


Figure 2.15: Reflection mode analysis for a grounded dielectric slab with permittivity $\varepsilon_r = 2.9 - 0.25j$ ($\hat{n} = 1.7 - 0.073j$) and different thicknesses between $50 \mu\text{m}$ and $95 \mu\text{m}$ with a step of $5 \mu\text{m}$.

2.9.3 Reflection mode: parametric sweep on the grounded slab permittivity

As further validation tests, I have considered a 20 μm -thick grounded dielectric slab with four relative electric permittivity values. For the real part ε' an initial value of 1.5 has been chosen with a step of 0.5, while the imaginary part ε'' starts from -0.1 and ends at -1.0 with steps of 0.3:

- $\varepsilon_r = 1.5 - 0.1j$;
- $\varepsilon_r = 2.0 - 0.4j$;
- $\varepsilon_r = 2.5 - 0.7j$;
- $\varepsilon_r = 3.0 - 1.0j$.

In Fig. 2.16, the obtained parameters increase at low frequencies; this is due to the choice of the initial values in the numerical routine, which are not known a priori. In fact, in the first phase, the implemented algorithm needs some runs to converge to the expected values.

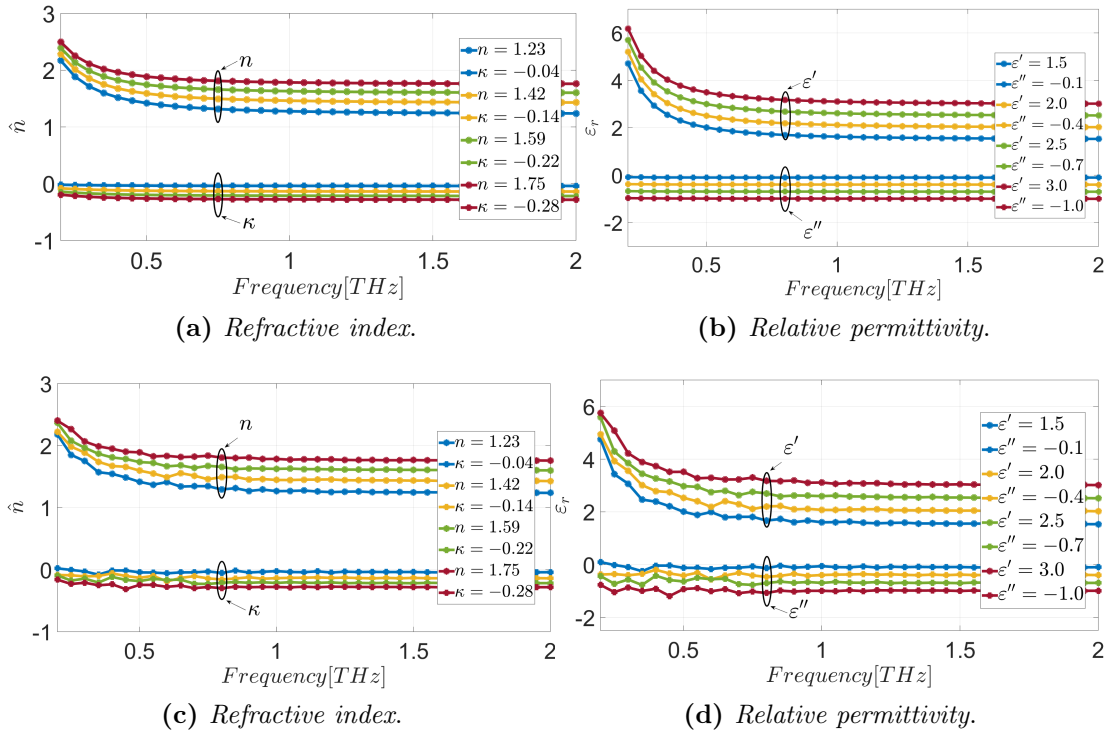


Figure 2.16: Reflection mode analysis with (a)-(b) Davidenko's method and (c)-(d) genetic algorithm for a 20 μm -thick grounded dielectric slab with different complex permittivity values.

2.9.4 Reflection mode: parametric sweep on the grounded slab permittivity in oblique incidence

In the case of oblique incidence under TE polarization, the reflection coefficient at the interface between two media with refractive indexes \hat{n}_1 and \hat{n}_2 is:

$$R_{TE} = \frac{\hat{n}_1 \cos \theta_i - \hat{n}_2 \cos \theta_t}{\hat{n}_1 \cos \theta_i + \hat{n}_2 \cos \theta_t}, \quad (2.107)$$

where θ_i and θ_t represent the incidence and transmitted angles, respectively, related through the Snell's law (see Section 2.2), $\theta_t = \arcsin(\frac{\hat{n}_1}{\hat{n}_2} \sin \theta_i)$.

Therefore, considering a grounded dielectric slab with a complex refractive index $\hat{n}_2 = \hat{n}$ and an upper air half-space $\hat{n}_1 = 1$ under oblique incidence, the analytical expression of the reflection transfer function in Eq. (2.106) when considering the Fabry-Pérot effect becomes:

$$\hat{R}_{theo}(\omega) = -R_{TE} + \frac{T_{TE}T'_{TE}e^{-2j\hat{n} \cos(\theta_i)\omega d/c}}{1 + R'_{TE}e^{-2j\hat{n} \cos(\theta_i)\omega d/c}}, \quad (2.108)$$

where R_{TE} , R'_{TE} , T_{TE} , and T'_{TE} assume analogous expressions as in Eqs. (2.31).

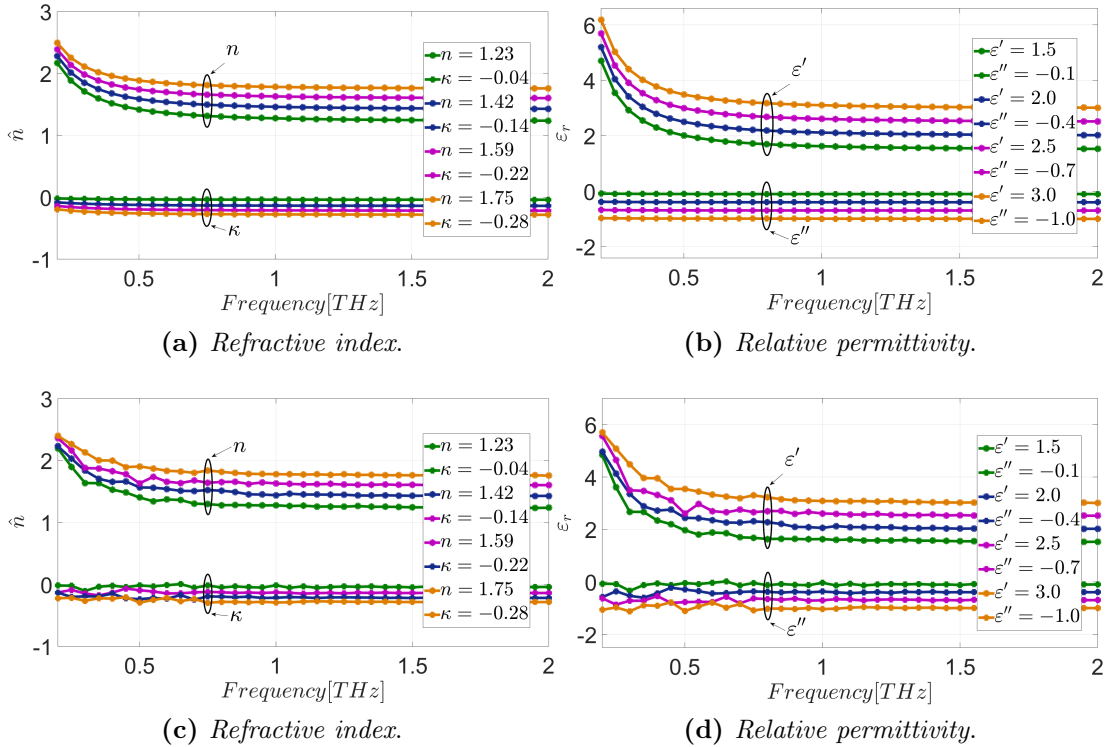


Figure 2.17: Reflection mode analysis under 30° oblique incidence with (a)-(b) Davidenko's method and (c)-(d) genetic algorithm for a $20 \mu\text{m}$ -thick grounded dielectric slab with different complex permittivity values.

2.10 Polarizability

The polarizability α is one of the most significant parameters in electrostatic scattering problems and represents a measure of the response to an incident electric field [34–36]. If we assume a uniform electric field \mathbf{E}_0 in a homogeneous space with permittivity ε and we introduce an object, the total field will be perturbed. If the object has no net charge, it becomes polarized and gives rise to a secondary electric field whose main component is of dipolar type. Thus, it can be approximated by its induced dipole moment \mathbf{p} . The polarizability is defined as the ratio of the induced dipole moment and the magnitude of the incident field \mathbf{E}_0 :

$$\mathbf{p} = \bar{\alpha} \cdot \mathbf{E}_0. \quad (2.109)$$

The normalized polarizability results:

$$\bar{\alpha}_n = \frac{\bar{\alpha}}{\varepsilon V}, \quad (2.110)$$

where ε is the permittivity of the surrounding environment and V is the volume of the object. Therefore, the normalized polarizability of a conducting object depends only on its shape.

In the scattering problems presented in this work, specifically in Chapter 10 and in Appendix C, I will consider rotationally symmetric objects, from which the polarizability dyadic must be axial. By choosing the coordinate system such that the symmetry axis is parallel to the z -axis, we can express the normalized polarizability as follows:

$$\bar{\alpha}_n = \alpha_t(\hat{\mathbf{x}}\hat{\mathbf{x}} + \hat{\mathbf{y}}\hat{\mathbf{y}}) + \alpha_z\hat{\mathbf{z}}\hat{\mathbf{z}} = \alpha_z\hat{\mathbf{z}}\hat{\mathbf{z}} + \alpha_t(\bar{I} - \hat{\mathbf{z}}\hat{\mathbf{z}}), \quad (2.111)$$

where α_t and α_z are the normalized transversal and axial polarizabilities, respectively.

References

- [1] C. A. Balanis, *Advanced engineering electromagnetics*. John Wiley & Sons, 1999.
- [2] J. A. Stratton, *Electromagnetic theory*. John Wiley & Sons, 2007.
- [3] R. E. Collin, *Field theory of guided waves*. IEEE, 1991.
- [4] C. Kittel *et al.*, *Introduction to solid state physics*, vol. 8. 1976.
- [5] B. A. Munk, *Frequency selective surfaces: theory and design*. John Wiley & Sons, 2005.
- [6] C. Caloz and T. Itoh, *Electromagnetic metamaterials: transmission line theory and microwave applications*. John Wiley & Sons, 2005.
- [7] V. G. Veselago, “The electrodynamics of substances with simultaneously negative values of ϵ and μ ,” *Soviet Physics Uspekhi*, vol. 10, no. 4, p. 509, 1968.
- [8] A. Nicolson and G. Ross, “Measurement of the intrinsic properties of materials by time-domain techniques,” *IEEE Trans. Instrum. Meas.*, vol. 19, no. 4, pp. 377–382, 1970.
- [9] W. B. Weir, “Automatic measurement of complex dielectric constant and permeability at microwave frequencies,” *Proceedings of the IEEE*, vol. 62, no. 1, pp. 33–36, 1974.
- [10] O. Luukkonen, S. I. Maslovski, and S. A. Tretyakov, “A stepwise Nicolson–Ross–Weir-based material parameter extraction method,” *IEEE Antennas and Wireless Propagation Letters*, vol. 10, pp. 1295–1298, 2011.
- [11] D. R. Smith, S. Schultz, P. Markoš, and C. M. Soukoulis, “Determination of effective permittivity and permeability of metamaterials from reflection and transmission coefficients,” *Physical Review B*, vol. 65, no. 19, p. 195104, 2002.
- [12] D. Smith, D. Vier, T. Koschny, and C. Soukoulis, “Electromagnetic parameter retrieval from inhomogeneous metamaterials,” *Physical Review E*, vol. 71, no. 3, p. 036617, 2005.
- [13] E. J. Rothwell, J. L. Frasch, S. M. Ellison, P. Chahal, and R. O. Ouedraogo, “Analysis of the Nicolson-Ross-Weir method for characterizing the electromagnetic properties of engineered materials,” *Progress in Electromagnetics Research*, vol. 157, pp. 31–47, 2016.
- [14] X. Chen, T. M. Grzegorzczak, B.-I. Wu, J. Pacheco Jr, and J. A. Kong, “Robust method to retrieve the constitutive effective parameters of metamaterials,” *Physical Review E*, vol. 70, no. 1, p. 016608, 2004.
- [15] C. Papadopoulos, *Nanofabrication: principles and applications*. Springer, 2016.
- [16] A. Benedetti, B. Alam, M. Esposito, V. Tasco, G. Leahu, A. Belardini, R. L. Voti, A. Passaseo, and C. Sibilia, “Precise detection of circular dichroism in a cluster of nano-helices by photoacoustic measurements,” *Scientific Reports*, vol. 7, no. 1, p. 5257, 2017.
- [17] J. Chamberlain, “Where optics meets electronics: recent progress in decreasing the terahertz gap,” *Philosophical Transactions of the Royal Society of London A: Mathematical, Physical and Engineering Sciences*, vol. 362, no. 1815, pp. 199–213, 2004.
- [18] P. U. Jepsen, D. G. Cooke, and M. Koch, “Terahertz spectroscopy and imaging—modern techniques and applications,” *Laser & Photonics Reviews*, vol. 5, no. 1, pp. 124–166, 2011.
- [19] M. C. Nuss and J. Orenstein, “Terahertz time-domain spectroscopy,” in *Millimeter and Submillimeter Wave Spectroscopy of Solids*, pp. 7–50, Springer, 1998.
- [20] D. H. Auston, “Picosecond optoelectronic switching and gating in silicon,” *Applied Physics Letters*, vol. 26, no. 3, pp. 101–103, 1975.
- [21] J. Valdmanis, G. Mourou, and C. Gobel, “Subpicosecond electrical sampling,” *IEEE Journal of Quantum Electronics*, vol. 19, no. 4, pp. 664–667, 1983.
- [22] H. Liu, C. Song, A. SpringThorpe, and J. Cao, “Terahertz quantum-well photodetector,” *Applied Physics Letters*, vol. 84, no. 20, pp. 4068–4070, 2004.

- [23] L. Duvillaret, F. Garet, J.-F. Roux, and J.-L. Coutaz, "Analytical modeling and optimization of terahertz time-domain spectroscopy experiments, using photo-switches as antennas," *IEEE Journal of Selected Topics in Quantum Electronics*, vol. 7, no. 4, pp. 615–623, 2001.
- [24] M. C. Kemp, P. Taday, B. E. Cole, J. Cluff, A. J. Fitzgerald, and W. R. Tribe, "Security applications of terahertz technology," in *Terahertz for Military and Security Applications*, vol. 5070, pp. 44–53, International Society for Optics and Photonics, 2003.
- [25] P. H. Siegel, "Terahertz technology in biology and medicine," *IEEE Transactions on Microwave Theory and Techniques*, vol. 52, no. 10, pp. 2438–2447, 2004.
- [26] E. Hendry, M. Koeberg, J. M. Schins, H.-K. Nienhuys, V. Sundström, L. Siebbeles, and M. Bonn, "Interchain effects in the ultrafast photophysics of a semiconducting polymer: THz time-domain spectroscopy of thin films and isolated chains in solution," *Physical Review B*, vol. 71, no. 12, p. 125201, 2005.
- [27] D. Davidenko, "On a new method of numerically integrating a system of nonlinear equations," *Doklady Akademii Nauk SSSR*, vol. 88, p. 601, 1953.
- [28] S. N. Atluri, C.-S. Liu, and C.-L. Kuo, "A modified Newton method for solving non-linear algebraic equations," *Journal of Marine Science and Technology*, vol. 17, no. 3, pp. 238–247, 2009.
- [29] H. A. Hejase, "On the use of Davidenko's method in complex root search," *IEEE Transactions on Microwave Theory and Techniques*, vol. 41, no. 1, pp. 141–143, 1993.
- [30] S. H. Talisa, "Application of Davidenko's method to the solution of dispersion relations in lossy waveguiding systems," *IEEE Transactions on Microwave Theory and Techniques*, vol. 33, no. 10, pp. 967–971, 1985.
- [31] U. Bodenhofer, "Genetic algorithms: theory and applications," 2003.
- [32] R. L. Haupt and S. E. Haupt, *Practical genetic algorithms*, vol. 2. Wiley New York, 1998.
- [33] D. A. Coley, *An introduction to genetic algorithms for scientists and engineers*. World Scientific Publishing Company, 1999.
- [34] A. H. Sihvola, *Electromagnetic mixing formulas and applications*. No. 47, IET, 1999.
- [35] A. Sihvola and I. Lindell, "Polarizability and effective permittivity of layered and continuously inhomogeneous dielectric spheres," *Journal of Electromagnetic Waves and Applications*, vol. 3, no. 1, pp. 37–60, 1989.
- [36] H. Kettunen, H. Wallén, and A. Sihvola, "Polarizability of a dielectric hemisphere," *Journal of Applied Physics*, vol. 102, no. 4, p. 044105, 2007.

Fully Analytical and Semi-Analytical Equivalent Circuit Models for Strip/Slit Gratings and Frequency Selective Surfaces

This Chapter focuses on the development of fully analytical and semi-analytical Equivalent-Circuit (EC) models capable of determining the transmission and reflection spectra of planar periodically distributed one-dimensional (1D) and two-dimensional (2D) arrangements, such as metal strips, slits made in thin metal screens, and Frequency Selective Surfaces (FSS). The strengths of this formulation include the ability to investigate the devices from the long wavelength limit to the grating lobes regime, thus guaranteeing a broadband analysis, and to incorporate dielectric slabs/grounded substrates by taking into account the higher order mode interactions. The electromagnetic behavior of these periodic elements can be approached by using Floquet's theorem (see Section 2.3).

3.1 Introduction

Over the past decades, the interaction of the electromagnetic waves with periodic structures of planar metallic patches or slot-based arrays has been extensively investigated [1–6]; this has enabled a variety of practical applications from microwaves to the terahertz regime. The scattering problems of waves by various types of transmission gratings had already attracted the attention of many researchers starting from Lord Rayleigh [7], going on to the present time [8–10]. These continuous efforts were addressed to the improvement of diverse applications in the antenna systems, frequency sensitive devices, diffraction gratings, and many others [11].

However, the scattering and the electromagnetic wave propagation problems contain an intrinsic dichotomy in the resolution approach: to resort directly to Maxwell's equations or to find a simplified model. The first choice usually gives

rise to extremely complex analytical/numerical solutions, while the second choice, developed in terms of EC models, provides both a physical insight on the electromagnetic responses and a useful tool in the design phase of periodic devices.

These devices usually exhibit a complex frequency-dependent behavior, which is why they are also called Frequency Selective Surfaces (FSS) [1]. Among the simplest geometries of FSSs, the infinite 1D periodic arrays of strip/slit planar gratings have found recent application in various frequency ranges, thanks to the ease of analytical preprocessing and numerical analysis [12–14]. An intuitive approach for modeling metallic strip/slit gratings consisted in exploiting the equivalent transmission-line circuits that took into account the behavior of the reflected and transmitted fields [15]. The wave propagation along homogeneous media was described through transmission line sections, with their wave impedances and propagation constants, while the energy stored around the zero-thickness discontinuities was synthesized by lumped impedances. The downside within this approach is that only the fundamental mode is assumed as propagative along the waveguide, while the infinite set of high-order modes excited by the discontinuity is evanescent. Thus, despite the simplicity of this one-mode interaction approach [16], it is not possible to fully analyze the structures in the most general case.

Therefore, with the aim to obtain a more versatile circuit network and to provide the potentialities of the EC approach, I have started to study the case of periodic strip/slit gratings by following the guidelines in Ref. [12]. This preliminary 1D analysis helps in better understanding and further progress of the EC models towards the two-dimensional and 2D stacked cases [17–21].

In this analysis, the 1D strip/slit gratings and 2D FSSs are exposed to incoming plane waves from different incident angles in both Transverse Electric (TE) and Transverse Magnetic (TM) polarizations. In order to verify the effectiveness of the EC models, I have compared the obtained results with those computed by the electromagnetic software COMSOL Multiphysics, based on the Finite-Element Method (FEM).

This Chapter is structured as follows. In Sections 3.2-3.4, the formal derivations of the equivalent-circuit models for the cases of strip and slit gratings are provided along with the related numerical validations; after this one-dimensional study, a discussion on how to extend the equivalent circuit networks to deal with the two-dimensional cases is reported. In Section 3.5, the analytical EC model is derived for the patch-based FSSs, accompanied by some numerical examples and by a semi-analytical approach in Section 3.6. In Sections 3.7-3.8, the analysis of slot-based FSSs, i.e., complementary FSSs, is considered, following a similar rationale as that of patch-based FSSs. Section 3.9 contains the conclusions.

3.2 Strip gratings

I considered an equivalent circuit model for 1D periodic array of strips based on an integral-equation approach. This model is able to describe the reflection/transmission responses of the grating from zero frequency up to the frequencies above the onset of the first grating lobes (or trapped modes) [1]. Therefore, an essential parameter in the analysis of periodic structures is the cutoff frequency; the cutoff frequency of the n th harmonic has to satisfy the Floquet dispersion relation (see Section 2.3):

$$\gamma_n^{2(i)} = \omega^2 \varepsilon_i \mu_0 - (k_t + k_n)^2 = 0, \quad (3.1)$$

which can be expressed as:

$$f_{c,n}^{(i)} = \frac{1}{4\pi} \left[\left(\frac{4\pi n c \sin \theta}{P(\varepsilon_{r,i} - \sin^2 \theta)} \right) + \sqrt{\left(\frac{4\pi n c \sin \theta}{P(\varepsilon_{r,i} - \sin^2 \theta)} \right)^2 + \frac{4(2\pi n c)^2}{P^2(\varepsilon_{r,i} - \sin^2 \theta)}} \right], \quad (3.2)$$

with $\varepsilon_i = \varepsilon_0 \varepsilon_{r,i}$ the permittivity of the i th medium where the periodic structure is embedded, μ_0 the free-space permeability, c the speed of light, $k_t = k_1 \sin \theta = \omega \sqrt{\varepsilon_1 \mu_0} \sin \theta$ the tangential component to the grating of the wave vector of the obliquely incident plane wave, θ the incident angle, $k_n = 2\pi n/P$, and P the grating periodicity. This means that for frequencies smaller than the first cutoff frequency $f_{c,\pm 1}$ at normal incidence, the only propagating Floquet harmonic is the fundamental one, which corresponds to $n = 0$, while higher modes are evanescent and decay exponentially away from the grating. However, if the periodic structure is embedded in dielectric media, trapped surface waves occur below the onset of the first grating lobe.

Let us assume a strip infinitely extended along the y -axis with periodicity P and width w along the x -axis, as shown in Fig. 3.1.

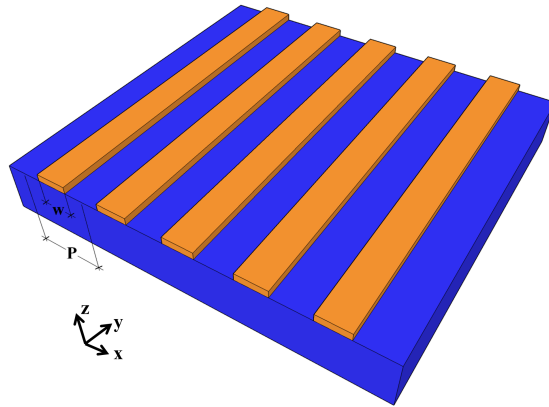


Figure 3.1: Strip grating on a dielectric substrate.

The expansion in a Floquet series of the transverse electric field at the screen interface $z = 0$ reads:

$$E(x) = \sum_{n=-\infty}^{+\infty} E_n e^{-j(k_t+k_n)x} = (1+R)e^{-jk_t x} + \sum_{n=-\infty, n \neq 0}^{+\infty} E_n e^{-j(k_t+k_n)x}, \quad (3.3)$$

where the amplitude of the incident wave has been normalized to unity and R is the reflection coefficient of the fundamental harmonic.

Since we are considering planar periodic metal strip grating, the boundary conditions imply that the electric field results continuous across the dielectric interface and zero on the Perfect Electric Conductor (PEC). Therefore, we can apply the same expansion coefficients at both sides of the grating ($z = 0^-$ and $z = 0^+$), obtaining $1+R=T$ where T is the transmission coefficient, and we can expand the transverse magnetic field as follows:

$$H^{(1)}(x) = Y_0^{(1)}(1-R)e^{-jk_t x} - \sum_{n=-\infty, n \neq 0}^{+\infty} Y_n^{(1)} E_n e^{-j(k_t+k_n)x} \quad z = 0^-, \quad (3.4)$$

$$H^{(2)}(x) = Y_0^{(2)}(1+R)e^{-jk_t x} + \sum_{n=-\infty, n \neq 0}^{+\infty} Y_n^{(2)} E_n e^{-j(k_t+k_n)x} \quad z = 0^+, \quad (3.5)$$

where

$$Y_n^{(i),TE} = \frac{\beta_n^{(i)}}{\omega\mu_0}, \quad (3.6)$$

$$Y_n^{(i),TM} = \frac{\omega\varepsilon_i}{\beta_n^{(i)}}, \quad (3.7)$$

are the transverse with respect to propagation direction z wave admittances of the n th harmonic in the i th medium for the TE and TM polarizations, respectively.

The propagation wavenumber along the z -direction reads:

$$\beta_n^{(i)} = \sqrt{\omega^2\varepsilon_i\mu_0 - (k_t + k_n)^2}. \quad (3.8)$$

In the analysis of the grating, we can consider the surface current on the strips $J_s(x)$ which must equal the discontinuity of the transverse magnetic field:

$$H^{(1)}(x) - H^{(2)}(x) = J_s(x). \quad (3.9)$$

We can substitute the previous expansions of the magnetic field (Eqs. (3.4)

and (3.5)) in the Eq. (3.9), obtaining

$$Y_0^{(1)}(1 - R) - Y_0^{(2)}(1 + R) = \frac{1}{P} \tilde{J}(k_t), \quad (3.10)$$

$$-Y_n^{(1)}E_n - Y_n^{(2)}E_n = \frac{1}{P} \tilde{J}(k_t + k_n), \quad (3.11)$$

where \tilde{J} denotes the Fourier transform of the surface current on the strip of width w :

$$\tilde{J}(k_t) = \int_{-w/2}^{w/2} J_s(x) e^{jk_t x} dx, \quad (3.12)$$

$$\tilde{J}(k_t + k_n) = \int_{-w/2}^{w/2} J_s(x) e^{j(k_t + k_n)x} dx. \quad (3.13)$$

From the Eq. (3.10), we can retrieve:

$$\frac{1}{P} = \frac{Y_0^{(1)}(1 - R) - Y_0^{(2)}(1 + R)}{\tilde{J}(k_t)}, \quad (3.14)$$

and by substituting Eq. (3.14) in Eq. (3.11), we can obtain the expansion coefficients E_n of every spatial harmonic as a function of the reflection coefficient:

$$E_n = \frac{\tilde{J}(k_t + k_n)}{\tilde{J}(k_t)} \frac{R(Y_0^{(1)} + Y_0^{(2)}) - Y_0^{(1)} + Y_0^{(2)}}{Y_n^{(1)} + Y_n^{(2)}}. \quad (3.15)$$

At this point, we can exploit the electric field integral equation:

$$\int_{-w/2}^{w/2} J_s^*(x) E(x) dx = 0. \quad (3.16)$$

In particular, for electrically narrow strips, we can assume that the surface electric current is given by:

$$J_s(x) = A(\omega) f(x), \quad (3.17)$$

where $A(\omega)$ is a frequency-dependent complex amplitude and $f(x)$ is the spatial profile of the surface current invariant with respect to the frequency.

In the final expression of the equivalent circuit impedance, the frequency-dependent term disappears since this impedance depends on the ratio of $\tilde{J}(k_t + k_n)$ to $\tilde{J}(k_t)$. This procedure can be considered as an application of the Method of Moments (MoM) with a Galerkin testing scheme of the Electric Field Integral Equation (EFIE) for the strip when using a single basis function $f(x)$ for the unknown electric current.

Useful choices for the surface electric current profile for TE and TM polarizations [12, 22], respectively, are:

$$f(x) \propto \frac{1}{\sqrt{1 - \left(\frac{2x}{w}\right)^2}} \quad \tilde{f}(x) \propto J_0\left(\frac{kw}{2}\right), \quad (3.18)$$

$$f(x) \propto \sqrt{1 - \left(\frac{2x}{w}\right)^2} \quad \tilde{f}(x) \propto \frac{2}{kw} J_1\left(\frac{kw}{2}\right), \quad (3.19)$$

where J_q represents the Bessel function of the first kind and order q .

Substituting the expansion coefficients of the Eq. (3.15) in the Eq. (3.16), we obtain:

$$\begin{aligned} \int_{-w/2}^{w/2} J_s^*(x) E(x) dx &= \int_{-w/2}^{w/2} J_s^*(x) \left[(1+R)e^{-jk_t x} \right. \\ &+ \left. \sum_{n=-\infty, n \neq 0}^{+\infty} \left(\frac{\tilde{J}(k_t + k_n)}{\tilde{J}(k_t)} \frac{R(Y_0^{(1)} + Y_0^{(2)}) - Y_0^{(1)} + Y_0^{(2)}}{Y_n^{(1)} + Y_n^{(2)}} \right) e^{-j(k_t + k_n)x} \right] dx = 0. \end{aligned} \quad (3.20)$$

From the definition of the Fourier transform, Eq. (3.20) becomes:

$$\begin{aligned} (1+R)\tilde{J}^*(k_t) \\ + \sum_{n=-\infty, n \neq 0}^{+\infty} \left(\frac{\tilde{J}(k_t + k_n)}{\tilde{J}(k_t)} \frac{R(Y_0^{(1)} + Y_0^{(2)}) - Y_0^{(1)} + Y_0^{(2)}}{Y_n^{(1)} + Y_n^{(2)}} \right) \tilde{J}^*(k_t + k_n) = 0; \end{aligned} \quad (3.21)$$

dividing the expression by $\tilde{J}^*(k_t)$:

$$\begin{aligned} (1+R) \\ + \sum_{n=-\infty, n \neq 0}^{+\infty} \left(\left| \frac{\tilde{J}(k_t + k_n)}{\tilde{J}(k_t)} \right|^2 \frac{R(Y_0^{(1)} + Y_0^{(2)}) - Y_0^{(1)} + Y_0^{(2)}}{Y_n^{(1)} + Y_n^{(2)}} \right) = 0, \end{aligned} \quad (3.22)$$

and assuming Eq. (3.17), we can write

$$\begin{aligned} (1+R) \\ + \sum_{n=-\infty, n \neq 0}^{+\infty} \left(\left[\frac{\tilde{f}(k_t + k_n)}{\tilde{f}(k_t)} \right]^2 \frac{R(Y_0^{(1)} + Y_0^{(2)}) - Y_0^{(1)} + Y_0^{(2)}}{Y_n^{(1)} + Y_n^{(2)}} \right) = 0. \end{aligned} \quad (3.23)$$

From the Eq. (3.23), it is possible to find the expression of the reflection

coefficient R :

$$\begin{aligned}
 R &= \frac{-1 + \sum_{n=-\infty, n \neq 0}^{+\infty} \left(\left[\frac{\tilde{f}(k_t + k_n)}{\tilde{f}(k_t)} \right]^2 \frac{Y_0^{(1)} - Y_0^{(2)}}{Y_n^{(1)} + Y_n^{(2)}} \right)}{1 + \sum_{n=-\infty, n \neq 0}^{+\infty} \left(\left[\frac{\tilde{f}(k_t + k_n)}{\tilde{f}(k_t)} \right]^2 \frac{Y_0^{(1)} + Y_0^{(2)}}{Y_n^{(1)} + Y_n^{(2)}} \right)} \\
 &= \frac{-1 + Z_{eq}(Y_0^{(1)} - Y_0^{(2)})}{1 + Z_{eq}(Y_0^{(1)} + Y_0^{(2)})}.
 \end{aligned} \tag{3.24}$$

Therefore, the global impedance of the equivalent circuit results:

$$Z_{eq} = \sum_{n=-\infty, n \neq 0}^{+\infty} \left[\frac{\tilde{f}(k_t + k_n)}{\tilde{f}(k_t)} \right]^2 \frac{1}{Y_n^{(1)} + Y_n^{(2)}}, \tag{3.25}$$

with the topology illustrated in Fig. 3.2.

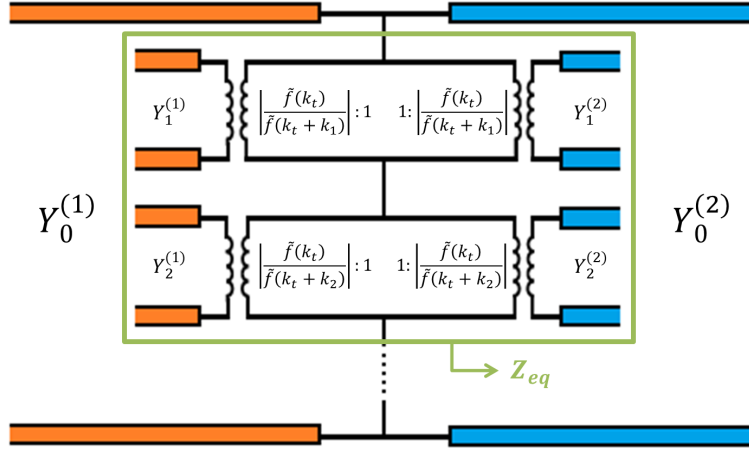


Figure 3.2: Equivalent circuit model for a strip grating embedded between two different dielectric half-spaces.

In the quasi-static limit, where the higher-order harmonics are well below cutoff and the periodicity P is much smaller than the operating wavelength, the periodic structure can be efficiently analyzed by using homogenized theory.

Making the following quasi-static assumptions:

$$\begin{aligned}
 k_t &\ll k_n, \\
 k_t \pm k_n &\approx k_n, \\
 \beta_{n,qs}^{(i)} &\approx -j|k_n|, \\
 Y_{n,qs}^{(i),TE} &= \frac{-j|k_n|}{\omega\mu_0}, \\
 Y_{n,qs}^{(i),TM} &= \frac{\omega\varepsilon_i}{-j|k_n|},
 \end{aligned} \tag{3.26}$$

the equivalent quasi-static impedance can be approximated as:

$$Z_{eq} = \sum_{n=-\infty, n \neq 0}^{+\infty} \left[\frac{\tilde{f}(k_n)}{\tilde{f}(k_t)} \right]^2 \frac{1}{Y_{n,qs}^{(1)} + Y_{n,qs}^{(2)}}, \quad (3.27)$$

and expressed in terms of a lumped inductance for TE harmonics and a lumped capacitance for TM harmonics, through the following frequency-independent series:

$$L_{qs} = \frac{\mu_0}{[\tilde{f}(k_t)]^2} \sum_{n=1}^{+\infty} \frac{[\tilde{f}(k_n)]^2}{k_n}, \quad (3.28)$$

$$\frac{1}{C_{qs}} = \frac{2}{\varepsilon_0(\varepsilon_{r,1} + \varepsilon_{r,2})[\tilde{f}(k_t)]^2} \sum_{n=1}^{+\infty} k_n [\tilde{f}(k_n)]^2. \quad (3.29)$$

The Eqs. (3.28)-(3.29), respectively representing the analytical formulas of the quasi-static inductance and capacitance of a narrow strip grating for TE/TM incidence, are valid when $P \ll \lambda$; therefore, in order to describe the behavior of the structure in the resonance region ($P < \lambda$) up to the grating lobes regime ($P > \lambda$), the equivalent impedance in Eq. (3.25) can be reformulated as:

$$Z_{eq}^{TE} \approx \sum_{n=-N, n \neq 0}^{+N} \left[\frac{\tilde{f}(k_t + k_n)}{\tilde{f}(k_t)} \right]^2 \frac{1}{Y_n^{(1)} + Y_n^{(2)}} + j\omega L_{ho}, \quad (3.30)$$

$$Z_{eq}^{TM} \approx \sum_{n=-N, n \neq 0}^{+N} \left[\frac{\tilde{f}(k_t + k_n)}{\tilde{f}(k_t)} \right]^2 \frac{1}{Y_n^{(1)} + Y_n^{(2)}} + \frac{1}{j\omega C_{ho}}, \quad (3.31)$$

where the first frequency-dependent series takes into account the dominant harmonics, while the lumped frequency-independent L_{ho} and C_{ho} incorporate the effect of all the scattered harmonics of order $|n| > N$:

$$L_{ho} = \frac{\mu_0}{[\tilde{f}(k_t)]^2} \sum_{n=N+1}^{+\infty} \frac{[\tilde{f}(k_n)]^2}{k_n}, \quad (3.32)$$

$$\frac{1}{C_{ho}} = \frac{2}{\varepsilon_0(\varepsilon_{r,1} + \varepsilon_{r,2})[\tilde{f}(k_t)]^2} \sum_{n=N+1}^{+\infty} k_n [\tilde{f}(k_n)]^2, \quad (3.33)$$

with the circuit topology illustrated in Fig. 3.3.

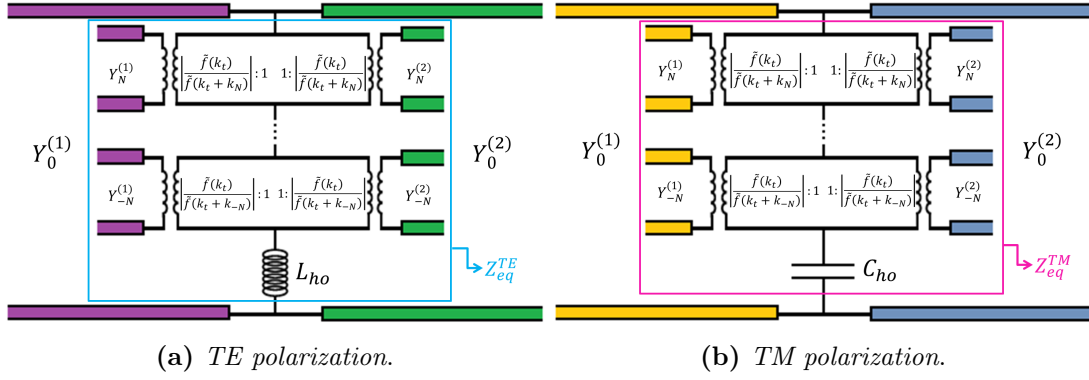


Figure 3.3: Equivalent circuit model for a strip grating between two dielectric half spaces for (a) TE polarization and (b) TM polarization.

3.2.1 Numerical results for a strip grating printed on a grounded dielectric slab under TE incidence

The analytical expression of the lumped frequency-independent inductance L_{ho} in the case of a strip grating on a grounded dielectric slab (see Fig. 3.4) can be extracted upon evaluating the admittance $Y_n^{(2)}$ in Eq. (3.30). This has now to be substituted with the equivalent admittance of a short-circuited transmission line of length equal to the dielectric thickness d (see Section 2.6):

$$Y_n^{(2)} = Y_{IN,n}^{(R)} = -jY_n^{(1)} \cot(\beta_n^{(1)}d). \quad (3.34)$$

Consequently, the lumped high-order inductance is:

$$\begin{aligned}
j\omega L_{ho} &= 2 \sum_{n=N+1}^{+\infty} \left[\frac{\tilde{f}(k_n)}{\tilde{f}(k_t)} \right]^2 \frac{1}{Y_n^{(0)} + Y_{IN,n}^{(R)}} \\
&= 2 \sum_{n=N+1}^{+\infty} \left[\frac{\tilde{f}(k_n)}{\tilde{f}(k_t)} \right]^2 \frac{1}{Y_n^{(0)} - jY_n^{(1)} \cot(\beta_n^{(1)}d)} \\
&= 2 \sum_{n=N+1}^{+\infty} \left[\frac{\tilde{f}(k_n)}{\tilde{f}(k_t)} \right]^2 \frac{1}{\frac{k_n}{j\omega\mu_0} - j\frac{k_n}{j\omega\mu_0} \cot(-jk_n d)} \\
&= 2 \sum_{n=N+1}^{+\infty} \left[\frac{\tilde{f}(k_n)}{\tilde{f}(k_t)} \right]^2 \frac{1}{\frac{k_n}{j\omega\mu_0} + \frac{k_n}{j\omega\mu_0} \coth(k_n d)} \\
&= 2 \sum_{n=N+1}^{+\infty} \left[\frac{\tilde{f}(k_n)}{\tilde{f}(k_t)} \right]^2 \frac{j\omega\mu_0}{k_n} [1 + \coth(k_n d)]^{-1},
\end{aligned} \quad (3.35)$$

from which

$$L_{ho} = \frac{2\mu_0}{[\tilde{f}(k_t)]^2} \sum_{n=N+1}^{+\infty} \frac{[\tilde{f}(k_n)]^2}{k_n} [1 + \coth(k_n d)]^{-1}, \quad (3.36)$$

where the factor 2 considers the symmetry of the series with respect to the index n .

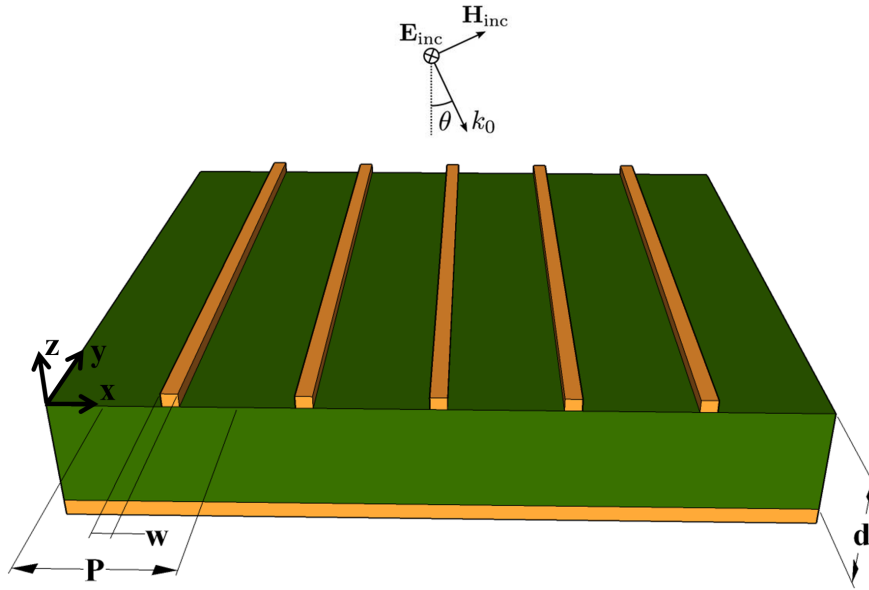


Figure 3.4: Strip grating on a grounded dielectric slab under TE oblique incidence.

In order to verify the correctness of the previous analytical assumptions, I have considered a strip grating under TE oblique incidence for $\theta = 0^\circ, 30^\circ, 60^\circ, 80^\circ$, printed on a lossless grounded slab with relative permittivity $\epsilon_r = 4$, periodicity $P = 1$ mm, dielectric thickness $d = 0.3P = 0.3$ mm, and strip width $w = 0.1P = 0.1$ mm.

Figures 3.5(a)-(d) show the comparison between the phase of the reflection coefficient S_{11} of the full-wave simulations carried out with a FEM-based electromagnetic solver (COMSOL Multiphysics) and the fully analytical equivalent circuit model. The frequency band of interest ranges from zero frequency up to 300 GHz, which in terms of normalized frequency P/λ_0 is comprised between 0 and 1. It should be noticed that, as frequency increases, there is a near-zero phase for the S_{11} parameter (artificial magnetic conductor) in a given frequency range. In particular, in the normal incidence case in Fig. 3.5(a), this characteristic behavior occurs around 156 GHz and this frequency remains almost the same also for the oblique incidence cases at $\theta = 30^\circ, 60^\circ, 80^\circ$ in Figs. 3.5(b)-(d). Instead, at the highest frequencies of the range of interest, the structures exhibit a more complex phase variation, especially under oblique incidence, well described by the EC model.

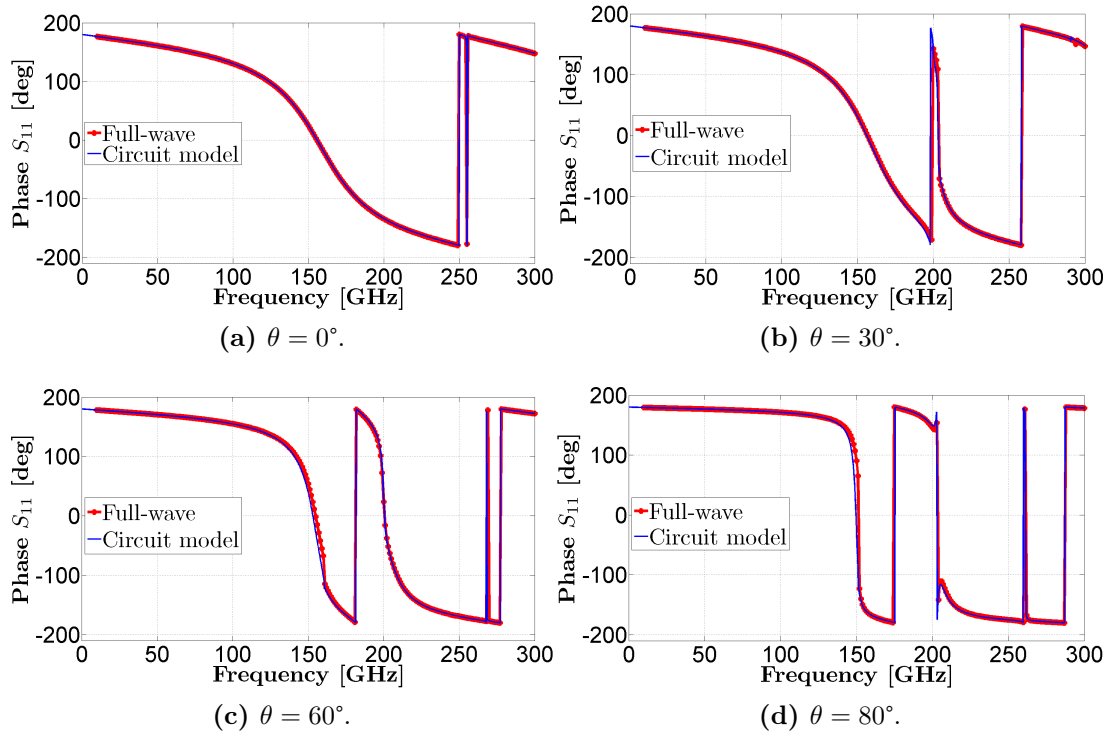


Figure 3.5: Phase of the S_{11} parameter for the grounded strip grating under $\theta = 0^\circ$, 30° , 60° , 80° TE incidence.

3.3 Slit gratings

In a specular way to the analysis adopted for the strip gratings, we may consider the case of a slit grating embedded within two different dielectric half spaces (see Fig. 3.6).

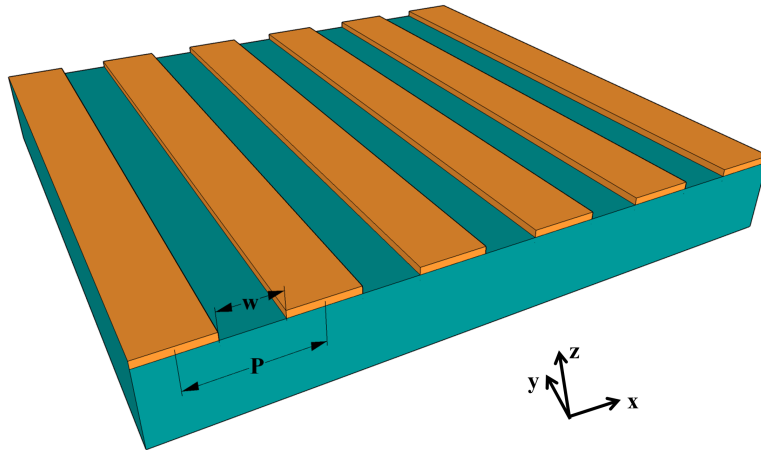


Figure 3.6: Slit grating on a dielectric substrate.

Assuming $E_s(x)$ the transverse electric field at the slit aperture, from Eq. (3.3) and the Fourier analysis, we can extract:

$$1 + R = \frac{1}{P} \int_{-w/2}^{w/2} E_s(x) e^{jk_t x} dx = \frac{1}{P} \tilde{E}_s(k_t), \quad (3.37)$$

$$E_n = \frac{1}{P} \int_{-w/2}^{w/2} E_s(x) e^{j(k_t+k_n)x} dx = \frac{1}{P} \tilde{E}_s(k_t + k_n), \quad (3.38)$$

from which

$$\frac{1}{P} = \frac{1 + R}{\tilde{E}_s(k_t)}, \quad (3.39)$$

and the expansion coefficients are:

$$E_n = (1 + R) \frac{\tilde{E}_s(k_t + k_n)}{\tilde{E}_s(k_t)}. \quad (3.40)$$

The condition of continuity of the magnetic field at the slit aperture is:

$$\int_{-w/2}^{w/2} E_s^*(x) [H^{(2)}(x) - H^{(1)}(x)] dx = 0. \quad (3.41)$$

Substituting the expansions of the magnetic field of the Eqs. (3.4)-(3.5), Eq. (3.41) becomes:

$$\begin{aligned} \int_{-w/2}^{w/2} E_s^*(x) \left[Y_0^{(2)} (1 + R) e^{-jk_t x} + \sum_{n=-\infty, n \neq 0}^{+\infty} Y_n^{(2)} E_n e^{-j(k_t+k_n)x} \right. \\ \left. - Y_0^{(1)} (1 - R) e^{-jk_t x} + \sum_{n=-\infty, n \neq 0}^{+\infty} Y_n^{(1)} E_n e^{-j(k_t+k_n)x} \right] dx = 0, \end{aligned} \quad (3.42)$$

which, using the Fourier transform, is simplified in:

$$\begin{aligned} \tilde{E}_s^*(k_t) Y_0^{(2)} (1 + R) + \sum_{n=-\infty, n \neq 0}^{+\infty} Y_n^{(2)} E_n \tilde{E}_s^*(k_t + k_n) \\ - Y_0^{(1)} (1 - R) \tilde{E}_s^*(k_t) + \sum_{n=-\infty, n \neq 0}^{+\infty} Y_n^{(1)} E_n \tilde{E}_s^*(k_t + k_n) = 0. \end{aligned} \quad (3.43)$$

Substituting the expansion coefficients in Eq. (3.40):

$$\begin{aligned} \tilde{E}_s^*(k_t) Y_0^{(2)} (1 + R) + \sum_{n=-\infty, n \neq 0}^{+\infty} Y_n^{(2)} (1 + R) \frac{\tilde{E}_s(k_t + k_n)}{\tilde{E}_s(k_t)} \tilde{E}_s^*(k_t + k_n) \\ - Y_0^{(1)} (1 - R) \tilde{E}_s^*(k_t) + \sum_{n=-\infty, n \neq 0}^{+\infty} Y_n^{(1)} (1 + R) \frac{\tilde{E}_s(k_t + k_n)}{\tilde{E}_s(k_t)} \tilde{E}_s^*(k_t + k_n) = 0, \end{aligned} \quad (3.44)$$

and dividing by $\tilde{E}_s^*(k_t)$:

$$\begin{aligned} Y_0^{(2)}(1+R) + \sum_{n=-\infty, n \neq 0}^{+\infty} Y_n^{(2)}(1+R) \left| \frac{\tilde{E}_s(k_t + k_n)}{\tilde{E}_s(k_t)} \right|^2 \\ - Y_0^{(1)}(1-R) + \sum_{n=-\infty, n \neq 0}^{+\infty} Y_n^{(1)}(1+R) \left| \frac{\tilde{E}_s(k_t + k_n)}{\tilde{E}_s(k_t)} \right|^2 = 0, \end{aligned} \quad (3.45)$$

the reflection coefficient R results:

$$\begin{aligned} R &= \frac{Y_0^{(1)} - Y_0^{(2)} - \sum_{n=-\infty, n \neq 0}^{+\infty} (Y_n^{(1)} + Y_n^{(2)}) \left| \frac{\tilde{E}_s(k_t + k_n)}{\tilde{E}_s(k_t)} \right|^2}{Y_0^{(1)} + Y_0^{(2)} + \sum_{n=-\infty, n \neq 0}^{+\infty} (Y_n^{(1)} + Y_n^{(2)}) \left| \frac{\tilde{E}_s(k_t + k_n)}{\tilde{E}_s(k_t)} \right|^2} \\ &= \frac{Y_0^{(1)} - Y_0^{(2)} - Y_{eq}}{Y_0^{(1)} + Y_0^{(2)} + Y_{eq}}, \end{aligned} \quad (3.46)$$

with the equivalent admittance:

$$Y_{eq} = \sum_{n=-\infty, n \neq 0}^{+\infty} (Y_n^{(1)} + Y_n^{(2)}) \left| \frac{\tilde{E}_s(k_t + k_n)}{\tilde{E}_s(k_t)} \right|^2. \quad (3.47)$$

We make a similar assumption for the aperture electric field as previously done for the surface electric current, in the case of electrically narrow slit:

$$E_s(x) = A(\omega)f(x), \quad (3.48)$$

with the precaution that now the aperture electric field is given by Eq. (3.18) for TM polarization and by Eq. (3.19) for TE polarization of the incident wave.

The expression of the equivalent admittance results:

$$Y_{eq} = \sum_{n=-\infty, n \neq 0}^{+\infty} (Y_n^{(1)} + Y_n^{(2)}) \left[\frac{\tilde{f}(k_t + k_n)}{\tilde{f}(k_t)} \right]^2, \quad (3.49)$$

with the circuit topology shown in Fig. 3.7.

In order to investigate the electromagnetic response of the periodic structure up to the grating lobe regime, the global equivalent admittance for TE/TM polarization (see Fig. 3.8) can be expressed as follows:

$$Y_{eq}^{TE} = \sum_{n=-N, n \neq 0}^{+N} \left[\frac{\tilde{f}(k_t + k_n)}{\tilde{f}(k_t)} \right]^2 (Y_n^{(1)} + Y_n^{(2)}) + \frac{1}{j\omega L_{ho}}, \quad (3.50)$$

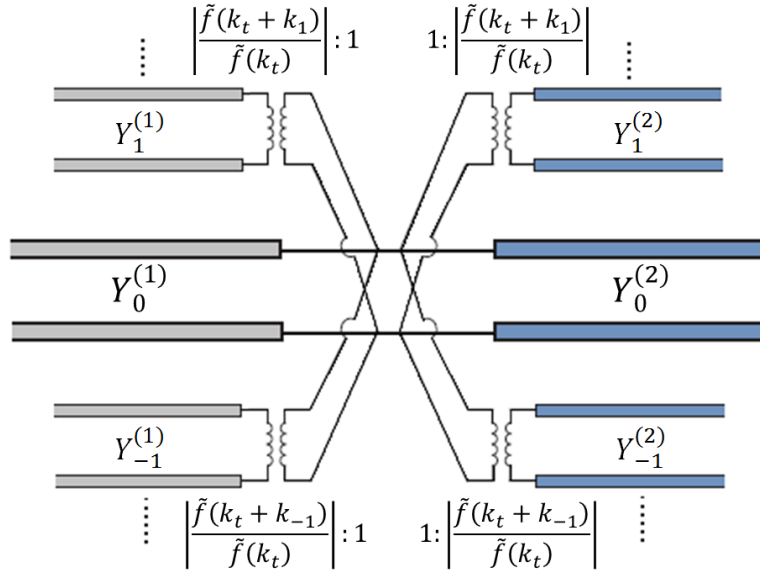


Figure 3.7: Equivalent circuit topology for a slit grating embedded between two different dielectric half-spaces.

$$Y_{eq}^{TM} = \sum_{n=-N, n \neq 0}^{+N} \left[\frac{\tilde{f}(k_t + k_n)}{\tilde{f}(k_t)} \right]^2 (Y_n^{(1)} + Y_n^{(2)}) + j\omega C_{ho}, \quad (3.51)$$

where the high-order inductance and capacitance are:

$$\frac{1}{L_{ho}} = \frac{4}{\mu_0 [\tilde{f}(k_t)]^2} \sum_{n=N+1}^{+\infty} [\tilde{f}(k_n)]^2 k_n, \quad (3.52)$$

$$C_{ho} = \frac{2\varepsilon_0(\varepsilon_{r,1} + \varepsilon_{r,2})}{[\tilde{f}(k_t)]^2} \sum_{n=N+1}^{+\infty} \frac{[\tilde{f}(k_n)]^2}{k_n}. \quad (3.53)$$

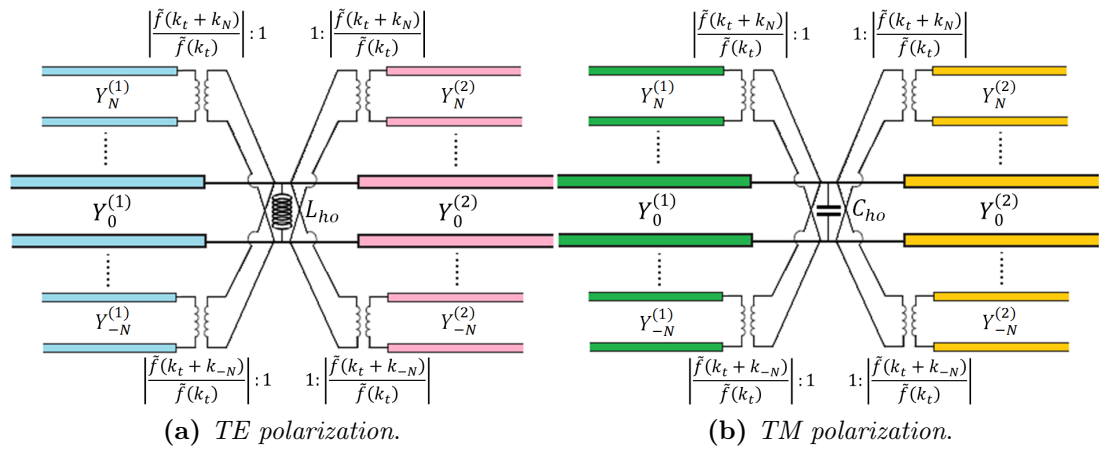


Figure 3.8: Equivalent circuit model for a slit grating between two dielectric half spaces for (a) TE polarization and (b) TM polarization.

3.3.1 Numerical results for a slit grating printed on a grounded dielectric slab under TM incidence

The analytical expression of the lumped frequency-independent capacitance C_{ho} in the case of a slit grating on a grounded slab (see Fig. 3.9) can be extracted upon evaluating the admittance $Y_n^{(2)}$ in Eq. (3.51). This needs to be substituted with the equivalent admittance of a short-circuited transmission line of length equal to the dielectric thickness d as in Eq. (3.34).

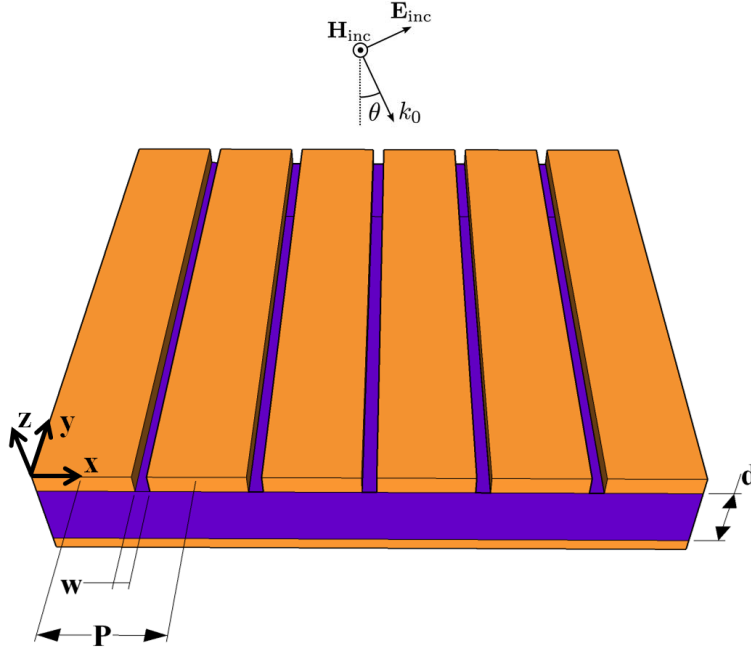


Figure 3.9: Slit grating on a grounded dielectric slab under TM oblique incidence.

Consequently, the lumped high-order capacitance results:

$$\begin{aligned}
 j\omega C_{ho} &= 2 \sum_{n=N+1}^{+\infty} \left[\frac{\tilde{f}(k_n)}{\tilde{f}(k_t)} \right]^2 (Y_n^{(0)} + Y_{IN,n}^{(R)}) \\
 &= 2 \sum_{n=N+1}^{+\infty} \left[\frac{\tilde{f}(k_n)}{\tilde{f}(k_t)} \right]^2 [Y_n^{(0)} - jY_n^{(1)} \cot(\beta_n^{(1)} d)] \\
 &= 2 \sum_{n=N+1}^{+\infty} \left[\frac{\tilde{f}(k_n)}{\tilde{f}(k_t)} \right]^2 \left[\frac{j\omega\epsilon_0}{k_n} - j \frac{j\omega\epsilon_0\epsilon_{r,1}}{k_n} \cot(-jk_n d) \right] \\
 &= 2 \sum_{n=N+1}^{+\infty} \left[\frac{\tilde{f}(k_n)}{\tilde{f}(k_t)} \right]^2 \left[\frac{j\omega\epsilon_0}{k_n} + \frac{j\omega\epsilon_0\epsilon_{r,1}}{k_n} \coth(k_n d) \right] \\
 &= 2 \sum_{n=N+1}^{+\infty} \left[\frac{\tilde{f}(k_n)}{\tilde{f}(k_t)} \right]^2 \frac{j\omega\epsilon_0}{k_n} [1 + \epsilon_{r,1} \coth(k_n d)],
 \end{aligned} \tag{3.54}$$

from which

$$C_{ho} = \frac{2\varepsilon_0}{[\tilde{f}(k_t)]^2} \sum_{n=N+1}^{+\infty} \frac{[\tilde{f}(k_n)]^2}{k_n} [1 + \varepsilon_{r,1} \coth(k_n d)], \quad (3.55)$$

where the factor 2 considers the symmetry of the series with respect to the index n .

As numerical validation, I have investigated a slit grating under TM oblique incidence for $\theta = 0^\circ, 30^\circ, 60^\circ, 80^\circ$, printed on a grounded slab with geometrical and material parameters previously assumed for the strip grating examples: relative permittivity $\varepsilon_r = 4$, periodicity $P = 1$ mm, dielectric thickness $d = 0.3P = 0.3$ mm, and slit width $w = 0.1P = 0.1$ mm. Figures 3.10(a)-(d) show the comparison between the reflection coefficient phase in degree of the full-wave simulations carried out with the electromagnetic solver and the fully analytical circuit model. Also, in this case, it should be noticed that, as frequency increases, this structure presents a near-zero phase for the S_{11} parameter (artificial magnetic conductor) in the lower frequency range. In particular, in the normal incidence case in Fig. 3.10(a), this characteristic behavior occurs around 48 GHz and this frequency remains almost the same also for the oblique incidence cases at $\theta = 30^\circ, 60^\circ, 80^\circ$ in Figs. 3.10(b)-(d). Instead, at the highest frequencies of the range of interest, the structures exhibit a more complex phase variation, especially under oblique incidence, well described by the EC model.

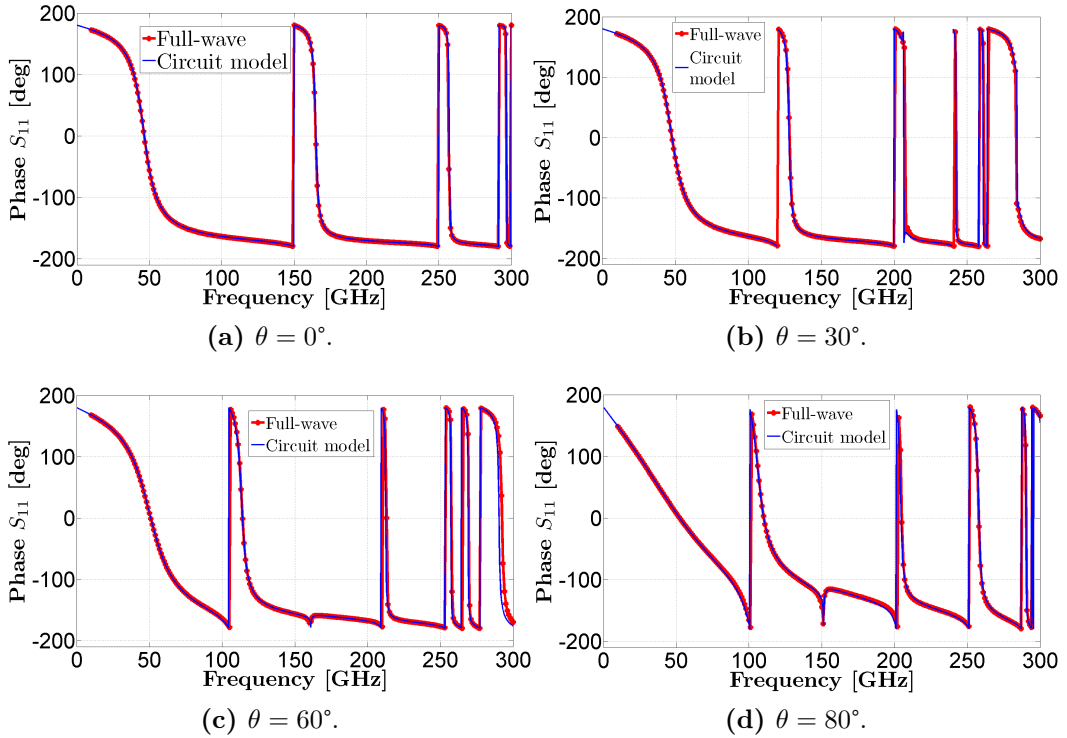


Figure 3.10: Phase of the S_{11} parameter for the grounded slit grating under $\theta = 0^\circ, 30^\circ, 60^\circ, 80^\circ$ TM incidence.

3.4 Semi-analytical circuit model for a strip grating

In what follows, as a further validation example, I have tested the functionality of the semi-analytical EC model in the case of the strip grating on a lossless grounded slab analyzed in Section 3.2.1. To this purpose, I have extracted the spatial profile of the surface electric current from a full-wave simulation of the freestanding structure at a single frequency and for different incidence angle with the aim to check the robustness. The spatial profiles of the y component of the surface electric current as a function of x -direction $J_y(x)$ and the corresponding phase in degree of the reflection coefficient are represented in Figs. 3.11-3.14.

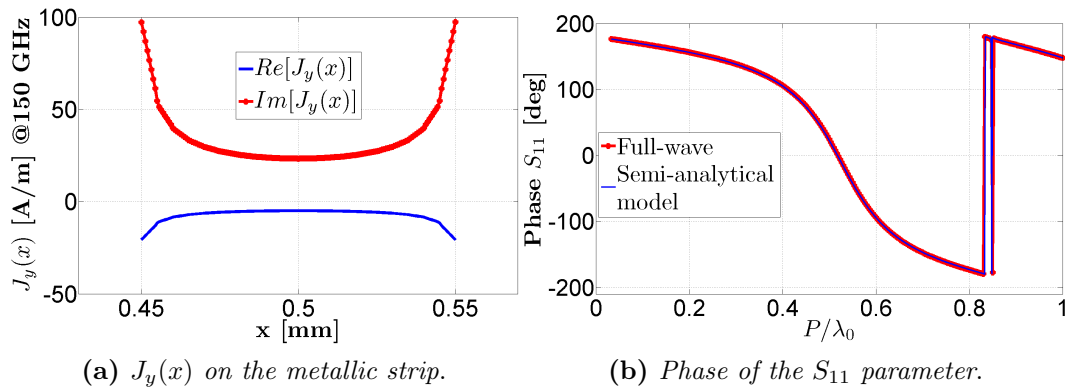


Figure 3.11: (a) Surface current density at 150 GHz and (b) phase of the S_{11} parameter for the grounded strip grating under $\theta = 0^\circ$ TE incidence.

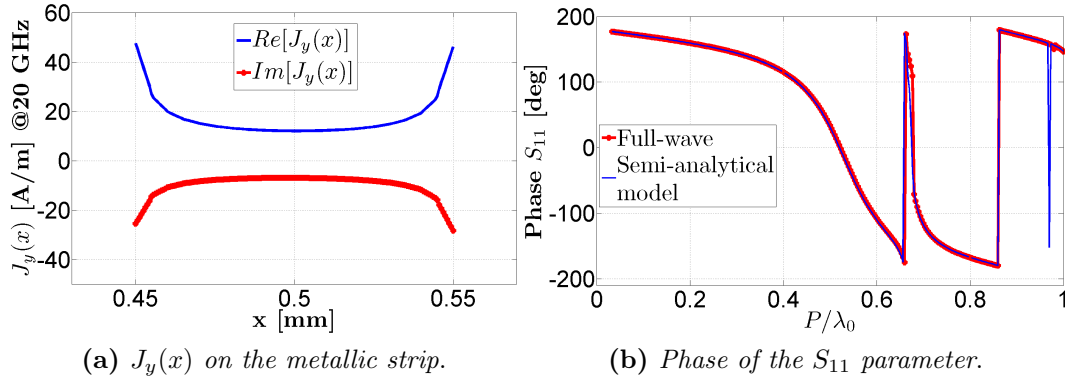


Figure 3.12: (a) Surface current density at 20 GHz and (b) phase of the S_{11} parameter for the grounded strip grating under $\theta = 30^\circ$ TE incidence.

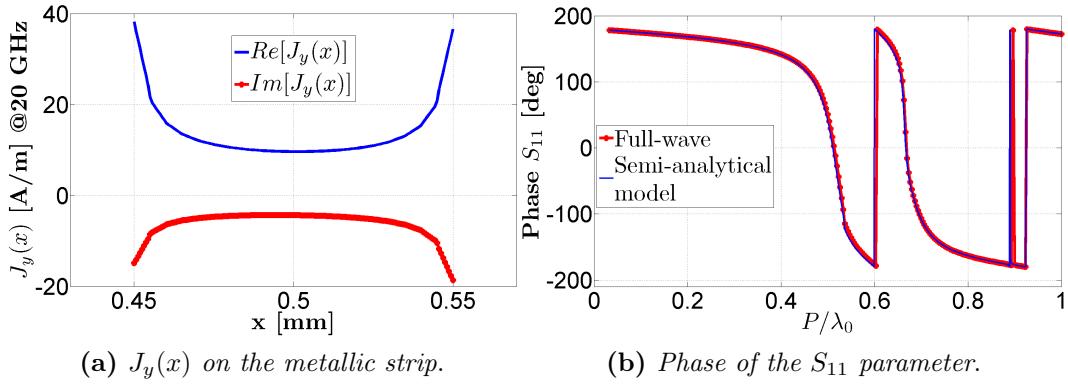


Figure 3.13: (a) Surface current density at 20 GHz and (b) phase of the S_{11} parameter for the grounded strip grating under $\theta = 60^\circ$ TE incidence.

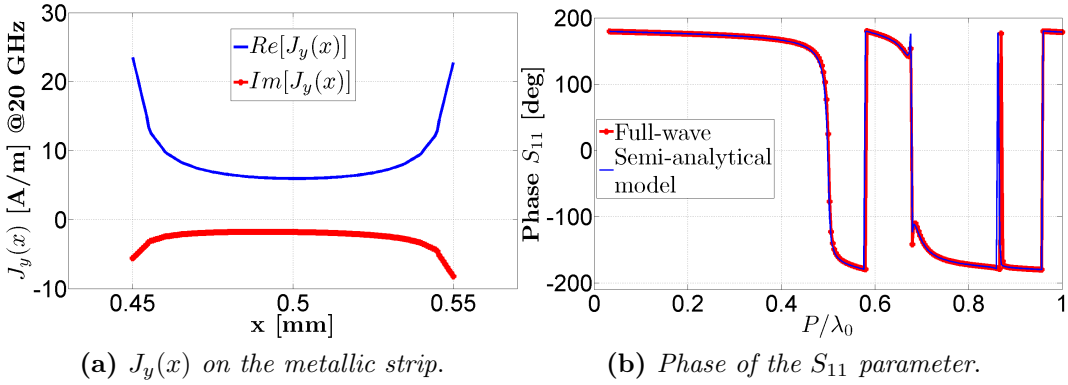


Figure 3.14: (a) Surface current density at 20 GHz and (b) phase of the S_{11} parameter for the grounded strip grating under $\theta = 80^\circ$ TE incidence.

3.5 Fully analytical circuit model for frequency selective surfaces of arbitrary geometry

In this Section, I extended the transmission-line-based equivalent circuit model to the analysis of 2D periodic structures of arbitrary geometry (see Fig. 3.15) for different cases of interest: in freestanding configuration, embedded between two different dielectric half-spaces, on a finite dielectric spacer and on a grounded dielectric layer [23–26].

Exploiting the periodicity of the metallic surface on the plane $z = 0$, the transverse electric field can be expanded in Floquet series:

$$\mathbf{E}(x, y) = (1 + R)e^{-jk_y y} \hat{\mathbf{x}} + \sum_{(n,m) \neq (0,0)} \mathbf{E}_{nm}^{TE} e^{-j(k_n x + k_y m y)} + \sum_{nm, n \neq 0} \mathbf{E}_{nm}^{TM} e^{-j(k_n x + k_y m y)}. \quad (3.56)$$

If we suppose for the expansion coefficients of the electric field the following

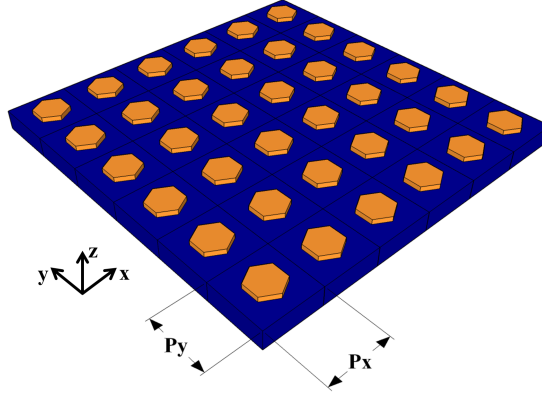


Figure 3.15: 3D sketch of hexagonal FSSs printed on a dielectric substrate.

Floquet harmonics [11]:

$$\mathbf{E}_{nm}^{TE} = E_{nm}^{TE} \frac{k_{ym}\hat{\mathbf{x}} - k_n\hat{\mathbf{y}}}{\sqrt{k_n^2 + k_{ym}^2}}, \quad (3.57)$$

$$\mathbf{E}_{nm}^{TM} = E_{nm}^{TM} \frac{k_n\hat{\mathbf{x}} + k_{ym}\hat{\mathbf{y}}}{\sqrt{k_n^2 + k_{ym}^2}}, \quad (3.58)$$

the transverse electric field results:

$$\begin{aligned} \mathbf{E}(x, y) = & (1 + R)e^{-jk_y y} \hat{\mathbf{x}} + \sum_{(n,m) \neq (0,0)} E_{nm}^{TE} \frac{k_{ym}\hat{\mathbf{x}} - k_n\hat{\mathbf{y}}}{\sqrt{k_n^2 + k_{ym}^2}} e^{-j(k_n x + k_{ym} y)} \\ & + \sum_{nm, n \neq 0} E_{nm}^{TM} \frac{k_n\hat{\mathbf{x}} + k_{ym}\hat{\mathbf{y}}}{\sqrt{k_n^2 + k_{ym}^2}} e^{-j(k_n x + k_{ym} y)}. \end{aligned} \quad (3.59)$$

The expansions of the transverse magnetic field on the FSS planes $z = 0^-$ and $z = 0^+$ are given by:

$$\begin{aligned} \mathbf{H}^{(1)}(x, y) = & Y_{00}^{TE(1)}(1 - R)e^{-jk_y y} \hat{\mathbf{y}} + \sum_{(n,m) \neq (0,0)} \mathbf{H}_{nm}^{TE(1)} e^{-j(k_n x + k_{ym} y)} \\ & + \sum_{nm, n \neq 0} \mathbf{H}_{nm}^{TM(1)} e^{-j(k_n x + k_{ym} y)}, \end{aligned} \quad (3.60)$$

$$\begin{aligned} \mathbf{H}^{(2)}(x, y) = & Y_{00}^{TE(2)}(1 + R)e^{-jk_y y} \hat{\mathbf{y}} + \sum_{(n,m) \neq (0,0)} \mathbf{H}_{nm}^{TE(2)} e^{-j(k_n x + k_{ym} y)} \\ & + \sum_{nm, n \neq 0} \mathbf{H}_{nm}^{TM(2)} e^{-j(k_n x + k_{ym} y)}, \end{aligned} \quad (3.61)$$

where

$$\mathbf{H}_{nm}^{(i)} = \mp Y_{nm}^{(i)}(\hat{\mathbf{z}} \times \mathbf{E}_{nm}); \quad (3.62)$$

the signs \mp correspond to the media ($i = 1$) and ($i = 2$), respectively.

In particular, the modal admittances assume the same form as in Eqs. (3.6)-(3.7) for TE and TM incidence, respectively, while the propagation wavenumber along the z -direction has now the expression:

$$k_{z,nm}^{(i)} = \begin{cases} \beta_{z,nm}^{(i)} = \sqrt{\omega^2 \varepsilon_i \mu_0 - (k_n + k_{ym})^2} & \text{if } f \geq f_{c,nm}, \\ -j\alpha_{z,nm}^{(i)} = -j\sqrt{(k_n + k_{ym})^2 - \omega^2 \varepsilon_i \mu_0} & \text{if } f < f_{c,nm}, \end{cases} \quad (3.63)$$

where $f_{c,nm}$ is the cut-off frequency of the nm th harmonic expressed as follows:

$$f_{c,nm} = \frac{mc \sin \theta}{P_y(\varepsilon_{r,i} - \sin^2 \theta)} + \sqrt{\left[\frac{mc \sin \theta}{P_y(\varepsilon_{r,i} - \sin^2 \theta)} \right]^2 + \frac{c^2}{\varepsilon_{r,i} - \sin^2 \theta} \left[\left(\frac{n}{P_x} \right)^2 + \left(\frac{m}{P_y} \right)^2 \right]}, \quad (3.64)$$

and

$$k_n = \frac{2\pi n}{P_x}, \quad (3.65)$$

$$k_{ym} = k_t + k_m = k_0 \sin \theta + \frac{2\pi m}{P_y}, \quad (3.66)$$

being P_x and P_y the periodicity of the single unit cell of the FSS along the x and y -directions, respectively.

The expansions of the magnetic field at both sides of the $z = 0$ plane are:

$$\begin{aligned} \mathbf{H}^{(1)}(x, y) = & Y_{00}^{TE(1)}(1 - R)e^{-jk_t y} \hat{\mathbf{y}} - \sum_{(n,m) \neq (0,0)} H_{nm}^{TE(1)} \frac{k_{ym} \hat{\mathbf{y}} + k_n \hat{\mathbf{x}}}{\sqrt{k_n^2 + k_{ym}^2}} e^{-j(k_n x + k_{ym} y)} \\ & - \sum_{nm, n \neq 0} H_{nm}^{TM(1)} \frac{k_n \hat{\mathbf{y}} - k_{ym} \hat{\mathbf{x}}}{\sqrt{k_n^2 + k_{ym}^2}} e^{-j(k_n x + k_{ym} y)}, \end{aligned} \quad (3.67)$$

$$\begin{aligned} \mathbf{H}^{(2)}(x, y) = & Y_{00}^{TE(2)}(1 + R)e^{-jk_t y} \hat{\mathbf{y}} + \sum_{(n,m) \neq (0,0)} H_{nm}^{TE(2)} \frac{k_n \hat{\mathbf{x}} + k_{ym} \hat{\mathbf{y}}}{\sqrt{k_n^2 + k_{ym}^2}} e^{-j(k_n x + k_{ym} y)} \\ & + \sum_{nm, n \neq 0} H_{nm}^{TM(2)} \frac{k_n \hat{\mathbf{y}} - k_{ym} \hat{\mathbf{x}}}{\sqrt{k_n^2 + k_{ym}^2}} e^{-j(k_n x + k_{ym} y)}, \end{aligned} \quad (3.68)$$

where the magnetic field coefficients are:

$$H_{nm}^{TE(i)} = E_{nm}^{TE} Y_{nm}^{TE(i)}, \quad (3.69)$$

$$H_{nm}^{TM(i)} = E_{nm}^{TM} Y_{nm}^{TM(i)}. \quad (3.70)$$

As made for the one-dimensional case, we approximate the surface current density

on the metallic FSS, adopting the same assumption in Ref. [12], as follows:

$$\mathbf{J}_s(x, y; \omega) = A(\omega) \mathbf{j}_s(x, y). \quad (3.71)$$

We apply the boundary condition for the magnetic field at the $z = 0$ interface:

$$\mathbf{J}_s = \hat{\mathbf{z}} \times (\mathbf{H}^{(2)} - \mathbf{H}^{(1)}), \quad (3.72)$$

obtaining

$$\begin{aligned} & -\hat{\mathbf{x}}Y_{00}^{TE(2)}(1+R) + \hat{\mathbf{x}}Y_{00}^{TE(1)}(1-R) \\ & - \sum_{(n,m) \neq (0,0)} E_{nm}^{TE} (Y_{nm}^{TE(1)} + Y_{nm}^{TE(2)}) \frac{k_{ym}\hat{\mathbf{x}} - k_n\hat{\mathbf{y}}}{\sqrt{k_n^2 + k_{ym}^2}} e^{-j(k_n x + k_m y)} \\ & - \sum_{nm, n \neq 0} E_{nm}^{TM} (Y_{nm}^{TM(1)} + Y_{nm}^{TM(2)}) \frac{k_n\hat{\mathbf{x}} + k_{ym}\hat{\mathbf{y}}}{\sqrt{k_n^2 + k_{ym}^2}} e^{-j(k_n x + k_m y)} = A(\omega) \mathbf{j}_s(x, y) e^{jk_t y}. \end{aligned} \quad (3.73)$$

Considering the Fourier transform of the $n = m = 0$ term and projecting along the x -direction, we obtain:

$$(Y_{00}^{TE(1)} - Y_{00}^{TE(2)}) - R(Y_{00}^{TE(1)} + Y_{00}^{TE(2)}) = \frac{A(\omega)}{P_x P_y} \iint_{FSS} \mathbf{j}_s(x, y) \cdot \hat{\mathbf{x}} e^{jk_t y} dx dy, \quad (3.74)$$

where we define with I_j the integral of the surface electric current on the metallic FSS:

$$I_j = \iint_{FSS} \mathbf{j}_s(x, y) \cdot \hat{\mathbf{x}} e^{jk_t y} dx dy. \quad (3.75)$$

From Eq. (3.74), it is possible to explicit the frequency-dependent term:

$$\frac{A(\omega)}{P_x P_y} = \frac{(Y_{00}^{TE(1)} - Y_{00}^{TE(2)}) - R(Y_{00}^{TE(1)} + Y_{00}^{TE(2)})}{I_j}. \quad (3.76)$$

At this point, we multiply the remaining terms in Eq. (3.73) by orthogonal functions, integrating on the single unit cell:

$$\begin{aligned} & \sum_{(n,m) \neq (0,0)} E_{nm}^{TE} (Y_{nm}^{TE(1)} + Y_{nm}^{TE(2)}) \frac{k_{ym}\hat{\mathbf{x}} - k_n\hat{\mathbf{y}}}{\sqrt{k_n^2 + k_{ym}^2}} \int_{-\frac{P_x}{2}}^{\frac{P_x}{2}} \int_{-\frac{P_y}{2}}^{\frac{P_y}{2}} e^{-jk_n x} e^{j\frac{2\pi q}{P_x} x} e^{-jk_m y} e^{j\frac{2\pi p}{P_y} y} dx dy \\ & + \sum_{nm, n \neq 0} E_{nm}^{TM} (Y_{nm}^{TM(1)} + Y_{nm}^{TM(2)}) \frac{k_n\hat{\mathbf{x}} + k_{ym}\hat{\mathbf{y}}}{\sqrt{k_n^2 + k_{ym}^2}} \int_{-\frac{P_x}{2}}^{\frac{P_x}{2}} \int_{-\frac{P_y}{2}}^{\frac{P_y}{2}} e^{-jk_n x} e^{j\frac{2\pi q}{P_x} x} e^{-jk_m y} e^{j\frac{2\pi p}{P_y} y} dx dy \\ & = -A(\omega) \int_{-\frac{P_x}{2}}^{\frac{P_x}{2}} \int_{-\frac{P_y}{2}}^{\frac{P_y}{2}} \mathbf{j}_s(x, y) e^{jk_t y} e^{j\frac{2\pi q}{P_x} x} e^{j\frac{2\pi p}{P_y} y} dx dy. \end{aligned} \quad (3.77)$$

We introduce for convenience the definition of the Kronecker delta function:

$$\delta_{nq} = \begin{cases} 1 & \text{if } n = q \\ 0 & \text{if } n \neq q \end{cases} \quad (3.78)$$

$$\delta_{mp} = \begin{cases} 1 & \text{if } m = p \\ 0 & \text{if } m \neq p \end{cases} \quad (3.79)$$

Equation (3.77) is initially projected along the x -axis, where we redefine $q = n$ and $p = m$:

$$\begin{aligned} & E_{nm}^{TE}(Y_{nm}^{TE(1)} + Y_{nm}^{TE(2)}) \frac{k_{ym}}{\sqrt{k_n^2 + k_{ym}^2}} P_x P_y + E_{nm}^{TM}(Y_{nm}^{TM(1)} + Y_{nm}^{TM(2)}) \frac{k_n}{\sqrt{k_n^2 + k_{ym}^2}} P_x P_y \\ &= -A(\omega) \iint_{FSS} \mathbf{j}_s(x, y) \cdot \hat{\mathbf{x}} e^{jk_t y} e^{jk_n x} e^{jk_m y} dx dy, \end{aligned} \quad (3.80)$$

and defining the integral of the x -component of the surface electric current as:

$$I_{jx} = \iint_{FSS} \mathbf{j}_s(x, y) \cdot \hat{\mathbf{x}} e^{jk_t y} e^{jk_n x} e^{jk_m y} dx dy, \quad (3.81)$$

we obtain:

$$\begin{aligned} & E_{nm}^{TE}(Y_{nm}^{TE(1)} + Y_{nm}^{TE(2)}) \frac{k_{ym}}{\sqrt{k_n^2 + k_{ym}^2}} + E_{nm}^{TM}(Y_{nm}^{TM(1)} + Y_{nm}^{TM(2)}) \frac{k_n}{\sqrt{k_n^2 + k_{ym}^2}} \\ &= -\frac{A(\omega)}{P_x P_y} I_{jx} = -\frac{I_{jx}}{I_j} \left[\left(Y_{00}^{TE(1)} - Y_{00}^{TE(2)} \right) - R \left(Y_{00}^{TE(1)} + Y_{00}^{TE(2)} \right) \right], \end{aligned} \quad (3.82)$$

where the ratio $A(\omega)/(P_x P_y)$ has been substituted with the Eq. (3.76).

Projecting now Eq. (3.77) along the y -axis:

$$\begin{aligned} & E_{nm}^{TE}(Y_{nm}^{TE(1)} + Y_{nm}^{TE(2)}) \frac{k_n}{\sqrt{k_n^2 + k_{ym}^2}} P_x P_y - E_{nm}^{TM}(Y_{nm}^{TM(1)} + Y_{nm}^{TM(2)}) \frac{k_{ym}}{\sqrt{k_n^2 + k_{ym}^2}} P_x P_y \\ &= A(\omega) \iint_{FSS} \mathbf{j}_s(x, y) \cdot \hat{\mathbf{y}} e^{jk_t y} e^{jk_n x} e^{jk_m y} dx dy, \end{aligned} \quad (3.83)$$

and defining the integral of the y -component of the surface electric current as:

$$I_{jy} = \iint_{FSS} \mathbf{j}_s(x, y) \cdot \hat{\mathbf{y}} e^{jk_t y} e^{jk_n x} e^{jk_m y} dx dy, \quad (3.84)$$

we obtain:

$$\begin{aligned} & E_{nm}^{TE} (Y_{nm}^{TE(1)} + Y_{nm}^{TE(2)}) \frac{k_n}{\sqrt{k_n^2 + k_{ym}^2}} - E_{nm}^{TM} (Y_{nm}^{TM(1)} + Y_{nm}^{TM(2)}) \frac{k_{ym}}{\sqrt{k_n^2 + k_{ym}^2}} \\ &= \frac{A(\omega)}{P_x P_y} I_{jy} = \frac{I_{jy}}{I_j} \left[\left(Y_{00}^{TE(1)} - Y_{00}^{TE(2)} \right) - R \left(Y_{00}^{TE(1)} + Y_{00}^{TE(2)} \right) \right]. \end{aligned} \quad (3.85)$$

Equation (3.82) and Eq. (3.85) represent a system of two equations in the two unknowns E_{nm}^{TE} and E_{nm}^{TM} , which assume the following expressions:

$$E_{nm}^{TE} = \frac{(Y_{00}^{TE(1)} - Y_{00}^{TE(2)}) - R(Y_{00}^{TE(1)} + Y_{00}^{TE(2)})}{Y_{nm}^{TE(1)} + Y_{nm}^{TE(2)}} \frac{I_{jy} k_n - I_{jx} k_{ym}}{I_j \sqrt{k_n^2 + k_{ym}^2}}, \quad (3.86)$$

$$E_{nm}^{TM} = - \frac{(Y_{00}^{TE(1)} - Y_{00}^{TE(2)}) - R(Y_{00}^{TE(1)} + Y_{00}^{TE(2)})}{Y_{nm}^{TM(1)} + Y_{nm}^{TM(2)}} \frac{I_{jx} k_n + I_{jy} k_{ym}}{I_j \sqrt{k_n^2 + k_{ym}^2}}. \quad (3.87)$$

Now, we can consider the following integral equation for the boundary condition of the electric field:

$$\iint_{FSS} \mathbf{J}_s^* \cdot \mathbf{E}(x, y) dx dy = \iint_{FSS} A^*(\omega) \mathbf{j}_s^*(x, y) \cdot \mathbf{E}(x, y) dx dy = 0; \quad (3.88)$$

substituting the expansion for the electric field of the Eq. (3.59) into the Eq. (3.88), we find:

$$\begin{aligned} & \iint_{FSS} \mathbf{J}_s^* \cdot \left[(1 + R) e^{-jk_t y} \hat{\mathbf{x}} + \sum_{(n,m) \neq (0,0)} \frac{E_{nm}^{TE} k_{ym} \hat{\mathbf{x}} - k_n \hat{\mathbf{y}}}{\sqrt{k_n^2 + k_{ym}^2}} e^{-j(k_n x + k_{ym} y)} \right. \\ & \left. + \sum_{nm, n \neq 0} \frac{E_{nm}^{TM} k_n \hat{\mathbf{x}} + k_{ym} \hat{\mathbf{y}}}{\sqrt{k_n^2 + k_{ym}^2}} e^{-j(k_n x + k_{ym} y)} \right] dx dy = 0. \end{aligned} \quad (3.89)$$

I will separately analyze the three terms of Eq. (3.89).

The first term can be rewritten as follows:

$$\iint_{FSS} A^*(\omega) \mathbf{j}_s^*(x, y) \cdot \hat{\mathbf{x}} (1 + R) e^{-jk_t y} dx dy = (1 + R) A^*(\omega) I_j^*. \quad (3.90)$$

For the second term we have:

$$\begin{aligned} & \iint_{FSS} A^*(\omega) \mathbf{j}_s^*(x, y) \cdot \sum_{(n,m) \neq (0,0)} \frac{E_{nm}^{TE} k_{ym} \hat{\mathbf{x}} - k_n \hat{\mathbf{y}}}{\sqrt{k_n^2 + k_{ym}^2}} e^{-j(k_n x + k_{ym} y)} dx dy \\ &= A^*(\omega) \sum_{(n,m) \neq (0,0)} \frac{E_{nm}^{TE}}{\sqrt{k_n^2 + k_{ym}^2}} (k_{ym} I_{jx}^* - k_n I_{jy}^*). \end{aligned} \quad (3.91)$$

Finally, the third term becomes:

$$\begin{aligned} & \iint_{FSS} A^*(\omega) \mathbf{j}_s^*(x, y) \cdot \sum_{nm, n \neq 0} E_{nm}^{TM} \frac{k_n \hat{\mathbf{x}} + k_{ym} \hat{\mathbf{y}}}{\sqrt{k_n^2 + k_{ym}^2}} e^{-j(k_n x + k_{ym} y)} dx dy \\ &= A^*(\omega) \sum_{nm, n \neq 0} \frac{E_{nm}^{TM}}{\sqrt{k_n^2 + k_{ym}^2}} (k_n I_{jx}^* + k_{ym} I_{jy}^*). \end{aligned} \quad (3.92)$$

From Eqs. (3.90)-(3.92), we obtain simplifying $A^*(\omega)$:

$$\begin{aligned} (1 + R)I_j^* + \sum_{(n,m) \neq (0,0)} \frac{E_{nm}^{TE}}{\sqrt{k_n^2 + k_{ym}^2}} (k_{ym} I_{jx}^* - k_n I_{jy}^*) \\ + \sum_{nm, n \neq 0} \frac{E_{nm}^{TM}}{\sqrt{k_n^2 + k_{ym}^2}} (k_n I_{jx}^* + k_{ym} I_{jy}^*) = 0. \end{aligned} \quad (3.93)$$

We substitute Eq. (3.86) and Eq. (3.87) in the Eq. (3.93):

$$\begin{aligned} & (1 + R)I_j^* \\ &+ \sum_{(n,m) \neq (0,0)} \frac{(Y_{00}^{TE(1)} - Y_{00}^{TE(2)}) - R(Y_{00}^{TE(1)} + Y_{00}^{TE(2)})}{Y_{nm}^{TE(1)} + Y_{nm}^{TE(2)}} \frac{(I_{jy} k_n - I_{jx} k_{ym})(k_{ym} I_{jx}^* - k_n I_{jy}^*)}{I_j(k_n^2 + k_{ym}^2)} \\ &- \sum_{nm, n \neq 0} \frac{(Y_{00}^{TE(1)} - Y_{00}^{TE(2)}) - R(Y_{00}^{TE(1)} + Y_{00}^{TE(2)})}{Y_{nm}^{TM(1)} + Y_{nm}^{TM(2)}} \frac{(I_{jx} k_n + I_{jy} k_{ym})(k_n I_{jx}^* + k_{ym} I_{jy}^*)}{I_j(k_n^2 + k_{ym}^2)} = 0, \end{aligned} \quad (3.94)$$

which can be rewritten as:

$$\begin{aligned} & (1 + R)I_j^* \\ &- \sum_{(n,m) \neq (0,0)} \frac{(Y_{00}^{TE(1)} - Y_{00}^{TE(2)}) - R(Y_{00}^{TE(1)} + Y_{00}^{TE(2)})}{Y_{nm}^{TE(1)} + Y_{nm}^{TE(2)}} \frac{|I_{jy} k_n - I_{jx} k_{ym}|^2}{I_j(k_n^2 + k_{ym}^2)} \\ &- \sum_{nm, n \neq 0} \frac{(Y_{00}^{TE(1)} - Y_{00}^{TE(2)}) - R(Y_{00}^{TE(1)} + Y_{00}^{TE(2)})}{Y_{nm}^{TM(1)} + Y_{nm}^{TM(2)}} \frac{|I_{jx} k_n + I_{jy} k_{ym}|^2}{I_j(k_n^2 + k_{ym}^2)} = 0. \end{aligned} \quad (3.95)$$

From Eq. (3.95), it is possible to retrieve the global reflection coefficient R , which assumes the form:

$$R = \frac{-1 + Z_{eq}(Y_{00}^{TE(1)} - Y_{00}^{TE(2)})}{1 + Z_{eq}(Y_{00}^{TE(1)} + Y_{00}^{TE(2)})}, \quad (3.96)$$

where the equivalent impedance results:

$$\begin{aligned} Z_{eq} &= \frac{1}{|I_j|^2} \left[\sum_{(n,m) \neq (0,0)} \frac{|I_{jy}k_n - I_{jx}k_{ym}|^2}{(Y_{nm}^{TE(1)} + Y_{nm}^{TE(2)})(k_n^2 + k_{ym}^2)} \right. \\ &\quad \left. + \sum_{nm, n \neq 0} \frac{|I_{jx}k_n + I_{jy}k_{ym}|^2}{(Y_{nm}^{TM(1)} + Y_{nm}^{TM(2)})(k_n^2 + k_{ym}^2)} \right] \\ &= Z_{eq}^{TE} + Z_{eq}^{TM}, \end{aligned} \quad (3.97)$$

with

$$Z_{eq}^{TE} = \frac{1}{|I_j|^2} \sum_{(n,m) \neq (0,0)} \frac{|I_{jy}k_n - I_{jx}k_{ym}|^2}{(Y_{nm}^{TE(1)} + Y_{nm}^{TE(2)})(k_n^2 + k_{ym}^2)}, \quad (3.98)$$

$$Z_{eq}^{TM} = \frac{1}{|I_j|^2} \sum_{nm, n \neq 0} \frac{|I_{jx}k_n + I_{jy}k_{ym}|^2}{(Y_{nm}^{TM(1)} + Y_{nm}^{TM(2)})(k_n^2 + k_{ym}^2)}. \quad (3.99)$$

From Eq. (3.97) we can define the transformer turn ratios for the TE and TM modes:

$$N_{nm}^{TE} = \left(\frac{|I_{jy}k_n - I_{jx}k_{ym}|}{|I_j| \sqrt{k_n^2 + k_{ym}^2}} \right)^{-1}, \quad (3.100)$$

$$N_{nm}^{TM} = \left(\frac{|I_{jx}k_n + I_{jy}k_{ym}|}{|I_j| \sqrt{k_n^2 + k_{ym}^2}} \right)^{-1}, \quad (3.101)$$

with the circuit topology illustrated in Fig. 3.16.

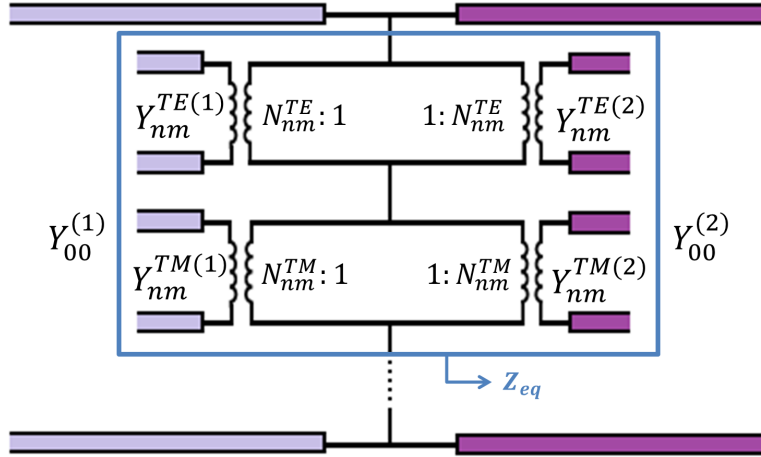


Figure 3.16: Equivalent circuit topology for FSSs embedded between two different semi-infinite dielectric media.

As done for the 1D strip/slit gratings, we can write a further expression for the equivalent global impedance, where we explicit the frequency-independent high-order inductance L_{ho} and capacitance C_{ho} which take into account the reactive energy store in the higher-order TE and TM modes, respectively. For this reason, we consider the quasi-static limit from which results:

$$k_{ym} = k_t + k_m \approx k_m, \quad (3.102)$$

$$\beta_{nm}^{(i)} \approx -j\sqrt{k_n^2 + k_m^2}, \quad (3.103)$$

and the admittances for TE/TM modes have these expressions:

$$Y_{nm,qs}^{TE(i)} = \frac{\sqrt{k_n^2 + k_m^2}}{j\omega\mu_0}, \quad (3.104)$$

$$Y_{nm,qs}^{TM(i)} = \frac{j\omega\varepsilon_0\varepsilon_{r,i}}{\sqrt{k_n^2 + k_m^2}}. \quad (3.105)$$

The high-order inductance and capacitance read:

$$j\omega L_{ho} \approx \frac{1}{|I_j|^2} \sum_{(n,m)=N_{TE}+1}^{+\infty} \frac{|I_{jy,qs}k_n - I_{jx,qs}k_m|^2}{(Y_{nm,qs}^{TE(1,L)} + Y_{nm,qs}^{TE(2,R)})(k_n^2 + k_m^2)}, \quad (3.106)$$

$$\frac{1}{j\omega C_{ho}} \approx \frac{1}{|I_j|^2} \sum_{(n,m)=N_{TM}+1}^{+\infty} \frac{|I_{jx,qs}k_n + I_{jy,qs}k_m|^2}{(Y_{nm,qs}^{TM(1,L)} + Y_{nm,qs}^{TM(2,R)})(k_n^2 + k_m^2)}, \quad (3.107)$$

where $Y_{nm,qs}^L$ and $Y_{nm,qs}^R$ are the input admittances seen by the corresponding harmonic to the left/right of the discontinuity, and the quasi-static integrals for the x and y components of the surface electric current are:

$$I_{jx,qs} = \iint_{FSS} \mathbf{j}_s(x, y) \cdot \hat{\mathbf{x}} e^{jk_n x} e^{jk_m y} dx dy, \quad (3.108)$$

$$I_{jy,qs} = \iint_{FSS} \mathbf{j}_s(x, y) \cdot \hat{\mathbf{y}} e^{jk_n x} e^{jk_m y} dx dy. \quad (3.109)$$

In the particular case of the analysis of narrow patches under TE incidence with the electric field along the x -axis, it is possible to neglect the y component of the surface electric current and for a patch array embedded between two different dielectric half-spaces, the high-order inductance (expressed in Henry) and capacitance (expressed in Farad) have the following expressions, respectively:

$$\begin{aligned} j\omega L_{ho} &\approx \frac{1}{|I_j|^2} \sum_{(n,m)=N_{TE}+1}^{+\infty} \frac{|I_{jx,qs}|^2 k_m^2}{(Y_{nm,qs}^{TE(1,L)} + Y_{nm,qs}^{TE(2,R)})(k_n^2 + k_m^2)} \\ &= \frac{1}{|I_j|^2} \sum_{(n,m)=N_{TE}+1}^{+\infty} \frac{|I_{jx,qs}|^2 k_m^2}{\left(\frac{\sqrt{k_n^2 + k_m^2}}{j\omega\mu_0} + \frac{\sqrt{k_n^2 + k_m^2}}{j\omega\mu_0}\right)(k_n^2 + k_m^2)} \\ &= \frac{1}{|I_j|^2} \sum_{(n,m)=N_{TE}+1}^{+\infty} \frac{j\omega\mu_0 |I_{jx,qs}|^2 k_m^2}{(2\sqrt{k_n^2 + k_m^2})(k_n^2 + k_m^2)}, \end{aligned} \quad (3.110)$$

from which:

$$L_{ho} = \frac{\mu_0}{2|I_j|^2} \sum_{(n,m)=N_{TE}+1}^{+\infty} \frac{|I_{jx,qs}|^2 k_m^2}{(k_n^2 + k_m^2) \sqrt{k_n^2 + k_m^2}}, \quad (3.111)$$

and

$$\begin{aligned} \frac{1}{j\omega C_{ho}} &\approx \frac{1}{|I_j|^2} \sum_{(n,m)=N_{TM}+1}^{+\infty} \frac{|I_{jx,qs}|^2 k_n^2}{(Y_{nm,qs}^{TM(1,L)} + Y_{nm,qs}^{TM(2,R)})(k_n^2 + k_m^2)} \\ &= \frac{1}{|I_j|^2} \sum_{(n,m)=N_{TM}+1}^{+\infty} \frac{|I_{jx,qs}|^2 k_n^2}{\left(\frac{j\omega\varepsilon_0\varepsilon_{r,1}}{\sqrt{k_n^2 + k_m^2}} + \frac{j\omega\varepsilon_0\varepsilon_{r,2}}{\sqrt{k_n^2 + k_m^2}}\right)(k_n^2 + k_m^2)} \\ &= \frac{1}{|I_j|^2} \sum_{(n,m)=N_{TM}+1}^{+\infty} \frac{|I_{jx,qs}|^2 k_n^2 \sqrt{k_n^2 + k_m^2}}{j\omega\varepsilon_0(\varepsilon_{r,1} + \varepsilon_{r,2})(k_n^2 + k_m^2)}, \end{aligned} \quad (3.112)$$

from which:

$$\frac{1}{C_{ho}} = \frac{1}{\varepsilon_0(\varepsilon_{r,1} + \varepsilon_{r,2})|I_j|^2} \sum_{(n,m)=N_{TM}+1}^{+\infty} \frac{|I_{jx,qs}|^2 k_n^2}{\sqrt{k_n^2 + k_m^2}}. \quad (3.113)$$

3.5.1 Array of metallic patches

Array of freestanding dipole-based frequency selective surfaces

As a first illustrative practical example, I have analyzed an array of free-standing metallic patches under TE polarization with incidence angle $\theta = 20^\circ$, $P_x = P_y = 5$ mm, $w_x = 2$ mm, $w_y = 0.5$ mm, and $\varepsilon_r = 1$, in order to validate the proposed circuit model.

I supposed for the surface electric current the following spatial profile [22]:

$$\mathbf{j}_s(x, y) = \sqrt{\frac{1 - (2x/w_x)^2}{1 - (2y/w_y)^2}} \hat{\mathbf{x}}, \quad (3.114)$$

where w_x and w_y are the dimensions of the patch along the x and y -directions, respectively, as represented in Fig. 3.17 for the particular case of a patch with $w_x = 3.5$ mm and $w_y = 0.5$ mm.

Figure 3.18 represents the comparison between the results of the full-wave simulation and the fully-analytical circuit model in the frequency range [0-80] GHz which corresponds to the normalized frequency (P/λ_0) band [0-1.3]. In the EC model it is necessary to evaluate two double infinite series which converge slowly, but exploiting the decomposition of the equivalent impedance Z_{eq} this computation must be done only once with a noticeable saving of memory resources and CPU time.

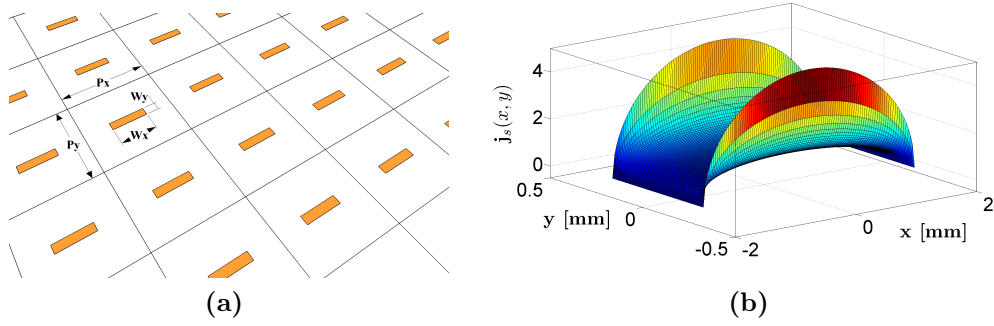


Figure 3.17: (a) Schematic of the freestanding dipole-based array and (b) spatial profile of the surface current density on a metallic patch with $w_x = 3.5$ mm and $w_y = 0.5$ mm.

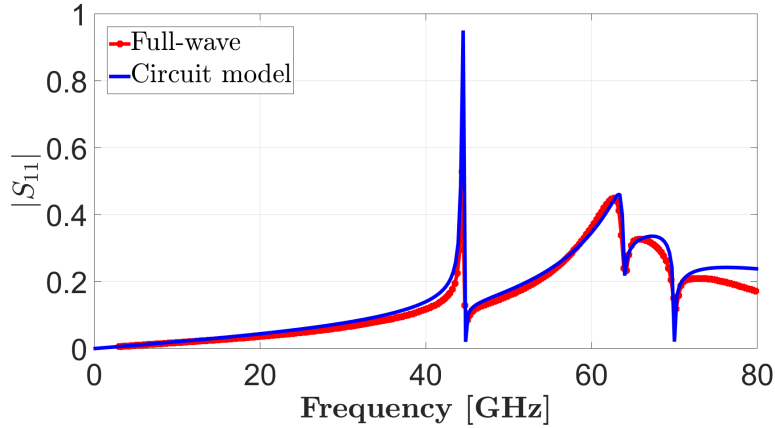


Figure 3.18: Magnitude of the S_{11} parameter under 20° TE incidence for an array of freestanding metallic patches with $\varepsilon_{r,1} = 1$, $P_x = P_y = 5$ mm, $w_x = 2$ mm, $w_y = 0.5$ mm, and $N_{TE} = N_{TM} = 4$.

An extraordinary resonance (i.e., a total reflection) at around 44.5 GHz is shown in Fig. 3.18 along with three nulls in the S_{11} parameter at 44.7, 64 and 70 GHz, due to the Wood's anomalies after that the higher order modes onset. These nulls correspond to the cutoff frequencies associated with the higher order nm th harmonics excited in the structure at 20° . In particular, the diffraction regime (the grating lobe region) starts with the first higher order harmonic. This way, a perfect reflection cannot be reached anymore above the first cutoff frequency. However, local maxima occur between two adjacent nulls.

It should be noted that depending on the length of the dipoles, the FSS can give rise to either Fabry–Pérot (conventional reflection) or Fano resonances (extraordinary reflection). The Fabry–Pérot behavior states that every thin metallic dipole in an array resonates at the frequency for which its length is close to $\lambda/2$. More specifically, the array totally reflects at this frequency if this condition is satisfied before the grating lobe region; otherwise an extraordinary total reflection, related to the Fano resonances, will be present below the first grating lobe.

Array of metallic patches embedded between two different dielectric half-spaces

Since we have completed the analysis of the freestanding scenario, we can now use the acquired experience to study the case of an array of metallic patches embedded between two different dielectric half-spaces with relative permittivity $\varepsilon_{r,1} = 1$ and $\varepsilon_{r,2} = 3$ under TE incidence with the electric field polarized along the x -axis. By using the spatial profile for the surface electric current in Eq. (3.114), it is possible to retrieve an analytical expression for the global equivalent impedance. To this purpose, I have calculated the following integrals of the surface electric current:

$$I_j = \iint_{Patch} \mathbf{j}_s(x, y) \cdot \hat{\mathbf{x}} e^{jk_t y} dx dy = \frac{\pi^2 w_x w_y}{8} J_0 \left(\frac{k_t w_y}{2} \right), \quad (3.115)$$

$$I_{jx} = \iint_{Patch} \mathbf{j}_s(x, y) \cdot \hat{\mathbf{x}} e^{jk_t y} e^{jk_n x} e^{jk_m y} dx dy = \frac{\pi^2 w_y}{2k_n} J_1 \left(\frac{k_n w_x}{2} \right) J_0 \left(\frac{k_{ym} w_y}{2} \right). \quad (3.116)$$

Substituting the analytical expressions of the above integrals in the general expression of the equivalent impedance in Eq. (3.97), we obtain:

$$\begin{aligned} Z_{eq} &= \frac{1}{|I_j|^2} \left[\sum_{(n,m) \neq (0,0)} \frac{|I_{jx}|^2}{(Y_{nm}^{TE(1)} + Y_{nm}^{TE(2)})} \frac{k_{ym}^2}{(k_n^2 + k_{ym}^2)} \right. \\ &\quad \left. + \sum_{nm, n \neq 0} \frac{|I_{jx}|^2}{(Y_{nm}^{TM(1)} + Y_{nm}^{TM(2)})} \frac{k_n^2}{(k_n^2 + k_{ym}^2)} \right] \\ &= \frac{1}{\left| \frac{\pi^2 w_x w_y}{8} J_0 \left(\frac{k_t w_y}{2} \right) \right|^2} \left[\sum_{(n,m) \neq (0,0)} \frac{\left| \frac{\pi^2 w_y}{2k_n} J_1 \left(\frac{k_n w_x}{2} \right) J_0 \left(\frac{k_{ym} w_y}{2} \right) \right|^2}{(Y_{nm}^{TE(1)} + Y_{nm}^{TE(2)})} \frac{k_{ym}^2}{(k_n^2 + k_{ym}^2)} \right. \\ &\quad \left. + \sum_{nm, n \neq 0} \frac{\left| \frac{\pi^2 w_y}{2k_n} J_1 \left(\frac{k_n w_x}{2} \right) J_0 \left(\frac{k_{ym} w_y}{2} \right) \right|^2}{(Y_{nm}^{TM(1)} + Y_{nm}^{TM(2)})} \frac{k_n^2}{(k_n^2 + k_{ym}^2)} \right] \\ &= \frac{16}{\left| w_x J_0 \left(\frac{k_t w_y}{2} \right) \right|^2} \left[\sum_{(n,m) \neq (0,0)} \frac{\left| J_1 \left(\frac{k_n w_x}{2} \right) J_0 \left(\frac{k_{ym} w_y}{2} \right) \right|^2}{(Y_{nm}^{TE(1)} + Y_{nm}^{TE(2)})} \frac{k_{ym}^2}{k_n^2 (k_n^2 + k_{ym}^2)} \right. \\ &\quad \left. + \sum_{nm, n \neq 0} \frac{\left| J_1 \left(\frac{k_n w_x}{2} \right) J_0 \left(\frac{k_{ym} w_y}{2} \right) \right|^2}{(Y_{nm}^{TM(1)} + Y_{nm}^{TM(2)})} \frac{1}{(k_n^2 + k_{ym}^2)} \right]. \end{aligned} \quad (3.117)$$

In Fig. 3.19 I compared the analytical equivalent-circuit results with numerical data provided by COMSOL Multiphysics in the normalized frequency range $[0-1] P/\lambda_0$. It can be noticed in Fig. 3.19(b) that, with the progressive increase of the number of TE and TM modes (N_{TE}, N_{TM}) considered in the numerical code, the EC results converge with increasing accuracy towards the expected values.

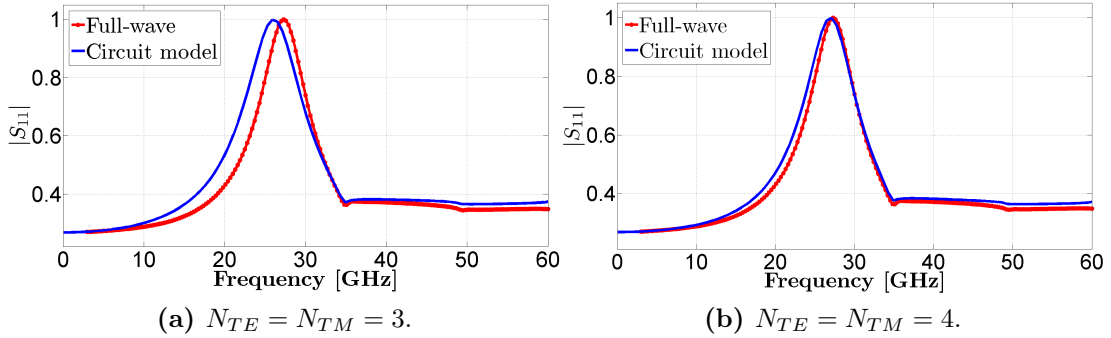


Figure 3.19: Magnitude of the S_{11} parameter under 0° TE incidence for an array of metallic patches embedded between two dielectric half-spaces with relative permittivity $\varepsilon_{r,1} = 1$ and $\varepsilon_{r,2} = 3$, $P_x = P_y = 5$ mm, $w_x = 3.5$ mm, and $w_y = 0.5$ mm.

Array of metallic patches printed on a finite thickness dielectric slab

I have considered a periodic 2D array of metallic patches printed on a dielectric slab with relative permittivity $\varepsilon_r = 3$ and of finite thickness $d = 0.5$ mm under $\theta = 40^\circ$ TE plane wave oblique incidence. Figure 3.20 shows the magnitude of the reflection coefficient for increasing values of the number of propagating TE/TM modes and for both electrically long and small dipoles (respectively, represented in Fig. 3.20(a)-(c) with $w_x = 3.5$ mm, and in Fig. 3.20(d) with $w_x = 2$ mm). It can be observed only one total reflection peak below the grating lobe regime starting at 36.5 GHz. However, there are only local minima instead of reflection nulls before the grating lobes onset, since total transmission is more difficult to reach due to the presence of different dielectric slabs.

Figure 3.21 represents the equivalent global impedance of the patch grating on a finite substrate, and it makes evident how the impedance is purely imaginary capacitive. In fact, from electrostatic relationships, it can be inferred that the static capacitance of an ideal parallel plate capacitor is directly proportional to the plate area A and inversely proportional to the plate separation d ($C = \varepsilon_0 \varepsilon_r A/d$). Therefore, the impedance of the patch grating is capacitive; in fact, the parallel plate capacitor formed by the two adjacent patches has a big area, and the capacitive coupling increases exponentially by reducing the gap between adjacent elements. On the contrary, the inductance is very low given the very large width of the patch; this dimension is comparable to the radius a of the wire in the formula of the inductance of two parallel wires of length l and separated

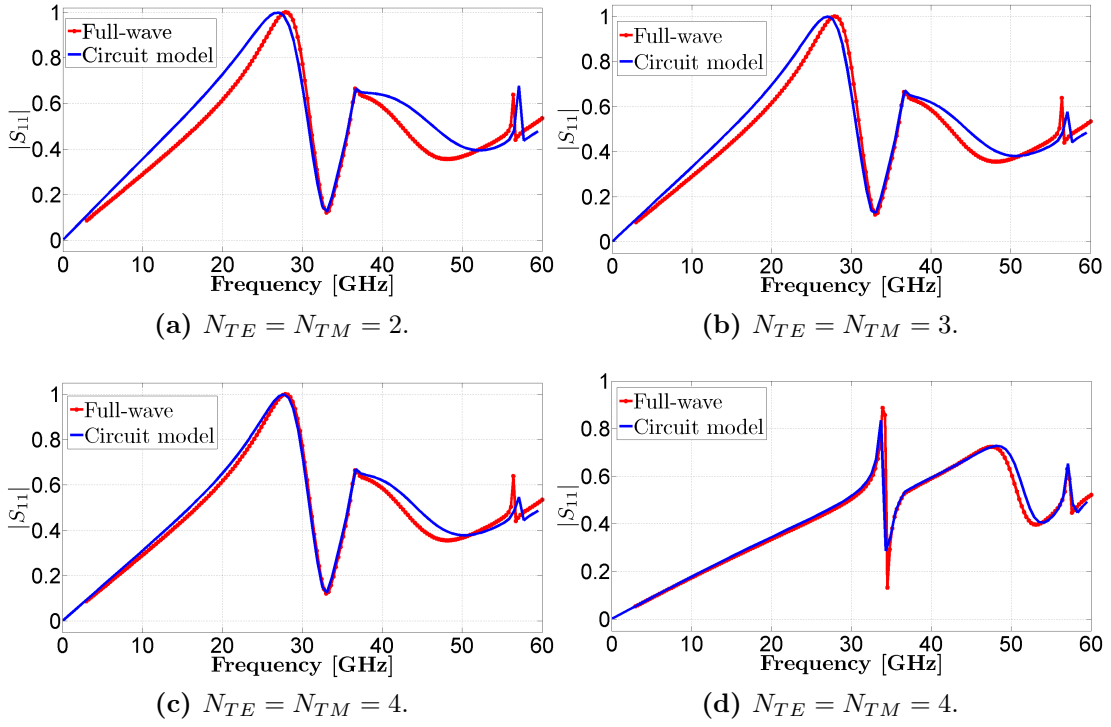


Figure 3.20: Magnitude of the S_{11} parameter under 40° TE incidence for an array of metallic patches with $\varepsilon_r = 3$, $d = 0.5$ mm, $P_x = P_y = 5$ mm, $w_y = 0.5$ mm, (a)-(c) $w_x = 3.5$ mm and (d) $w_x = 2$ mm.

by a distance d ($L = l/\pi \ln(a/d)$).

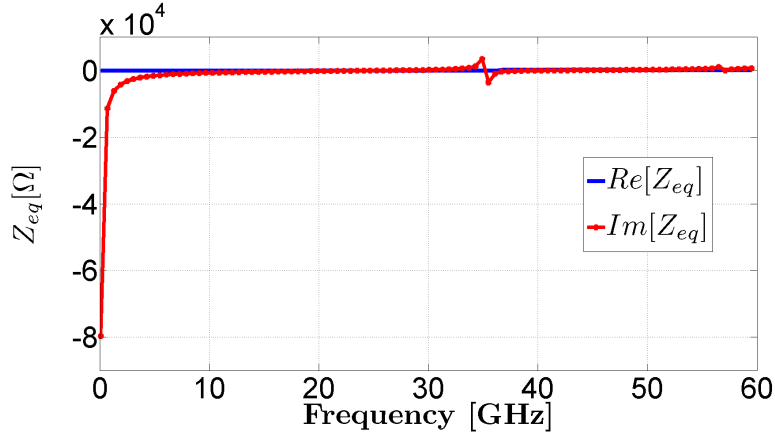


Figure 3.21: Equivalent impedance of an array of metallic patches with $\varepsilon_r = 3$, $d = 0.5$ mm, $P_x = P_y = 5$ mm, $w_x = 3.5$ mm, and $w_y = 0.5$ mm under 40° TE incidence.

3.5.2 Array of 2D metallic crosses

The analyzed EC networks allow modeling more complex FSS shapes such as crosses. I have considered an array of metallic crosses under TE incidence with the electric field polarized along the x axis. I suppose for the x and y components

of the surface electric current the following spatial profiles [22]:

$$j_{s,x}(x, y) = \cos\left(\frac{\pi x}{w_x}\right) \left[1 - \left(\frac{2y}{w_y}\right)^2\right]^{-1/2} \begin{cases} -w_x/2 \leq x \leq w_x/2 \\ -w_y/2 \leq y \leq w_y/2 \end{cases} \quad (3.118)$$

$$j_{s,y}(x, y) = \cos\left(\frac{\pi y}{w_y}\right) \left[1 - \left(\frac{2x}{w_x}\right)^2\right]^{-1/2} \begin{cases} -w_y/2 \leq x \leq w_y/2 \\ -w_x/2 \leq y \leq w_x/2 \end{cases} \quad (3.119)$$

being the global spatial profile of the surface electric current given by:

$$\mathbf{j}_s(x, y) = j_{s,x}(x, y)\hat{\mathbf{x}} + j_{s,y}(x, y)\hat{\mathbf{y}}, \quad (3.120)$$

as shown in Fig. 3.22 for a cross with dimensions $w_x = 10$ mm and $w_y = 1$ mm.

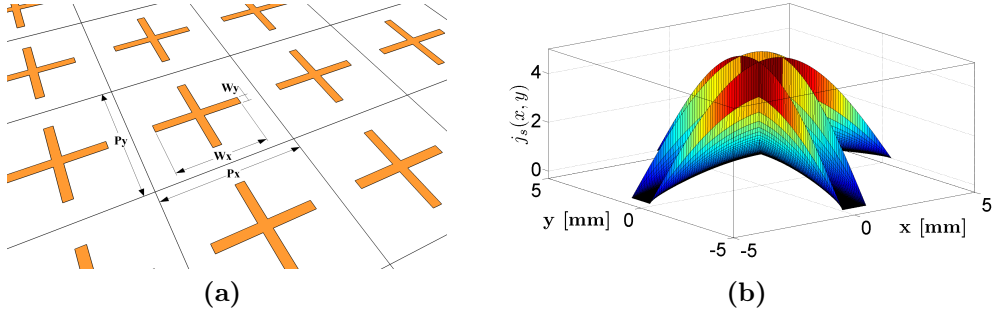


Figure 3.22: (a) Schematic of the freestanding cross-based array and (b) spatial profile of the surface current density on a metallic cross with $w_x = 10$ mm and $w_y = 1$ mm.

Another possible choice for the spatial profiles of the surface electric current is the following:

$$j_{s,x}(x, y) = \left\{ \sin\left[\frac{\pi}{w_x}\left(x + \frac{w_x}{2}\right)\right] + \cos\left(\frac{\pi x}{w_x}\right) \right\} \text{rect}\left(\frac{x}{w_x}\right) \text{rect}\left(\frac{y}{w_y}\right), \quad (3.121)$$

$$j_{s,y}(x, y) = \left\{ \sin\left[\frac{\pi}{w_y}\left(y + \frac{w_y}{2}\right)\right] - \cos\left(\frac{\pi y}{w_y}\right) \right\} \text{rect}\left(\frac{x}{w_x}\right) \text{rect}\left(\frac{y}{w_y}\right), \quad (3.122)$$

where the functions *rect* read

$$\text{rect}\left(\frac{x}{w_{x,y}}\right) = \begin{cases} 1 & \text{if } |x| \leq \frac{w_{x,y}}{2} \\ 0 & \text{otherwise} \end{cases} \quad (3.123)$$

$$\text{rect}\left(\frac{y}{w_{y,x}}\right) = \begin{cases} 1 & \text{if } |y| \leq \frac{w_{y,x}}{2} \\ 0 & \text{otherwise} \end{cases} \quad (3.124)$$

Array of 2D freestanding metallic crosses

In this subsection, the electromagnetic behavior of an array of freestanding metallic crosses is numerically simulated. In Fig. 3.23, it can be observed how the first resonance corresponds to a cross length equal to $\lambda_0/2$ at around $f = 17$ GHz, while the second resonance arises when the periodicity approaches λ_0 . In this case, the first resonance frequency appears before the onset of the grating lobes.

Figure 3.23 illustrates the S_{11} reflection parameter of the freestanding FSS with $P_x = P_y = 10$ mm, $w_x = 8.75$ mm, and $w_y = 1.25$ mm, obtained using the two proposed global spatial profiles of the surface electric currents in Eq. (3.118) and Eqs. (3.121)-(3.122), respectively. In particular, the capacitive contribution is mainly due to the strong electric field between the adjacent crosses, while the inductive contribution depends on the surface electric currents induced by the incident electric field.

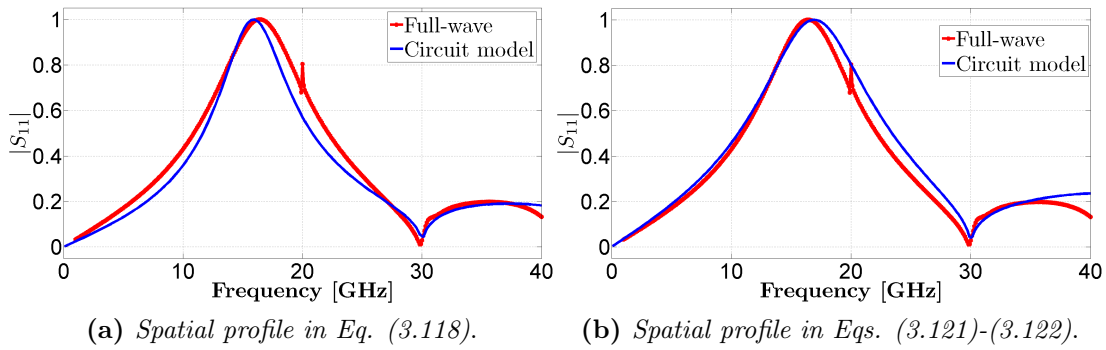


Figure 3.23: Magnitude of the S_{11} parameter under 0° TE incidence for an array of freestanding metallic crosses with $P_x = P_y = 10$ mm, $w_x = 8.75$ mm, $w_y = 1.25$ mm, and $N_{TE} = N_{TM} = 4$.

Array of 2D metallic crosses on a dielectric substrate

As a further example, I have considered the case of an array of cross-shaped FSS on a finite lossless substrate of thickness $d = 2$ mm and relative electric permittivity $\epsilon_r = 2.1$. The frequency sensitive device has been investigated in the frequency range [0-20] GHz, which corresponds to the normalized frequency band [0-1] P/λ_0 , as shown in Fig. 3.24.

In general, it can be noticed that the choice of the number of TE/TM harmonics is based on the following criterion: in the calculation of the derived low-order equivalent impedances/admittances, I have considered N_{TE} and N_{TM} propagating harmonics above the cutoff frequencies with respect to the highest permittivity dielectric, plus some evanescent high-order modes operating below, but close to their cutoff frequencies. An increasing agreement between the EC model and the

full-wave results can systematically be reached by adding higher-order modes.

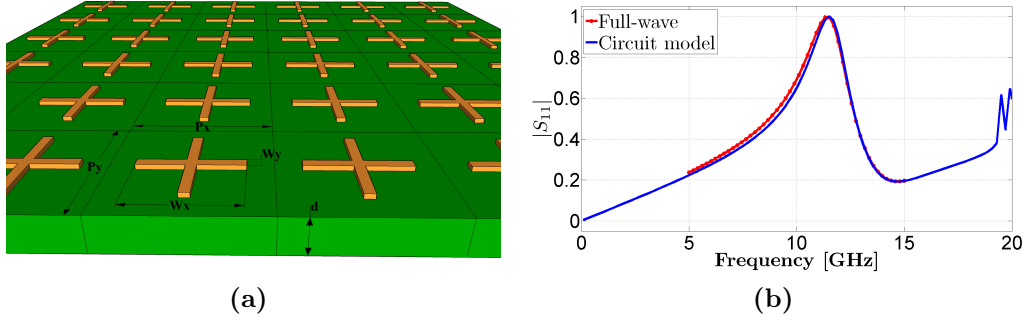


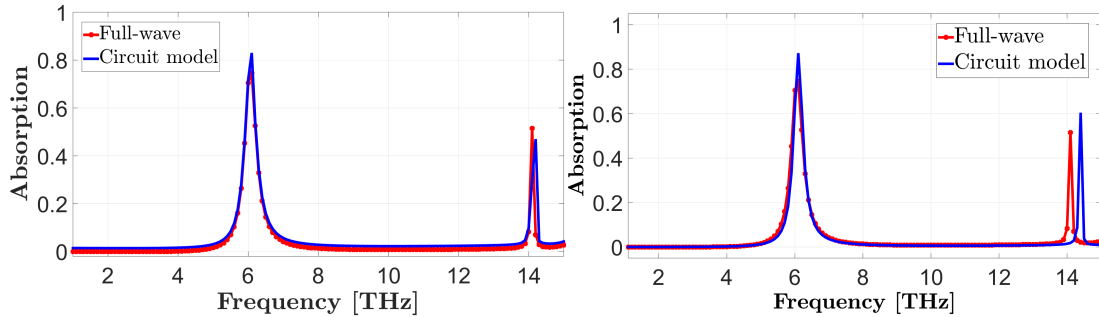
Figure 3.24: (a) Schematic of the cross-based array and (b) magnitude of the S_{11} parameter under 0° TE incidence for an array of metallic crosses with $\epsilon_r = 2.1$, $d = 2$ mm, $P_x = P_y = 15$ mm, $w_x = 10$ mm, $w_y = 1$ mm, and $N_{TE} = N_{TM} = 5$, using the spatial profile in Eqs. (3.121)-(3.122).

Metamaterial absorber of metallic crosses on a lossy grounded dielectric slab at THz

EC models can be applied to analyze the absorption properties of metamaterial absorbers composed of an array of crosses with dimensions $P_x = P_y = 20$ μm , $w_x = 15$ μm , $w_y = 3$ μm on a grounded Mylar substrate of thickness $d = 1.5$ μm , relative permittivity $\epsilon_r = 2.89$ and loss tangent $\tan \delta = 0.02$.

The power absorbed by the metamaterial absorber is shown in Fig. 3.25 in the normalized frequency range $[0-1] P/\lambda_0$ for both the spatial profile of the surface electric currents in Eqs. (3.118)-(3.119) and in Eqs. (3.121)-(3.122).

In this case, being the crosses low capacitive elements, the absorption profile is very selective: in fact, the capacitance of an FSS increases with the coupling area and the small distances between the adjacent elements, while the inductance reduces with the length of the elements.



(a) Spatial profile in Eqs. (3.118)-(3.119). (b) Spatial profile in Eqs. (3.121)-(3.122).

Figure 3.25: Absorption under 0° TE incidence for a cross-shaped metamaterial absorber with $\epsilon_r = 2.89$, $\tan \delta = 0.02$, $d = 1.5$ μm , $P_x = P_y = 20$ μm , $w_x = 15$ μm , $w_y = 3$ μm , (a) $N_{TE} = N_{TM} = 4$ and (b) $N_{TE} = N_{TM} = 2$.

3.6 Semi-analytical circuit model for arrays of 2D metallic FSSs

In what follows, I present some numerical results obtained from semi-analytical circuit models, where the spatial profiles of the surface electric current are extracted at a single low frequency. All the geometrical and circuit element details are provided in the captions of the figures for the case studies:

1. Array of freestanding patches (see Fig. 3.26);
2. Array of patches on a finite dielectric spacer (see Figs. 3.27-3.28 for $w_x = 3.5$ mm, and Figs. 3.29-3.31 for $w_x = 2$ mm);
3. Array of crosses on a finite lossless dielectric slab (see Figs. 3.32-3.34);
4. Array of rings on a finite lossless dielectric slab (see Figs. 3.35-3.37);
5. Array of split ring resonators on a finite lossless dielectric slab (see Figs. 3.38-3.40).

3.6.1 Array of freestanding patches

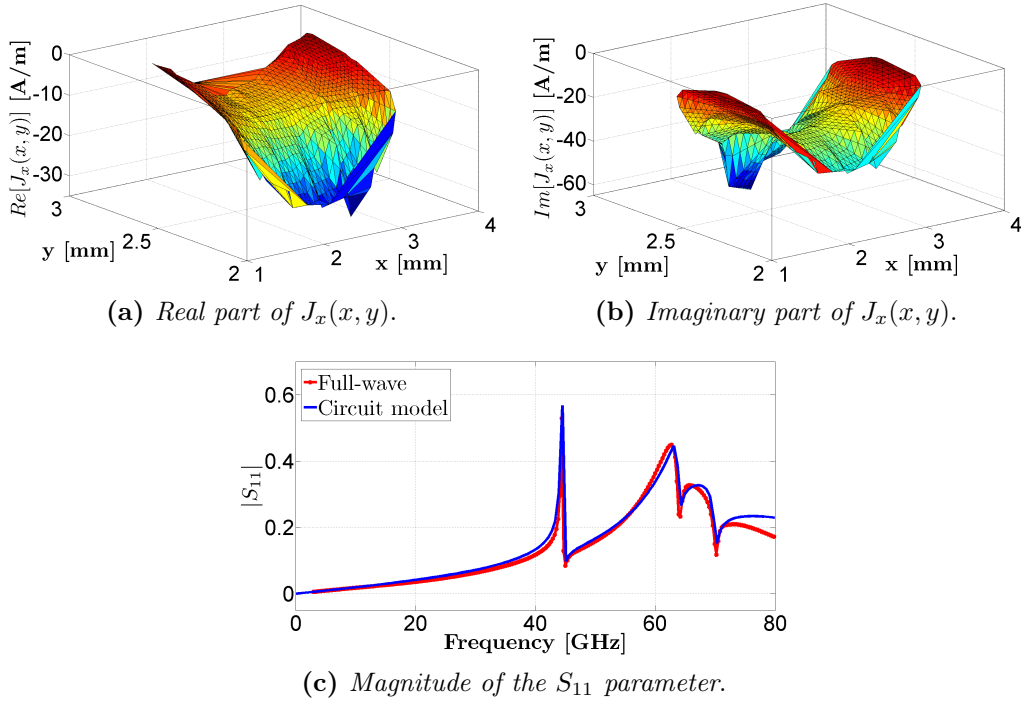
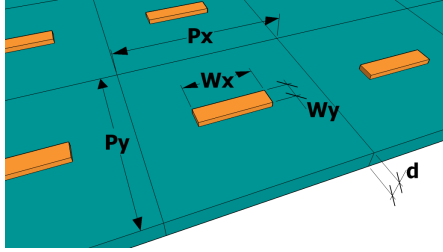
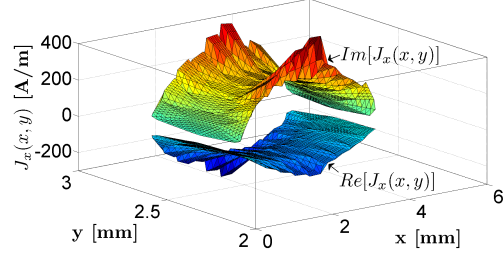


Figure 3.26: (a)-(b) Spatial profile of $J_x(x, y)$ on a metallic freestanding patch with $P_x = P_y = 5$ mm, $w_x = 2$ mm, $w_y = 0.5$ mm at 30 GHz, and (c) magnitude of the S_{11} parameter under 20° TE incidence with $N_{TE} = N_{TM} = 4$.

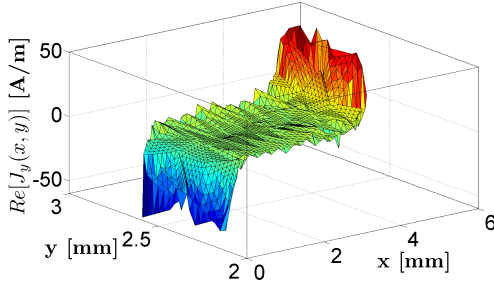
3.6.2 Array of patches printed on a finite dielectric spacer

Patch with $w_x = 3.5$ mm

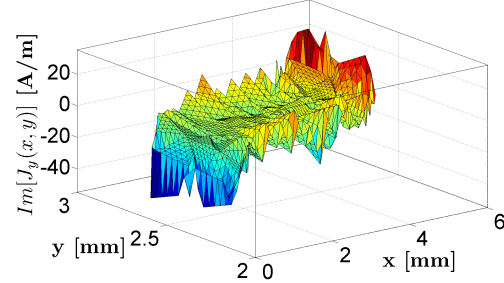
(a) Geometry of the patch-based array.



(b) Spatial profile of the x-component.



(c) Real part of the y-component.



(d) Imaginary part of the y-component.

Figure 3.27: (a) Schematic and (b)-(d) spatial profiles of the surface current density on a freestanding metallic patch with $w_x = 3.5$ mm and $w_y = 0.5$ mm at 30 GHz.

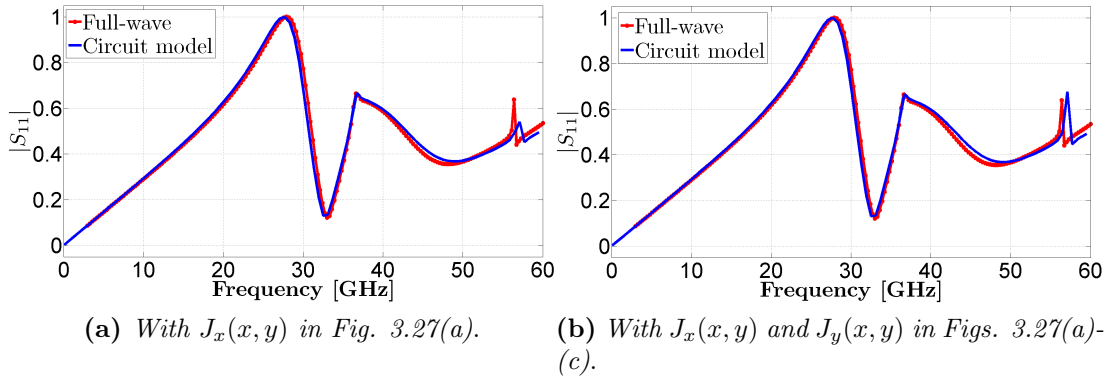
(a) With $J_x(x, y)$ in Fig. 3.27(a).(b) With $J_x(x, y)$ and $J_y(x, y)$ in Figs. 3.27(a)-(c).

Figure 3.28: Magnitude of the S_{11} parameter under 40° TE incidence for an array of metallic patches with $\epsilon_r = 3$, $d = 0.5$ mm, $P_x = P_y = 5$ mm, $w_x = 3.5$ mm, $w_y = 0.5$ mm, and $N_{TE} = N_{TM} = 4$.

Patch with $w_x = 2$ mm

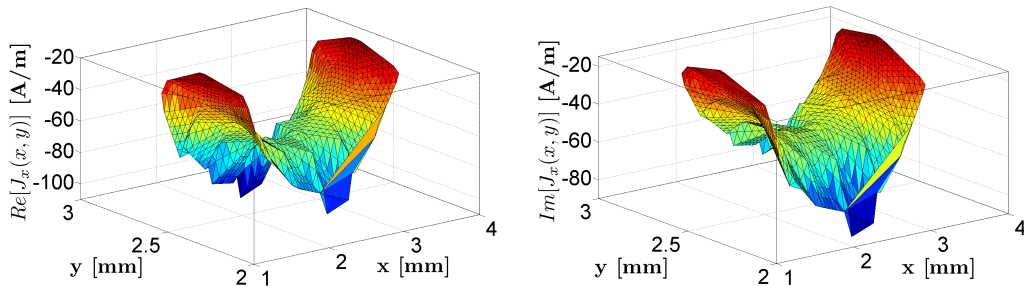


Figure 3.29: Spatial profile of the x -component of the surface current density on a metallic patch with $w_x = 2$ mm and $w_y = 0.5$ mm at 30 GHz.

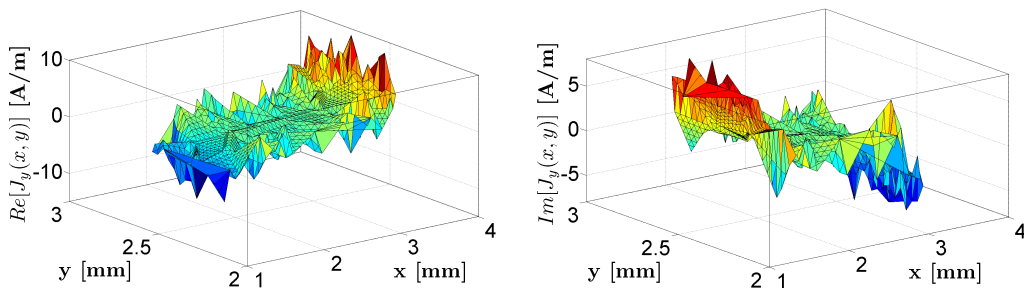


Figure 3.30: Spatial profile of the y -component of the surface current density on a metallic patch with $w_x = 2$ mm and $w_y = 0.5$ mm at 30 GHz.

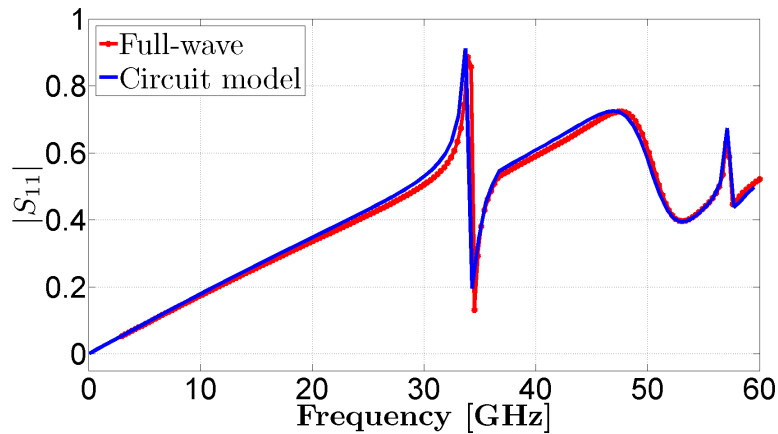


Figure 3.31: Magnitude of the S_{11} parameter under 40° TE incidence for an array of metallic patches with $\epsilon_r = 3$, $d = 0.5$ mm, $P_x = P_y = 5$ mm, $w_x = 2$ mm, $w_y = 0.5$ mm, and $N_{TE} = N_{TM} = 4$.

3.6.3 Array of crosses on a finite lossless dielectric slab

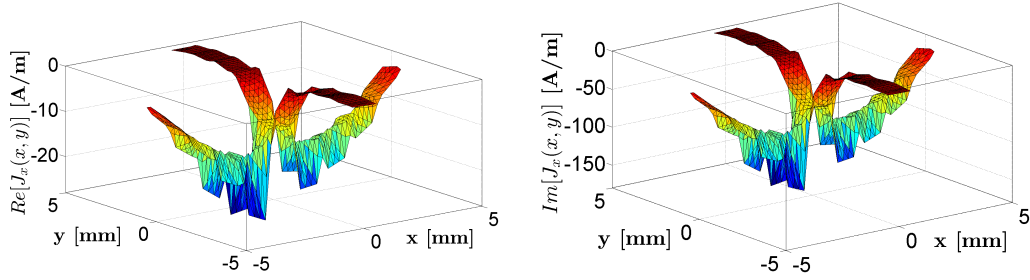


Figure 3.32: Real and imaginary parts of the x -component of the surface current density on a metallic cross with $w_x = 10$ mm and $w_y = 1$ mm at 10 GHz.

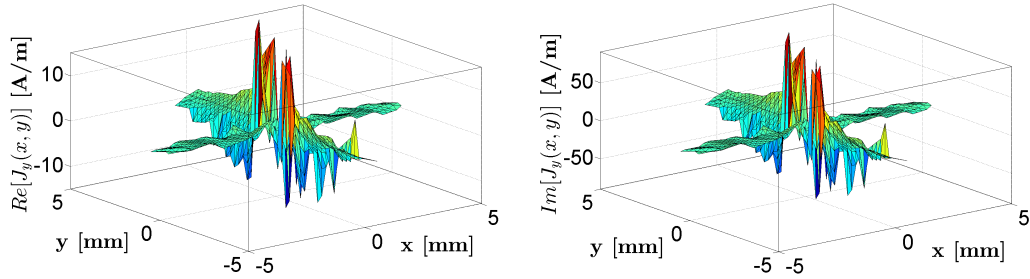


Figure 3.33: Real and imaginary parts of the y -component of the surface current density on a metallic cross with $w_x = 10$ mm and $w_y = 1$ mm at 10 GHz.

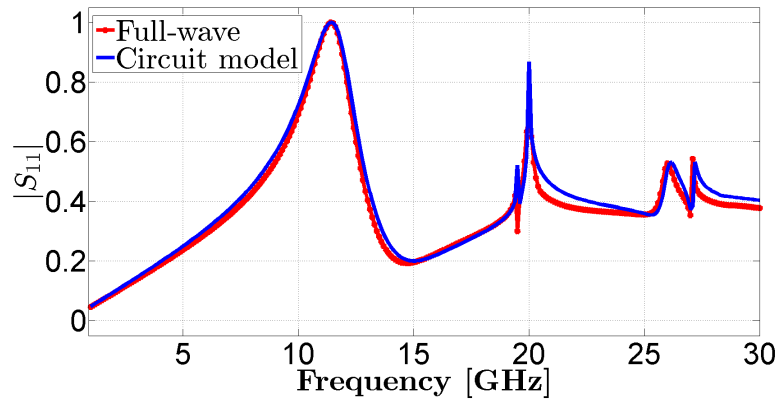


Figure 3.34: Magnitude of the S_{11} parameter under 0° TE incidence for an array of metallic crosses with $\epsilon_r = 2.1$, $d = 2$ mm, $P_x = P_y = 15$ mm, $w_x = 10$ mm, $w_y = 1$ mm, and $N_{TE} = N_{TM} = 4$ using the spatial profiles $J_x(x, y)$ and $J_y(x, y)$ in Figs. 3.32-3.33.

3.6.4 Array of rings on a finite lossless dielectric slab

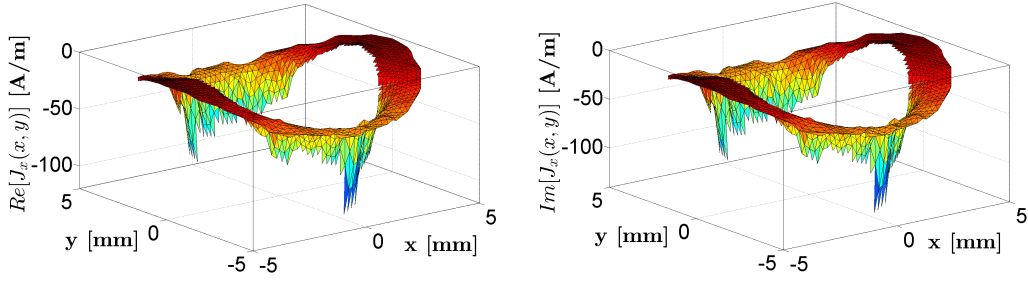


Figure 3.35: Real and imaginary parts of the x -component of the surface current density on a metallic ring with inner radius $r_i = 3.5$ mm and outer radius $r_o = 5$ mm at 11 GHz.

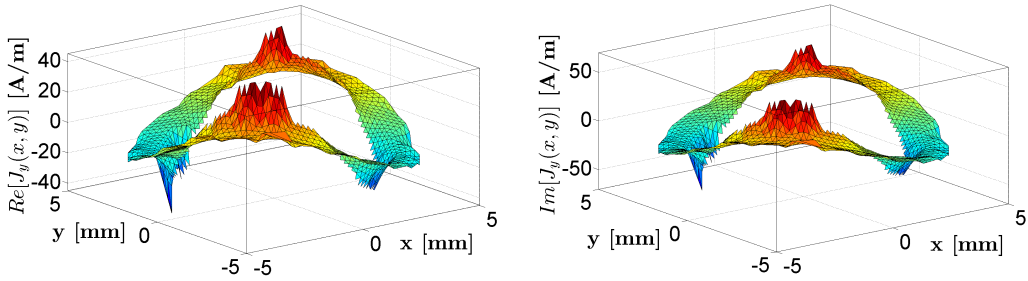


Figure 3.36: Real and imaginary parts of the y -component of the surface current density on a metallic ring with inner radius $r_i = 3.5$ mm and outer radius $r_o = 5$ mm at 11 GHz.

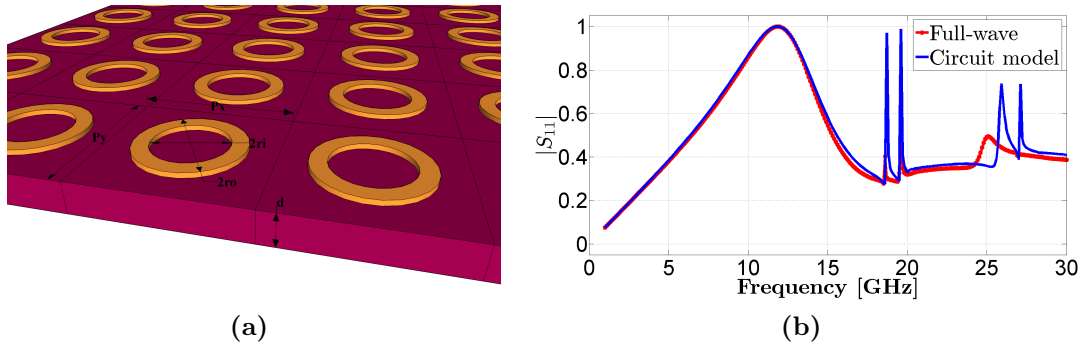


Figure 3.37: (a) Schematic of the ring-based array and (b) magnitude of the S_{11} parameter under 0° TE incidence for an array of metallic rings with $\epsilon_r = 2.1$, $d = 2$ mm, $P_x = P_y = 15$ mm, inner radius $r_i = 3.5$ mm, outer radius $r_o = 5$ mm, and $N_{TE} = N_{TM} = 4$ using the spatial profiles $J_x(x, y)$ and $J_y(x, y)$ in Figs. 3.35-3.36.

3.6.5 Array of split ring resonators (SRRs) on a finite lossless dielectric slab

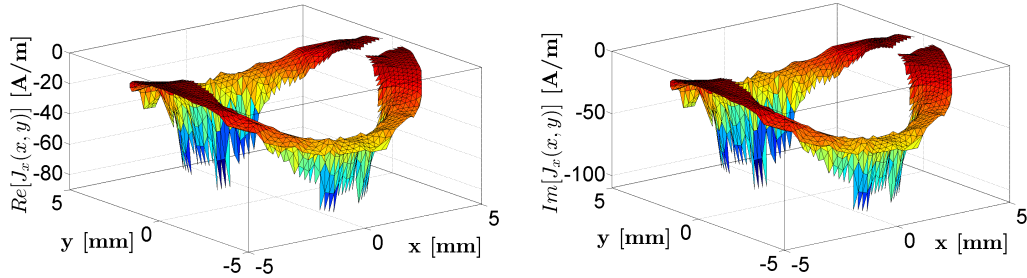


Figure 3.38: Real and imaginary parts of the x -component of the surface current density on a metallic SRR with inner radius $r_i = 3.5$ mm, outer radius $r_o = 5$ mm, and gap size $g = 1$ mm at 11 GHz.

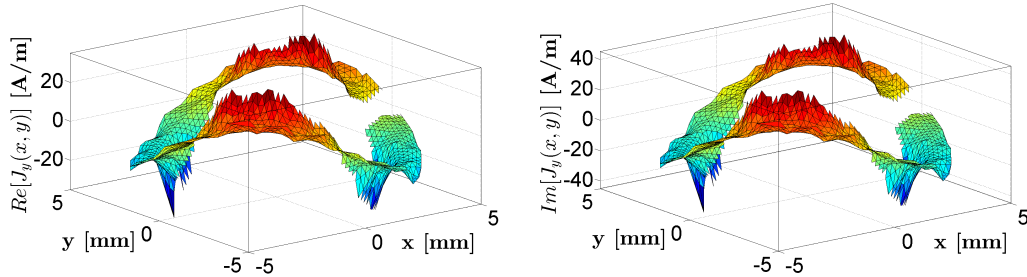


Figure 3.39: Real and imaginary parts of the y -component of the surface current density on a metallic SRR with inner radius $r_i = 3.5$ mm, outer radius $r_o = 5$ mm, and gap size $g = 1$ mm at 11 GHz.

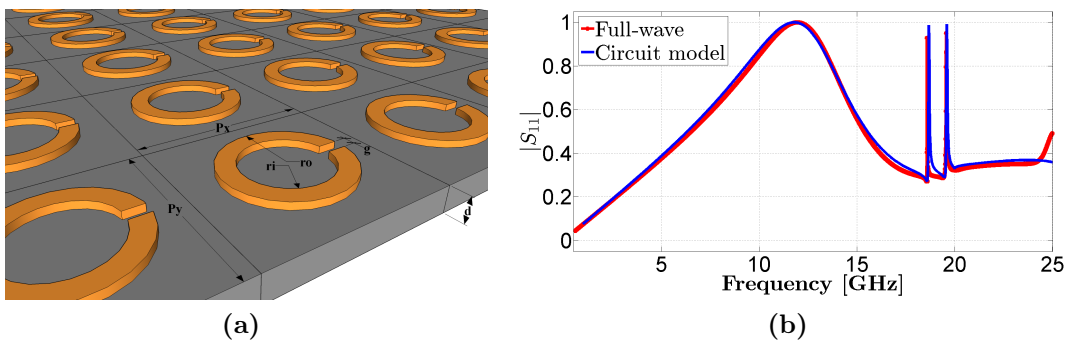


Figure 3.40: (a) Schematic of the SRR-based array and (b) magnitude of the S_{11} parameter under 0° TE incidence for an array of metallic SRRs with $\varepsilon_r = 2.1$, $d = 2$ mm, $P_x = P_y = 15$ mm, inner radius $r_i = 3.5$ mm, outer radius $r_o = 5$ mm, gap size $g = 1$ mm, and $N_{TE} = N_{TM} = 4$ using the spatial profiles $J_x(x, y)$ and $J_y(x, y)$ in Figs. 3.38-3.39.

3.7 Fully analytical circuit model for complementary frequency selective surfaces of arbitrary geometry

Here I consider the case of complementary FSS embedded within two different dielectric half-spaces, as illustrated in Fig. 3.41.

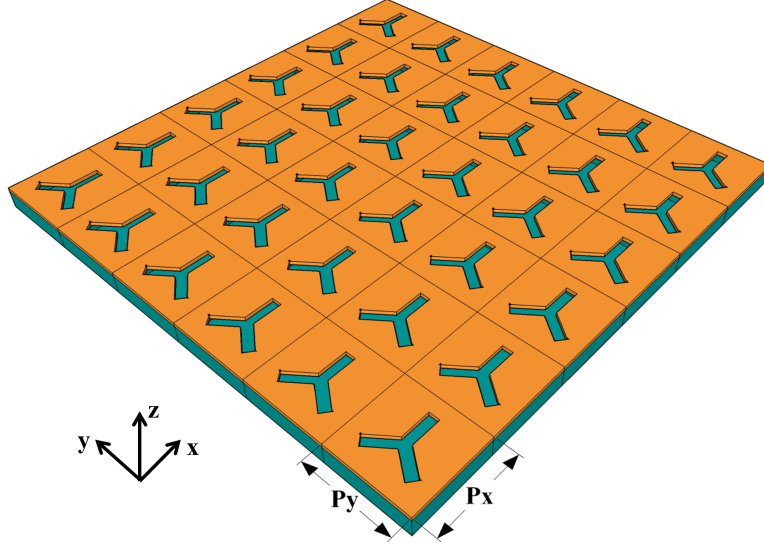


Figure 3.41: 3D sketch of complementary FSSs printed on a dielectric substrate.

Applying the Fourier transform of the $n = m = 0$ term in Eq. (3.59) and projecting along the x -direction, we can extract:

$$1 + R = \frac{A(\omega)}{P_x P_y} \iint_{ap} \mathbf{e}_s(x, y) \cdot \hat{\mathbf{x}} e^{jk_x y} dx dy = \frac{A(\omega)}{P_x P_y} I_e, \quad (3.125)$$

where I have defined with I_e the integral of the transverse aperture electric field on the complementary FSS:

$$I_e = \iint_{ap} \mathbf{e}_s(x, y) \cdot \hat{\mathbf{x}} e^{jk_x y} dx dy, \quad (3.126)$$

and, as made for the one-dimensional case, I have approximated the aperture electric field on the metallic complementary FSS with

$$\mathbf{E}_s(x, y; \omega) = A(\omega) \mathbf{e}_s(x, y). \quad (3.127)$$

From Eq. (3.125), it is possible to explicit the frequency-dependent term

$$\frac{A(\omega)}{P_x P_y} = \frac{1 + R}{I_e}. \quad (3.128)$$

At this point, I have multiplied the remaining terms in Eq. (3.59) by orthog-

onal functions, integrating on the single unit cell of dimensions P_x and P_y :

$$\begin{aligned}
& \sum_{(n,m) \neq (0,0)} E_{nm}^{TE} \frac{k_{ym} \hat{\mathbf{x}} - k_n \hat{\mathbf{y}}}{\sqrt{k_n^2 + k_{ym}^2}} \int_{-\frac{P_x}{2}}^{\frac{P_x}{2}} \int_{-\frac{P_y}{2}}^{\frac{P_y}{2}} e^{-jk_n x} e^{j\frac{2\pi q}{P_x} x} e^{-jk_m y} e^{j\frac{2\pi p}{P_y} y} dx dy \\
& + \sum_{nm, n \neq 0} E_{nm}^{TM} \frac{k_n \hat{\mathbf{x}} + k_{ym} \hat{\mathbf{y}}}{\sqrt{k_n^2 + k_{ym}^2}} \int_{-\frac{P_x}{2}}^{\frac{P_x}{2}} \int_{-\frac{P_y}{2}}^{\frac{P_y}{2}} e^{-jk_n x} e^{j\frac{2\pi q}{P_x} x} e^{-jk_m y} e^{j\frac{2\pi p}{P_y} y} dx dy \quad (3.129) \\
& = A(\omega) \int_{-\frac{P_x}{2}}^{\frac{P_x}{2}} \int_{-\frac{P_y}{2}}^{\frac{P_y}{2}} \mathbf{e}_s(x, y) e^{jk_t y} e^{j\frac{2\pi q}{P_x} x} e^{j\frac{2\pi p}{P_y} y} dx dy.
\end{aligned}$$

Equation (3.129) is initially projected along the x -axis, where I have used the Kronecker delta function in Eqs. (3.78)-(3.79), redefining $q = n$ and $p = m$:

$$\begin{aligned}
& E_{nm}^{TE} \frac{k_{ym}}{\sqrt{k_n^2 + k_{ym}^2}} P_x P_y + E_{nm}^{TM} \frac{k_n}{\sqrt{k_n^2 + k_{ym}^2}} P_x P_y \\
& = A(\omega) \iint_{ap} \mathbf{e}_s(x, y) \cdot \hat{\mathbf{x}} e^{jk_t y} e^{jk_n x} e^{jk_m y} dx dy, \quad (3.130)
\end{aligned}$$

and introducing the integral of the x -component of the aperture electric field as:

$$I_{ex} = \iint_{ap} \mathbf{e}_s(x, y) \cdot \hat{\mathbf{x}} e^{jk_t y} e^{jk_n x} e^{jk_m y} dx dy, \quad (3.131)$$

we can obtain:

$$E_{nm}^{TE} \frac{k_{ym}}{\sqrt{k_n^2 + k_{ym}^2}} + E_{nm}^{TM} \frac{k_n}{\sqrt{k_n^2 + k_{ym}^2}} = \frac{A(\omega)}{P_x P_y} I_{ex} = \frac{I_{ex}}{I_e} (1 + R), \quad (3.132)$$

where the ratio $A(\omega)/(P_x P_y)$ has been substituted with the Eq. (3.128).

Projecting now Eq. (3.129) along the y -axis:

$$\begin{aligned}
& - E_{nm}^{TE} \frac{k_n}{\sqrt{k_n^2 + k_{ym}^2}} P_x P_y + E_{nm}^{TM} \frac{k_{ym}}{\sqrt{k_n^2 + k_{ym}^2}} P_x P_y \\
& = A(\omega) \iint_{ap} \mathbf{e}_s(x, y) \cdot \hat{\mathbf{y}} e^{jk_t y} e^{jk_n x} e^{jk_m y} dx dy, \quad (3.133)
\end{aligned}$$

and defining the integral of the y -component of the aperture electric field as:

$$I_{ey} = \iint_{ap} \mathbf{e}_s(x, y) \cdot \hat{\mathbf{y}} e^{jk_t y} e^{jk_n x} e^{jk_m y} dx dy, \quad (3.134)$$

we obtain:

$$- E_{nm}^{TE} \frac{k_n}{\sqrt{k_n^2 + k_{ym}^2}} + E_{nm}^{TM} \frac{k_{ym}}{\sqrt{k_n^2 + k_{ym}^2}} = \frac{A(\omega)}{P_x P_y} I_{ey} = \frac{I_{ey}}{I_e} (1 + R). \quad (3.135)$$

Equation (3.132) and Eq. (3.135) represent a system of two equations in the two unknowns E_{nm}^{TE} and E_{nm}^{TM} that assume the following expressions:

$$E_{nm}^{TE} = (1 + R) \frac{I_{ex}k_{ym} - I_{ey}k_n}{I_e \sqrt{k_n^2 + k_{ym}^2}}, \quad (3.136)$$

$$E_{nm}^{TM} = (1 + R) \frac{I_{ex}k_n + I_{ey}k_{ym}}{I_e \sqrt{k_n^2 + k_{ym}^2}}. \quad (3.137)$$

I then applied the condition of continuity of the Poynting vector through the aperture:

$$\iint_{ap} \left[\mathbf{E}_s^* \times (\mathbf{H}^{(2)} - \mathbf{H}^{(1)}) \right] \cdot \hat{\mathbf{z}} dx dy = 0, \quad (3.138)$$

obtaining from the substitution of the magnetic field expansion:

$$\begin{aligned} & \iint_{ap} \mathbf{E}_s^* \times \left[Y_{00}^{TE(2)} (1 + R) e^{-jk_t y} \hat{\mathbf{y}} + \sum_{(n,m) \neq (0,0)} H_{nm}^{TE(2)} \frac{k_n \hat{\mathbf{x}} + k_{ym} \hat{\mathbf{y}}}{\sqrt{k_n^2 + k_{ym}^2}} e^{-j(k_n x + k_{ym} y)} \right. \\ & + \sum_{nm, n \neq 0} H_{nm}^{TM(2)} \frac{k_n \hat{\mathbf{y}} - k_{ym} \hat{\mathbf{x}}}{\sqrt{k_n^2 + k_{ym}^2}} e^{-j(k_n x + k_{ym} y)} - Y_{00}^{TE(1)} (1 - R) e^{-jk_t y} \hat{\mathbf{y}} \\ & + \sum_{(n,m) \neq (0,0)} H_{nm}^{TE(1)} \frac{k_{ym} \hat{\mathbf{y}} + k_n \hat{\mathbf{x}}}{\sqrt{k_n^2 + k_{ym}^2}} e^{-j(k_n x + k_{ym} y)} \\ & \left. + \sum_{nm, n \neq 0} H_{nm}^{TM(1)} \frac{k_n \hat{\mathbf{y}} - k_{ym} \hat{\mathbf{x}}}{\sqrt{k_n^2 + k_{ym}^2}} e^{-j(k_n x + k_{ym} y)} \right] \cdot \hat{\mathbf{z}} dx dy = 0. \end{aligned} \quad (3.139)$$

From the definitions in Eqs. (3.69)-(3.70) of the expansion coefficients of the magnetic field, Eq. (3.139) becomes:

$$\begin{aligned} & A^*(\omega) \iint_{ap} \mathbf{e}_s^* \times \left\{ \left[(Y_{00}^{TE(2)} - Y_{00}^{TE(1)}) + R(Y_{00}^{TE(2)} + Y_{00}^{TE(1)}) \right] e^{-jk_t y} \hat{\mathbf{y}} \right. \\ & + \sum_{(n,m) \neq (0,0)} E_{nm}^{TE} (Y_{nm}^{TE(1)} + Y_{nm}^{TE(2)}) \frac{k_n \hat{\mathbf{x}} + k_{ym} \hat{\mathbf{y}}}{\sqrt{k_n^2 + k_{ym}^2}} e^{-j(k_n x + k_{ym} y)} \\ & \left. + \sum_{nm, n \neq 0} E_{nm}^{TM} (Y_{nm}^{TM(1)} + Y_{nm}^{TM(2)}) \frac{k_n \hat{\mathbf{y}} - k_{ym} \hat{\mathbf{x}}}{\sqrt{k_n^2 + k_{ym}^2}} e^{-j(k_n x + k_{ym} y)} \right\} \cdot \hat{\mathbf{z}} dx dy = 0. \end{aligned} \quad (3.140)$$

The term $n = m = 0$ in Eq. (3.140) can be rewritten as:

$$\begin{aligned} A^*(\omega) & \left[(Y_{00}^{TE(2)} - Y_{00}^{TE(1)}) + R(Y_{00}^{TE(2)} + Y_{00}^{TE(1)}) \right] \iint_{ap} \mathbf{e}_s^* \times \hat{\mathbf{y}} \cdot \hat{\mathbf{z}} e^{-jk_t y} dx dy \\ & = A^*(\omega) \left[(Y_{00}^{TE(2)} - Y_{00}^{TE(1)}) + R(Y_{00}^{TE(2)} + Y_{00}^{TE(1)}) \right] I_e^*, \end{aligned} \quad (3.141)$$

and TE harmonics in Eq. (3.140) as:

$$\begin{aligned} A^*(\omega) & \iint_{ap} \left[\mathbf{e}_s^* \times \sum_{(n,m) \neq (0,0)} E_{nm}^{TE} (Y_{nm}^{TE(1)} + Y_{nm}^{TE(2)}) \frac{k_n \hat{\mathbf{x}} + k_{ym} \hat{\mathbf{y}}}{\sqrt{k_n^2 + k_{ym}^2}} \right] \cdot \hat{\mathbf{z}} e^{-j(k_n x + k_{ym} y)} dx dy \\ & = A^*(\omega) \sum_{(n,m) \neq (0,0)} E_{nm}^{TE} \frac{Y_{nm}^{TE(1)} + Y_{nm}^{TE(2)}}{\sqrt{k_n^2 + k_{ym}^2}} \iint_{ap} [k_n \mathbf{e}_s^* \times \hat{\mathbf{x}} + k_{ym} \mathbf{e}_s^* \times \hat{\mathbf{y}}] \cdot \hat{\mathbf{z}} e^{-j(k_n x + k_{ym} y)} dx dy \\ & = A^*(\omega) \sum_{(n,m) \neq (0,0)} E_{nm}^{TE} (Y_{nm}^{TE(1)} + Y_{nm}^{TE(2)}) \frac{-k_n I_{ey}^* + k_{ym} I_{ex}^*}{\sqrt{k_n^2 + k_{ym}^2}}, \end{aligned} \quad (3.142)$$

and finally the TM harmonics as:

$$\begin{aligned} A^*(\omega) & \sum_{nm, n \neq 0} E_{nm}^{TM} \frac{Y_{nm}^{TM(1)} + Y_{nm}^{TM(2)}}{\sqrt{k_n^2 + k_{ym}^2}} \iint_{ap} [k_n \mathbf{e}_s^* \times \hat{\mathbf{y}} - k_{ym} \mathbf{e}_s^* \times \hat{\mathbf{x}}] \cdot \hat{\mathbf{z}} e^{-j(k_n x + k_{ym} y)} dx dy \\ & = A^*(\omega) \sum_{nm, n \neq 0} E_{nm}^{TM} (Y_{nm}^{TM(1)} + Y_{nm}^{TM(2)}) \frac{k_n I_{ex}^* + k_{ym} I_{ey}^*}{\sqrt{k_n^2 + k_{ym}^2}}. \end{aligned} \quad (3.143)$$

After substituting the expansion coefficients of the electric field E_{nm}^{TE} and E_{nm}^{TM} in Eqs. (3.136)-(3.137), Eq. (3.139) becomes:

$$\begin{aligned} & \left[(Y_{00}^{TE(2)} - Y_{00}^{TE(1)}) + R(Y_{00}^{TE(2)} + Y_{00}^{TE(1)}) \right] I_e^* \\ & + \sum_{(n,m) \neq (0,0)} (1 + R) \frac{|I_{ex} k_{ym} - I_{ey} k_n|^2}{I_e (k_n^2 + k_{ym}^2)} (Y_{nm}^{TE(1)} + Y_{nm}^{TE(2)}) \\ & + \sum_{nm, n \neq 0} (1 + R) \frac{|I_{ex} k_n + I_{ey} k_{ym}|^2}{I_e (k_n^2 + k_{ym}^2)} (Y_{nm}^{TM(1)} + Y_{nm}^{TM(2)}) = 0. \end{aligned} \quad (3.144)$$

Being the expression of the reflection coefficient equal to:

$$R = \frac{(Y_{00}^{TE(1)} - Y_{00}^{TE(2)}) - Y_{eq}}{(Y_{00}^{TE(1)} + Y_{00}^{TE(2)}) + Y_{eq}}, \quad (3.145)$$

the equivalent admittance is:

$$\begin{aligned}
 Y_{eq} &= Y_{eq}^{TE} + Y_{eq}^{TM} \\
 &= \sum_{(n,m) \neq (0,0)} \frac{|I_{ex}k_{ym} - I_{ey}k_n|^2}{|I_e|^2(k_n^2 + k_{ym}^2)} (Y_{nm}^{TE(1)} + Y_{nm}^{TE(2)}) \\
 &\quad + \sum_{nm, n \neq 0} \frac{|I_{ex}k_n + I_{ey}k_{ym}|^2}{|I_e|^2(k_n^2 + k_{ym}^2)} (Y_{nm}^{TM(1)} + Y_{nm}^{TM(2)}).
 \end{aligned} \tag{3.146}$$

From Eq. (3.146), we can introduce the transformer turn ratios:

$$A_{nm}^{TE} = \frac{|I_{ex}k_{ym} - I_{ey}k_n|}{|I_e|\sqrt{k_{xn}^2 + k_{ym}^2}}, \tag{3.147}$$

$$A_{nm}^{TM} = \frac{|I_{ex}k_n + I_{ey}k_{ym}|}{|I_e|\sqrt{k_{xn}^2 + k_{ym}^2}}, \tag{3.148}$$

with the relevant circuit topology shown in Fig. 3.42.

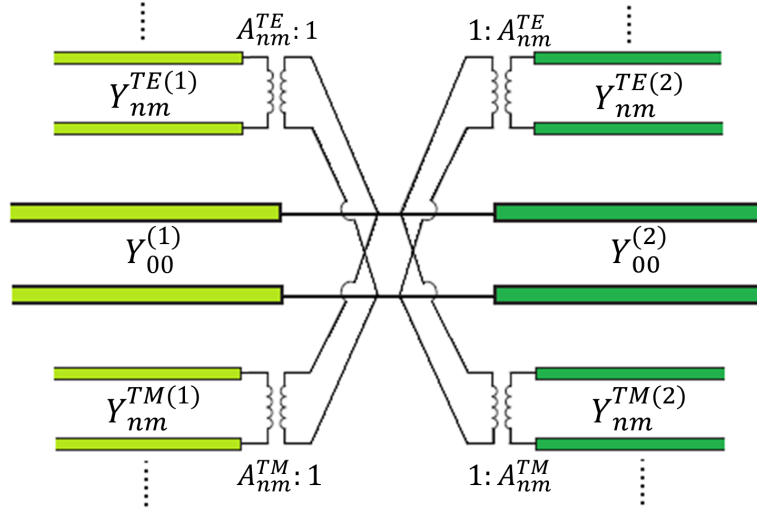


Figure 3.42: Equivalent circuit topology for complementary FSSs embedded between two different dielectric half-spaces.

Then, considering separately the contribution of high-order harmonics and exploiting Eqs. (3.102)-(3.105), the high-order inductance and capacitance read:

$$\frac{1}{j\omega L_{ho}} \approx \frac{1}{|I_e|^2} \sum_{(n,m)=N_{TE}+1}^{+\infty} 2Y_{nm,qs}^{TE} \frac{|I_{ex,qs}k_m - I_{ey,qs}k_n|^2}{(k_n^2 + k_m^2)}, \tag{3.149}$$

$$j\omega C_{ho} \approx \frac{1}{|I_e|^2} \sum_{(n,m)=N_{TM}+1}^{+\infty} \frac{|I_{ex,qs}k_n + I_{ey,qs}k_m|^2}{(k_n^2 + k_m^2)} (Y_{nm,qs}^{TM(1,L)} + Y_{nm,qs}^{TM(2,R)}), \tag{3.150}$$

where $Y_{nm,qs}^L$ and $Y_{nm,qs}^R$ are the input admittances seen by the corresponding

harmonic to the left/right of the aperture, and the quasi-static integrals for the x and y components of the aperture electric field are:

$$I_{ex,qs} = \iint_{ap} \mathbf{e}_s(x, y) \cdot \hat{\mathbf{x}} e^{jk_n x} e^{jk_m y} dx dy, \quad (3.151)$$

$$I_{ey,qs} = \iint_{ap} \mathbf{e}_s(x, y) \cdot \hat{\mathbf{y}} e^{jk_n x} e^{jk_m y} dx dy. \quad (3.152)$$

In the analysis of electrically narrow rectangular apertures under TM incidence with the transverse electric field component along the y -axis, it is possible to neglect the x component of the aperture electric field. In particular, for a slot array embedded between two different dielectric half-spaces, the high-order inductance and capacitance have, respectively, the following expressions:

$$\begin{aligned} \frac{1}{j\omega L_{ho}} &\approx \frac{1}{|I_e|^2} \sum_{(n,m)=N_{TE}+1}^{+\infty} 2Y_{nm,qs}^{TE} \frac{|I_{ey,qs}|^2 k_n^2}{(k_n^2 + k_m^2)} \\ &= \frac{1}{|I_e|^2} \sum_{(n,m)=N_{TE}+1}^{+\infty} \frac{2\sqrt{k_n^2 + k_m^2} |I_{ey,qs}|^2 k_n^2}{j\omega\mu_0 (k_n^2 + k_m^2)}, \end{aligned} \quad (3.153)$$

from which:

$$\frac{1}{L_{ho}} = \frac{2}{\mu_0 |I_e|^2} \sum_{(n,m)=N_{TE}+1}^{+\infty} \frac{|I_{ey,qs}|^2 k_n^2}{\sqrt{k_n^2 + k_m^2}}, \quad (3.154)$$

and

$$\begin{aligned} j\omega C_{ho} &\approx \frac{1}{|I_e|^2} \sum_{(n,m)=N_{TM}+1}^{+\infty} (Y_{nm,qs}^{TM(1,L)} + Y_{nm,qs}^{TM(2,R)}) \frac{|I_{ey,qs}|^2 k_m^2}{(k_n^2 + k_m^2)} \\ &= \frac{1}{|I_e|^2} \sum_{(n,m)=N_{TM}+1}^{+\infty} \frac{j\omega\varepsilon_0}{\sqrt{k_n^2 + k_m^2}} (\varepsilon_{r,1} + \varepsilon_{r,2}) \frac{|I_{ey,qs}|^2 k_m^2}{(k_n^2 + k_m^2)}, \end{aligned} \quad (3.155)$$

from which:

$$C_{ho} = \frac{\varepsilon_0(\varepsilon_{r,1} + \varepsilon_{r,2})}{|I_e|^2} \sum_{(n,m)=N_{TM}+1}^{+\infty} \frac{|I_{ey,qs}|^2 k_m^2}{\sqrt{k_n^2 + k_m^2}}. \quad (3.156)$$

3.7.1 Rectangular slot-based filters on a finite lossless silicon slab

I initially analyzed an array of rectangular slots under TM polarization with incidence angle $\theta = 20^\circ$, $P_x = P_y = 236 \mu\text{m}$, $w_x = 183 \mu\text{m}$, $w_y = 30 \mu\text{m}$, dielectric thickness $d = 302 \mu\text{m}$, and relative permittivity $\epsilon_r = 11.8$, and magnitude of the S_{11} parameter as shown in Fig. 3.43.

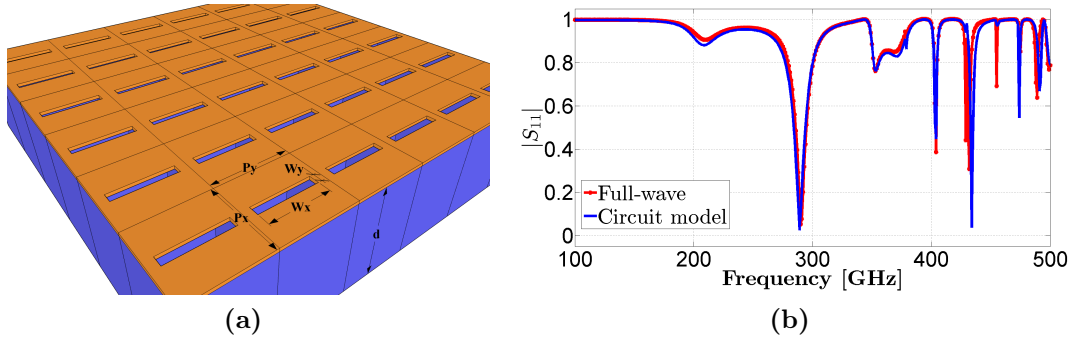


Figure 3.43: (a) Schematic of the rectangular slot-based array and (b) magnitude of the S_{11} parameter under 20° TM incidence for an array of rectangular slots with $\epsilon_r = 11.8$, $P_x = P_y = 236 \mu\text{m}$, $w_x = 183 \mu\text{m}$, $w_y = 30 \mu\text{m}$, $d = 302 \mu\text{m}$, and $N_{TE} = N_{TM} = 4$ using the spatial profile $e_y(x, y)$ in Eq. (3.157).

In order to retrieve the reflection response (see Fig. 3.43(b)), I supposed for the aperture electric field the following spatial profile [22]:

$$\mathbf{e}_s(x, y) = \cos\left(\frac{\pi x}{w_x}\right) \sqrt{\frac{1}{1 - (2x/w_x)^2}} \hat{\mathbf{y}}, \quad (3.157)$$

where w_x and w_y are the dimensions of the slot along the x and y -directions, respectively, as represented in Fig. 3.44 for this particular case.

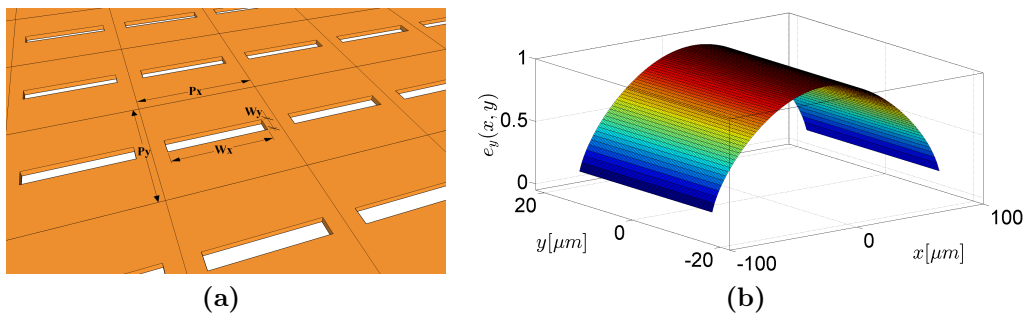


Figure 3.44: (a) Schematic of the freestanding rectangular slot-based array and (b) spatial profile of the aperture electric field on a rectangular slot with $w_x = 183 \mu\text{m}$ and $w_y = 30 \mu\text{m}$.

3.8 Semi-analytical circuit model for complementary FSSs

3.8.1 Filters based on rectangular slots

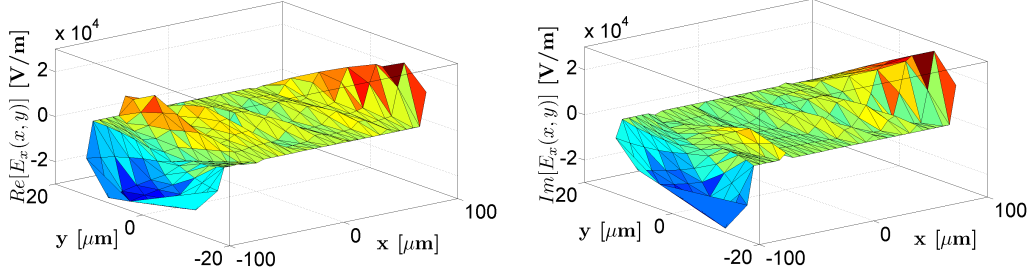


Figure 3.45: Real and imaginary parts of the x -component of the aperture electric field on a rectangular slot with $w_x = 183 \mu\text{m}$ and $w_y = 30 \mu\text{m}$ at 200 GHz.

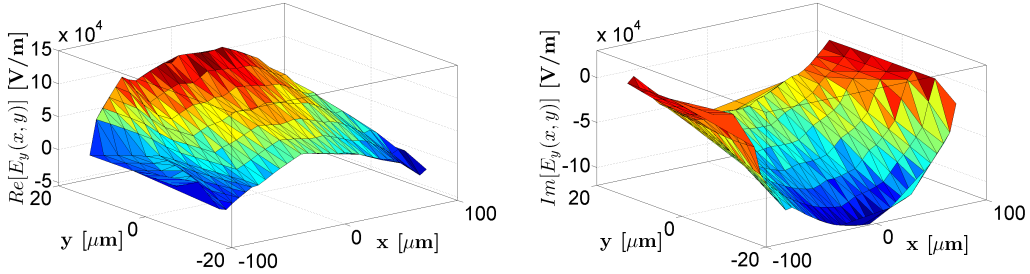


Figure 3.46: Real and imaginary parts of the y -component of the aperture electric field on a rectangular slot with $w_x = 183 \mu\text{m}$ and $w_y = 30 \mu\text{m}$ at 200 GHz.

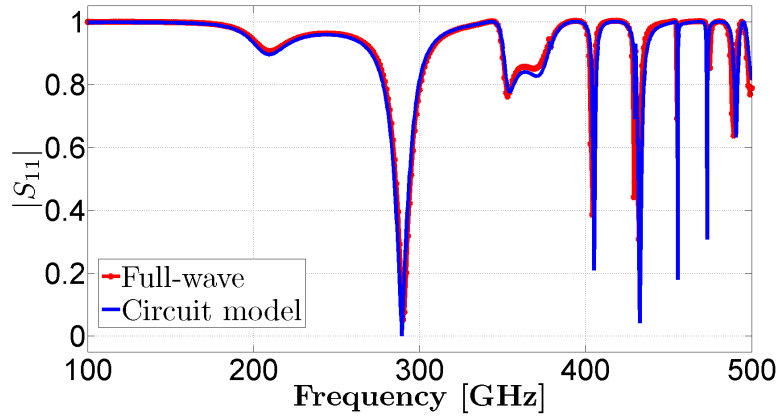


Figure 3.47: Magnitude of the S_{11} parameter under 20° TM incidence for an array of rectangular slots with $\varepsilon_r = 11.8$, $P_x = P_y = 236 \mu\text{m}$, $w_x = 183 \mu\text{m}$, $w_y = 30 \mu\text{m}$, $d = 302 \mu\text{m}$, and $N_{TE} = N_{TM} = 4$ using the spatial profiles $E_x(x, y)$ and $E_y(x, y)$ in Figs. 3.45-3.46.

3.8.2 Filters based on dogbone-shaped holes

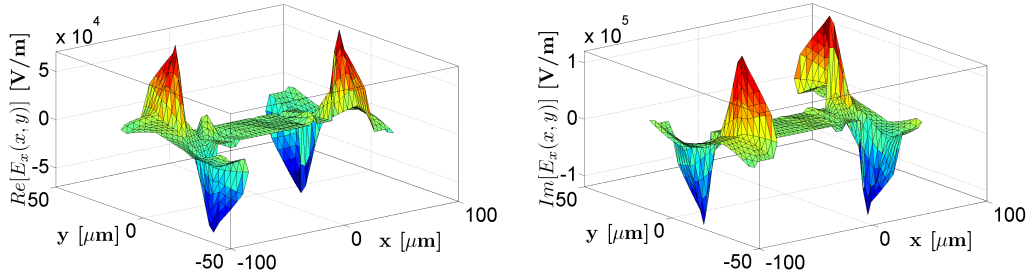


Figure 3.48: Real and imaginary parts of the x -component of the aperture electric field on a dogbone-shaped hole with $w_x = 147 \mu\text{m}$ and $w_y = 60 \mu\text{m}$ at 200 GHz.

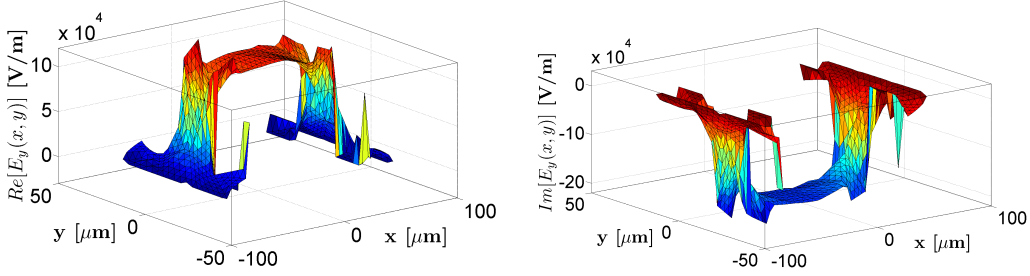


Figure 3.49: Real and imaginary parts of the y -component of the aperture electric field on a dogbone-shaped hole with $w_x = 147 \mu\text{m}$ and $w_y = 60 \mu\text{m}$ at 200 GHz.

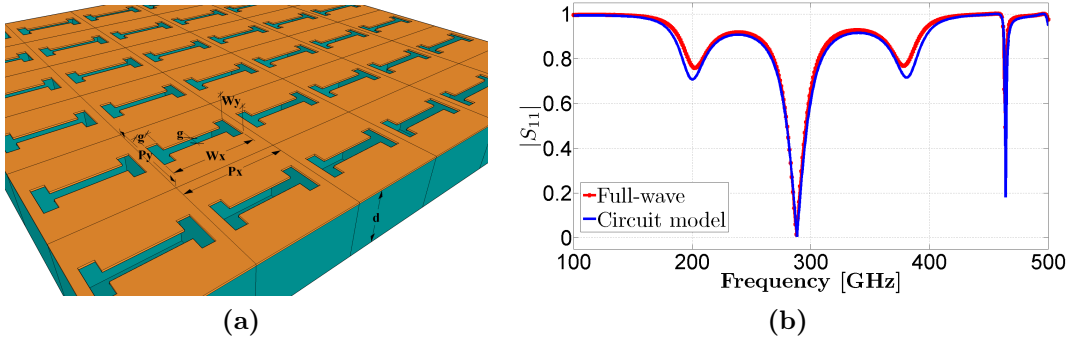


Figure 3.50: (a) Schematic of dogbone-based holes and (b) magnitude of the S_{11} parameter under 20° TM incidence for an array of dogbone-shaped holes with $\epsilon_r = 11.8$, $P_x = P_y = 176 \mu\text{m}$, $w_x = 147 \mu\text{m}$, $w_y = 60 \mu\text{m}$, $g = 20 \mu\text{m}$, $d = 302 \mu\text{m}$, and $N_{TE} = N_{TM} = 4$ using the spatial profiles $E_x(x, y)$ and $E_y(x, y)$ in Figs. 3.48-3.49.

3.8.3 Filters based on cross-shaped holes

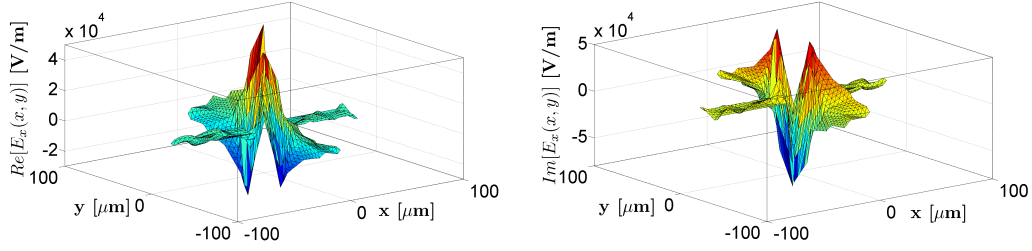


Figure 3.51: Real and imaginary parts of the x -component of the aperture electric field on a cross-shaped hole with $w_x = 150 \mu\text{m}$ and $w_y = 20 \mu\text{m}$ at 200 GHz.

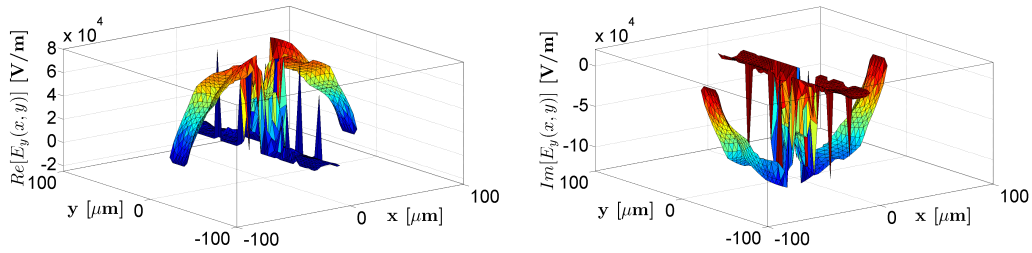


Figure 3.52: Real and imaginary parts of the y -component of the aperture electric field on a cross-shaped hole with $w_x = 150 \mu\text{m}$ and $w_y = 20 \mu\text{m}$ at 200 GHz.

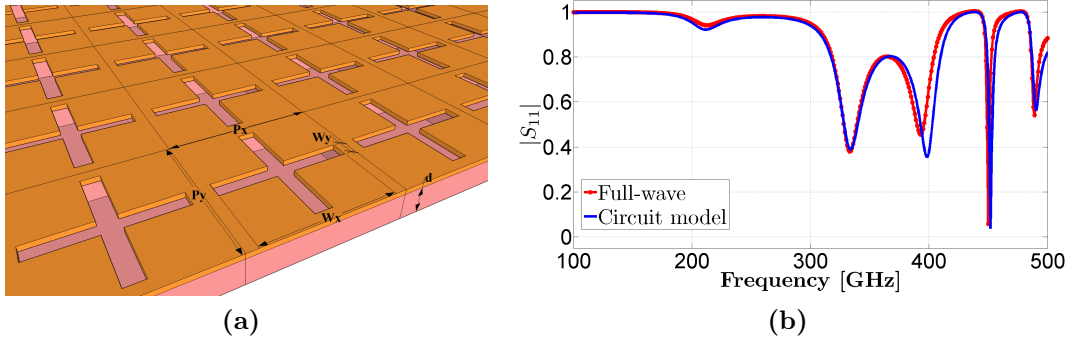


Figure 3.53: (a) Schematic of cross-based holes and (b) magnitude of the S_{11} parameter under 30° TM incidence for an array of cross-shaped holes with $\epsilon_r = 11.8$, $P_x = P_y = 176 \mu\text{m}$, $w_x = 150 \mu\text{m}$, $w_y = 20 \mu\text{m}$, $d = 302 \mu\text{m}$, and $N_{TE} = N_{TM} = 4$ using the spatial profiles $E_x(x, y)$ and $E_y(x, y)$ in Figs. 3.51-3.52.

3.9 Conclusions

In this Chapter, I have derived the topology of equivalent circuit models for the scattering analysis of one-dimensional periodic strip and slit gratings embedded in a dielectric layered scenario.

Thanks to the periodic arrangement, only a single unit cell needs to be considered by applying Floquet's theorem. The system thus reduces to a planar discontinuity inside a generalized waveguide with apposite boundary conditions, which depend on the polarization of the incidence wave. I have retrieved close-form and fully-analytical expressions of the circuit elements by splitting the contributions in low-order and high-order. It is useful to underline that only few propagative low-order circuit elements have to be included in the network, while the evanescent high-order modes are synthesized by a reactive lumped element (inductance or capacitance).

Following a similar rationale, I have extended the analysis to deal with the two-dimensional case of periodic frequency selective surfaces. I have presented two different topological models, one for patch-based and one for slot-based FSSs, considering various study examples: free-standing configuration, layered media, grounded slabs, etc.

For both one- and two-dimensional networks, the validity of the equivalent circuit approach has been provided by comparing the obtained results with that of a FEM-based electromagnetic solver (COMSOL Multiphysics), proving the agreement in normal and oblique incidence. These equivalent circuits can deal with lossy dielectrics and can be also extended to consider no ideal metallic elements. The frequency range of validity starts from the long wavelength limit, when the wavelength is much larger than the structure size (quasi-static case), and ends beyond the onset of the grating lobe regime.

Moreover, I have derived semi-analytical circuit models particularly useful to account for more complex geometric shapes. The equivalent networks here presented allow to reach a deep physical insight into the electromagnetic scattering behavior of periodic devices, as well as a noticeable saving of computational resources; quantitative estimates have been performed in Chapter 4.

References

- [1] B. A. Munk, *Frequency selective surfaces: theory and design*. John Wiley & Sons, 2005.
- [2] M. Guglielmi and A. A. Oliner, "Multimode network description of a planar periodic metal-strip grating at a dielectric interface. II: small-aperture and small-obstacle solutions," *IEEE Transactions on Microwave Theory and Techniques*, vol. 37, no. 3, pp. 542–552, 1989.
- [3] M. Guglielmi and H. Hochstadt, "Multimode network description of a planar periodic metal-strip grating at a dielectric interface. III: Rigorous solution," *IEEE Transactions on Microwave Theory and Techniques*, vol. 37, no. 5, pp. 902–909, 1989.
- [4] S. Monni, G. Gerini, A. Neto, and A. G. Tijhuis, "Multimode equivalent networks for the design and analysis of frequency selective surfaces," *IEEE Transactions on Antennas and Propagation*, vol. 55, no. 10, pp. 2824–2835, 2007.
- [5] A. G. Schuchinsky, D. E. Zelenchuk, A. M. Lerer, and R. Dickie, "Full-wave analysis of layered aperture arrays," *IEEE Transactions on Antennas and Propagation*, vol. 54, no. 2, pp. 490–502, 2006.
- [6] J. Vardaxoglou and E. A. Parker, "Modal analysis of scattering from two-layer frequency-selective surfaces," *International Journal of Electronics*, vol. 58, no. 5, pp. 827–830, 1985.
- [7] J. W. Strutt, "On the dynamical theory of gratings," *Proc. R. Soc. Lond. A*, vol. 79, no. 532, pp. 399–416, 1907.
- [8] F. Medina, F. Mesa, and R. Marques, "Extraordinary transmission through arrays of electrically small holes from a circuit theory perspective," *IEEE Transactions on Microwave Theory and Techniques*, vol. 56, no. 12, pp. 3108–3120, 2008.
- [9] F. Capolino, A. Vallecchi, and M. Albani, "Equivalent transmission line model with a lumped X-circuit for a metalayer made of pairs of planar conductors," *IEEE Transactions on Antennas and Propagation*, vol. 61, no. 2, pp. 852–861, 2013.
- [10] M. Beruete, M. Navarro-Cia, and M. S. Ayza, "Understanding anomalous extraordinary transmission from equivalent circuit and grounded slab concepts," *IEEE Transactions on Microwave Theory and Techniques*, vol. 59, no. 9, pp. 2180–2188, 2011.
- [11] F. Mesa, R. Rodríguez-Berral, and F. Medina, "Unlocking complexity using the ECA: The equivalent circuit model as an efficient and physically insightful tool for microwave engineering," *IEEE Microwave Magazine*, vol. 19, no. 4, pp. 44–65, 2018.
- [12] R. Rodríguez-Berral, C. Molero, F. Medina, and F. Mesa, "Analytical wideband model for strip/slit gratings loaded with dielectric slabs," *IEEE Transactions on Microwave Theory and Techniques*, vol. 60, no. 12, pp. 3908–3918, 2012.
- [13] C. Molero, R. Rodríguez-Berral, F. Mesa, F. Medina, and A. B. Yakovlev, "Wideband analytical equivalent circuit for one-dimensional periodic stacked arrays," *Physical Review E*, vol. 93, no. 1, p. 013306, 2016.
- [14] C. Molero, R. Rodríguez-Berral, F. Mesa, and F. Medina, "Wideband analytical equivalent circuit for coupled asymmetrical nonaligned slit arrays," *Physical Review E*, vol. 95, no. 2, p. 023303, 2017.
- [15] C. Caloz and T. Itoh, *Electromagnetic metamaterials: transmission line theory and microwave applications*. John Wiley & Sons, 2005.
- [16] S.-W. Lee, G. Zarrillo, and C.-L. Law, "Simple formulas for transmission through periodic metal grids or plates," *IEEE Transactions on Antennas and Propagation*, vol. 30, no. 5, pp. 904–909, 1982.
- [17] R. Rodríguez-Berral, F. Mesa, and F. Medina, "Analytical multimodal network approach for 2-D arrays of planar patches/apertures embedded in a layered medium," *IEEE Transactions on Antennas and Propagation*, vol. 63, no. 5, pp. 1969–1984, 2015.

-
- [18] C. S. Kaipa, A. B. Yakovlev, F. Medina, and F. Mesa, "Transmission through stacked 2D periodic distributions of square conducting patches," *Journal of Applied Physics*, vol. 112, no. 3, p. 033101, 2012.
- [19] F. Mesa, R. Rodríguez-Berral, M. García-Vigueras, F. Medina, and J. R. Mosig, "Simplified modal expansion to analyze frequency-selective surfaces: An equivalent circuit approach," *IEEE Transactions on Antennas and Propagation*, vol. 64, no. 3, pp. 1106–1111, 2016.
- [20] M. García-Vigueras, F. Mesa, F. Medina, R. Rodríguez-Berral, and J. L. Gomez-Tornero, "Simplified circuit model for arrays of metallic dipoles sandwiched between dielectric slabs under arbitrary incidence," *IEEE Transactions on Antennas and Propagation*, vol. 60, no. 10, pp. 4637–4649, 2012.
- [21] V. Torres, F. Mesa, M. Navarro-Cía, R. Rodríguez-Berral, M. Beruete, and F. Medina, "Accurate circuit modeling of fishnet structures for negative-index-medium applications," *IEEE Transactions on Microwave Theory and Techniques*, vol. 64, no. 1, pp. 15–26, 2016.
- [22] S. R. Rengarajan, "Choice of basis functions for accurate characterization of infinite array of microstrip reflectarray elements," *IEEE Antennas and Wireless Propagation Letters*, vol. 4, no. 1, pp. 47–50, 2005.
- [23] M. G. Vigueras, J. R. Mosig, F. Mesa, R. R. Berral, and F. Medina, "Closed-form expressions for modeling diffraction at printed dipole-based FSS," in *Microwave, Antenna, Propagation and EMC Technologies for Wireless Communications (MAPE), 2013 IEEE 5th International Symposium on*, pp. 275–278, IEEE, 2013.
- [24] M. García-Vigueras, F. Mesa, R. Rodríguez-Berral, F. Medina, and J. R. Mosig, "Efficient network representation of grounded patch-based FSS," in *Antennas and Propagation (EuCAP), 2014 8th European Conference on*, pp. 1960–1963, IEEE, 2014.
- [25] M. García-Vigueras, F. Mesa, R. Rodríguez-Berral, F. Medina, and J. R. Mosig, "Insightful circuit modeling of FSS with arbitrary scatterers," in *Antennas and Propagation (EuCAP), 2015 9th European Conference on*, pp. 1–4, IEEE, 2015.
- [26] S. V. Hum and B. Du, "Equivalent circuit modeling for reflectarrays using Floquet modal expansion," *IEEE Transactions on Antennas and Propagation*, vol. 65, no. 3, pp. 1131–1140, 2017.

Equivalent-Circuit Model for Stacked Slot-based 2D Periodic Arrays of Arbitrary Geometry for Broadband Analysis

The analysis of the transmission and reflection spectra of stacked slot-based 2D periodic structures of arbitrary geometry, and the ability to devise and control their electromagnetic responses have been a matter of extensive research for many decades. The purpose of this Chapter is to develop an equivalent Π circuit model based on the transmission-line theory and Floquet harmonic interactions, for broadband and short longitudinal period analysis. The proposed circuit model overcomes the limits of identical and symmetrical configurations imposed by the even/odd excitation approach, exploiting both the circuit topology of a single 2D periodic array of apertures and the ABCD matrix formalism. The transmission spectra obtained through the equivalent-circuit model have been validated by comparison with full-wave simulations carried out with a finite-element commercial electromagnetic solver. This allowed for a physical insight into the spectral and angular responses of multilayer devices with arbitrary aperture shapes, guaranteeing a noticeable saving of computational resources.

The contents of this Chapter have been published in Ref. [1].

4.1 Introduction

The long-tradition study of one-dimensional (1D) and two-dimensional (2D) periodic arrays of patches or apertures etched on metallic films [2–8] is receiving renewed attention from the scientific community thanks to the development of increasingly innovative applications: quasi-optical Frequency Selective Surfaces (FSSs) [9], polarizers [10], High-Impedance Surfaces (HIS) [11], metasurfaces [12], metamaterial absorbers [13–15], Electromagnetic Band-Gap (EBG) structures [16], photonic and optoelectronic devices [17].

The working range spans from the microwave, terahertz, and infrared frequencies up to the optical spectrum, where strict performance control and efficient analysis tools are required to accurately shape the desired electromagnetic behavior.

In particular, the capability to predict and design the spectral response of stacked arrays in dielectric layered environments is of great interest [18, 19].

To overcome these challenges, numerous solutions, most of which are of heuristic nature, have been proposed in the past years. Conventional techniques use the Method of Moments (MoM) to solve the Electric Field Integral Equation (EFIE) derived from the boundary value problem for 1D and 2D arrays [20, 21]. However, the analysis of complex patch/aperture shapes and the choice of the basis functions still result critical for the accuracy of the MoM solution. Further approaches are based on rigorous full-wave analysis through the solution of a system of integro-differential equations by Galerkin method [22] and on multimode equivalent networks [23]. Among other techniques for studying periodic arrays, the Equivalent Circuit (EC) models offer an intuitive physical insight as well as a quantitative interpretation without having to resort to costly full-wave numerical simulations in terms of Central Processing Unit (CPU) time consumption and memory capacity.

Recently, EC models based on the transmission line theory have been developed for analyzing both 1D strip/slit gratings and 2D arrays of printed periodic patterns on dielectric slabs, in order to provide closed-form expressions for the circuit elements [24–29]. In particular, in Ref. [30] an EC for stacked metallic plates with a 2D periodic distribution of sub-wavelength rectangular apertures has been designed for Negative-Index-Medium (NIM) applications. However, this EC is valid only for cascaded identical and symmetrical FSSs, where it is possible to apply the standard even/odd excitation approach [30, 31]. The analysis is thus reduced to two independent problems consisting of a single FSS loaded with a half-thick dielectric slab on a Perfect Electric Conductor (PEC) and on a Perfect Magnetic Conductor (PMC), respectively.

In this Chapter, I aim at further developing the previous ECs for analyzing stacked slot-based 2D periodic arrays of arbitrary geometry in a wide frequency range. The proposed EC model, composed of transmission-line sections and transformers, can easily be extended to consider different polarizations of the incident plane wave, the oblique incidence case, losses in dielectric, and finite metallic conductivity.

This EC can be regarded as a fully-analytical model for known aperture field profiles for conventional geometries (rectangular aperture, circular aperture, thin slot, cross slot) [32], or as a semi-analytical model for apertures with more complex

shapes. In the latter case, the aperture field profile is extracted from a single low-frequency full-wave simulation of the free-standing periodic array, which, although it does not provide closed-form formulas for the circuit elements, weakly affects the computational capacity.

The adopted Π topology for the EC describes the interactions between an arbitrary number of adjacent aperture arrays through Floquet harmonics of any order. This formulation is, therefore, suitable for the analysis of stacked slot-based FSSs having the same unit cell 2D transverse periodicities, but with any electrical dimension and dielectric thickness between the arrays.

This Chapter is organized as follows. In Section 4.2, the equivalent Π -circuit topology for stacked 2D periodic slot-based arrays of arbitrary geometry is described, along with the expressions of the distributed and lumped circuit parameters. In Section 4.3, some significant examples of the application of the EC are presented in both normal and oblique Transverse Magnetic (TM) incidence for various multi-layer aperture configurations. The retrieved electromagnetic responses are compared with full-wave simulations, using a Finite-Element Method (FEM) based software, in order to check the validity of the proposed network. In Section 4.4, the main conclusions are drawn, and finally, in Appendix A, the EC model of a single periodic aperture array between two arbitrary dielectric half-spaces is described.

4.2 Equivalent Π circuit topology for stacked slot-based 2D periodic arrays

An example of stacked slot-based 2D periodic arrays with periodicities P_x and P_y along the x and y -directions is shown in Fig. 4.1, respectively. The multilayer configuration is infinite in the transverse directions and the FSSs are aligned, i.e., the center of the apertures is located at the same height.

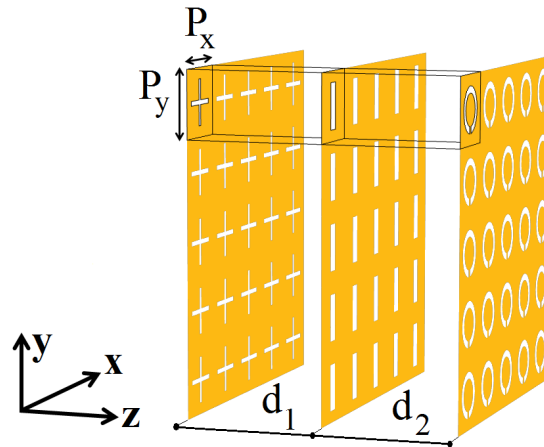


Figure 4.1: Example of three stacked slot-based 2D periodic arrays of arbitrary geometries, printed on different dielectric layers of thicknesses d_1 and d_2 .

The arrays are separated by dielectric layers of arbitrary thickness and permittivity. The FSSs can assume different complex geometries, overcoming the restrictions of the even/odd excitation technique [30, 31].

The analysis is based on the assumption of a frequency-independent aperture field profile [24, 28] (see Eq. (A.9) in Appendix A) and on the ABCD matrix formalism of microwave network analysis [33]. Once the procedure described in Appendix A is carried out (see also Section 3.7 in Chapter 3), the equivalent admittance of an aperture-based FSS embedded between two semi-infinite dielectric media under TM incidence (the transverse electric field component along the x axis) is given by the following analytical expression:

$$\begin{aligned}
 Y_{eq} &= Y_{eq}^{TE} + Y_{eq}^{TM} \\
 &= \sum_{nm, m \neq 0} \frac{|I_{ex}k_{ym} - I_{ey}k_{xn}|^2}{|I_e|^2(k_{xn}^2 + k_{ym}^2)} (Y_{nm}^{TE(1)} + Y_{nm}^{TE(2)}) \\
 &+ \sum_{(n,m) \neq (0,0)} \frac{|I_{ex}k_{xn} + I_{ey}k_{ym}|^2}{|I_e|^2(k_{xn}^2 + k_{ym}^2)} (Y_{nm}^{TM(1)} + Y_{nm}^{TM(2)}),
 \end{aligned} \tag{4.1}$$

where the superscripts TE and TM stand for transverse electric and transverse magnetic polarizations, and the TM_{00} harmonic is the fundamental one $(n, m) = (0, 0)$ associated with the incident plane wave. The transverse wave admittances are given in Eqs. (A.7)-(A.8), while I_e , I_{ex} , and I_{ey} represent the Fourier transforms of the transverse aperture electric field on the unit cell of the fundamental harmonic, and of the x and y -components, respectively, provided in Eqs. (A.12)-(A.14).

From Eq. (4.1), it is possible to extract the turn ratios of the transformers which connect each harmonic (TE or TM) with all the others:

$$A_{nm}^{TE} = \frac{|I_{ex}k_{ym} - I_{ey}k_{xn}|}{|I_e| \sqrt{k_{xn}^2 + k_{ym}^2}}, \tag{4.2}$$

$$A_{nm}^{TM} = \frac{|I_{ex}k_{xn} + I_{ey}k_{ym}|}{|I_e| \sqrt{k_{xn}^2 + k_{ym}^2}}, \tag{4.3}$$

where k_{xn} and k_{ym} are described in Appendix A.

Initially, two different coupled 2D periodic slot-based arrays separated by a dielectric slab of thickness d and relative permittivity ε_r , between two air half-spaces, are investigated (see Fig. 4.2). The information about the geometric characteristics of the two FSSs (FSS1 on the left and FSS2 on the right) and the contributions of both TE and TM harmonics described in Eqs. (4.2)-(4.3) are included in the expressions of the transformer turn ratios A_{nm}^{FSS1} and A_{nm}^{FSS2} which, in the case of identical coupled complementary FSSs, coincide. With

the characteristic admittances Y_{nm} and the propagation constants of the nm -th transmission line in a specific medium being equal, it is possible to directly connect the transmission lines of each harmonic with the ones of the same order within the dielectric slab. These transmission line sections will have a total length equal to the dielectric thickness d .

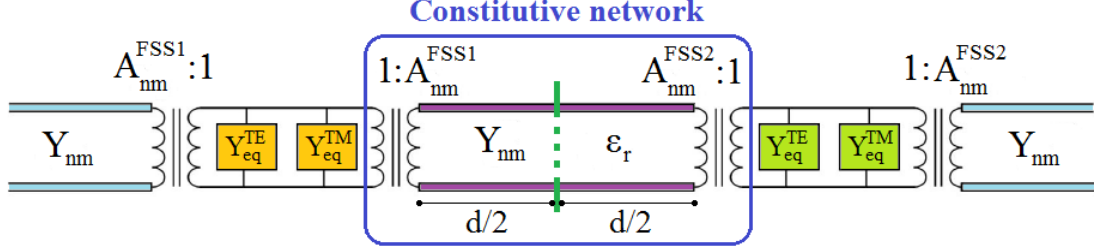


Figure 4.2: EC of two coupled periodic FSSs, separated by a d -thick dielectric slab of relative permittivity ϵ_r , with transformer turn ratios A_{nm}^{FSS1} and A_{nm}^{FSS2} , respectively.

Depending on the electrical distance between the FSS arrays, the presence of several evanescent harmonics, which give rise to an interaction between the two coupled FSSs, has to be considered, while as the electrical distance increases, the contribution of these evanescent modes becomes negligible, and the so-called one-mode interaction approach can be reasonably applied [34].

Then, the ABCD matrix formalism has been exploited to describe the constitutive network (see the details in Fig. 4.2) as the cascade of three two-port networks through the product of three ABCD matrices representing the leftmost transformer ($A_{nm}^L = A_{nm}^{FSS1}$), the nm -th transmission line, and the rightmost transformer ($A_{nm}^R = A_{nm}^{FSS2}$), respectively:

$$\begin{pmatrix} A & B \\ C & D \end{pmatrix} = \begin{pmatrix} \frac{1}{A_{nm}^L} & 0 \\ 0 & A_{nm}^L \end{pmatrix} \begin{pmatrix} \cos(\beta_{nm}d) & jZ_{nm} \sin(\beta_{nm}d) \\ jY_{nm} \sin(\beta_{nm}d) & \cos(\beta_{nm}d) \end{pmatrix} \begin{pmatrix} A_{nm}^R & 0 \\ 0 & \frac{1}{A_{nm}^R} \end{pmatrix},$$

where the superscripts L and R represent the leftmost and rightmost transformers, and $Z_{nm} = Y_{nm}^{-1}$ is the nm -th modal impedance.

The elements of the resulting nm -th ABCD matrix are found to be:

$$\begin{pmatrix} \frac{A_{nm}^R}{A_{nm}^L} \cos(\beta_{nm}d) & j \frac{1}{A_{nm}^R A_{nm}^L} Z_{nm} \sin(\beta_{nm}d) \\ j A_{nm}^R A_{nm}^L Y_{nm} \sin(\beta_{nm}d) & \frac{A_{nm}^L}{A_{nm}^R} \cos(\beta_{nm}d) \end{pmatrix}.$$

The nm -th ABCD matrix is thus converted into the nm -th admittance matrix $[Y]_{nm}$ of a two-port network in which the elements assume the following

expressions:

$$Y_{11} = \frac{D}{B} = -j(A_{nm}^L)^2 Y_{nm} \cot(\beta_{nm}d), \quad (4.4)$$

$$Y_{12} = \frac{BC - AD}{B} = jA_{nm}^L A_{nm}^R Y_{nm} \csc(\beta_{nm}d), \quad (4.5)$$

$$Y_{21} = -\frac{1}{B} = jA_{nm}^L A_{nm}^R Y_{nm} \csc(\beta_{nm}d), \quad (4.6)$$

$$Y_{22} = \frac{D}{B} = -j(A_{nm}^R)^2 Y_{nm} \cot(\beta_{nm}d). \quad (4.7)$$

The derived network is reciprocal and lossless, i.e., $Y_{12} = Y_{21}$, and it can be represented as a Π equivalent topology as shown in Fig. 4.3, whose circuit parameters are [33]:

$$Y_1^L = Y_{11} + Y_{12} = -j(A_{nm}^L)^2 Y_{nm} \cot(\beta_{nm}d) + jA_{nm}^L A_{nm}^R Y_{nm} \csc(\beta_{nm}d), \quad (4.8)$$

$$Y_2^R = Y_{22} + Y_{12} = -j(A_{nm}^R)^2 Y_{nm} \cot(\beta_{nm}d) + jA_{nm}^L A_{nm}^R Y_{nm} \csc(\beta_{nm}d), \quad (4.9)$$

$$Y_3 = -Y_{12} = -jA_{nm}^L A_{nm}^R Y_{nm} \csc(\beta_{nm}d). \quad (4.10)$$

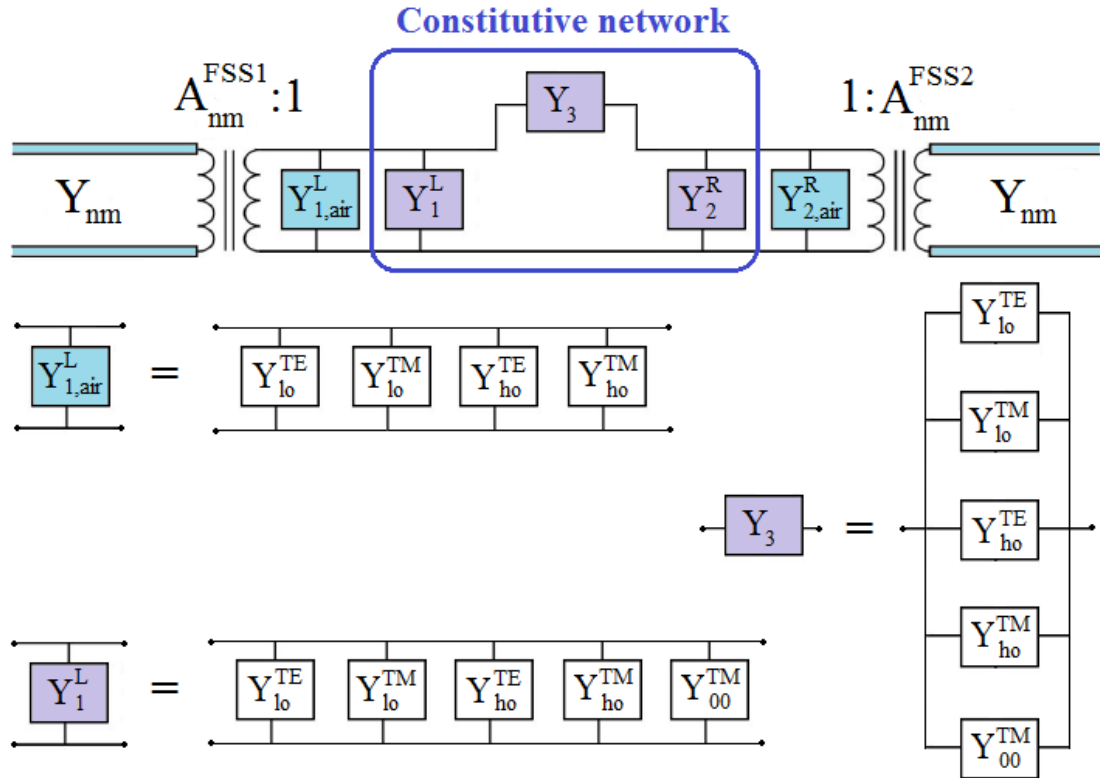


Figure 4.3: EC of two coupled periodic FSSs between two air half-spaces, where the constitutive network is made of an infinite number of Π circuits connected in parallel. The details of the admittances $Y_{1,air}^L$, Y_1^L , and Y_3 show explicitly the low-order (lo) and high-order (ho) contributions of the TE/TM Floquet harmonics as well as the one of the fundamental mode TM_{00} in the dielectric region.

From Eqs. (4.8)-(4.10), the case of two identical coupled complementary FSSs considered by the even/odd excitation approach is easily recovered, assuming $A_{nm}^L = A_{nm}^R$.

The constitutive network results, therefore, represented by an equivalent Π circuit block which describes the influence of the low-order and high-order harmonics in the dielectric region. In particular, the parallel admittances of the Π network represent the near field around the apertures, while the series admittance accounts for the coupling field between the two complementary FSSs. Indeed, for a large electrical distance between the arrays, i.e., in the long longitudinal period regime, the series admittance can be neglected, while for closely spaced FSSs, i.e., in the short longitudinal period regime, the contributions of the lowest-order harmonics of high-order nature have to be taken into account through the Y_3 series admittance.

The leftmost and rightmost equivalent parallel admittances Y_1^L and Y_2^R of the constitutive network in the dielectric region can be separated into different contributions (supposing an incident TM polarized plane wave) as follows:

$$\begin{aligned}
 Y_1^L = & Y_{1,00}^{TM(2)} + \sum_{(n,m)=1}^{N_{TE}} Y_{1,lo}^{TE(2)} + \sum_{(n,m)=1}^{N_{TM}} Y_{1,lo}^{TM(2)} \\
 & + \sum_{(n,m)=N_{TE}+1}^{+\infty} Y_{1,ho}^{TE(2)} + \sum_{(n,m)=N_{TM}+1}^{+\infty} Y_{1,ho}^{TM(2)}, \tag{4.11}
 \end{aligned}$$

where N_{TE}/N_{TM} represent the accessible propagating TE/TM modes, and the subscripts *lo* and *ho* stand for the low-order and high-order harmonics, respectively. In particular, for the high-order harmonics well below the cut-off in the frequency range of interest, the assumption $k_{xn} = k_t + k_n \approx k_n$ is valid, and the propagation wavenumber reads $\beta_{nm}^{(i)} \approx -j\sqrt{k_n^2 + k_m^2}$. The equivalent admittances $Y_{ho}^{TE/TM}$ assume, therefore, the form of lumped frequency-independent inductances and capacitances, thus further reducing the computational effort.

The parallel admittances $Y_{1,air}^L$ and $Y_{2,air}^R$ in the external regions to the constitutive network can be, instead, split into the following contributions:

$$\begin{aligned}
 Y_{1,air}^L = & \sum_{nm,n \neq 0} (A_{nm}^{TE})^2 Y_{nm}^{TE(1)} + \sum_{(n,m) \neq (0,0)} (A_{nm}^{TM})^2 Y_{nm}^{TM(1)} \\
 = & \sum_{(n,m)=1}^{N_{TE}} Y_{nm,lo}^{TE(1)} + \sum_{(n,m)=1}^{N_{TM}} Y_{nm,lo}^{TM(1)} \\
 & + \sum_{(n,m)=N_{TE}+1}^{+\infty} Y_{nm,ho}^{TE(1)} + \sum_{(n,m)=N_{TM}+1}^{+\infty} Y_{nm,ho}^{TM(1)}. \tag{4.12}
 \end{aligned}$$

In an equivalent way, the series admittances of the Π network can be divided into their low-order and high-order elements:

$$\begin{aligned}
 Y_3 = & Y_{3,00}^{TM(2)} + \sum_{(n,m)=1}^{N_{TE}} Y_{3,lo}^{TE(2)} + \sum_{(n,m)=1}^{N_{TM}} Y_{3,lo}^{TM(2)} \\
 & + \sum_{(n,m)=N_{TE}+1}^{+\infty} Y_{3,ho}^{TE(2)} + \sum_{(n,m)=N_{TM}+1}^{+\infty} Y_{3,ho}^{TM(2)}.
 \end{aligned} \tag{4.13}$$

These retrieved internal Π constitutive blocks can be cascaded exploiting the ABCD matrix formalism to consider an arbitrary number of stacked complementary FSSs in the general case of oblique incidence, different complex aperture shapes, and lossy dielectric slabs of arbitrary thickness (see Fig. 4.4).

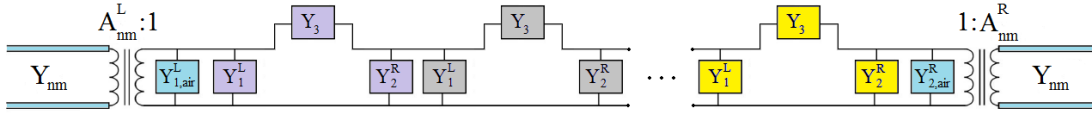


Figure 4.4: EC for stacked slot-based 2D periodic arrays with different aperture shapes and dielectric layers, made by cascading an arbitrary number of Π constitutive networks.

It should be noticed that for the fundamental harmonic TM_{00} , the transformer turn ratio $A_{00}^{TM} = 1$, and the reflection and transmission coefficients for the $(n, m) = (0, 0)$ harmonic can be obtained from the ABCD parameters of the cascaded Π networks through the following relationships [33]:

$$S_{11} = \frac{A + BY_{00}^{(1)} - C/Y_{00}^{(1)} - D}{A + BY_{00}^{(1)} + C/Y_{00}^{(1)} + D}, \tag{4.14}$$

$$S_{12} = \frac{2(AD - BC)}{A + BY_{00}^{(1)} + C/Y_{00}^{(1)} + D}, \tag{4.15}$$

$$S_{21} = \frac{2}{A + BY_{00}^{(1)} + C/Y_{00}^{(1)} + D}, \tag{4.16}$$

$$S_{22} = \frac{-A + BY_{00}^{(1)} - C/Y_{00}^{(1)} + D}{A + BY_{00}^{(1)} + C/Y_{00}^{(1)} + D}. \tag{4.17}$$

4.3 Numerical results

In order to verify the validity and accuracy of the proposed EC model, some significant numerical applications are presented in this section in the short period regime, i.e., for a longitudinal period d less than half the shortest transverse period $P = \min\{P_x, P_y\}$. In all the analyzed cases, I assumed a square unit cell $P_x = P_y = P$ and normalized the frequencies in terms of P/λ_0 , where λ_0 is the free-space wavelength. In the calculation of the derived low-order equivalent

admittances, I have considered N_{TE} and N_{TM} propagating harmonics above the cutoff with respect to the highest permittivity dielectric, plus some evanescent high-order modes operating below, but close to their cutoff frequencies. The cutoff frequencies are calculated solving the equation $(\beta_{nm}^{(i)})^2 = \omega^2 \varepsilon_i \mu_0 - k_{xn}^2 - k_{ym}^2 = 0$:

$$f_{c,nm} = \frac{mc \sin \theta}{P_y(\varepsilon_{r,i} - \sin^2 \theta)} + \sqrt{\left[\frac{mc \sin \theta}{P_y(\varepsilon_{r,i} - \sin^2 \theta)} \right]^2 + \frac{c^2}{\varepsilon_{r,i} - \sin^2 \theta} \left[\left(\frac{n}{P_x} \right)^2 + \left(\frac{m}{P_y} \right)^2 \right]}, \quad (4.18)$$

where c is the speed of light.

The multilayer periodic structures have been numerically simulated by means of a full-wave electromagnetic software, COMSOL Multiphysics (RF module), based on the Finite-Element Method (FEM) in the frequency domain, for comparison purposes, supposing an incident plane wave under TM illumination, with the magnetic field fixed along the y -axis. The unit cells have been analyzed adopting Floquet periodic boundary conditions for the side boundaries perpendicular to the plane of the FSSs, Perfectly Matched Layers (PMLs) on the top and bottom of the unit cell, and port boundary conditions on the interior boundaries of the PMLs.

In general, the electric field profile is only known in closed form for specific geometries [32]. In order to analyze apertures of more complex shapes, the tangential field profiles have been extracted from a single low-frequency full-wave simulation of the free-standing periodic array under normal incidence in TM polarization.

As a first validation example, a finite stacked fishnet for NIM applications [30] composed of five equal metallic screens with rectangular apertures of dimensions w_x and w_y along the x and y -directions, respectively, has been investigated under normal and oblique incidence (see the inset in Fig. 4.5(a)). The screens are embedded in a lossless dielectric slab with relative permittivity $\varepsilon_r = 1.4$, and the whole structure is between two air half-spaces. I have used a scale between -120 dB and 0 dB in order to facilitate the comparison with the results published in Ref. [30]. Figure 4.5(a) presents the transmission coefficient under normal incidence in the case of the short-period regime $d = 0.2P$, where the dip at $P/\lambda_0 = 1$ is associated with the first Rayleigh-Wood anomaly. The EC model obtained considering $N_{TE} = 2$ and $N_{TM} = 2$ low-order propagating harmonics is capable of providing a good qualitative matching with the full-wave simulations and of well reproducing the transmission spectrum and the wide pass-band with five peaks at $0.75 < P/\lambda_0 < 1$. A better quantitative agreement between the EC model and the full-wave result can be reached by increasing the number of TE/TM harmonics ($N_{TE} = N_{TM} = 3$) in the range of $0.75 < P/\lambda_0 < 1.1$, as shown in Fig. 4.5(b). The TE_{n0} harmonics do not satisfy the boundary conditions

because of the unit cell symmetry and the polarization of the incident wave. The fundamental harmonic TM_{00} is, instead, explicitly considered as a distributed element in the EC through the relevant transmission line sections, while the high-order mode interactions are described by the admittances Y_{ho}^{TE} and Y_{ho}^{TM} , approximated as lumped frequency-independent inductances and capacitances, respectively. In Fig. 4.5(c), the same 5-layer slot-based arrays are investigated under 45° TM polarization, showing two transmission bands for $0.50 < P/\lambda_0 < 0.52$ and $0.88 < P/\lambda_0 < 0.96$. The EC model is able to reproduce the main features of the transmission spectrum in oblique incidence, reducing noticeably the computational CPU time, which is negligible in comparison with the one required by COMSOL. Indeed, in the case of equal stacked slot-based FSS, the computation of only one ABCD matrix is needed, with the total transfer matrix being obtained as the cascade of these equal transfer matrices.

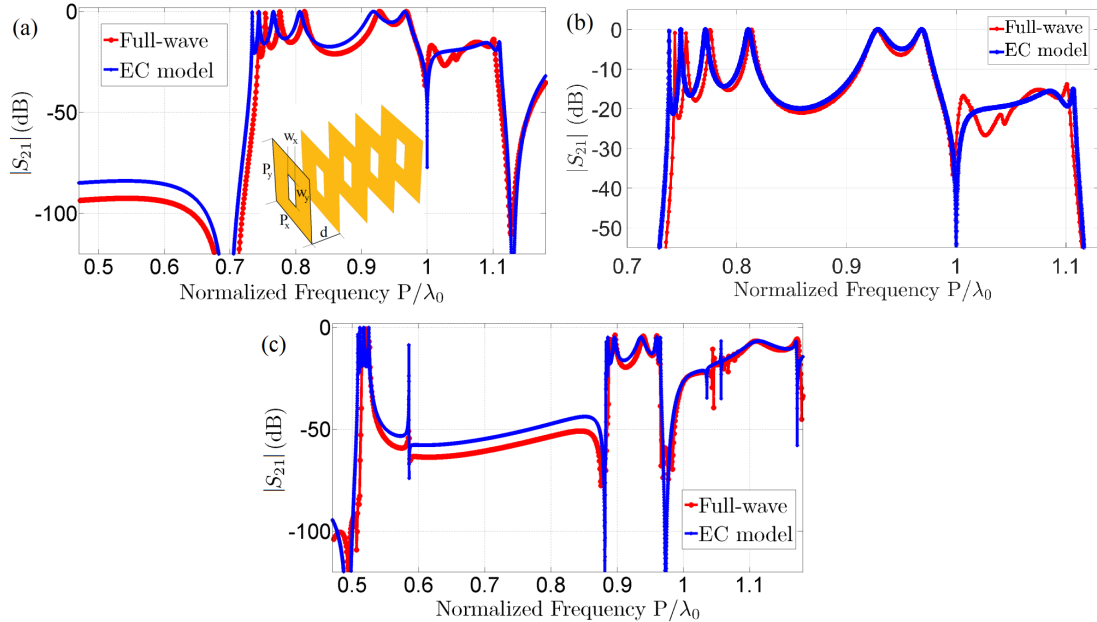


Figure 4.5: Transmission coefficient of a 5-layer FSS structure of rectangular apertures with periodicity $P_x = P_y = P$ and dimensions $w_x = 0.2P$, $w_y = 0.4P$, $d = 0.2P$, and $\varepsilon_r = 1.4$ under (a)-(b) 0° and (c) 45° TM polarization.

Next, the EC model has been applied to the analysis of stacked slot-based arrays of arbitrary geometry, in order to show how this network can overcome the symmetry limits imposed by the even/odd excitation approach.

To this end, the cases of 2-layer and 4-layer alternate stacked arrays of rectangular and circular apertures with transverse dimensions w_x and w_y , and radius r (see the inset in Fig. 4.6(a)), have been considered in the short period regime $d = 0.2P$. In the 2-layer case of Fig. 4.6(a), a transmission band between $0.82 < P/\lambda_0 < 1$ can be observed, while in the 4-layer case of Fig. 4.6(b), a more complex spectrum is recognizable with three transmission peaks in the range of

$0.8 < P/\lambda_0 < 0.95$.

In particular, the total $ABCD_t$ matrix of the 4-layer structure is expressed as the product of the cascade connection of five ABCD matrices:

$$ABCD_t = ABCD_{air}^L ABCD_1 ABCD_2 ABCD_1 ABCD_{air}^R, \quad (4.19)$$

where the matrices $ABCD_1$ and $ABCD_2$ represent the Π networks of the coupled arrays of rectangular/circular and circular/rectangular apertures, respectively, while the matrices $ABCD_{air}^{L/R}$ take into account the effect of the reactive fields around the external faces of the leftmost rectangular-shaped and rightmost circular-shaped aperture-based arrays, as well as the low-order fields, as expressed in Eq. (4.12).

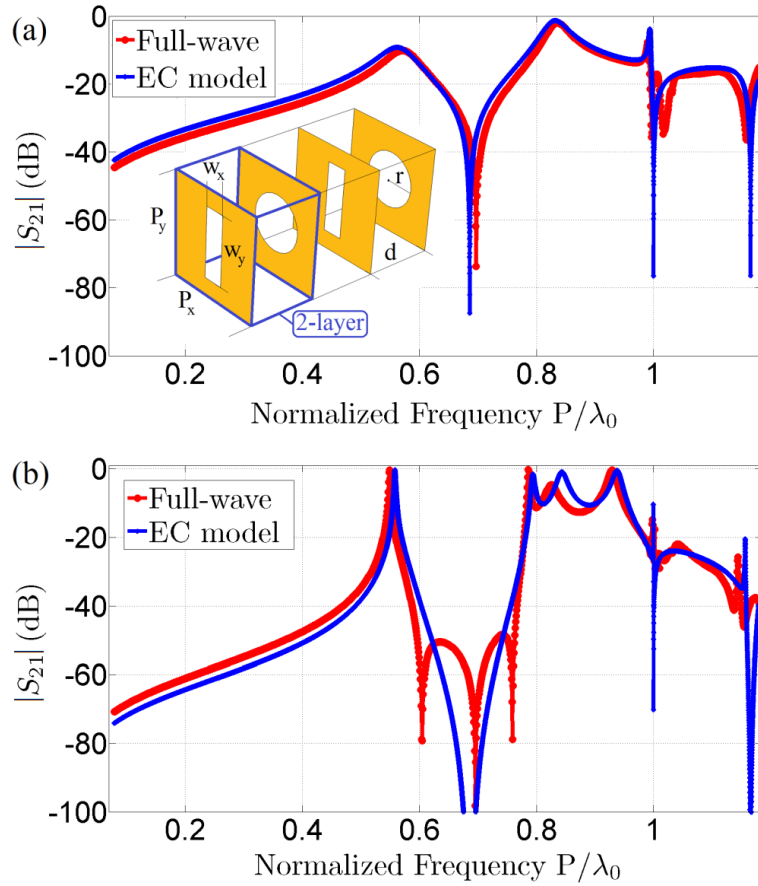


Figure 4.6: Transmission coefficient of (a) 2-layer and (b) 4-layer FSS structures of alternate rectangular and circular apertures with periodicity $P_x = P_y = P$ and dimensions $w_x = 0.13P$, $w_y = 0.8P$, $r = 0.25P$, $d = 0.2P$, and $\epsilon_r = 1.4$ under 0° TM polarization.

As a further example, two different 3-layer arrays of circular-rectangular-split ring (see the inset in Fig. 4.7(a)) and circular-rectangular-cross (see the inset in Fig. 4.7(b)) apertures are studied under normal TM incidence in the short longitudinal period regime. In both multilayer structures, a transmission peak

and a pass-band are presented at $P/\lambda_0 = 0.52$ and $P/\lambda_0 = 0.55$, and $0.81 < P/\lambda_0 < 0.95$ and $0.75 < P/\lambda_0 < 0.97$, respectively, as shown in Fig. 4.7(a)-(b). Although there is a slight discrepancy in the middle band of the transmission spectrum between the EC model and the full-wave simulation, the qualitative behavior of these complex stacked structures is still well described in a wide frequency range.

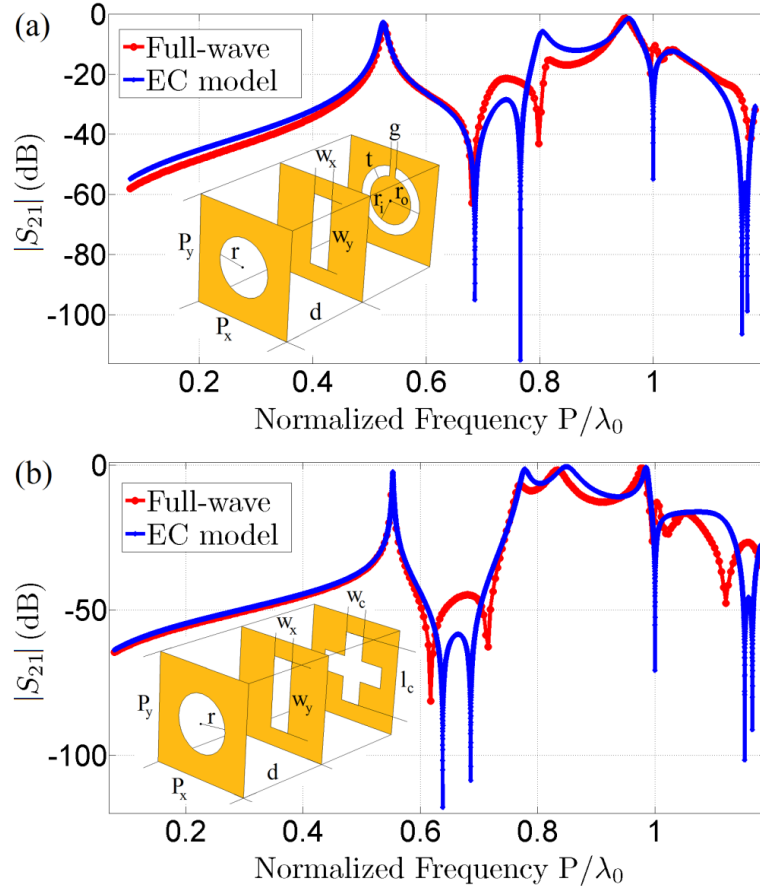


Figure 4.7: Transmission coefficient of 3-layer FSS structures of (a) circular, rectangular, and split ring apertures and (b) circular, rectangular, and cross apertures with periodicity $P_x = P_y = P$ and dimensions $w_x = 0.13P$, $w_y = 0.8P$, $r = 0.25P$, $t = 0.06P$, $g = 0.04P$, $r_i = r - t/2$, $r_o = r + t/2$, $l_c = 0.5P$, $w_c = 0.1P$, $d = 0.2P$, and $\varepsilon_r = 1.4$ under 0° TM polarization.

To take into account the high-order interactions between the three different slot-based FSSs, the total $ABCD_t$ matrix has been computed as the product of four transfer matrices:

$$ABCD_t = ABCD_{air}^L ABCD_1 ABCD_2 ABCD_{air}^R, \quad (4.20)$$

where the $ABCD_1$ matrix describes the Π circuit topology of the coupled array of circular/rectangular apertures, while the $ABCD_2$ matrix considers the coupled arrays of rectangular/split ring or rectangular/cross apertures, respectively.

As a practical example, a 3-layer array of gradually scaled elliptical shaped holes with an aspect ratio of 1.7:1 and a periodicity of $P = 340 \mu\text{m}$ is investigated in the 0.1 – 1.5 THz frequency band, corresponding to the normalized range of $0.11 < P/\lambda_0 < 1.7$ (see the inset in Fig. 4.8(a)). Benzocyclobutane (BCB) is used as a dielectric interlayer between the metallic plates, with $\varepsilon_r = 2.6$. The electromagnetic behavior of the structure is analyzed in the short longitudinal period regime, considering dielectric thicknesses of $d = 0.2P = 68 \mu\text{m}$ and $d = 0.1P = 34 \mu\text{m}$ in Fig. 4.8(a)-(b), respectively. The comparison allows to better appreciate the coupling of the evanescent modes through the BCB spacers when the electrical distance between the metallic layers decreases. Another practical aspect to take into account in the design phase is the presence of losses in the materials. Figure 4.9(a) shows the effect of a lossy dielectric with a complex permittivity of $\varepsilon_r = 2.6 - 0.2j$ compared with the lossless BCB in Fig. 4.8(a) under normal incidence. Finally, in Fig. 4.9(b), both a lossy dielectric and 30° oblique incidence have been implemented in the numerical code, describing with a good accuracy the broadband transmission spectrum.

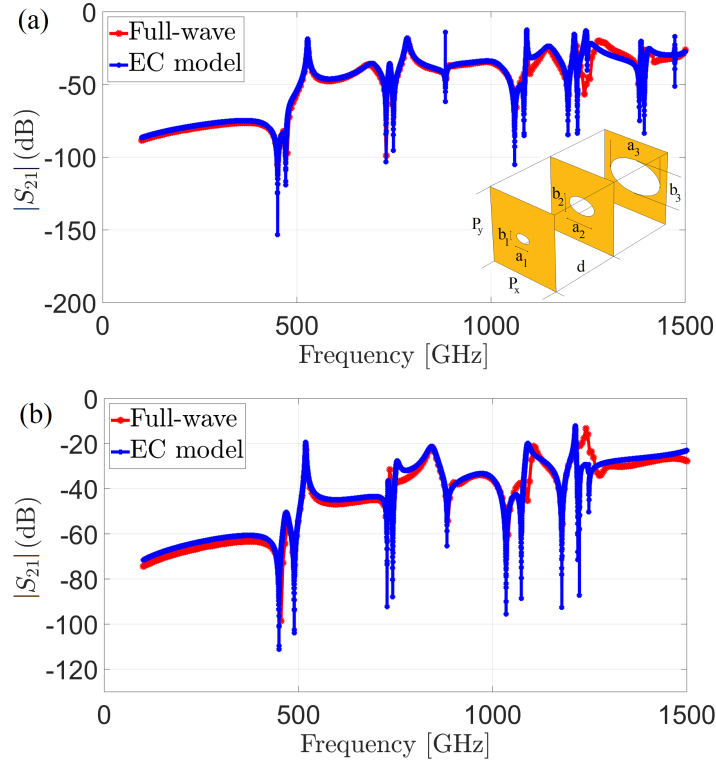


Figure 4.8: Transmission coefficient of 3-layer FSS structures of elliptical apertures with periodicity $P_x = P_y = P = 340 \mu\text{m}$, dimensions $a_1 = a_3/4 = 59.5 \mu\text{m}$, $b_1 = b_3/4 = a_1/1.7 = 35 \mu\text{m}$, $a_2 = a_3/2 = 119 \mu\text{m}$, $b_2 = b_3/2 = a_2/1.7 = 70 \mu\text{m}$, $a_3 = 238 \mu\text{m}$, $b_3 = a_3/1.7 = 140 \mu\text{m}$, dielectric thickness (a) $d = 0.2P = 68 \mu\text{m}$ and (b) $d = 0.1P = 34 \mu\text{m}$, and $\varepsilon_r = 2.6$ under 0° TM polarization.

Hence, the proposed EC model can be extended to deal with stacked dielec-

120 **4. Equivalent-Circuit Model for Stacked Slot-based 2D Periodic Arrays of Arbitrary Geometry for Broadband Analysis**

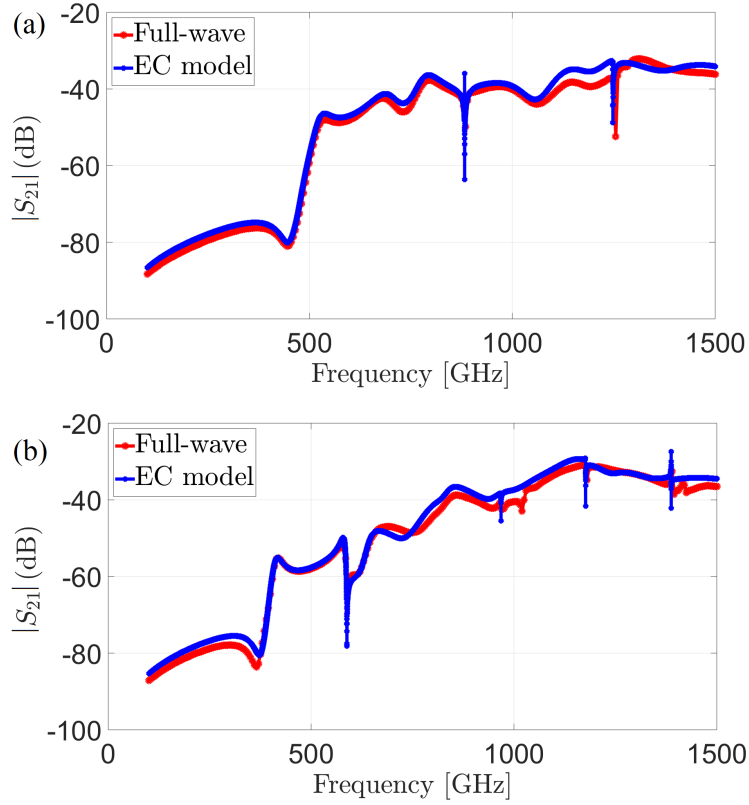


Figure 4.9: Transmission coefficient of 3-layer FSS structures of elliptical apertures with $d = 0.2P = 68 \mu\text{m}$ and complex permittivity $\epsilon_r = 2.6 - 0.2j$ under (a) 0° and (b) 30° TM polarization.

tric layers of various permittivities and thicknesses, as well as with lossy media, through the cascade of a finite number of constitutive Π networks, able to describe the electromagnetic interactions between arbitrarily shaped slot-based arrays in the short longitudinal period regime, guaranteeing a substantial saving of computational CPU time (see Table 4.1).

Table 4.1: CPU time comparison between the electromagnetic FEM solver and the EC model inclusive of the low-frequency full-wave simulation of the free-standing periodic array.

Structures	FEM solver	EC model	+	Free-standing FSS	=	CPU time
5-layer Fig. 4.5(a)	47 m 9 s	3.5 s		3 s		6.5 s
5-layer Fig. 4.5(b)	47 m 9 s	3.9 s		3 s		6.9 s
5-layer Fig. 4.5(c)	59 m 48 s	3.7 s		3 s		6.7 s
2-layer Fig. 4.6(a)	1 h 24 m 5 s	2.1 s		3 s+2.5 s		7.6 s
4-layer Fig. 4.6(b)	1 h 31 m 51 s	2.7 s		3 s+2.5 s		8.2 s
3-layer Fig. 4.7(a)	1 h 26 m 15 s	2.5 s		3 s+2.5 s+2.4 s		10.4 s
3-layer Fig. 4.7(b)	1 h 28 m 43 s	2.4 s		3 s+2.5 s+2.2 s		10.1 s
3-layer Fig. 4.8(a)	1 h 2 m 11 s	2.4 s		2.5 s+2.8 s+2 s		9.7 s
3-layer Fig. 4.8(b)	1 h 11 m 22 s	2.5 s		2.5 s+2.8 s+2 s		9.8 s
3-layer Fig. 4.9(a)	1 h 4 m 41 s	2.6 s		2.5 s+2.8 s+2 s		9.9 s
3-layer Fig. 4.9(b)	1 h 33 m 38 s	2.8 s		2.5 s+2.8 s+2 s		10.1 s

4.4 Conclusions

In this Chapter, an equivalent-circuit model for the analysis of stacked slot-based 2D periodic arrays of arbitrary geometry has been deduced for a wide operating frequency range. The proposed EC overcomes the symmetry limits due to the even/odd excitation approach, which is only useful in the case of identical stacked frequency selective surfaces, and it can account for normal and oblique incidence.

The constitutive Π networks, describing two closely coupled arrays, can easily be cascaded to obtain the electromagnetic response of the whole device composed of an arbitrary number of stacked arrays, through the ABCD matrix formalism. The EC has been validated by analyzing the transmission spectra of some complex multi-layered devices with arbitrary aperture shapes. This allowed to gain a physical insight into the spectral and angular responses of the structures under test, that can be extended even in the more general cases of lossy dielectric and finite electric conductivity.

The EC can be also implemented as a fully-analytical model for standard aperture geometries, being the transverse aperture profile of the electric field given by closed-form expressions. In the more general case of complex configurations, a quasi-analytical model is needed and the aperture profiles are extracted from a single low-frequency full-wave simulation of the free-standing 2D periodic FSS, with a noticeable saving of resources and computational CPU time (as demonstrated by Table 4.1), especially in the design phase.

The results presented in this Chapter have been published in Ref. [1].

References

- [1] M. D. Astorino, F. Frezza, and N. Tedeschi, "Equivalent-circuit model for stacked slot-based 2D periodic arrays of arbitrary geometry for broadband analysis," *Journal of Applied Physics*, vol. 123, no. 10, p. 103106, 2018.
- [2] M. Guglielmi and A. A. Oliner, "Multimode network description of a planar periodic metal-strip grating at a dielectric interface. I: Rigorous network formulations," *IEEE Transactions on Microwave Theory and Techniques*, vol. 37, pp. 534–541, Mar 1989.
- [3] M. Guglielmi and A. A. Oliner, "Multimode network description of a planar periodic metal-strip grating at a dielectric interface. II: small-aperture and small-obstacle solutions," *IEEE Transactions on Microwave Theory and Techniques*, vol. 37, pp. 542–552, Mar 1989.
- [4] J. Vardaxoglou and E. A. Parker, "Modal analysis of scattering from two-layer frequency-selective surfaces," *International Journal of Electronics*, vol. 58, no. 5, pp. 827–830, 1985.
- [5] C.-C. Chen, "Scattering by a two-dimensional periodic array of conducting plates," *IEEE Transactions on Antennas and Propagation*, vol. 18, no. 5, pp. 660–665, 1970.
- [6] B. A. Munk, *Frequency selective surfaces: theory and design*, vol. 29. John Wiley & Sons, 2000.
- [7] R. Mittra, C. H. Chan, and T. Cwik, "Techniques for analyzing frequency selective surfaces—a review," *Proceedings of the IEEE*, vol. 76, no. 12, pp. 1593–1615, 1988.
- [8] T. Cwik and R. Mittra, "Scattering from a periodic array of free-standing arbitrarily shaped perfectly conducting or resistive patches," *IEEE Transactions on Antennas and Propagation*, vol. 35, no. 11, pp. 1226–1234, 1987.
- [9] R. Martin and D. Martin, "Quasi-optical antennas for radiometric remote-sensing," *Electronics & Communication Engineering Journal*, vol. 8, no. 1, pp. 37–48, 1996.
- [10] L. Martinez-Lopez, J. Rodriguez-Cuevas, J. I. Martinez-Lopez, and A. E. Martynyuk, "A multilayer circular polarizer based on bisected split-ring frequency selective surfaces," *IEEE Antennas and Wireless Propagation Letters*, vol. 13, pp. 153–156, 2014.
- [11] C. R. Simovski, P. de Maagt, and I. V. Melchakova, "High-impedance surfaces having stable resonance with respect to polarization and incidence angle," *IEEE Transactions on Antennas and Propagation*, vol. 53, pp. 908–914, March 2005.
- [12] N. Yu and F. Capasso, "Flat optics with designer metasurfaces," *Nature Materials*, vol. 13, no. 2, p. 139, 2014.
- [13] M. D. Astorino, F. Frezza, and N. Tedeschi, "Ultra-thin narrow-band, complementary narrow-band, and dual-band metamaterial absorbers for applications in the THz regime," *Journal of Applied Physics*, vol. 121, no. 6, p. 063103, 2017.
- [14] M. D. Astorino, R. Fastampa, F. Frezza, L. Maiolo, M. Marrani, M. Missori, M. Muzi, N. Tedeschi, and A. Veroli, "Polarization-maintaining reflection-mode THz time-domain spectroscopy of a polyimide based ultra-thin narrow-band metamaterial absorber," *Scientific Reports*, vol. 8, no. 1, p. 1985, 2018.
- [15] M. D. Astorino, F. Frezza, and N. Tedeschi, "Broad-band terahertz metamaterial absorber with stacked electric ring resonators," *Journal of Electromagnetic Waves and Applications*, vol. 31, no. 7, pp. 727–739, 2017.
- [16] G. Goussetis, A. P. Feresidis, and J. C. Vardaxoglou, "Tailoring the AMC and EBG characteristics of periodic metallic arrays printed on grounded dielectric substrate," *IEEE Transactions on Antennas and Propagation*, vol. 54, no. 1, pp. 82–89, 2006.
- [17] T. F. Krauss, R. M. De La Rue, and S. Brand, "Two-dimensional photonic-bandgap structures operating at near-infrared wavelengths," *Nature*, vol. 383, no. 6602, p. 699, 1996.
- [18] R. C. Hall, R. Mittra, and K. M. Mitzner, "Analysis of multilayered periodic structures using generalized scattering matrix theory," *IEEE Transactions on Antennas and Propagation*, vol. 36, no. 4, pp. 511–517, 1988.

- [19] C. Wan and J. A. Encinar, "Efficient computation of generalized scattering matrix for analyzing multilayered periodic structures," *IEEE Transactions on Antennas and Propagation*, vol. 43, no. 11, pp. 1233–1242, 1995.
- [20] D. Colton and R. Kress, *Integral equation methods in scattering theory*. SIAM, 2013.
- [21] V. Prakash and R. Mittra, "Characteristic basis function method: A new technique for efficient solution of method of moments matrix equations," *Microwave and Optical Technology Letters*, vol. 36, no. 2, pp. 95–100, 2003.
- [22] A. G. Schuchinsky, D. E. Zelenchuk, A. M. Lerer, and R. Dickie, "Full-wave analysis of layered aperture arrays," *IEEE Transactions on Antennas and Propagation*, vol. 54, no. 2, pp. 490–502, 2006.
- [23] S. Monni, G. Gerini, A. Neto, and A. G. Tijhuis, "Multimode equivalent networks for the design and analysis of frequency selective surfaces," *IEEE Transactions on Antennas and Propagation*, vol. 55, no. 10, pp. 2824–2835, 2007.
- [24] R. Rodríguez-Berral, C. Molero, F. Medina, and F. Mesa, "Analytical wideband model for strip/slit gratings loaded with dielectric slabs," *IEEE Transactions on Microwave Theory and Techniques*, vol. 60, no. 12, pp. 3908–3918, 2012.
- [25] C. Molero, R. Rodríguez-Berral, F. Mesa, F. Medina, and A. B. Yakovlev, "Wideband analytical equivalent circuit for one-dimensional periodic stacked arrays," *Physical Review E*, vol. 93, no. 1, p. 013306, 2016.
- [26] C. Molero, R. Rodríguez-Berral, F. Mesa, and F. Medina, "Wideband analytical equivalent circuit for coupled asymmetrical nonaligned slit arrays," *Physical Review E*, vol. 95, no. 2, p. 023303, 2017.
- [27] M. García-Vigueras, F. Mesa, F. Medina, R. Rodríguez-Berral, and J. L. Gomez-Tornero, "Simplified circuit model for arrays of metallic dipoles sandwiched between dielectric slabs under arbitrary incidence," *IEEE Transactions on Antennas and Propagation*, vol. 60, no. 10, pp. 4637–4649, 2012.
- [28] F. Mesa, R. Rodríguez-Berral, M. García-Vigueras, F. Medina, and J. R. Mosig, "Simplified modal expansion to analyze frequency-selective surfaces: An equivalent circuit approach," *IEEE Transactions on Antennas and Propagation*, vol. 64, no. 3, pp. 1106–1111, 2016.
- [29] R. Rodríguez-Berral, F. Mesa, and F. Medina, "Analytical multimodal network approach for 2-D arrays of planar patches/apertures embedded in a layered medium," *IEEE Transactions on Antennas and Propagation*, vol. 63, no. 5, pp. 1969–1984, 2015.
- [30] V. Torres, F. Mesa, M. Navarro-Cía, R. Rodríguez-Berral, M. Beruete, and F. Medina, "Accurate circuit modeling of fishnet structures for negative-index-medium applications," *IEEE Transactions on Microwave Theory and Techniques*, vol. 64, no. 1, pp. 15–26, 2016.
- [31] C. S. Kaipa, A. B. Yakovlev, F. Medina, and F. Mesa, "Transmission through stacked 2D periodic distributions of square conducting patches," *Journal of Applied Physics*, vol. 112, no. 3, p. 033101, 2012.
- [32] S. R. Rengarajan, "Choice of basis functions for accurate characterization of infinite array of microstrip reflectarray elements," *IEEE Antennas and Wireless Propagation Letters*, vol. 4, no. 1, pp. 47–50, 2005.
- [33] D. M. Pozar, *Microwave Engineering*. John Wiley & Sons, 2011.
- [34] S.-W. Lee, G. Zarrillo, and C.-L. Law, "Simple formulas for transmission through periodic metal grids or plates," *IEEE Transactions on Antennas and Propagation*, vol. 30, no. 5, pp. 904–909, 1982.

Ultra-thin narrow-band, complementary narrow-band, and dual-band metamaterial absorbers for applications in the THz regime

In this Chapter, ultra-thin narrow-band, complementary narrow-band, and dual-band metamaterial absorbers (MMAs), exploiting the same Electric Ring Resonator (ERR) configuration, are investigated at normal and oblique incidence for both Transverse Electric (TE) and Transverse Magnetic (TM) polarizations, and with different physical properties in the THz regime. In the analysis of the ultra-thin narrow-band MMA, the limit of applicability of the Transmission Line Model (TLM) has been overcome with the introduction of a capacitance which considers the z component of the electric field. These absorbing structures have shown a wide angular response and a polarization-insensitive behavior due to the introduction of a conducting ground plane and to the four-fold rotational symmetry of the resonant elements around the propagation axis. I have adopted a retrieval procedure to extract the effective electromagnetic parameters of the proposed MMAs and I have compared the simulated and analytical results through the interference theory.

The contents of this Chapter have been published in Refs. [1–3].

5.1 Introduction

The interest in the application of electromagnetic resonant absorbers was initially focused in the microwave range and great potentialities were primarily exploited in the military field. Thanks to the work of researchers like Salisbury and Jaumann, performance of radar equipment in both detection and concealment towards other radar systems was optimized [4, 5]. The Salisbury screen is a classic example of a passive microwave resonant absorber constituted by a Perfect Electric Conductor (PEC) placed $\lambda/4$ behind the resistive sheet. The Jaumann

absorber can be considered as an evolution of the Salisbury screen with two or more resistive sheets placed in front of a single ground plane. The Dällenbach layer uses, instead, a lossy homogeneous layer backed by a ground plane to absorb the incident radiation.

Circuit Analog (CA) absorbers, resulting from the Salisbury screen, are obtained by spacing in front of the ground plane layers of lossy Frequency Selective Surfaces (FSSs), that are resistive and reactive components, which derive their filtering properties from the lattice constant and are realized using periodically perforated metallic screens or metal particles on a dielectric substrate [6]. The FSSs, however, because of their periodic structure and size comparable to the wavelength, cause problems with unwanted passbands, off-normal incidence, and polarizations. Therefore, high peaks of absorption for wide angles of incidence and frequency bands were obtained only in the latest models of absorbers arranged with analog circuits.

Active metamaterial absorbers are another type of artificial structure that can be dynamically tuned to the operational wavelength, through external excitations and employment of diodes [7]. These offer significant potential in achieving electromagnetic features ranging from dynamic filtering to reconfigurable detectors through mechanical orientation of resonators inside the unit cells [8].

In particular, metamaterial absorbers have found specific applications depending on their operating frequency range. In the optical regime, they are employed in thermophotovoltaic systems [9], according to Kirchhoff's law of radiation, as thermal emitters, sensors, and spatial light modulators [10]. At microwaves, they are used for reducing sidelobe radiation for antennas and radar cross section to limit radar echo [11]. Significant uses concern electromagnetic compatibility in order to reduce interference and spurious radiation between components and electronic circuits assembled on the same platform. In the terahertz range, MMAs are employed in microbolometers of image devices as spectrally sensitive photodetectors [12], in the field of security, in sensing elements, and imaging applications [13]. Not least are the uses in wireless communications to reduce health risks of exposure to specific electromagnetic radiation. This Chapter is indeed dedicated to the design of ultra-thin MMAs in the THz frequency range, where it is difficult to find naturally occurring materials with very strong absorption.

MMAs are constituted by repeating unit cells positioned in two or three-dimensional periodic structures. The ideal MMA is a type of engineered device in which the entire incident radiation is absorbed at a specified frequency with a high angular stability of the absorption profile. The absorption describes the percentage of electromagnetic energy absorbed by the MMA and it is defined as $A = 1 - R - T = 1 - |S_{11}|^2 - |S_{21}|^2$. This means that to achieve a high absorption,

reflection R and transmission T must be simultaneously minimized. Therefore, known material properties, assigning appropriate excitations and suitable boundary conditions, the periodic array can be adequately modeled simulating the unit cell.

The Chapter is organized as follows: in Section 5.2, starting from the ERR in Ref. [13], I present the design of a narrow-band MMA, showing how the conventional transmission line model fails when the dielectric slab is not thick enough, due to the presence of higher order Floquet modes. In Sections 5.3 and 5.4, I propose designs of complementary narrow-band and dual-band MMAs, respectively. All models are examined and numerically demonstrated in the THz regime, at normal and oblique incidence for both transverse electric and transverse magnetic polarizations. In Section 5.5, I apply a homogenization technique for extracting the effective electromagnetic parameters of the structures and the interference theory to verify the simulated and analytical results. Finally, in Section 5.6, I draw the conclusions.

5.2 Ultra-thin narrow-band MMA

The proposed ultra-thin narrow-band MMA (see Fig. 5.1) is $\lambda_0/45$ thick at the resonance frequency, where λ_0 is the free-space wavelength. Its single unit cell consists of a top metallic ERR and a bottom ground plane, both made of lossy gold with 270 nm thickness, separated by a $5.8 \mu\text{m}$ thick dielectric layer of benzocyclobutane (BCB) with relative permittivity $\epsilon_r = 2.5$ and dielectric loss tangent $\tan\delta = 0.005$.

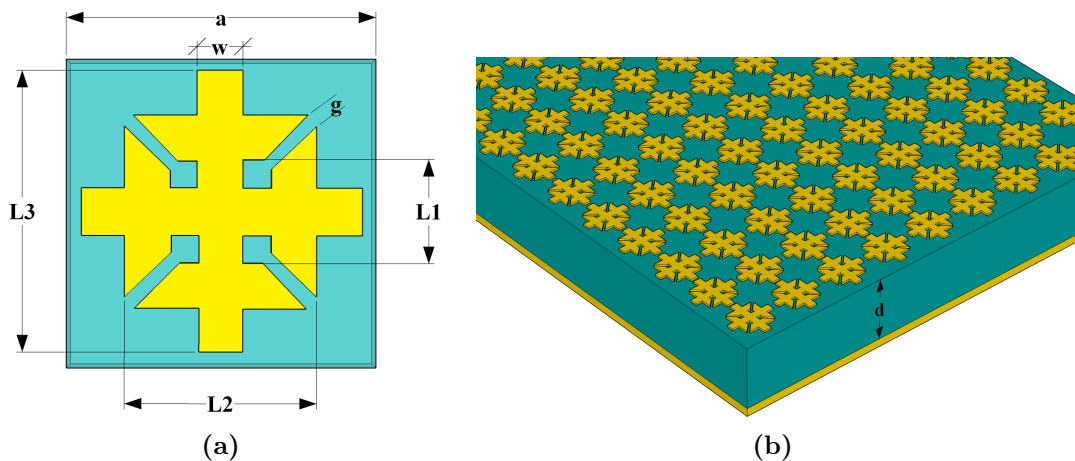


Figure 5.1: (a) Geometry of the single unit cell and (b) 3D sketch of the ultra-thin narrow-band MMA with dimensions (in microns) $a=80$, $g=3.5$, $w=11$, $L_1=26$, $L_2=48$, $L_3=70$, $d=5.8$.

This MMA causes the incident electric and magnetic fields to be simultaneously absorbed and the effective permittivity and permeability to be independently tuned by modifying the electric and magnetic responses. In fact, through

geometrical variations of the upper ERR, developed on the model of the Split Ring Resonator (SRR), it is possible to achieve the desired electric response, exploiting the capacitances formed by the four gaps. These, positioned at an equal distance and rotated by 90° each other, generate an electric response in the ERR for a wide range of polarizations of the incident field. By varying, instead, the distance between the metal layers, the magnetic response can be tuned since the incident magnetic field is coupled to the antiparallel currents.

In synthesis, this metal-dielectric-metal structure allows the upper ERR to couple to the incident electric field and it allows the antiparallel currents between the two metal layers to couple to the magnetic field.

Since the back side of the MMA is covered with a metal plate thicker than the penetration depth of the THz wave, there is no transmission ($T = |S_{21}|^2 = 0$) and the absorption is maximized by minimizing the reflection from the absorber ($A = 1 - R = 1 - |S_{11}|^2$). To minimize the reflection, the relative effective impedance of the structure should be matched to free space at the absorption frequency (i.e., the impedance relative to vacuum is $z = \sqrt{\mu_r/\epsilon_r} = 1$, where the total impedance $Z = Z_0 z$, being $Z_0 = \sqrt{\mu_0/\epsilon_0} = 120\pi \Omega$ the free-space impedance), that is the relative effective permittivity and permeability must be approximately equal.

To analyze an infinite array of these periodic structures, the unit cell is simulated through a commercial Finite Element Method (FEM) solver by applying periodic boundary conditions for both x and y directions, and considering the case of a plane wave that normally impinges on the MMA in the xz incident plane (where the azimuthal angle $\phi = 0^\circ$, which is the angle between the projection of incident wave vector on xy plane and x direction). The curves of absorption, reflection, and transmission are plotted in Fig. 5.2 in the 0.9-1.4 THz frequency range.

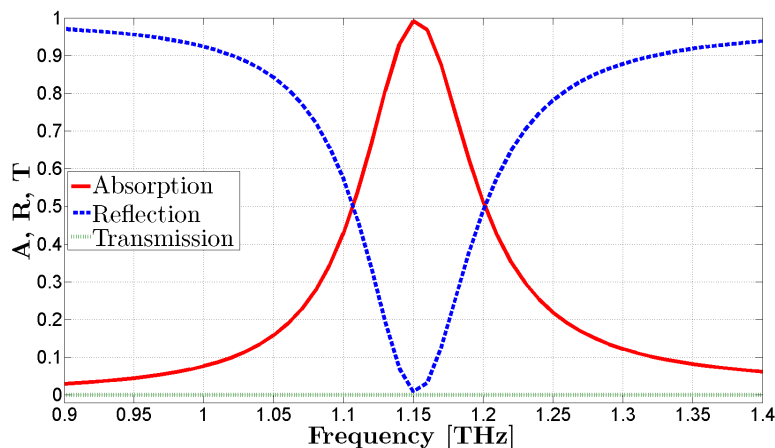


Figure 5.2: Absorption, reflection, and transmission of the narrow-band MMA.

Thanks to the insertion of the metallic ground plane, there is no transmission over the entire range of simulated frequencies and a nearly perfect resonance peak is reached at 1.15 THz with 99.13% absorption. The relative Full Width at Half-Maximum (FWHM) absorption bandwidth (the ratio of FWHM, namely the 3 dB linewidth, to the resonance frequency) is 8.26% and the quality factor Q is 12.11.

It is also noteworthy how the geometric dimensions of the ERR influence the position of the absorption peak, since the resonance frequency of a metamaterial scales as a function of the operational wavelength. To obtain, therefore, a shift of the resonance towards higher frequencies, the dimensions of the resonator must be proportionally reduced requiring greater precision in the manufacturing techniques.

In order to obtain physical insight into the absorption mechanism, the distributions of the z component of the electric field on the ERR and the ground plane are shown in Fig. 5.3 at the resonance frequency. In Fig. 5.3(a), we can observe the excitation of an electric dipole on the ERR: in fact, charges of opposite signs accumulate at the ends of the ERR and the electric field is mainly distributed at the corners of horizontal and vertical arms. Moreover, as shown in Fig. 5.3(b), there is another electric-dipole resonance on the metallic ground plane which oscillates in anti-phase compared with the one on the ERR. These electric dipoles are strongly coupled with each other and generate a magnetic polariton which gives rise to a magnetic resonance, responsible for the near-unity absorption peak.

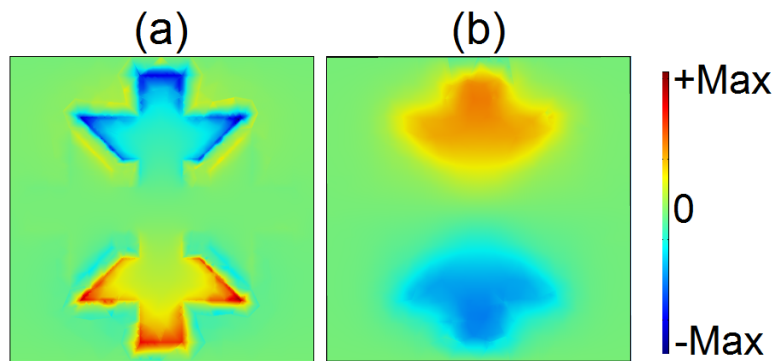


Figure 5.3: Distributions of the z component electric field [V/m] at the resonance frequency on (a) the ERR and (b) the ground plane.

The investigated MMA has been represented through an equivalent circuit based on the TLM as reported in Fig. 5.4. The impedance Z_{ERR} of the ERR can be described as a series RLC circuit whose expression can be obtained as follows:

$$Z_{ERR} = R_{ERR} + jX_{ERR} = -\frac{Z_0^2(1 + \Gamma)}{2Z_0\Gamma}, \quad (5.1)$$

where Γ represents the reflection coefficient of the ERR printed on the BCB dielectric layer of thickness $d = 5.8 \mu\text{m}$ in order to take into account the substrate which influences the value of the capacitance. In fact, the impedance of the ERR has to be modified in the presence of the dielectric substrate in comparison with the freestanding configuration.

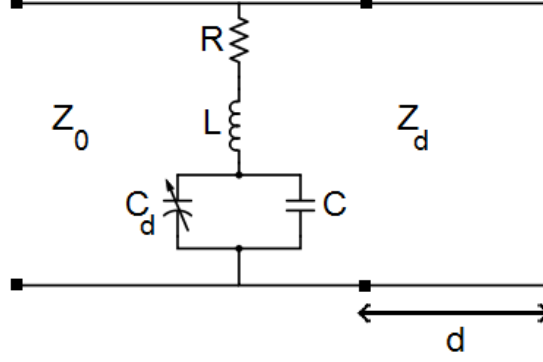


Figure 5.4: Transmission-line model of the ultra-thin narrow-band MMA composed of the ERR arrays backed by a grounded substrate with characteristic impedance Z_d .

The series RLC circuit representing the ERR is then placed in parallel to the impedance of the grounded dielectric substrate Z_{GS} :

$$Z_{GS} = jZ_d \tan(k_d d) = j \frac{Z_0}{\sqrt{\epsilon' - j\epsilon''}} \tan(k_0 \sqrt{\epsilon' - j\epsilon''} d), \quad (5.2)$$

where k_0 is the free-space propagation constant.

The input impedance Z_{IN} of the MMA is obtained as the parallel connection between the complex impedances of the grounded substrate Z_{GS} and of the ERR Z_{ERR} . The absorption spectrum of the MMA is derived from

$$A = 1 - |S_{11}|^2 = 1 - \left| \frac{Z_{IN} - Z_0}{Z_{IN} + Z_0} \right|^2, \quad (5.3)$$

where S_{11} represents the reflection coefficient of the MMA.

In Fig. 5.5, the comparison of the frequency responses of the ultra-thin narrow-band MMA (solid line) and the TLM (dashed line) is illustrated and it is evident that the difference between the resonance frequencies is 1.15 THz and 1.37 THz, respectively.

This shift of the resonant frequency is due to the ultra-thin geometry of the absorber. MMAs are basically a sub-wavelength resonant cavity and it is known that the accuracy of the TLM reduces as the thickness decreases $d < \lambda/4$. In the case of ultra-thin MMAs, the z component of the electric field is produced by high-order evanescent Floquet modes [14], but this component is not taken into account in the TLM: in fact, at normal incidence, the propagating mode

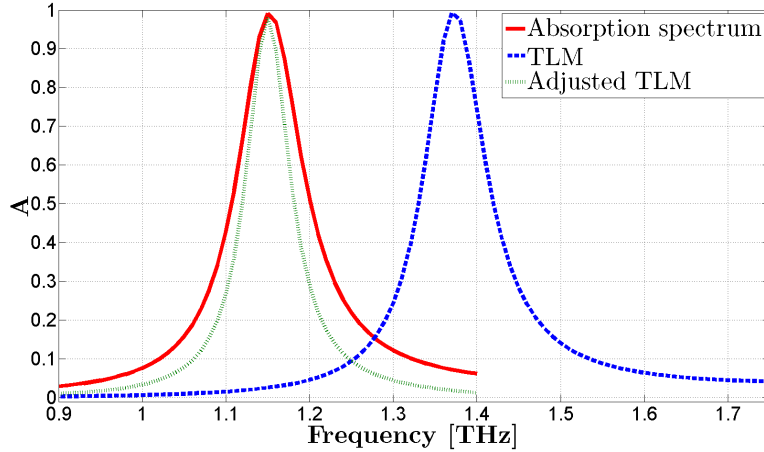


Figure 5.5: Comparison of the frequency response of the ultra-thin narrow-band MMA absorber and the TLMs.

is transverse electromagnetic (TEM) and contains no z -directed component. In the conventional $\lambda/4$ MMA, the E_z component is negligible in comparison with the transverse component of the electric field and it does not contribute to the impedance of the ERR arrays. On the contrary, for the ultra-thin MMAs, the E_z component is fundamental to describe the absorption mechanism. For this reason, the capacitance of TLM has been adjusted in order to obtain the same resonant frequency of the FEM analysis (see the adjusted TLM in Fig. 5.5), reaching the following expression for the Z_{ERR} impedance:

$$Z_{ERR} = R + j\omega L + \frac{1}{j\omega(C + C_d)}, \quad (5.4)$$

where C_d is the thickness-dependent capacitance due to the z component of the electric field between the ground plane and the ERR, generally not evaluated in the TLM.

In the following, I will study the polarization behavior of the ultra-thin narrow-band MMA when the incident angle θ increases from 0° to 80° in steps of 20° and the azimuthal angle $\phi = 0^\circ$, by performing FEM-based simulations.

In Fig. 5.6(a), for TE polarization (the electric field is fixed along the y direction), a distinct amplitude reduction of the absorption peak can be observed when increasing the incident angle. However, for incident angle $\theta \leq 40^\circ$, the absorption spectrum is almost overlapped with the one for normal incidence. An absorption level of 86.3% at the resonant frequency is still achieved when $\theta = 60^\circ$. Beyond this angle, the amplitude of the absorption peak drops quickly (for 80° incidence, the simulation shows a substantial decay of the peak close to 46%), as the x component of the incident magnetic field decreases rapidly to zero and can no longer efficiently induce antiparallel currents in the top layer of the

metamaterial and in the lower ground plane, thus implying a reduction of the magnetic flux. In fact, a wide angular absorption for TE polarization is difficult to obtain, because the TE free space impedance increases as the incident angle θ increases ($Z_0^{TE} = Z_0/\cos\theta$); therefore, the almost angle-independent input impedance Z_{IN} of the MMA is no more matched to the angle-dependent free space impedance Z_0^{TE} as θ varies.

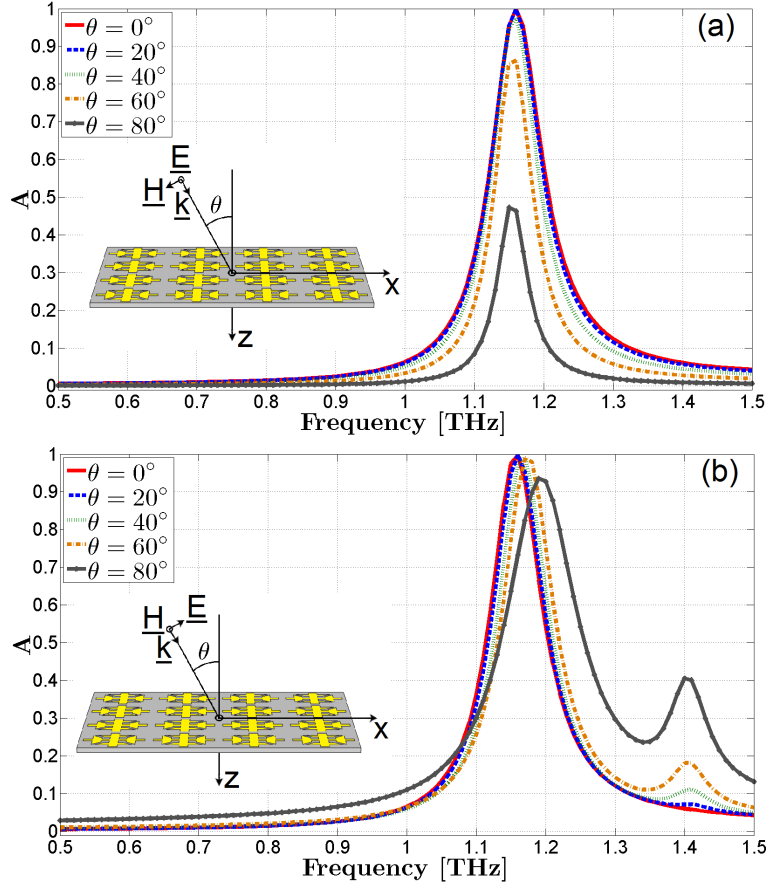


Figure 5.6: Absorption spectra at different incidence angles with (a) TE and (b) TM polarizations depicted in the inset for the narrow-band MMA.

In the case of TM polarization (the magnetic field is fixed along the y direction), it can be seen from Fig. 5.6(b) that a significant absorption above 99% occurs for angles less than 60° , while for the angle of 80° , there are two absorption peaks of 93.56% and 40.56%, respectively, at the frequencies of 1.19 THz and 1.4 THz. Therefore, as the incident angle increases, the amplitude of the absorption peak decreases slightly, even when $\theta = 80^\circ$, at which angle the electric field is nearly normal to the ERR. This angle-independent absorption of the TM wave is due to the fact that the magnetic field can effectively drive circulating currents for the various angles of incidence, an essential condition to maintain the impedance matching. In this case, the TM free-space impedance decreases as the incident angle increases ($Z_0^{TM} = Z_0 \cos\theta$) and the real part of Z_{IN} is proportional to the

square of the imaginary part of Z_{GS} which having the same dependence on θ as Z_0^{TM} generates a wide angular response. The appearance of the additional peaks in TM polarization is probably due to the particular shape and dimensions of the ERR: in fact, an analogous behavior can be observed in Ref. [15] in which I have found very similar ratios between the wavelength and the geometric dimensions at the second resonant frequency [16].

Besides, with increasing incidence angle, a shift of the absorption peak is observed towards higher frequencies, which is relatively small (0.03 THz) for $\theta \leq 80^\circ$, unlike the case of TE polarization for which the resonance frequency remains virtually unchanged. In fact, in the case of normal incidence (the electric field is along the x axis and the magnetic field is along the y axis), the electric dipole of the ERR in each unit cell oscillates in phase and, therefore, along the x direction the attractive force between the positive and negative charges of the neighboring ERRs weakens the restoring force of the charge oscillation inside the ERR due to the interaction between the adjacent unit cells. In the case of TM polarization, the dipole oscillation of the adjacent ERRs in the x direction is no longer in phase as the incident angle θ increases. This causes a blueshift of the resonant frequency, due to the reduction of the attractive force between the adjacent unit cells.

As shown in Fig. 5.7, due to the four-fold rotational symmetry around the propagation axis of the ERR, this absorber is quite robust to variations of the incidence angle θ and it is not polarization sensitive: in fact, at normal incidence, the absorption spectra for TE (with the electric field perpendicular to xz plane) and TM (with the magnetic field perpendicular to xz plane) polarizations are identical. This underlines a strong analogy with the uniaxial anisotropic media having the optical axis perpendicular to the air/absorber interface [17, 18], and confers on the absorber appreciable efficiency and versatility, making it suitable to operate under different conditions and in various environments.

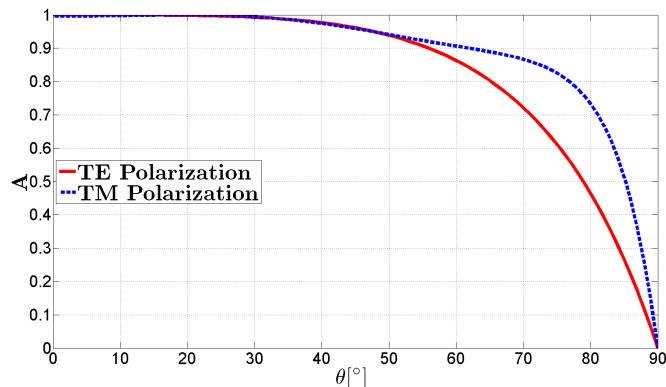


Figure 5.7: Angular response at the resonant frequency of the narrow-band MMA in TE and TM polarizations when azimuthal angle $\phi = 0^\circ$.

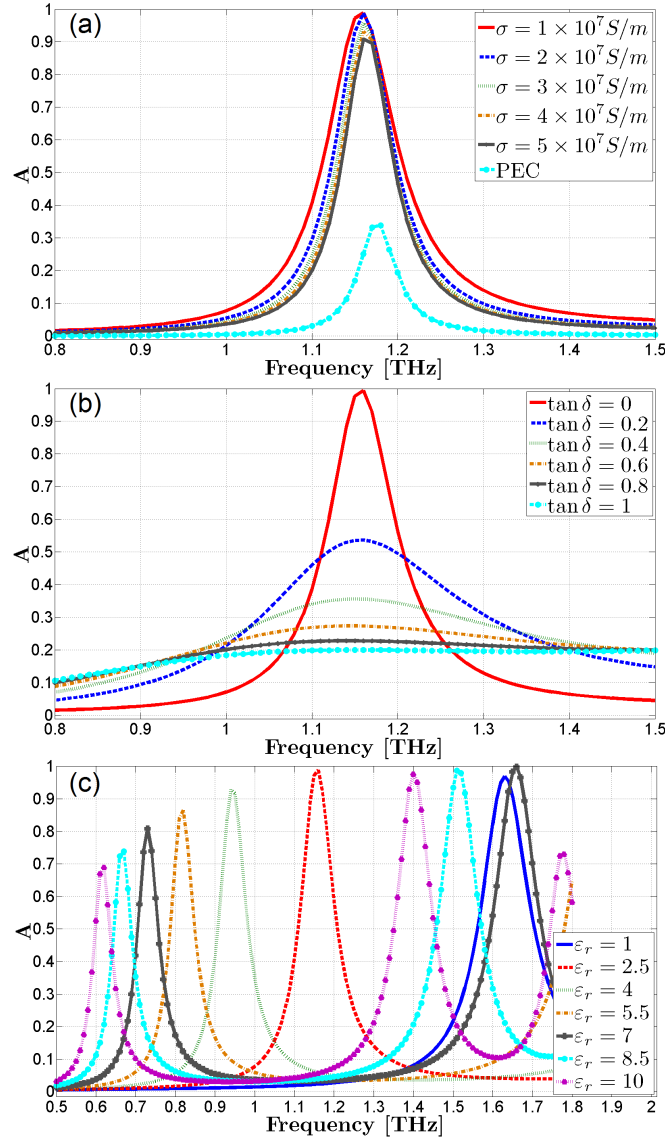


Figure 5.8: Absorption spectra when increasing (a) the electric conductivity of the metallic layers, (b) the loss tangent and (c) the relative permittivity of the dielectric layer.

Absorption spectra for different physical properties of metallic and dielectric layers are represented in Fig. 5.8 at normal incidence. In Fig. 5.8(a), one can observe a progressive reduction and blueshift of the absorption peaks with increasing electric conductivity σ from $1 \times 10^7 \text{ S/m}$ to infinity (PEC). This is due to the impedance mismatching to free space that determines a growing reflection and, consequently, a reduction of the absorption levels. Instead, in Fig. 5.8(b), the resonance peak is plotted as the loss tangent $\tan \delta$ of the BCB layer varies from 0 (lossless BCB) to 1. Therefore, the majority of THz radiation is absorbed by ERR and metal backplane as an oscillating electric current.

To further study the resonant behavior of the proposed narrow-band MMA, I analyzed the dependence of the absorption on the electric permittivity (see Fig.

5.8(c)). We observed the appearance of multiple resonance peaks along with both a progressive narrowing of the absorption bandwidth and a decay of the absorption levels as the dielectric constant increases. Furthermore, while the resonance frequency undergoes a redshift, near-unity peaks appear at higher frequencies. This behavior is due to the different values of the capacitance that increases with the increase of the permittivity. Therefore, the resonant frequency undergoes a redshift being inversely proportional to the capacitance. The variation of the electric permittivity generates, indeed, an impedance mismatch to free space and a reduction of the absorption. This characteristic could be exploited to realize multiple-band metamaterial absorbers with the unit cell constituted by more resonant elements sharing the same ground plane, but with different dielectric layers. So, it should also be possible the overlapping of the absorption spectra for specific values of the employed electric permittivity, in order to develop broadband MMAs.

5.3 Ultra-thin complementary narrow-band MMA

Another configuration of the ultra-thin narrow-band MMA backed by a metal plate with the same dimensions, material parameters and simulation set-up previously chosen was obtained by considering a complementary ERR (see Fig. 5.9).

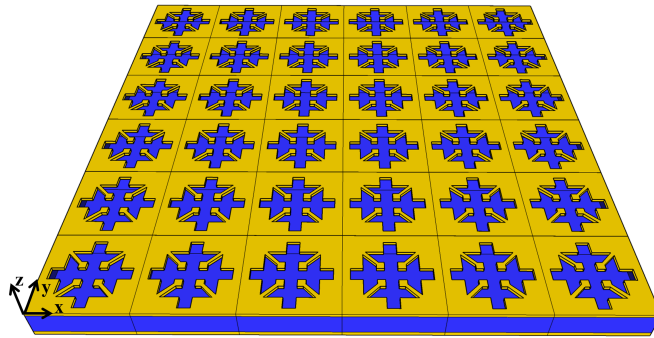


Figure 5.9: Geometry of the complementary narrow-band MMA.

In Fig. 5.10, we observe at normal incidence a level of absorption of 99.08% at the frequency of 1.49 THz with a relative FWHM absorption bandwidth equal to 7.38% and a quality factor Q of 13.54.

The complementary narrow-band MMA was then tested at oblique incidence for TE polarization with a parametric sweep for the incidence angle θ from 0° to 80° and $\phi = 0^\circ$. A decrease in the absorption level along with a slight blueshift was observed as the incidence angle increases and an additional absorption peak occurs at the frequency of 1.59 THz: its value for the angle of 80° is close to 23.31%.

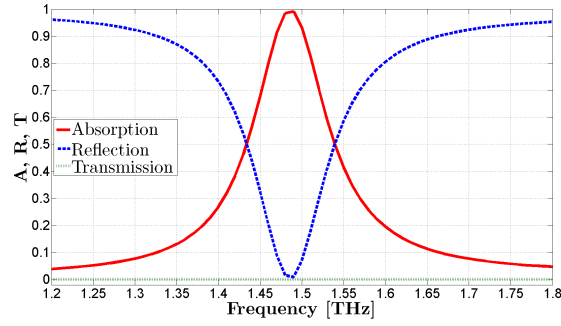


Figure 5.10: Absorption, reflection, and transmission of complementary narrow-band MMA.

In the TM configuration, a remarkable red-shift of the resonance frequency has been detected with the incidence angle increasing. Absorption levels of 99.50% are obtained for the angle of 20° at 1.45 THz, of 99.39% for the angle of 40° at 1.38 THz, of 98.50% for the angle of 60° at 1.32 THz, and of 79.91% for the angle of 80° at 1.3 THz. This angular dependence of the absorption in TM polarization could be used to achieve polarization-selective devices or mechanically frequency-tunable absorbers.

In comparison with simulations carried out for TE and TM polarizations, a monotonic decrease in the absorption as a function of the incidence angle was noticed for TE polarization, while there is an apparent shift of the resonance peaks for TM polarization.

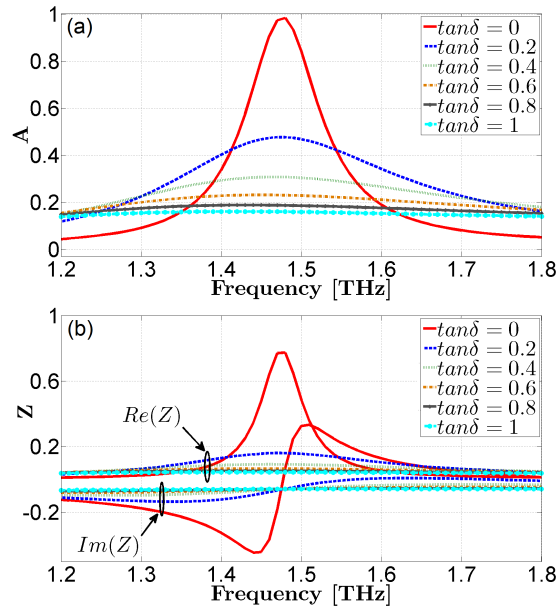


Figure 5.11: (a) Absorption spectra and (b) wave impedance when increasing the loss tangent for complementary narrow-band MMA.

To investigate the causes of the absorption mechanism, I initially analyzed the effect of the dielectric and Ohmic losses on both the absorption levels and

the impedance matching to free space at normal incidence. In Fig. 5.11(a), one can see that the absorption peaks undergo a strong decay and broadening with increasing $\tan\delta$ from 0 (lossless BCB) to 1. Therefore, the wave impedance z loses the matching to free space and most of the incident wave is reflected by the MMA (Fig. 5.11(b)).

The effect of the Ohmic losses has been, instead, analyzed through a parametric sweep on the electric conductivity σ and I observed an absorption of about 40% for the case of the complementary ERR and the ground plane made of PEC (Fig. 5.12(a)). Also, in this case, the wave impedance loses the matching to free space as the conductivity increases, determining a growing reflection (see Fig. 5.12(b)). Therefore, high absorption is mainly due to the Ohmic losses of metallizations and, to a smaller extent, to the dielectric losses of BCB layer.

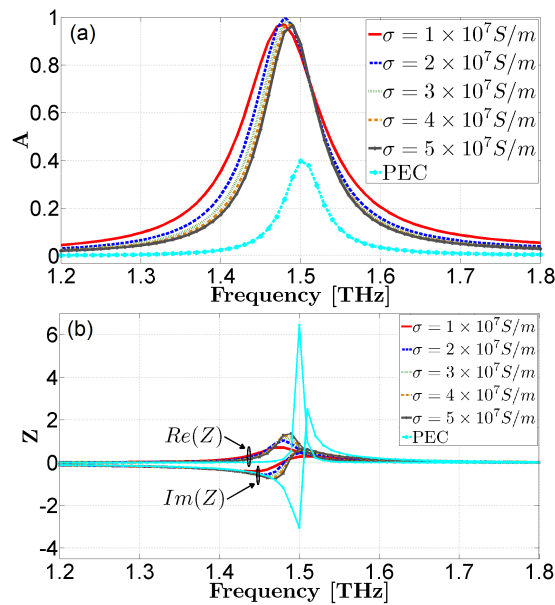


Figure 5.12: (a) Absorption spectra and (b) wave impedance when increasing the electric conductivity for complementary narrow-band MMA.

5.4 Ultra-thin dual-band MMA

THz technology covers a widespread range of applications including medical imaging, reduction of environmental disturbances, remote sensing, and determination of semiconductor electrical properties since terahertz radiation is able to penetrate non-conducting materials without any ionizing effect. For these purposes, selective absorbers in multiple frequency bands that increase the sensitivity and resolution of the images are used in spectroscopic applications and development of detectors [19, 20]. A particular case is represented by dual-band absorbers that, instead of a single resonant cell in different areas and at different frequencies, utilize two resonant structures separately [21–24].

In Fig. 5.13, the unit cell of the ultra-thin dual-band MMA with a thickness of about $\lambda_0/16$ is observable at the higher operating frequency.

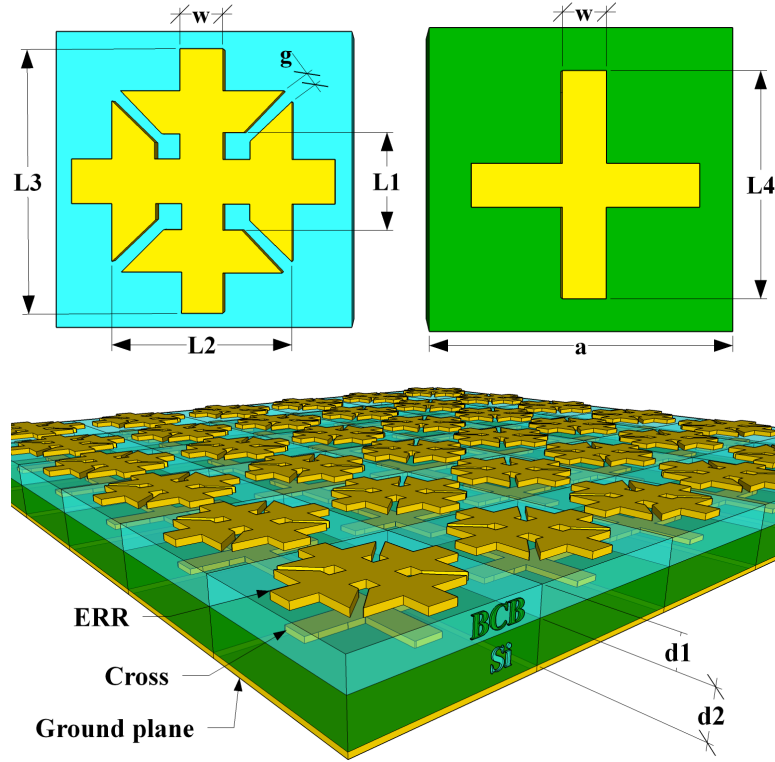


Figure 5.13: Geometry of the dual-band MMA with dimensions (in microns) $a=80$, $g=3.5$, $w=11$, $L_1=26$, $L_2=48$, $L_3=70$, $L_4=60$, $d_1=5$, and $d_2=6.5$.

This is composed of an upper ERR, a central cross, and a lower metal plate made of gold and spaced above by a $5 \mu\text{m}$ thick dielectric layer of BCB and below by a layer of silicon with a thickness of $6.5 \mu\text{m}$, relative permittivity $\epsilon_r = 11.7$, and electric conductivity $\sigma = 10^{-12} \text{ S/m}$.

The infinite array of absorbers, simulated with Floquet periodic boundary conditions and at normal incidence, highlights two significant absorption peaks of 98.67% and 99.15%, respectively, at the frequencies of 0.75 THz and 1.15 THz, as shown in Fig. 5.14 for 0° incidence. The relative FWHM absorption bandwidth and the quality factor Q relevant to the first absorption peak are equal to 8.00% and 12.5, while the ones for the second absorption peak are of 9.57% and 10.45, respectively.

For practical applications, MMAs are required to have a high absorption and to be insensitive to the incident radiation. Therefore, the performance of this ultra-thin dual-band MMA was investigated at oblique incidence for TE and TM polarizations with a parametric sweep on the incident angle θ of initial value 0° , final value 80° and step of 20° when azimuthal angle $\phi = 0^\circ$.

In TE polarization, the absorption levels decrease, while the resonance frequencies remain the same as the incidence angle increases (see Fig. 5.14(a)) and

it can be observed that the second peak has an absorption greater than 99% for incidence angles below 40° , exhibiting absorption values higher than those of the first peak. In the case of 80° incidence, however, the simulation shows a substantial decay of the absorption levels close to 47.00% and 51.50% at frequencies of 0.75 THz and 1.15 THz, respectively.

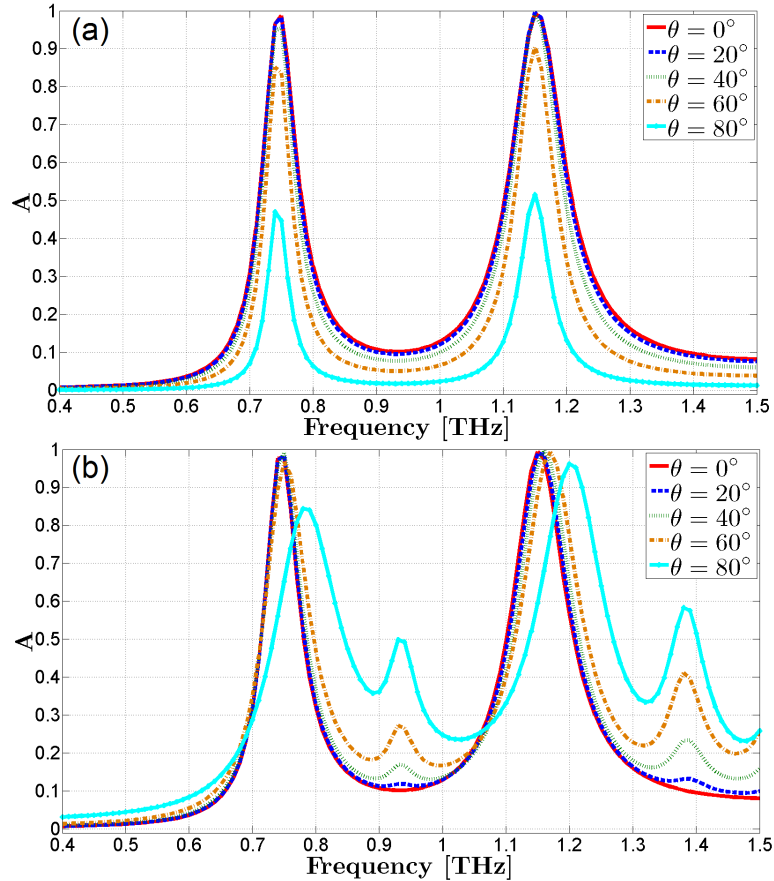


Figure 5.14: Absorption spectra for different incidence angles with (a) TE and (b) TM polarizations for the dual-band MMA.

The ultra-thin dual-band MMA was simulated for the TM-wave case and, in this configuration, we observe in Fig. 5.14(b), with the increase of the incidence angle θ , both a slight shift towards higher frequencies of the resonance peaks and two additional absorption peaks at the frequencies of 0.93 THz and 1.38 THz. For the incidence angle of 80° , two absorption peaks of 84.40% and 96.20% are still delineated at the frequencies of 0.78 THz and 1.20 THz, respectively.

The underlying physical mechanisms of the TE/TM polarization behavior (see Fig. 5.14) are equivalent to the ones observed in Fig. 5.6 for the narrow-band MMA.

The simulated absorption spectra as functions of the incident angle are analogous to those of Fig. 5.7. In particular, the comparison between the absorptions relevant to the two resonance frequencies yields a better performance at 1.15 THz

for TE polarization and a higher efficiency at 0.75 THz for TM polarization.

Since each obliquely incident electromagnetic wave can be decomposed into TE and TM modes, the obtained results confirm that the proposed absorber can work effectively even under oblique incidence and for a wide range of incidence angles.

Then, I study the influence of the loss tangent $\tan\delta$ of BCB on the absorption peaks, increasing gradually $\tan\delta$ from 0 (lossless dielectric) to 1 (see Fig. 5.15).

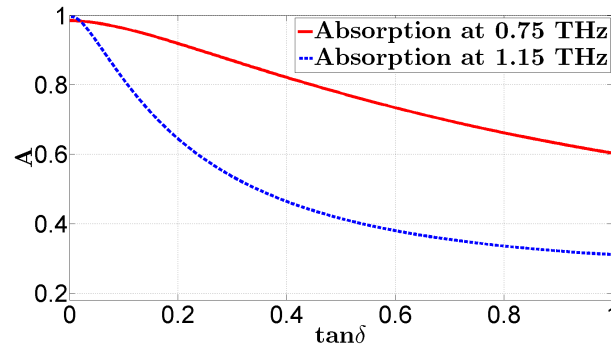


Figure 5.15: Comparison between absorptions at two resonance frequencies as a function of the loss tangent.

The absorber shows a different behavior for the two resonance frequencies and, in general, the absorption levels decrease with increasing $\tan\delta$ especially at 1.15 THz. We can also observe that at the resonance peaks 98.54% and 99.73% energy is absorbed, respectively, with a lossless BCB.

Consequently, high absorption is mainly generated by the Ohmic losses of the metallizations, rather than by the dielectric losses of the BCB layer. This is also proved by the comparison with the PEC case, where the resonance peaks are strongly reduced (see Fig. 5.16) and depend weakly on the dielectric losses.

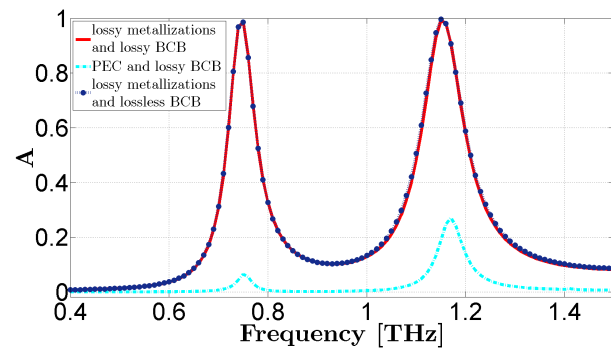


Figure 5.16: Absorption spectra for different material properties of the metallic layers and the BCB dielectric.

5.5 Retrieval of effective electromagnetic parameters

The theory of homogenization allows us to calculate the effective electromagnetic parameters (electric permittivity ε_r , magnetic permeability μ_r , wave impedance z and refractive index n) of a homogeneous slab from the transmission and reflection coefficients obtained by simulations.

In particular, to retrieve the electromagnetic parameters of the ultra-thin MMAs previously analyzed, I have adopted the algorithm of Nicolson, Ross, and Weir (NRW) [25, 26]. This procedure, requiring the transformation of the scattering parameters from the reference planes to the surfaces of the homogeneous slab, introduces significant errors [27, 28]. In fact, the phases of transmission and reflection signals are heavily dependent on the positions of the reference planes, but, at the same time, NRW method has the advantage of a broadband characterization of materials and devices. Transmission/Reflection methods determine the effective electromagnetic parameters extracting overall reflection and transmission coefficients, that is the scattering parameters, calculated for a wave normally incident on a slab of metamaterial positioned in a transmission line. The classic NRW retrieval procedure starts from the derivation of the mathematical relationships between the scattering parameters and the material parameters [29–31]. Scattering of electromagnetic waves has been analyzed according to the model of multiple reflections. Considering the case of normally incident plane waves, the expressions of the scattering coefficients for the slab read:

$$S_{11}(\omega) = \frac{\Gamma(1 - t^2)}{1 - \Gamma^2 t^2}, \quad (5.5)$$

$$S_{21}(\omega) = \frac{t(1 - \Gamma^2)}{1 - \Gamma^2 t^2}, \quad (5.6)$$

where Γ represents the direct reflection from the slab, $t = \exp(-jk'_z d)$ is the propagation factor between the faces of the slab, k'_z is the component of the propagation vector along z in the slab, and d is the thickness of the medium.

The effective material parameters can be obtained from the scattering parameters by introducing the equations:

$$z = z' - jz'' = \left(\frac{\mu_r}{\varepsilon_r} \right)^{1/2} = \pm \left[\frac{(1 + S_{11})^2 - S_{21}^2}{(1 - S_{11})^2 - S_{21}^2} \right]^{1/2}, \quad (5.7)$$

$$n = n' - jn'' = (\mu_r \varepsilon_r)^{1/2} = \pm \frac{j\lambda_0}{2\pi d} \ln \left(\frac{1}{t} \right), \quad (5.8)$$

$$\varepsilon_r = \varepsilon' - j\varepsilon'' = \frac{n}{z}, \quad (5.9)$$

$$\mu_r = \mu' - j\mu'' = nz, \quad (5.10)$$

where the superscripts ' and '' indicate the real part and imaginary part, respectively. To solve the uncertainties due to the choice of the signs of the wave impedance and refractive index, I considered the passivity condition of the medium, i.e., $z' \geq 0$ and $n'' \geq 0$.

The previous expressions obtained in the case of a slab in a vacuum have been implemented in a Matlab code. Real and imaginary parts of the scattering coefficients, extracted by simulations with finite-element method, were then processed in Matlab to retrieve the electromagnetic parameters related to different types of absorbers. Since metamaterial absorbers are interposed between two layers of air of the same thickness l , the scattering parameters are strictly defined by the relationships of the multiple-reflection model:

$$S_{11} = R_1^2 \frac{\Gamma(1 - t^2)}{1 - \Gamma^2 t^2}, \quad (5.11)$$

$$S_{21} = R_1 R_2 \frac{t(1 - \Gamma^2)}{1 - \Gamma^2 t^2}, \quad (5.12)$$

in which $R_1 = R_2 = \exp(-jk_0 l)$ are the reference-plane transformation expressions and l is the distance from the reference planes to the sample.

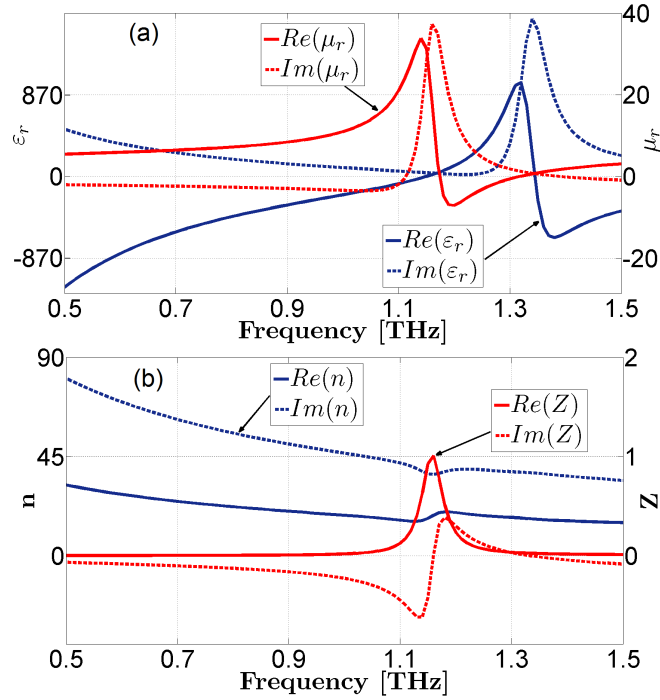


Figure 5.17: Real and imaginary parts of the (a) permittivity and permeability, and (b) refractive index and wave impedance of the narrow-band MMA.

The electromagnetic parameters extracted at normal incidence of the three different models of MMAs have exhibited a resonant behavior typical of the Lorentz oscillator response, as it can be seen from the real and imaginary parts of the

effective quantities of the proposed ultra-thin narrow-band MMA in Fig. 5.17.

These plots highlight how, in the case of thin dielectric layers, the relative effective permittivity assumes high values due to the presence of the ground plane that acts as a dielectric with a quasi-infinite permittivity. The absorbers, furthermore, reach a near-perfect impedance matching to free space. In fact, the real part of the relative impedance close to unity $Re(z) \cong 1$ and the minimized imaginary part $Im(z) \cong 0$ produce a reflection almost null at the frequencies of the absorption peaks. Therefore, dielectric and magnetic losses in the system expressed by the imaginary part of the refractive index produce considerable attenuation of the wave.

By means of the interference theory [32], the MMAs can be divided into two interfaces, respectively, tuned with the upper electric ring resonator and the lower ground plane, that interact through multiple reflections within the dielectric slab, that is, the interference theory considers the ERR array as a zero thickness, impedance tuned interface between free space and the dielectric layer. In fact, if I consider a metamaterial slab backed by a metal plate described as a perfect reflector with reflection coefficient -1 , I can apply the method of multiple reflections examining the model of the grounded slab:

$$\begin{aligned}
 S_{11} &= \Gamma - TT' \exp(-2jk'_z d) + R'TT' \exp(-4jk'_z d) - R'^2 TT' \exp(-6jk'_z d) + \dots \\
 &= \Gamma - TT' \exp(-2jk'_z d) \sum_{n=0}^{\infty} [-R' \exp(-2jk'_z d)]^n \\
 &= \Gamma - \frac{TT' \exp(-2jk'_z d)}{1 + R' \exp(-2jk'_z d)}, \tag{5.13}
 \end{aligned}$$

where Γ and R' , T and T' are the reflection and transmission coefficients at the air/spacer interface with the ERR array, impinging from the air (port 1) and the spacer (port 2) sides, respectively, as shown in Fig. 5.18.

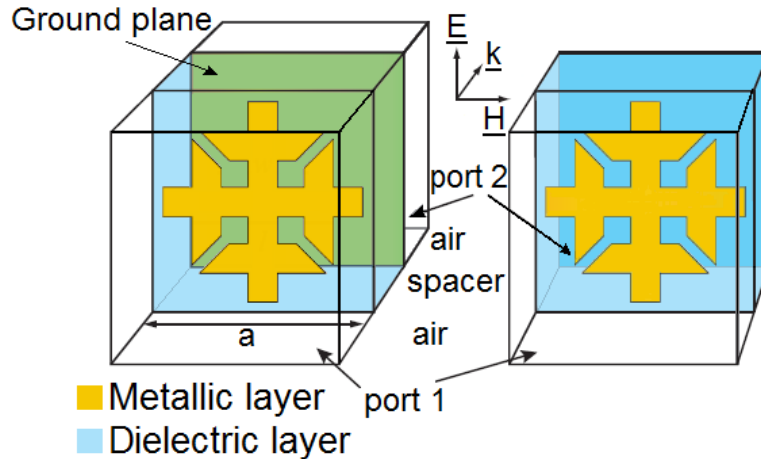


Figure 5.18: Metamaterial absorber with and without the ground plane.

In order to obtain these four reflection and transmission S-parameters, it is necessary to simulate the unit cell formed by the ERR located at a semi-infinite air/spacer interface, i.e., without the ground plane (decoupled-model). In this case, I have neglected the near-field coupling between the ERR array and the ground plane, that actually does not affect the resonance of the ERRs, unlike the case of the coupled-model where the possible near-field interactions and magnetic resonances have been taken into account through numerical simulations.

Figure 5.19 shows an apparent agreement between the theoretically calculated (decoupled model) and numerically simulated (coupled model) absorption spectra of the ultra-thin narrow-band, complementary narrow-band, and dual-band MMAs, validating the interference model.

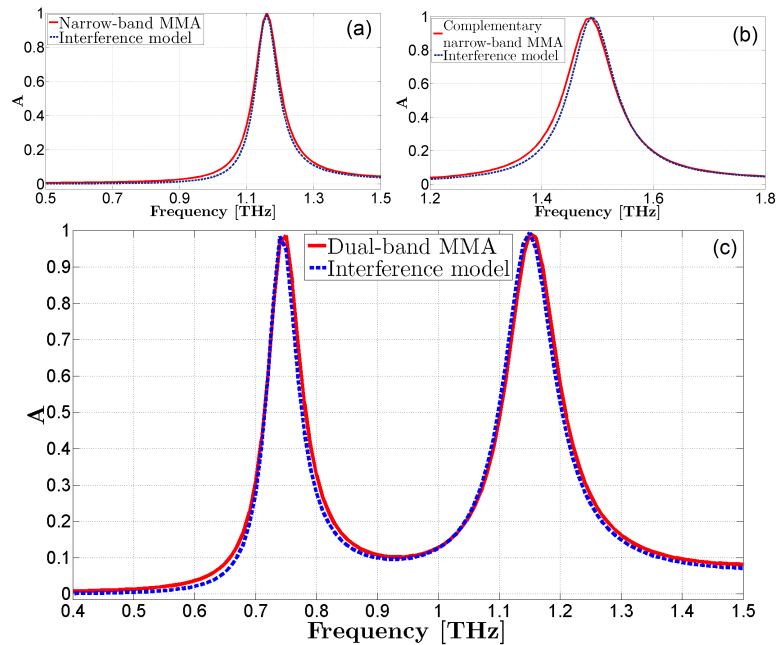


Figure 5.19: Simulated absorptions for the coupled and decoupled (a) narrow-band, (b) complementary narrow-band, and (c) dual-band metamaterial absorbers.

5.6 Conclusions

In this Chapter, I have analyzed and designed ultra-thin narrow-band, complementary narrow-band, and dual-band MMAs, i.e., compact absorbing devices for THz applications exploiting the same ERR configuration.

The unit cell of the narrow-band MMA is constituted by an ERR and a ground plane spaced by a dielectric layer. The resulting absorption spectrum shows a level of 99.13% at the resonance frequency of 1.15 THz (see Section 5.2).

In Section 5.3, an alternative model of narrow-band MMA with an absorption of 99.08% at the frequency of 1.49 THz was obtained metalizing the complementary of the ERR. It is noteworthy that, compared with the narrow-band absorber,

the resonance frequency undergoes a significant blueshift.

The dual-band MMA was designed by spacing an upper BCB dielectric layer between the ERR and the cross and a lower highly resistive silicon layer between the cross and the metallic plate, obtaining two remarkable absorption peaks higher than 98% at 0.75 THz and 1.15 THz, as described in Section 5.4.

In general, it was observed that as the incidence angle increases, the resonance frequencies remain unchanged for the TE polarization, showing, however, a monotonic decay of the absorption peaks, while the TM polarization presents a shift of the resonance frequencies and the appearance of additional absorption peaks.

The transmission-line model has been applied in the case of the narrow-band MMA, showing that the retrieved frequency response is shifted compared with the FEM analysis due to the ultra-thin thickness of the absorber. Therefore, in the TLM, it has been considered a capacitance that takes the z component of the electric field between the ERR array and the ground plane into account.

In Section 5.5, the homogenization technique has allowed to describe the ultra-thin MMAs as effective homogeneous media, whose electromagnetic properties can be controlled by modifying the geometric parameters of the structure. Through the implementation in a Matlab code of NRW algorithm, developed on the basis of the interference theory and multiple reflections, it was possible to extract the electromagnetic parameters of MMAs. Each unit cell of the proposed ultra-thin MMAs has exhibited a typical Lorentz oscillator response for the electric and magnetic fields separately. A specific analysis, developed on the interference theory and the grounded-slab model, has provided an actual correspondence with the simulated absorption spectra.

In conclusion, these ultra-thin MMAs have potential applications in, e.g., THz imaging and thermal detectors, and allow us to separately tune the electric and magnetic responses. By suitably adjusting the geometry of the ERR, it is possible to tune the position of the absorption frequency and the intensity of the Lorentz resonance. The metallic ERRs and the ground plane provide at the resonance frequency an adequate electric response due to the strong coupling with the incident electric field. Instead, varying the spacing between the metallic layers, the magnetic response can be changed. In fact, when the magnetic field component of a transverse electromagnetic wave (TEM) couples to the central sections of the metallizations perpendicular to the propagation vector, antiparallel currents are induced. Therefore, an incident time-varying magnetic field by coupling to the antiparallel currents can provide a Lorentz-like response as verified.

The results of the current analysis have been published in Refs. [1–3].

References

- [1] M. D. Astorino, F. Frezza, and N. Tedeschi, "Ultra-thin narrow-band, complementary narrow-band, and dual-band metamaterial absorbers for applications in the THz regime," *Journal of Applied Physics*, vol. 121, no. 6, p. 063103, 2017.
- [2] M. D. Astorino, F. Frezza, and N. Tedeschi, "Narrow-band and dual-band metamaterial absorbers in the THz regime," in *Electromagnetic Theory (EMTS), 2016 URSI International Symposium on*, pp. 34–37, IEEE, 2016.
- [3] M. D. Astorino and N. Tedeschi, "Design and analysis of an ultra-thin dual-band metamaterial absorber for THz applications," in *XXI Riunione Nazionale di Elettromagnetismo (RiNEm)*, 2016.
- [4] R. L. Fante and M. T. McCormack, "Reflection properties of the Salisbury screen," *IEEE Transactions on Antennas and Propagation*, vol. 36, pp. 1443–1454, October 1988.
- [5] E. F. Knott and C. D. Lunden, "The two-sheet capacitive Jaumann absorber," *IEEE Transactions on Antennas and Propagation*, vol. 43, pp. 1339–1343, 1995.
- [6] C. A. Kyriazidou, R. E. Diaz, and N. G. Alexopoulos, "Novel material with narrow-band transparency window in the bulk," *IEEE Transactions on Antennas and Propagation*, vol. 48, pp. 107–116, January 2000.
- [7] L. Qi, C. Li, and G. Fang, "Tunable terahertz metamaterial absorbers using active diodes," *International Journal of Electromagnetics and Applications*, vol. 4, no. 3, pp. 57–60, 2014.
- [8] F. Zhang, S. Feng, K. Qiu, Z. Liu, Y. Fan, W. Zhang, Q. Zhao, and J. Zhou, "Mechanically stretchable and tunable metamaterial absorber," *Applied Physics Letters*, vol. 106, p. 091907, March 2015.
- [9] C. Wu, B. Neuner, J. John, A. Milder, B. Zollars, S. Savoy, and G. Shvets, "Metamaterial-based integrated plasmonic absorber/emitter for solar thermophotovoltaic systems," *J. Opt.*, vol. 14, p. 024005, January 2012.
- [10] S. Savo, D. Shrekenhamer, and W. J. Padilla, "Liquid crystal metamaterial absorber spatial light modulator for THz applications," *Advanced Optical Materials*, vol. 2, pp. 275–279, 2014.
- [11] C. M. Watts, X. Liu, and W. J. Padilla, "Metamaterial electromagnetic wave absorbers," *Advanced Optical Materials*, vol. 24, pp. 98–120, June 2012.
- [12] K. Du, Q. Li, W. Zhang, Y. Yang, and M. Qiu, "Wavelength and thermal distribution selectable microbolometers based on metamaterial absorbers," *IEEE Photonics Journal*, vol. 7, p. 2406763, June 2015.
- [13] N. I. Landy, C. M. Bingham, T. Tyler, N. Jokerst, D. R. Smith, and W. J. Padilla, "Design, theory, and measurement of a polarization-insensitive absorber for terahertz imaging," *Phys. Rev. B*, vol. 79, no. 12, p. 125104, 2009.
- [14] A. Kazemzadeh and A. Karlsson, "On the absorption mechanism of ultra thin absorbers," *IEEE Transactions on Antennas and Propagation*, vol. 58, pp. 3310–3315, October 2010.
- [15] F. Costa, S. Genovesi, A. Monorchio, and G. Manara, "A circuit-based model for the interpretation of perfect metamaterial absorbers," *IEEE Transactions on Antennas and Propagation*, vol. 61, pp. 1201–1209, March 2013.
- [16] A. Vallecchi, R. J. Langley, and A. G. Schuchinsky, "Metasurfaces with interleaved conductors: Phenomenology and applications to frequency selective and high impedance surfaces," *IEEE Transactions on Antennas and Propagation*, vol. 64, pp. 599–608, February 2016.
- [17] N. Tedeschi, F. Frezza, and A. Sihvola, "Reflection and transmission at the interface with an electric–magnetic uniaxial medium with applications to boundary conditions," *IEEE Transactions on Antennas and Propagation*, vol. 61, pp. 5666–5675, November 2013.
- [18] M. Khalid, N. Tedeschi, and F. Frezza, "On a lossy electric–magnetic uniaxial medium and its applications to boundary conditions," *IEEE Transactions on Antennas and Propagation*, vol. 63, pp. 1686–1692, April 2015.

-
- [19] F. Hu, L. Wang, B. Quan, X. Xu, Z. Li, Z. Wu, and X. Pan, "Design of a polarization insensitive multiband terahertz metamaterial absorber," *Journal of Physics D: Applied Physics*, vol. 46, no. 19, p. 195103, 2013.
- [20] C. Gu, S. B. Qu, Z. B. Pei, Z. Xu, J. Liu, and W. Gu, "Multiband terahertz metamaterial absorber," *Chinese Physical B*, vol. 20, no. 1, p. 017801, 2011.
- [21] Q. Y. Wen, H. W. Zhang, Y. S. Xie, Q. H. Yang, and Y. L. Liu, "Dual band terahertz metamaterial absorber: Design, fabrication, and characterization," *Applied Physics Letters*, vol. 95, p. 241111, 2009.
- [22] M. H. Li, H. L. Yang, and X. W. Hou, "Perfect metamaterial absorber with dual bands," *Progress in Electromagnetics Research*, vol. 108, pp. 37–49, 2010.
- [23] H. Tao, C. M. Bingham, D. Pilon, K. Fan, A. C. Strikwerda, D. Shrekenhamer, W. J. Padilla, X. Zhang, and R. D. Averitt, "A dual band terahertz metamaterial absorber," *Journal of Physics D: Applied Physics*, vol. 43, p. 225102, 2010.
- [24] Y. Ma, Q. Chen, J. Grant, S. C. Saha, A. Khalid, and D. R. S. Cumming, "A terahertz polarization insensitive dual band metamaterial absorber," *Optics Letters*, vol. 36, pp. 945–947, March 2011.
- [25] A. M. Nicolson and G. F. Ross, "Measurements of the intrinsic properties of materials by time-domain techniques," *IEEE Transactions on Instrumentation and Measurement*, vol. 19, pp. 377–382, November 1970.
- [26] W. B. Weir, "Automatic measurement of complex dielectric constant and permeability at microwave frequencies," *Proceedings of the IEEE*, vol. 62, pp. 33–36, January 1974.
- [27] K. Chalapat, K. Sarvala, J. Li, and G. S. Paraoanu, "Wideband reference-plane invariant method for measuring electromagnetic parameters of materials," *IEEE Transactions on Microwave Theory and Techniques*, vol. 57, no. 9, pp. 2257–2267, 2009.
- [28] O. Luukkonen, S. I. Maslovski, and S. A. Tretyakov, "A stepwise Nicolson-Ross-Weir-based material parameter extraction method," *IEEE Antennas and Wireless Propagation Letters*, vol. 10, pp. 1295–1298, 2011.
- [29] D. R. Smith, S. Schultz, P. Markos, and C. M. Soukoulis, "Determination of negative permittivity and permeability of metamaterials from reflection and transmission coefficients," *Physical Review B*, vol. 65, p. 195104, 2002.
- [30] D. R. Smith, D. C. Vier, T. Koschny, and C. M. Soukoulis, "Electromagnetic parameter retrieval from inhomogeneous metamaterials," *Physical Review E*, vol. 71, p. 036617, 2005.
- [31] X. Chen, T. M. Grzegorzczuk, B. I. Wu, J. Pacheco, and J. A. Kong, "Robust method to retrieve the constitutive effective parameters of metamaterials," *Physical Review E*, vol. 70, p. 016608, 2004.
- [32] H. T. Chen, "Interference theory of metamaterial perfect absorbers," *Opt. Express*, vol. 20, no. 7, pp. 7165–7172, 2012.

Broad-band terahertz metamaterial absorber with stacked electric ring resonators

In this Chapter, I have devised an ultra-thin broad-band metamaterial absorber composed of a periodic array of three-layered Electric Ring Resonators (ERRs) within a dielectric spacer and backed by a metallic ground plane for THz applications. The overlapping of the resonance peaks relevant to the ERRs leads to a broad spectral absorption bandwidth over a wide range of incidence angles under both Transverse Electric (TE) and Transverse Magnetic (TM) polarizations. I have analyzed the effect of different physical properties on the absorption spectra in order to estimate the dielectric and Ohmic losses in the metamaterial structure. In addition, the Nicolson, Ross, and Weir (NRW) algorithm is adopted as homogenization technique to retrieve the effective electromagnetic parameters, while the interference theory is employed to compare the simulated and analytical results for the multi-layered absorber.

The contents of this Chapter have been published in Ref. [1].

6.1 Introduction

Many advanced applications, e.g., thermal detectors, microbolometers and photovoltaic cells, require perfect wide-angle and polarization-insensitive absorption on broad spectral bands [2–4]. Nevertheless, in the terahertz frequency regime, materials with high absorption characteristics are particularly rare.

Broad-band metamaterial absorbers, working over a wide band of frequencies [5–7], result more versatile and needful in some particular technologies compared to resonant absorbers which exploit the interaction of the material with the incident radiation at the desired frequency. These broad-band absorbing structures, having the ability to filter out unwanted frequencies, are mostly employed to reduce electromagnetic interference.

Recently sophisticated design techniques have been developed by integrating more unit cells impedance-matched to free space at multiple frequencies [8]. Changing the geometric dimensions of the resonant elements, different resonance frequencies are obtained through multi-resonant coplanar structures [9, 10]. The various resonators, assembled with this process in a unit cell, can achieve multiple resonances in the absorption spectrum. To develop broad-band absorbers, it is necessary that the peaks are overlapped in frequency, while if the peaks are distant from one another multiple-band absorbers are obtained [11, 12]. However, a possible coupling between the resonators can affect the resonance frequency, determining a total shift with respect to the resonances of the individual structures.

These construction techniques have problems in the design strategy, related to the largest size of the unit cell, as well as difficulty in the manufacture, especially at higher frequencies such as terahertz, infrared, and visible spectrum. Therefore, to design a broad-band absorber it is necessary to conceive compact metamaterial structures that involve a reduction in both the number of stacked layers and the size of the unit cell [13].

For these purposes, in Section 6.2, the design of an ultra-thin broad-band metamaterial absorber is proposed at normal and oblique incidence for both transverse electric and transverse magnetic polarizations with an impedance gradient in the THz spectral range. In Section 6.3, the Nicolson, Ross, and Weir (NRW) retrieval procedure [14, 15] is applied for extracting the effective electromagnetic parameters and the interference theory is employed for validating the simulated results. Finally, in Section 6.4, the conclusions are drawn.

6.2 Ultra-thin broad-band metamaterial absorber

6.2.1 Design and analysis at normal incidence

In this section, I have dealt with the analysis of an ultra-thin broad-band metamaterial absorber (see Fig. 6.1), which exploits a particular ERR pattern, based on the model of the Split Ring Resonator (SRR) and the geometry suggested in Ref. [16], with a fourfold rotational symmetry around the stratification direction z .

The structure has been obtained by superimposing, above the metallic ground plane, three ERRs, made of lossy gold with 270 nm thickness, suitably spaced out and embedded within a dielectric layer of benzocyclobutane (BCB) with relative permittivity $\varepsilon_r = 2.5$ and dielectric loss tangent $\tan\delta = 0.005$.

The total thickness of the absorbing structure is equal to $\lambda_0/19$ at the center frequency of the absorption bandwidth, where λ_0 is the free-space wavelength. This multi-layer configuration was inspired by pyramidal absorbers which possess an intrinsic broad-band behavior and are mostly used in anechoic chambers [17].

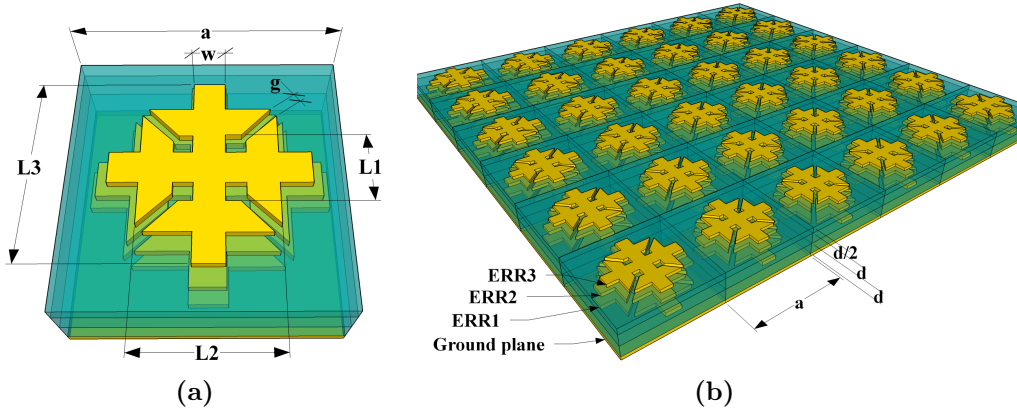


Figure 6.1: (a) Geometry of the single unit cell and (b) 3D sketch of the ultra-thin broad-band metamaterial absorber.

In order to simulate an infinite array of broad-band absorbers, I have applied two-dimensional Floquet periodic boundary conditions for both x and y directions of a single unit cell through a commercial Finite-Element Method (FEM) solver. I have considered the case of a normally incident electromagnetic plane wave on the metamaterial absorber in the xz incident plane with the azimuthal angle $\varphi = 0^\circ$ (where φ is the angle between the projection of incident wave vector on xy plane and x direction).

The dimensions of the three gradually scaled ERRs given in Table 6.1, determine, at normal incidence (the electric field is along the y direction), three resonance frequencies at 0.95, 1.01, and 1.11 THz, respectively, with an absorption of 95.94, 96.08, and 92.00% as shown in Fig. 6.2. The overlapping of the adjacent anti-reflection peaks generates, thereby, a considerable widening of the absorption bandwidth.

Table 6.1: Dimensions (in microns) of the ultra-thin broad-band metamaterial absorber with $a = 84$, $g = 4$, $w = 11$, and $d = 5.8$.

Parameter	ERR1	ERR2	ERR3
L_1	30	28	26
L_2	52	50	48
L_3	74	72	70

The absorption is calculated as $A(\omega) = 1 - R(\omega) - T(\omega) = 1 - |S_{11}|^2 - |S_{21}|^2$, where $R(\omega) = |S_{11}|^2$ is the reflection and $T(\omega) = |S_{21}|^2 = 0$ is the zero transmission due to the presence of the metallic ground plane thicker than the penetration depth of the THz wave.

I have compared, in Fig. 6.2, the absorption spectra of the ultra-thin broad-band metamaterial absorber of different unit-cell size ($a = 80 \mu\text{m}$ and $a = 84$

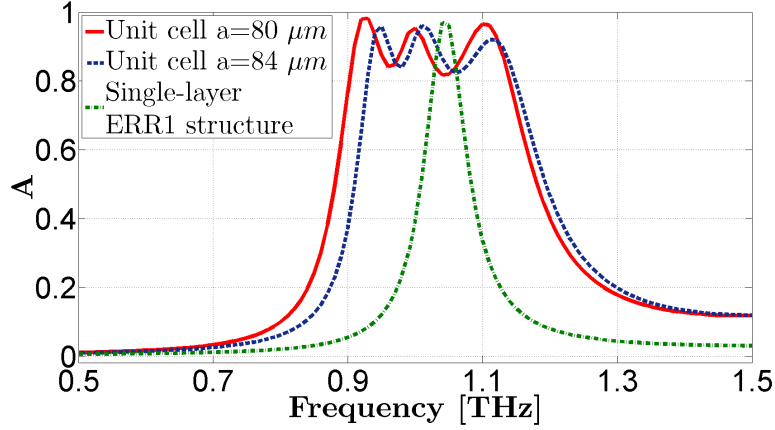


Figure 6.2: Comparison between broad-band metamaterial absorber with $a = 80$ and $84 \mu\text{m}$, respectively, and narrow-band absorber with single-layer ERR1 structure.

μm) with a single-layer structure constituted by the ERR1 on a grounded BCB slab of thickness $d = 5.8 \mu\text{m}$ and lattice constant $a = 84 \mu\text{m}$. It is evident that the absorption bandwidth of the single-layer model is very narrow with a relative Full Width at Half-Maximum (FWHM) absorption bandwidth (the ratio of FWHM, namely the 3 dB linewidth, to the center frequency) approximately equal to 6.73%, and the resonant frequency depends on the size of the structure. Exploiting the coupling between the three ERRs, I was able to enhance the absorption bandwidth from the narrow-band of the single-layer structure to the broad-band of the three-layer structure: the broad-band absorber with $a = 84 \mu\text{m}$ highlights an absorption bandwidth of approximately 291.1 GHz with a relative FWHM absorption bandwidth close to 27.50%. The comparison, in Fig. 6.2, with the unit cell of reduced dimension $a = 80 \mu\text{m}$ allows to better observe the influence of geometric parameters of the structure on the electromagnetic response. The broad-band absorber with $a = 80 \mu\text{m}$ denotes, indeed, an enlarged relative FWHM absorption bandwidth equal to 29.13%, which is more than four times larger than that of the one-layer absorber. It can be observed how the overlapping of the three absorption peaks of 98.20, 95.39, and 96.54%, respectively, at the frequencies of 0.93, 1.00, and 1.10 THz generates a widening of the absorption band close to 302.3 GHz.

In Fig. 6.3, I have shown the distributions of the z component of the electric field on the three ERRs and the ground plane at the frequencies 0.93, 1.00, and 1.10 THz with a lattice constant $a = 80 \mu\text{m}$. The electric-field z component is due to the higher-order evanescent Floquet modes that are no more negligible in the case of ultra-thin metamaterial absorbers [18].

As represented in Fig. 6.3(a), at 0.93 THz, charges of opposite signs accumulate at the ends of the ERR1, determining an electric-dipole resonance. The latter is strongly coupled with its own image, which oscillates in anti-phase on the lower

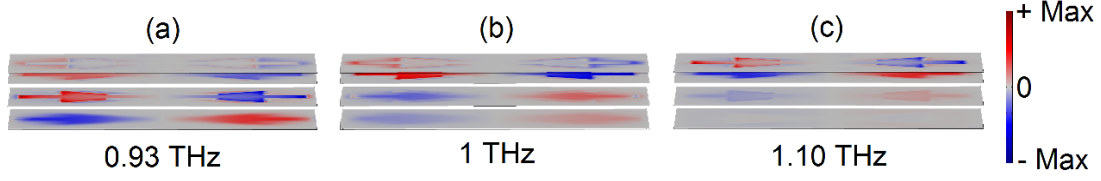


Figure 6.3: Distributions of the electric-field z component on the ERRs and the ground plane at the three resonance frequencies of (a) 0.93 THz, (b) 1 THz, and (c) 1.10 THz with $a = 80 \mu\text{m}$.

metallic plate, while only small magnetic resonances can be observed in the ERR2 and ERR3 at this frequency. At 1 THz, the resonance frequency of the second peak (see Fig. 6.3(b)), two electric dipoles oscillating in anti-phase are induced on the ERR1 and ERR2, respectively, with a weak magnetic resonance in the ERR3, while at 1.10 THz as Fig. 6.3(c) shows, the coupling is between the ERR2 and ERR3 being the resonant frequency of the absorber determined by the length of the ERR. Consequently, this ultra-thin broad-band metamaterial absorber can be regarded as a hybridization system, in which the magnetic resonances of the ERR2 and ERR3, strongly depending on the separation distance, contribute to the blueshift of the absorption frequency and, therefore, to the broadening of the bandwidth. In fact, at a certain frequency, the electromagnetic field is resonantly localized and then absorbed at some part of the multi-layer structure. In particular, at the lower frequency, the electromagnetic field is localized at the bottom ERR1, while as the frequency increases, it is localized at the upper ERR2 and ERR3 which, having smaller dimensions, resonate at higher frequencies.

A smoother absorption spectrum was, instead, obtained covering the stacked ERRs with a further BCB layer with $1.45 \mu\text{m}$ thickness as shown in Fig. 6.4(a). The achieved broad-band metamaterial absorber is still ultra-thin with a total thickness nearly equal to $\lambda_0/18$ with respect to the central frequency and with a wide absorption bandwidth of 253.2 GHz due to the overlapping of the three resonant peaks of 99.58, 98.55, and 99.79% at the frequencies of 0.94, 1.00, and 1.05 THz, respectively (see Fig. 6.4(b)).

In order to provide a further interpretation of the absorption mechanism, I have adopted the Transmission-Line Model (TLM) of the unit cell as described in Fig. 6.5. The three ERRs are modeled with three parallel RLC circuits, in which $R^{(1)}$, $R^{(2)}$, $R^{(3)}$ represent the Ohmic resistances, $L^{(1)}$, $L^{(2)}$, $L^{(3)}$ the equivalent inductances, and $C^{(1)}$, $C^{(2)}$, $C^{(3)}$ the equivalent capacitances of the ERR1, ERR2, and ERR3, respectively. In particular, the inductance of each ERR can be approximated through $L^{(n)} \approx \mu_0 L_3^{(n)} d/w$, while the capacitance can be defined by $C^{(n)} \approx \varepsilon_0 L_3^{(n)} w/d$, where n represents the ERRs, d is the thickness of the BCB dielectric slab, w is the width of the ERR, and L_3 is the outer side

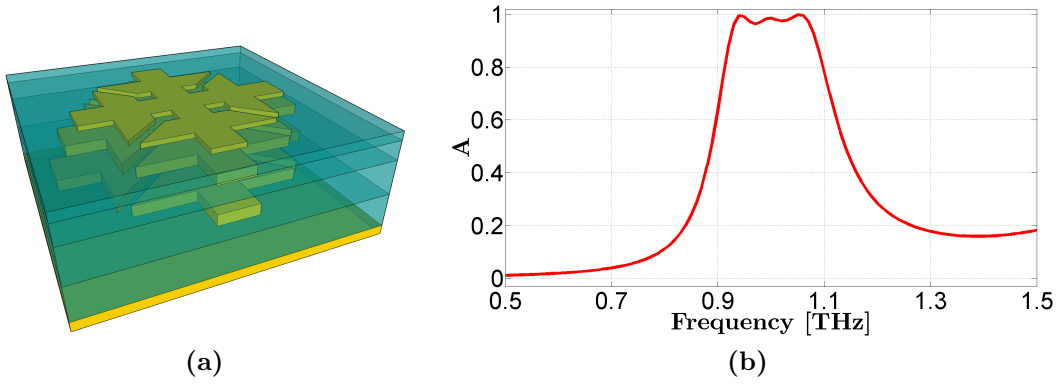


Figure 6.4: (a) Single unit cell of the broad-band metamaterial absorber with $a = 84 \mu\text{m}$ and upper BCB layer, and (b) the relevant absorbance spectrum.

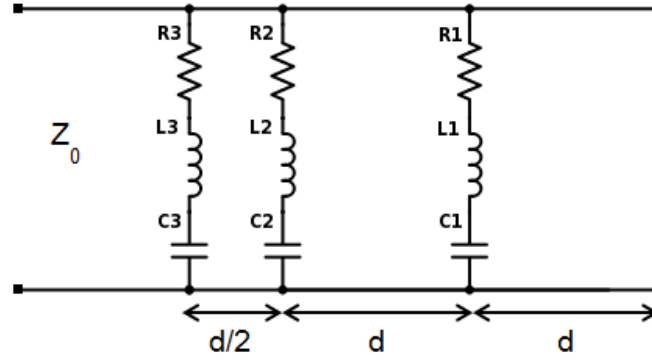


Figure 6.5: Transmission line model of the ultra-thin broad-band metamaterial absorber.

length of the ERR. The resonant frequency of each ERR is given by:

$$f_n \approx \frac{1}{2\pi\sqrt{L^{(n)}C^{(n)}/2}} \approx \frac{1}{\pi L_3^{(n)}\sqrt{2\mu_0\varepsilon_0}} \quad n = 1, 2, 3. \quad (6.1)$$

Therefore, the bandwidth can be widened by varying the outer length L_3 of the three ERRs, being the resonant frequency f_n an approximately linear function of $1/L_3^{(n)}$ as shown in Fig. 6.6 for the case of the narrow-band single-layer model. Moreover, the resonant frequency depends on the ultra-thin separation distance between the resonators that produces the higher-order Floquet modes not taken into account in the proposed zeroth-order TLM where, at normal incidence, the propagating mode is transverse electromagnetic (TEM) without z -directed electric field component. However, this simplified model is capable of keeping an easy relation between the geometric parameters and the electromagnetic behavior of the structures with the advantage of an initial, even if coarse, estimate, despite it neglects the effect of the interactions.

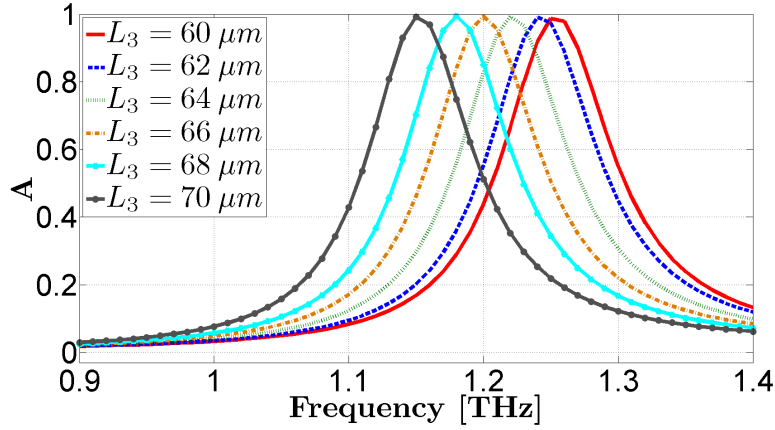


Figure 6.6: Absorption spectra for different values of the outer side length L_3 of the single-layer model.

6.2.2 Analysis at oblique incidence for TE and TM polarizations

In order to investigate the polarization behavior of the ultra-thin broad-band metamaterial absorber, the structure has been tested at oblique incidence through a parametric sweep on the incidence angle θ (i.e., the angle between the wave vector and the surface normal of the absorber as depicted in the insets of Fig. 6.7) from 0° to 80° with steps of 20° and the azimuthal angle $\varphi = 0^\circ$.

By performing the simulation of the broad-band metamaterial absorber for TE polarization in which the electric field is fixed along the y direction, it is apparent in Fig. 6.7(a) that the absorption bandwidth becomes narrower when increasing the incidence angle θ . Besides, the first two absorption peaks are considerably reduced, while the third peak maintains high absorption levels at least for angles below 60° . In the case of 80° incidence, in fact, I detected a substantial reduction of the three absorption peaks of 44.12, 38.05, and 67.69%, respectively, at the frequencies of 0.94, 1.01, and 1.12 THz: such peaks remain substantially at the same frequencies of the normal incidence. The decrease of absorption levels with the increase of the angle of incidence occurs because the x component of the incident magnetic field decreases rapidly to zero and can no longer efficiently induce antiparallel currents on the metallizations, thus implying a reduction of the magnetic flux. In fact, a wide angular absorption for TE polarization is difficult to obtain, because the TE free space impedance increases as the incident angle θ increases, being $Z_0^{TE} = Z_0/\cos\theta$, where Z_0 is the free-space impedance. Therefore, the almost angle-independent input impedance of the metamaterial absorber is no more matched to the angle-dependent free space impedance Z_0^{TE} as θ varies [19]. This behavior prevents from obtaining a wide angular absorption for TE polarization, as shown in Fig. 6.7(a).

For TM polarization in which the magnetic field is fixed along the y direction, one can observe in Fig. 6.7(b) both a blueshift and a progressive broadening

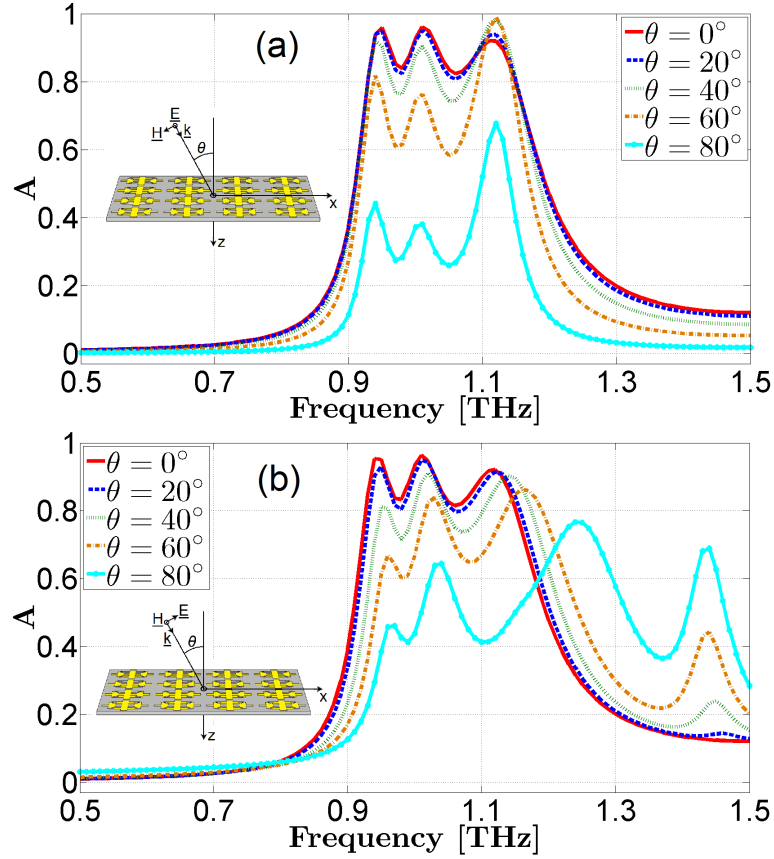


Figure 6.7: Absorption spectra at different incidence angles for (a) TE and (b) TM polarizations depicted in the insets for broad-band metamaterial absorber.

of the absorption band as the angle of incidence increases. Moreover, it is to underline the appearance of a fourth absorption peak at the frequency of 1.44 THz that for the angle of 80° takes a considerable absorption level of 68.89%. This further resonance frequency is probably due to the particular ratio between the wavelength and the geometric dimensions of the ERRs at 1.44 THz: in fact, I have observed a similar behavior for the analyzed device in Ref. [19].

In this case, the magnetic field remaining parallel to the air/metamaterial interface can drive resonant currents on the metallic layers for the various incidence angles, showing higher absorption levels compared with the TE polarization. This condition allows keeping the matching to free-space impedance which decreases as the incident angle increases ($Z_0^{TM} = Z_0 \cos\theta$), determining a wide angular response, because the real part of the input impedance of the absorber is proportional to the square of the imaginary part of the grounded slab impedance which has the same dependence on θ as Z_0^{TM} [19].

In particular, in TM polarization, a blueshift of the absorption peaks with increasing incidence angle is observed, unlike the case of TE polarization for which the resonance frequencies remain virtually unchanged. Considering the normal

incidence with the electric field along the x axis and the magnetic field along the y axis, the electric dipoles of the three ERRs in each unit cell oscillate in phase compared with the adjacent ERRs. Therefore, due to the interaction between the adjacent unit cells, the attractive force between the positive and negative charges of the neighboring ERRs along the x direction weakens the restoring force (strongly related to the resonance frequency) of the charge oscillation inside each ERR. As the incident angle θ increases in TM polarization, a shift towards higher frequencies of the resonant peaks appears due to the reduction of the attractive force, i.e., the reduction of the tangential component of the electric field, between the adjacent unit cells, being the dipole oscillation of the adjacent ERRs in the x direction no longer in phase, because the interface of the absorber no longer coincides with the constant-phase planes of the wave. The smaller is the attractive force between the adjacent cells, the larger is the restoring force of each unit cell, and consequently the larger is the resonance frequency.

The performances of the proposed broad-band metamaterial absorbers could be compared with the ones in Ref. [20], in which a terahertz metamaterial absorber has been presented, with a broad and flat absorption top over a wide incidence angle range for either TE or TM polarization depending on the incident direction. The metamaterial absorber unit cell of $78 \mu\text{m}$ in Ref. [20] consists of three I-shaped resonators separated from a ground plane using a dielectric spacer, resonating at different but close frequencies. This metamaterial device presents an FWHM of about 17.61% compared to the center frequency of 0.93 THz. Our devices present, instead, an enlarged relative FWHM absorption bandwidth equal to 29.13% in the case of broad-band metamaterial absorber with unit cell dimension $a=80 \mu\text{m}$ and equal to 25.32% for the metamaterial absorber covered with a further BCB layer and a smoother absorption top, respectively, as it can be seen in Fig. 6.8. The proposed broad-band metamaterial absorbers optimize, therefore, the FWHM absorption bandwidth compared to the center resonance frequency of the metamaterial device in Ref. [20]. Moreover, our broad-band metamaterial absorber, having a four-fold rotational symmetry about the propagation axis, exhibits, as shown in Fig. 6.7, a broad spectral absorption bandwidth over a wide range of incidence angles under both TE and TM polarizations and is, therefore, polarization insensitive, while the particular I-shaped configuration of the absorber in Ref. [20] is more influenced by the polarization of the incident field, not being the resonator rotationally symmetric around the propagation direction.

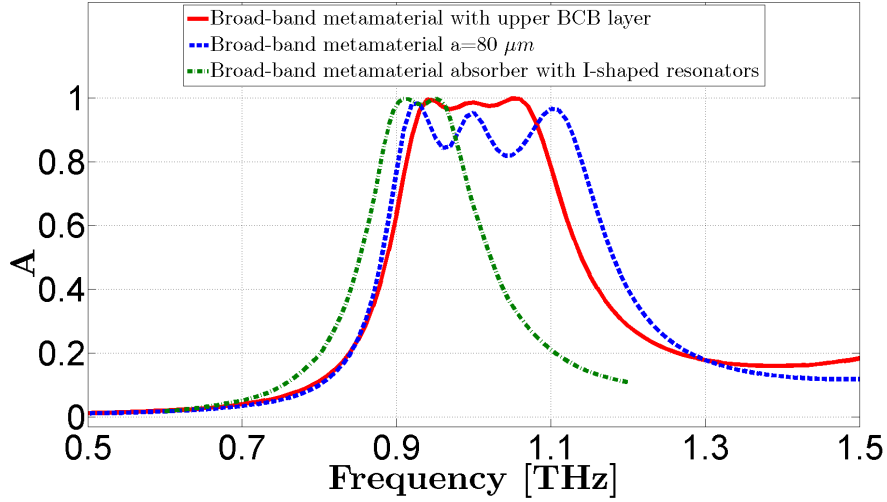


Figure 6.8: Comparison between the proposed broad-band metamaterial absorbers and the device in Ref. [20].

6.2.3 Absorption mechanism: dielectric and Ohmic losses

To further inquire into the causes of the absorption mechanism, the physical properties of the absorbing device have been gradually modified. This allows an evaluation of the dielectric and Ohmic losses which occur in the absorber.

Figure 6.9(a) represents the absorption spectra for growing values of the electric conductivity σ , showing both a narrowing of the bandwidth and a decay of the absorption levels, especially for the third peak in the Perfect Electric Conductor (PEC) case.

In Fig. 6.9(b), an analogous study has been conducted as the loss tangent $\tan \delta$ increases from 0 (lossless dielectric) to 1, giving rise to a smoother and wider absorption band. From this analysis, it is evident that the absorption is mainly due to the Ohmic losses of the ERRs and the metallic ground plane.

Finally, the absorption behavior has been investigated when increasing the relative electric permittivity ϵ_r of the dielectric spacer from 2.5 to 8.5. One can observe in Fig. 6.9(c) that the spectra undergo a marked redshift and further resonance peaks appear at higher frequencies. It is to point out how the third peak maintains a nearly perfect absorption, depending strongly on changes of the electric conductivity, while the other two peaks can be tuned by varying the electric permittivity.

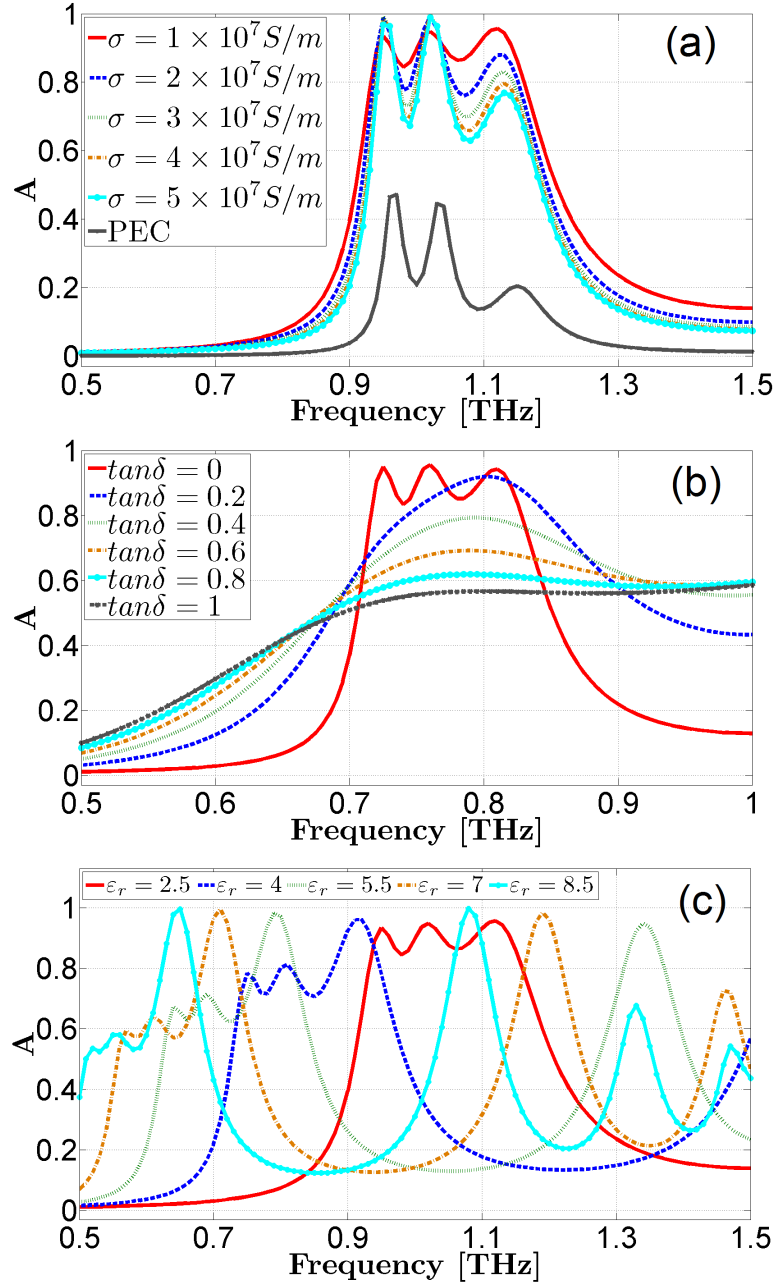


Figure 6.9: Absorption spectra when increasing (a) electric conductivity, (b) loss tangent, and (c) electric permittivity for broad-band metamaterial absorber.

6.3 Effective-medium theory and interference theory

6.3.1 Retrieval of the effective electromagnetic parameters

In order to characterize the ultra-thin broad-band metamaterial absorber, I adopted a retrieval procedure based on the NRW algorithm [14, 15], supposing a plane wave normally incident on the metamaterial composite slab.

This approach of computing the effective complex electromagnetic quantities from the S-parameters is a typical non-resonant technique which allows a broad-

band characterization of the metamaterial device under investigation.

In Figs. 6.10-6.11, the relative electric permittivity $\varepsilon_r = \varepsilon' - i\varepsilon''$, magnetic permeability $\mu_r = \mu' - i\mu''$, wave impedance $z = z' - iz'' = (\mu_r/\varepsilon_r)^{1/2}$, and refractive index $n = n' - in'' = (\mu_r\varepsilon_r)^{1/2}$ values are derived from the transmission and reflection scattering parameters obtained by simulations, implementing the following relations in a Matlab code:

$$z = \pm \left[\frac{(1 + S_{11})^2 - S_{21}^2}{(1 - S_{11})^2 - S_{21}^2} \right]^{1/2}, \quad (6.2)$$

$$n = \pm \frac{i}{k_0 d_t} \ln \left(\frac{1}{t} \right) = \pm \frac{i\lambda_0}{2\pi d_t} \ln \left(\frac{1}{t} \right), \quad (6.3)$$

$$\varepsilon_r = n/z, \quad (6.4)$$

$$\mu_r = nz, \quad (6.5)$$

where $k_0 = \omega(\mu_0\varepsilon_0)^{1/2}$ is the free space wave number, d_t is the total thickness of the metamaterial absorber, $t = \exp(-ik'_z d_t)$ is the propagation factor between the faces of the absorber, k'_z is the component of propagation vector along the propagation direction z in the slab, and the prime and double prime superscripts indicate the real part and imaginary part operators, respectively.

The uncertainties due to the choice of the signs of the wave impedance and refractive index are solved considering the passivity condition of the medium:

$$z' \geq 0, \quad (6.6)$$

$$n'' \geq 0. \quad (6.7)$$

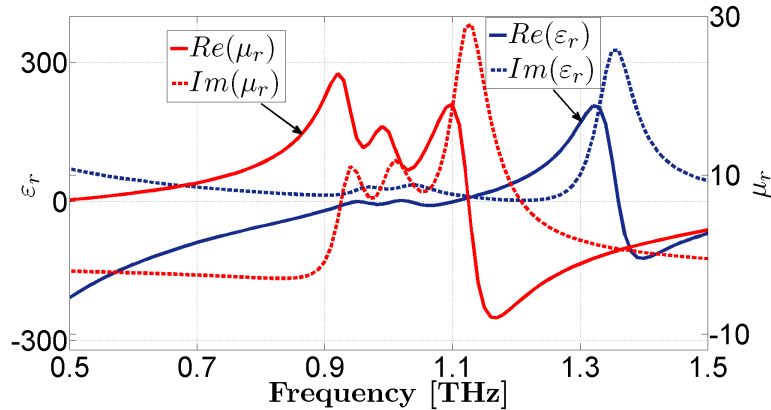


Figure 6.10: Real and imaginary parts of the permittivity and permeability of broad-band metamaterial absorber.

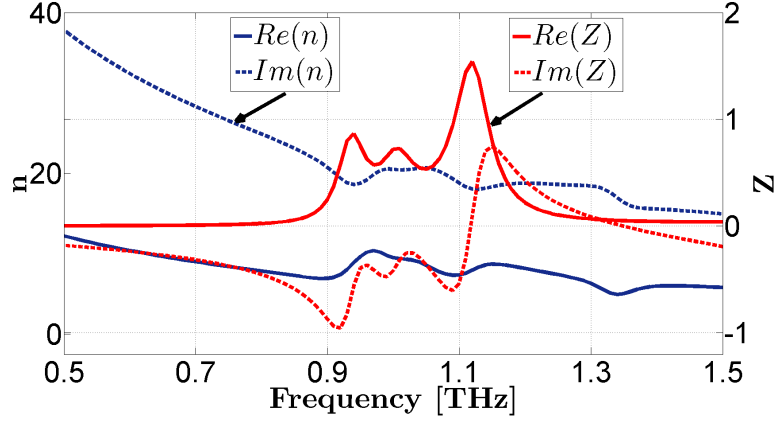


Figure 6.11: Real and imaginary parts of the refractive index and wave impedance of broad-band metamaterial absorber.

From the plots, one can observe how the relative effective permittivity reaches high values. This behavior is mainly due to the ultra-thin thickness of the absorbing device, the metallic ground plane acting as a dielectric with a quasi-infinite permittivity. Besides, the absorber results nearly perfectly impedance-matched to free space, in fact, the real part of the normalized impedance z relevant to the resonances of the three ERRs is close to 1, while the imaginary part is close to zero.

6.3.2 Grounded-slab model

The high absorption of this metamaterial structure has its origins in the destructive interference of the incident and reflected waves at the air/metamaterial interface. The metallic plate behaves as an electromagnetic mirror without transmission that reflects back all the incident radiation and gives a phase shift of π for the reflection. Therefore, adopting the interference theory [21] which assumes negligible the near-field coupling between the ERR array and the ground plane, the broad-band metamaterial absorber can be regarded as a grounded slab. In particular, I considered the two metallic layers, the ERR3 and the ground plane, as zero-thickness impedance-tuned surfaces that form a resonant cavity where the incident electromagnetic wave is dissipated, integrating the resonant effect of the ERR1 and ERR2 through the multiple reflections in the dielectric spacer.

For this purpose, I analyzed the decoupled system, simulating the unit cell of the absorber without the metallic ground plane and reconstructing the absorption spectrum of the overall device with the relation:

$$\Gamma = R - \frac{TT' \exp(-2ik'_z d_t)}{1 + R' \exp(-2ik'_z d_t)}, \quad (6.8)$$

where R and T represent the Fresnel reflection and transmission coefficients at

the air/metamaterial interface, and R' and T' are the reflection and transmission coefficients at the metamaterial/air interface, respectively. In this case, two different simulations are, indeed, necessary to extract the four S-parameters S_{11} , S_{21} , S_{22} and S_{12} and to verify the applicability of Eq. (6.8) to a multi-layered structure as the designed broad-band metamaterial absorber. In Fig. 6.12, the comparison between the coupled (numerically simulated) and decoupled (theoretically calculated) systems shows a good agreement validating the interference model.

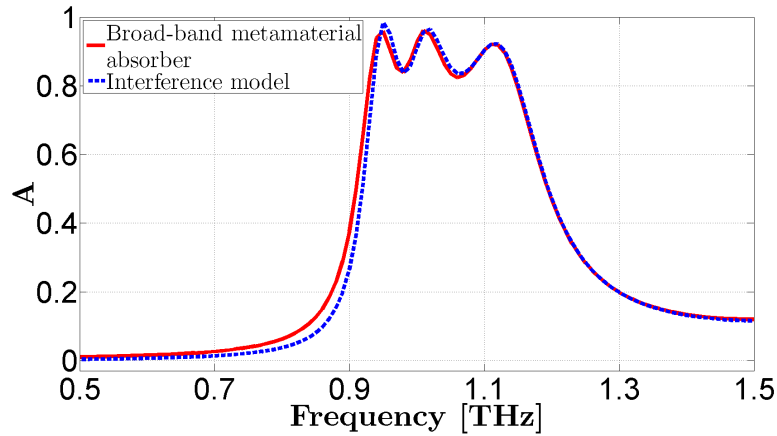


Figure 6.12: Simulated absorptions for the coupled and decoupled broad-band metamaterial absorber.

6.4 Conclusions

In this Chapter (see Section 6.2), I have analyzed and designed a THz broad-band metamaterial absorber with a thickness of $\lambda_0/19$, consisting of three ERRs appropriately scaled and spaced in a dielectric. This stratified ultra-thin structure backed with a metal plate has achieved high absorption levels for both TE and TM polarizations, showing a significant widening of the spectral bandwidth above 300 GHz.

Through a parametric analysis on the physical properties of the materials, the absorption mechanism has been investigated, showing the prevalence of the Ohmic losses and the dependence of the resonance frequency range on the permittivity of the dielectric spacer.

In Section 6.3, a retrieval non-resonant procedure, based on the NRW algorithm, has been introduced to extract the effective complex electromagnetic parameters which can be controlled independently by varying the dimensions of the ERRs and the distance between the metallic layers. Finally, the simulation of the decoupled system has allowed validating the grounded-slab model exploiting the interference theory even for this compact multi-layer structure.

The results of the current analysis have been published in Ref. [1].

References

- [1] M. D. Astorino, F. Frezza, and N. Tedeschi, "Broad-band terahertz metamaterial absorber with stacked electric ring resonators," *Journal of Electromagnetic Waves and Applications*, vol. 31, no. 7, pp. 727–739, 2017.
- [2] S. Gu, B. Su, and X. Zhao, "Planar isotropic broadband metamaterial absorber," *Journal of Applied Physics*, vol. 114, no. 16, p. 163702, 2013.
- [3] Y. Liu, S. Gu, C. Luo, and X. Zhao, "Ultra-thin broadband metamaterial absorber," *Applied Physics A*, vol. 108, no. 1, pp. 19–24, 2012.
- [4] Y. Q. Ye, Y. Jin, and S. He, "Omnidirectional, polarization-insensitive and broadband thin absorber in the terahertz regime," *JOSA B*, vol. 27, no. 3, pp. 498–504, 2010.
- [5] I. E. Carranza, J. P. Grant, J. Gough, and D. Cumming, "Terahertz metamaterial absorbers implemented in CMOS technology for imaging applications: scaling to large format focal plane arrays," *IEEE Journal of Selected Topics in Quantum Electronics*, vol. 23, no. 4, pp. 1–8, 2017.
- [6] M. P. Hokmabadi, D. S. Wilbert, P. Kung, and S. M. Kim, "Terahertz metamaterial absorbers," *Terahertz Science and Technology*, vol. 6, no. 1, pp. 40–58, 2013.
- [7] N. Han, Z. Chen, C. Lim, B. Ng, and M. Hong, "Broadband multi-layer terahertz metamaterials fabrication and characterization on flexible substrates," *Optics Express*, vol. 19, no. 8, pp. 6990–6998, 2011.
- [8] G. Dayal and S. A. Ramakrishna, "Design of multi-band metamaterial perfect absorbers with stacked metal–dielectric disks," *Journal of Optics*, vol. 15, no. 5, p. 055106, 2013.
- [9] B. A. Munk, *Frequency selective surfaces: theory and design*. John Wiley & Sons, 2005.
- [10] H.-M. Lee and H.-S. Lee, "A method for extending the bandwidth of metamaterial absorber," *International Journal of Antennas and Propagation*, vol. 2012, 2012.
- [11] F. Hu, L. Wang, B. Quan, X. Xu, Z. Li, Z. Wu, and X. Pan, "Design of a polarization insensitive multiband terahertz metamaterial absorber," *Journal of Physics D: Applied Physics*, vol. 46, no. 19, p. 195103, 2013.
- [12] G. Chao, Q. Shao-Bo, P. Zhi-Bin, and X. Zhuo, "A metamaterial absorber with direction-selective and polarisation-insensitive properties," *Chinese Physics B*, vol. 20, no. 3, p. 037801, 2011.
- [13] B.-X. Wang, L.-L. Wang, G.-Z. Wang, W.-Q. Huang, X.-F. Li, and X. Zhai, "A simple design of a broadband, polarization-insensitive, and low-conductivity alloy metamaterial absorber," *Applied Physics Express*, vol. 7, no. 8, p. 082601, 2014.
- [14] A. Nicolson and G. Ross, "Measurement of the intrinsic properties of materials by time-domain techniques," *IEEE Transactions on Instrumentation and Measurement*, vol. 19, no. 4, pp. 377–382, 1970.
- [15] W. B. Weir, "Automatic measurement of complex dielectric constant and permeability at microwave frequencies," *Proceedings of the IEEE*, vol. 62, no. 1, pp. 33–36, 1974.
- [16] N. Landy, C. Bingham, T. Tyler, N. Jokerst, D. Smith, and W. Padilla, "Design, theory, and measurement of a polarization-insensitive absorber for terahertz imaging," *Physical Review B*, vol. 79, no. 12, p. 125104, 2009.
- [17] M. Lobet, M. Lard, M. Sarrazin, O. Deparis, and L. Henrard, "Plasmon hybridization in pyramidal metamaterials: a route towards ultra-broadband absorption," *Optics Express*, vol. 22, no. 10, pp. 12678–12690, 2014.
- [18] A. Kazemzadeh and A. Karlsson, "On the absorption mechanism of ultra thin absorbers," *IEEE Transactions on Antennas and Propagation*, vol. 58, no. 10, pp. 3310–3315, 2010.
- [19] F. Costa, S. Genovesi, A. Monorchio, and G. Manara, "A circuit-based model for the interpretation of perfect metamaterial absorbers," *IEEE Transactions on Antennas and Propagation*, vol. 61, no. 3, pp. 1201–1209, 2013.

- [20] L. Huang, D. R. Chowdhury, S. Ramani, M. T. Reiten, S.-N. Luo, A. J. Taylor, and H.-T. Chen, “Experimental demonstration of terahertz metamaterial absorbers with a broad and flat high absorption band,” *Optics Letters*, vol. 37, no. 2, pp. 154–156, 2012.
- [21] H.-T. Chen, “Interference theory of metamaterial perfect absorbers,” *Optics Express*, vol. 20, no. 7, pp. 7165–7172, 2012.

Parametric Macromodels for Optimization of Metamaterial Devices

A procedure for the efficient design of metamaterial devices based on parametric macromodels is presented in this Chapter. These models are used to describe the frequency-domain behavior of complex systems as a function of frequency and design parameters (e.g., layout features). Parametric macromodels are very efficient and can be used to speed up the design flow in comparison with using electromagnetic simulators for design tasks. The use of quasi-random sequences for the sampling of the design space, and of radial basis functions and polynomial functions for the model construction is proposed. Numerical results validate the efficiency and accuracy of the proposed technique for multiple optimizations of the ultra-thin narrow-band metamaterial absorber described in Chapter 5.

The contents of this Chapter have been published in Ref. [1].

7.1 Introduction

Recently, metamaterial absorbers (MMAs) have aroused a huge interest and a large amount of research has been dedicated to the design of such devices [2] with specific characteristics ranging from the wide-angular response [3–5] to the polarization insensitivity [5–9] and the bandwidth enhancement [10, 11]. Moreover, their applications span from microwave [12] to terahertz (THz) [13], near infrared and optical frequencies [14, 15], such as electromagnetic compatibility, thermal emitters [16], solar cells and micro-bolometers [17, 18].

The Salisbury screen was one of the first microwave absorbers [19], constituted of a resistive sheet and a dielectric layer backed by a metallic plate capable of achieving impedance matching with free space through quarter-wave antireflection interference, but with the disadvantage of a $\lambda/4$ thick dielectric spacer. Other examples, in the microwave range, are the Jaumann absorber [20] which exploits

multiple resistive sheets to broaden the bandwidth and the high-impedance surfaces [21], i.e., periodic structures able to perform near-unity absorption at the desired frequency through the introduction of an amount of Ohmic or dielectric losses.

In the THz regime, instead, these absorbing devices are suitable for many applications in sensing, spectroscopy, monitoring, imaging and THz detectors, allowing to overcome the so-called “THz gap” [22, 23].

As pointed out in Ref. [24], it is not a challenging task to design an absorber working at a single frequency, at normal incidence, and with an arbitrary thickness. In the last decades, many efforts have been spent to reduce the absorbers thickness, and to improve the working bandwidth and the angular response. Moreover, another important property of an absorber is the polarization insensitivity, i.e., the possibility to absorb the incident radiation independently of its polarization. Several techniques have been implemented to achieve such requirements. Metamaterial absorbers, i.e., stratifications of metamaterial surfaces and dielectric slabs, usually allow to realize thin absorbers, at least for narrow-band applications. In order to obtain the polarization insensitivity with a metamaterial absorber, it is enough to consider isotropic surfaces, i.e., isotropic unit cells in the directions transverse to the stratification one. In order to increase the bandwidth, the most common strategy is to superpose several layers, covering the upper layer with a dielectric superstrate [24–26].

Among the configurations of MMAs proposed in the literature, the most performable is composed of subwavelength Frequency Selective Surfaces (FSSs) [25] printed on a grounded dielectric slab, i.e., a compact three-layer system in which the FSS is formed by Electric Ring Resonators (ERRs) that allow controlling and independently tune the effective permittivity of the device.

While this setting has been found effective, its efficient optimization and design space exploration have never been addressed. These tasks are usually performed by multiple frequency-domain electromagnetic (EM) simulations for different design parameter values (e.g., layout features), trying to meet the desired requirements. It is also obvious that both design space exploration and optimization can be very time consuming since multiple EM simulations are needed, even for a single unit cell that is assumed to constitute a periodic structure.

In this Chapter, we focus on design optimization. In the literature, multiple optimization approaches have been proposed, e.g. based on particle swarm and genetic algorithms [27] and on space mapping methods [28–32].

A different framework to efficiently and accurately perform design activities is based on parametric macromodels. These models [33–37] are able to accurately and efficiently model the behavior of complex systems as a function of frequency

(or time) and additional parameters (such as layout features). Once built, these models can be used to efficiently perform multiple design tasks such as design space exploration, optimization and variability analysis, which will otherwise result very computationally expensive if only based on EM simulations. We show that parametric macromodels are not only useful for a single design optimization, but they can be re-used to optimize the design to meet multiple sets of specifications. This is the main feature that distinguishes the proposed method from existing optimization methods proposed for EM systems. Also, the proposed technique leads to a model in a state-space form that provides an engineering interpretation: for example, poles and zeros of the system transfer function can be computed and analyzed as a function of design parameters.

This Chapter is organized as follows. Section 7.2 briefly reviews the metamaterial absorbers with a special focus on the ultra-thin narrow-band MMA discussed in Chapter 5 [38]. Then, the parametric macromodeling technique adopted to capture the dependence of the metamaterial absorber frequency-domain behavior on the design parameters is presented in Section 7.3. A design space composed of six design parameters has to be handled. We propose the use of quasi-random sequences for the sampling of the design space and of radial basis functions and polynomial functions for the model construction. Such a high-dimensional design space and model generation procedure have not been investigated in previous parametric macromodeling techniques. The effectiveness of the proposed approach is confirmed by the numerical results presented in Section 7.4. Finally, the conclusions are drawn in Section 7.5.

7.2 Metamaterial absorber

The analyzed ultra-thin narrow-band MMA with a four-fold rotational symmetry with respect to the incidence z -direction (see Fig. 7.1), follows a three-layer arrangement as discussed in Refs. [38, 39]. Its unit cell with a lattice constant $a = 80 \mu\text{m}$ consists of a top metallic ERR and a lower ground plane separated by a $5.8 \mu\text{m}$ thick dielectric layer of benzocyclobutane (BCB) with relative permittivity $\varepsilon_r = 2.5$ and dielectric loss tangent $\tan\delta = 0.005$. Both the top and bottom layers are made up of lossy gold with a conductivity of $1 \times 10^7 \text{ S/m}$ and a thickness of 270 nm. In Ref. [38], an equivalent circuit is proposed in order to have a circuital (and more intuitive) interpretation of the EM phenomena related to the absorber. The numerical values of the circuit elements are identified only after the EM response of the absorber is obtained by an EM solver. Therefore, it is not a circuit model based on analytical equations, which can replace the EM solver to calculate the EM response of the absorber.

In order to consider an infinitely periodic MMA, the unit cell has been simulated through the RF module of the EM solver of COMSOL Multiphysics [40]

based on the Finite Element Method (FEM) applying Floquet periodic boundary conditions along the x and y axes and assuming an EM wave impinging at normal incidence along the z direction. We note that the use of a FEM solver is not mandatory for the proposed technique. Any EM solvers can be used. We employ Perfectly Matched Layers (PMLs) on the top and bottom of the unit cell to absorb the excited mode from the source port and any higher order modes generated by the periodic MMA along with port boundary conditions on the interior boundaries of the PMLs to retrieve the reflection and transmission coefficients in terms of scattering parameters. In fact, the absorbed power can be expressed as $A(\omega) = 1 - R(\omega) - T(\omega) = 1 - |S_{11}(\omega)|^2 - |S_{21}(\omega)|^2$, meaning that in a perfect MMA, the reflection and transmission need to be simultaneously minimized. Since, in this case, the backside is grounded by metallic plane thicker than the skin depth, the absorption equation reduced to $A(\omega) = 1 - R(\omega)$, and as the effective impedance is matched to the free space impedance, it is possible to obtain a perfect absorption at the resonant frequency on a wide angular spectrum. This behavior can be reached by properly adjusting and selecting the geometric dimensions of the top ERR, the thickness and physical properties of the dielectric substrate, being these parameters responsible both for the electric and magnetic responses.

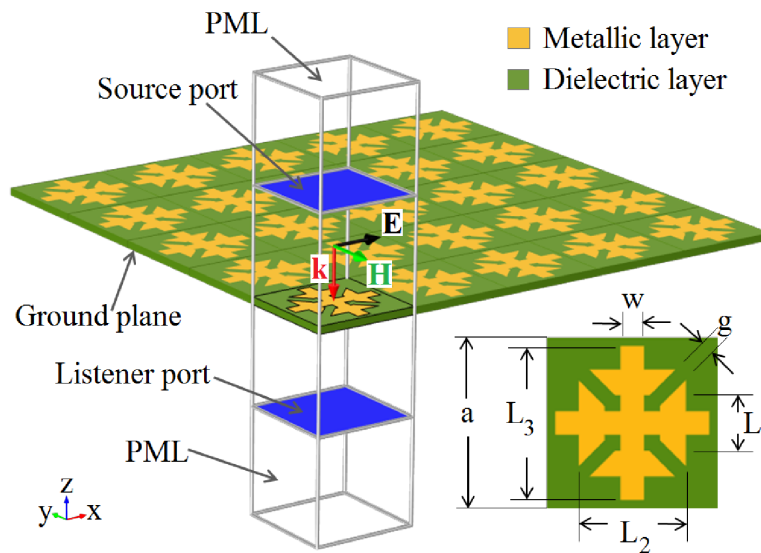


Figure 7.1: Unit cell of the ultra-thin narrow-band MMA and virtual infinite 2D array.

In summary, the physical mechanism underlying this narrow-band MMA with a near unity absorption, is based on anti-parallel currents between the two metal layers that allow the coupling to the magnetic field, while the coupling to the incident electric field is due to the ERR that basically determines the absorption frequency. Indeed, when the electric field of the incident THz wave is parallel to

one of the rods of the ERR, an electric dipole is excited on this rod, while no dipole exists on the orthogonal rod, but there is instead an electric-dipole resonance oscillating in anti-phase on the ground plane. Therefore, if the polarization is not parallel to a particular rod, the electric dipoles of both rods will contribute to the absorption mechanism, giving results close to the case of parallel polarization due to the symmetry of the unit cell. In what follows, we will determine the optimum set of geometric dimensions of the unit cell and the ERR able to guarantee the maximum absorption at a desired frequency.

7.3 Parametric macromodeling

In this Section, we describe the modeling method that will be used to generate parametric macromodels for efficient design. It aims to build a parametric macromodel $\mathbf{R}(s, \mathbf{g})$ that accurately describes the behavior of a system as a function of the Laplace variable s and a set of design parameters $\mathbf{g} = (\mathbf{g}^{(m)})_{m=1}^M$, such as layout features.

A parametric macromodel in the form

$$\mathbf{R}(s, \mathbf{g}) = \mathbf{C}(\mathbf{g}) (s\mathbf{I} - \mathbf{A}(\mathbf{g}))^{-1} \mathbf{B}(\mathbf{g}) + \mathbf{D}(\mathbf{g}), \quad (7.1)$$

is computed, where $\mathbf{A}(\mathbf{g}) \in \mathbb{R}^{n_x \times n_x}$, $\mathbf{B}(\mathbf{g}) \in \mathbb{R}^{n_x \times n_u}$, $\mathbf{C}(\mathbf{g}) \in \mathbb{R}^{n_y \times n_x}$, $\mathbf{D}(\mathbf{g}) \in \mathbb{R}^{n_y \times n_u}$.

Let us consider a set of Q frequency-domain ($s = j\omega$) EM simulations at different values \mathbf{g}_q , $q = 1, \dots, Q$ of the design parameters. Each EM simulation corresponding at the \mathbf{g}_q sample provides the scattering parameters of the structure under study for a certain set of frequency samples $\mathbf{S}(j\omega_f, \mathbf{g}_q)$, $f = 1, \dots, F$. Based on these frequency-domain data sets, a set of local Linear Time-Invariant (LTI) state-space models $\mathbf{A}(\mathbf{g}_q)$, $\mathbf{B}(\mathbf{g}_q)$, $\mathbf{C}(\mathbf{g}_q)$, $\mathbf{D}(\mathbf{g}_q)$ can be identified using any system identification techniques for LTI systems [41–43]. The local LTI models $\mathbf{R}(s, \mathbf{g}_q) = \mathbf{C}(\mathbf{g}_q) (s\mathbf{I} - \mathbf{A}(\mathbf{g}_q))^{-1} \mathbf{B}(\mathbf{g}_q) + \mathbf{D}(\mathbf{g}_q)$ model the scattering parameters data $\mathbf{S}(j\omega_f, \mathbf{g}_q)$, $f = 1, \dots, F$.

The state-space matrices of the local LTI models can be interpolated as a function of \mathbf{g} :

$$\begin{aligned} \mathbf{A}(\mathbf{g}) &= \sum_{q=1}^Q l_q(\mathbf{g}) \mathbf{A}(\mathbf{g}_q), & \mathbf{B}(\mathbf{g}) &= \sum_{q=1}^Q l_q(\mathbf{g}) \mathbf{B}(\mathbf{g}_q), \\ \mathbf{C}(\mathbf{g}) &= \sum_{q=1}^Q l_q(\mathbf{g}) \mathbf{C}(\mathbf{g}_q), & \mathbf{D}(\mathbf{g}) &= \sum_{q=1}^Q l_q(\mathbf{g}) \mathbf{D}(\mathbf{g}_q), \end{aligned} \quad (7.2)$$

to obtain a parametric macromodel. The interpolation models can use interpolation functions $l_q(\mathbf{g})$ whose value is based on the distribution of the design

parameters values \mathbf{g}_q in the design space (e.g. multilinear interpolation [44]) and $\mathbf{A}(\mathbf{g}_q), \mathbf{B}(\mathbf{g}_q), \mathbf{C}(\mathbf{g}_q), \mathbf{D}(\mathbf{g}_q)$ are the state-space matrices estimated for the local LTI models identified at fixed design parameters values \mathbf{g}_q [45]. Other interpolation models select a set of interpolation functions $l_q(\mathbf{g})$ and compute the matrix coefficients $\mathbf{A}_q, \mathbf{B}_q, \mathbf{C}_q, \mathbf{D}_q$ of the functions $l_q(\mathbf{g})$ by means of the solution of a linear system of equations (e.g. polynomial interpolation) [46, 47]:

$$\begin{aligned} \mathbf{A}(\mathbf{g}) &= \sum_{q=1}^Q l_q(\mathbf{g}) \mathbf{A}_q, & \mathbf{B}(\mathbf{g}) &= \sum_{q=1}^Q l_q(\mathbf{g}) \mathbf{B}_q, \\ \mathbf{C}(\mathbf{g}) &= \sum_{q=1}^Q l_q(\mathbf{g}) \mathbf{C}_q, & \mathbf{D}(\mathbf{g}) &= \sum_{q=1}^Q l_q(\mathbf{g}) \mathbf{D}_q. \end{aligned} \quad (7.3)$$

We highlight that the matrix coefficients $\mathbf{A}_q, \mathbf{B}_q, \mathbf{C}_q, \mathbf{D}_q$ are different from $\mathbf{A}(\mathbf{g}_q), \mathbf{B}(\mathbf{g}_q), \mathbf{C}(\mathbf{g}_q), \mathbf{D}(\mathbf{g}_q)$.

In this work, we use an interpolation scheme based on radial basis functions and polynomial basis functions [48–50] where the interpolation for each entry of the state-space matrices can be written as:

$$\sum_{q=1}^Q w_q \phi(\mathbf{g} - \mathbf{g}_q) + \sum_{b=1}^B w_b p_b(\mathbf{g}). \quad (7.4)$$

Different radial basis functions $\phi(\mathbf{g} - \mathbf{g}_q)$ exist in the literature; we have chosen the multiquadrics basis functions:

$$\phi(\mathbf{g} - \mathbf{g}_q) = \sqrt{r_q^2 + c^2}, \quad (7.5)$$

where r_q represents the euclidian distance between \mathbf{g} and \mathbf{g}_q and c is a positive parameter. The B polynomial functions have been chosen to be $[1, g^{(1)}, g^{(2)}, \dots, g^{(M)}]$.

The local LTI models are generated by independent system identification steps [41–43]. We use the Vector Fitting (VF) technique [41] to first obtain pole-residue models for each design space samples \mathbf{g}_q :

$$\mathbf{S}(j\omega_f, \mathbf{g}_q) \simeq \mathbf{D}(\mathbf{g}_q) + \sum_{p=1}^P \frac{\mathbf{Res}_p(\mathbf{g}_q)}{j\omega - poles_p(\mathbf{g}_q)}. \quad (7.6)$$

Then, different state-space realization techniques can be used to generate the state-space matrices of the local LTI models $\mathbf{A}(\mathbf{g}_q), \mathbf{B}(\mathbf{g}_q), \mathbf{C}(\mathbf{g}_q), \mathbf{D}(\mathbf{g}_q)$ starting from the pole-residue models in Eq. (7.6). The state-space representation of LTI models is unique up to a similarity transformation. The state-space matrices of the local LTI models need to be represented in a common state-space form

to avoid potentially large variations as a function of the design parameters due to underlying similarity transformations, which might degrade the accuracy of the interpolation significantly. In the literature, several approaches have been proposed to transform the local LTI models into a state-space representation suitable for interpolation [36, 46, 47]; we have used the barycentric realization discussed in Ref. [36].

If using one specific state-space realization would not provide the desired accuracy, then the technique in Ref. [51] could be used to compute similarity transformation matrices that transform the set of local LTI models into a state-space form suitable to interpolation.

7.3.1 Design space sampling and model cross-validation

Multiple schemes can be used to choose the location of the Q samples in the \mathbf{g} space: for example, Latin hypercube design [52] and quasi-random sequences [53]. Sobol and Halton sequences [53] are famous among quasi-random sequences. In this work, we have chosen the Sobol quasi-random sequence scheme [53]. Simple sampling schemes such as a regular tensor-product sampling will immediately provide a high number of samples as soon as the number of dimensions of the design space increases. Let us imagine to have M design parameters and to sample each design parameters interval with L samples. By taking the combination of all these samples (tensor-product), the total number of samples is equal to L^M . This is clearly not an efficient sampling scheme.

To estimate the accuracy of a parametric macromodel, of all Q simulations (then of all Q samples in the design space), a part of it is used to build the parametric macromodel (estimation) and another part is used to validate the model (validation). A scheme inspired by k – *fold* cross validation is used to subdivide estimation and validation samples in the design space [54]. The set of Q simulations is randomly partitioned into k sets of approximately equal size. Then, for $i = 1, \dots, k$, a parametric macromodel is built considering all but the i –*th* data partition and the excluded dataset is used to evaluate the corresponding validation model error. An average validation model error based on the validation model errors of all the k iterations is used to estimate the average error over the design space for the parametric macromodel built by using all the data samples [54]. A 10 – *fold* ($k = 10$) cross validation has been used as illustrated in Fig. 7.2.

Once the parametric macromodel is built, it can be used for design tasks, such as design optimization. The same model can be reused for different optimization tasks.

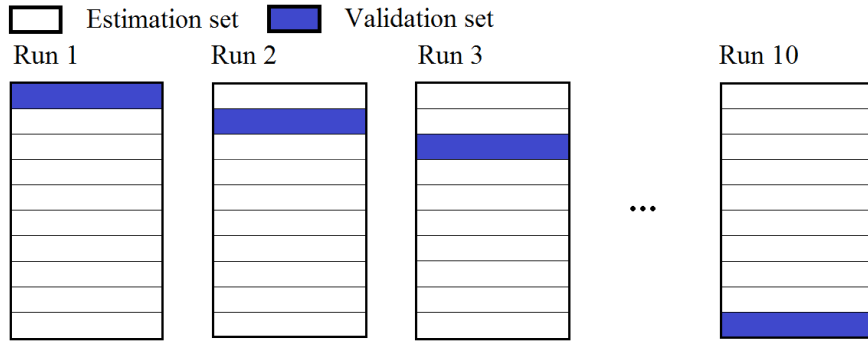


Figure 7.2: 10-fold cross-validation process.

Concerning some computational considerations:

- If an EM solver-based approach is used, each iteration of a design optimization task leads to an EM simulation. Since each EM simulation can be computationally expensive, such an approach is very inefficient.
- Instead, in the case of the proposed technique, there is an initial computational cost needed to generate the parametric macromodel (the Q EM simulations previously mentioned). This initial computational effort becomes negligible when the model is used in multiple optimization cases. The parametric macromodel is an analytical model and therefore its evaluation is extremely fast. The same model is reused in multiple optimization tasks with different optimization objectives. This allows obtaining a very significant computational speed-up with respect to optimizations directly based on EM simulations. The proposed technique is based on system identification tools, interpolation schemes and cross-validation algorithms.

These computational considerations will be fully supported by numerical results in Section 7.4.

Figure 7.3 summarizes the main steps of the proposed modeling techniques.

7.4 Numerical results

A narrow-band MMA structure is used to validate the proposed modeling technique. The design parameters of the narrow-band MMA are: the lattice constant a , the gap g , the width w and the lengths L_1 , L_2 , L_3 that vary over the ranges $[77-90] \mu\text{m}$, $[3-7] \mu\text{m}$, $[5-15] \mu\text{m}$, $[22-35] \mu\text{m}$, $[40-55] \mu\text{m}$ and $[60-75] \mu\text{m}$, respectively, as shown in Fig. 7.1. The 6D design space (a, g, w, L_1, L_2, L_3) includes 150 samples (Sobol sampling scheme) and each sample has required an EM simulation, examined over the frequency range $[0.9-1.4]$ THz with a frequency resolution of 10 GHz (i.e., 51 frequency points for each simulation).

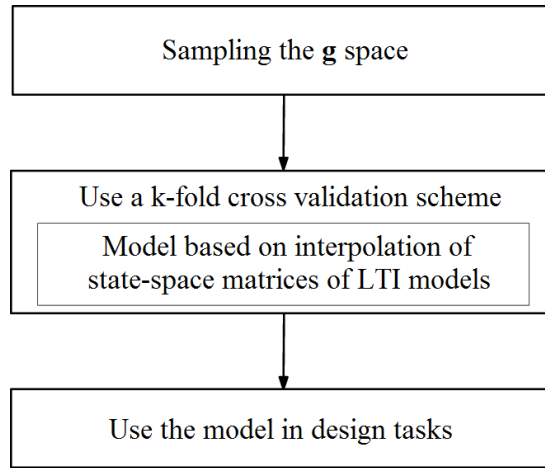


Figure 7.3: Main steps of the proposed modeling techniques.

In order to obtain the frequency-domain data samples of the reflection spectra for all 150 design space samples, it is necessary an overall CPU time equal to 237 h 30 m with an average CPU time for one EM simulation of about 1 h 35 m. Considering the 150 simulations, the VF technique [41] has been used to obtain pole-residue models as in Eq. (7.6) with $P = 6$ as number of poles.

Figure 7.4 shows the location of the poles in the Laplace domain corresponding to the 150 pole-residue models.

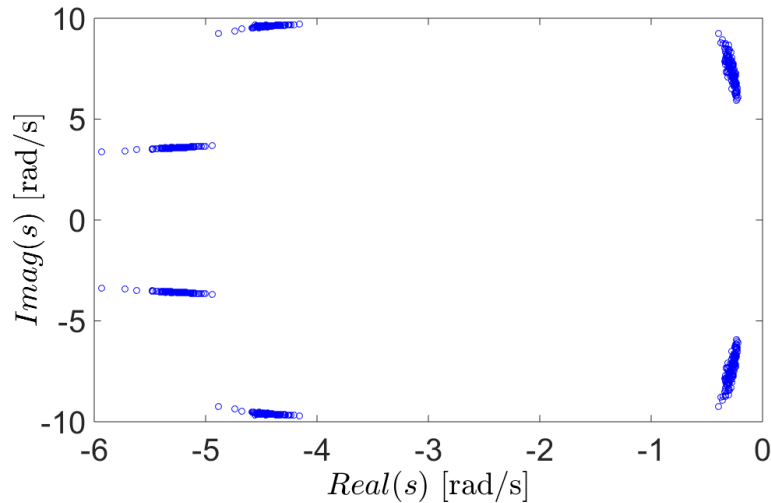


Figure 7.4: Location of the poles in the Laplace domain corresponding to the 150 pole-residue models.

Then, the barycentric realization [36] has been used to generate the state-space matrices of the local LTI models $\mathbf{A}(\mathbf{g}_q)$, $\mathbf{B}(\mathbf{g}_q)$, $\mathbf{C}(\mathbf{g}_q)$, $\mathbf{D}(\mathbf{g}_q)$ starting from the pole-residue models. Finally, an interpolation scheme based on multiquadrics radial basis functions and polynomial basis functions [48] has been used to construct the parametric macromodel.

A 10 – *fold* cross-validation has been used to estimate the average absolute error of the final parametric macromodel in the design space. This estimated error is equal to 0.0208. The CPU time needed to perform the 10 – *fold* cross-validation and to build the final parametric macromodel using all data samples is equal to 58 s and 8.6 s, respectively.

The parametric macromodel has been used for three multiobjective optimizations whose objective is to achieve a maximum absorption at three different frequencies, namely $freq_{optim} = 1.1$ THz (Case I), $freq_{optim} = 1.2$ THz (Case II) and $freq_{optim} = 1.3$ THz (Case III). Therefore, we have three optimization tasks. The function gamultiobj in Matlab® (R2014) has been used to run the three multiobjective optimizations with the default Matlab settings. The parametric macromodel has provided the value of S_{11} over a dense frequency grid of 501 points and for each design parameters value required by the optimizer. The obtained optimal values of the design parameters are shown in Table 7.1 for the three optimization cases.

Table 7.1: Optimal design parameters values (μm).

Case	a	g	w	L_1	L_2	L_3
I	78.68	4.61	12.67	27.59	52.89	73.13
II	82.66	5.67	12.60	27.09	49.66	69.87
III	84.99	5.06	12.75	26.78	45.57	66.76

To achieve these optimal values, the routine gamultiobj has required 9811, 10081 and 9451 function evaluations and a CPU time equal to 84 s, 88 s and 82 s using the parametric macromodel, respectively.

Three additional EM simulations have been performed to confirm the accuracy of the optimization results provided by the parametric macromodel. Figure 7.5 shows the absorbance response obtained by the parametric macromodel and the EM solver at the three optimal points. A very good agreement is achieved.

Table 7.2 summarizes the computational cost related to 1) using COMSOL Multiphysics and 2) using the proposed parametric macromodeling technique for the three optimization tasks. The speed-up obtained by using the proposed technique for the three optimizations is mentioned. It becomes evident that the initial computational effort for the parametric macromodel construction is justified by the very significant computational saving obtained for multiple design optimizations.

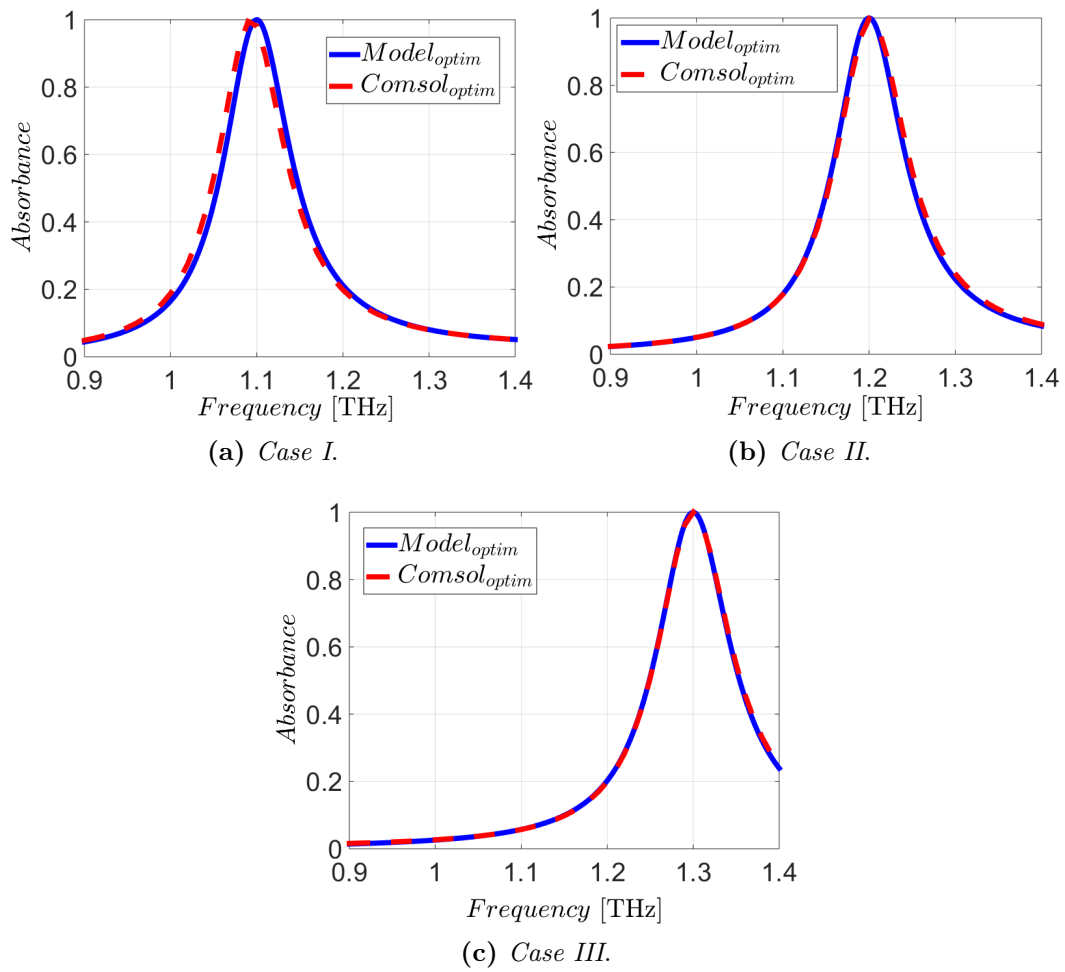


Figure 7.5: Optimization results: cases I-II-III of Table 7.1.

Table 7.2: CPU time comparison.

	Model generation
Proposed	$150 \times 1 \text{ h } 35 \text{ m} + 58 \text{ s} + 8.6 \text{ s}$
	Optimization 1
EM FEM solver	$9811 \times 1 \text{ h } 35 \text{ m}$
Proposed	84 s
	Optimization 2
EM FEM solver	$10081 \times 1 \text{ h } 35 \text{ m}$
Proposed	88 s
	Optimization 3
EM FEM solver	$9451 \times 1 \text{ h } 35 \text{ m}$
Proposed	82 s
	Speed-up
Proposed	195x

7.5 Conclusions

In this Chapter, we have proposed an approach for the efficient design of metamaterial devices based on a parametric macromodeling technique. With this method the electromagnetic behavior of complex systems can be modeled as functions of frequency/time and design features. As study example, in Section 7.2, we have considered the ultra-thin narrow-band metamaterial absorber previously devised and analyzed in Chapter 5, by handling a design space of six geometric parameters.

In Section 7.3, we have used quasi-random sequences for the sampling of the design space, and we have adopted an interpolation scheme based on radial basis functions and polynomial functions of the state-space matrices of a set of linear time-invariant models for the macromodel construction. In order to compute the poles and zeros of the system transfer function, we have applied the vector fitting technique for each design space sample, thus providing an engineering interpretation. The average absolute error of the parametric macromodel has been estimated through a 10 – *fold* cross validation in the design space.

In Section 7.4, the parametric macromodel has been applied to three multiobjective optimizations of the metamaterial absorber’s dimensions. The objective was to achieve ideal near-unity absorption values at three different frequencies in the THz range. The numerical results have confirmed the efficiency and accuracy of the proposed technique, which enabled the calculation of optimal design values with reduced computational resources and amount of time.

Also, this modeling method can be applied to deal with various design tasks (design space exploration, optimization and variability analysis) and with metamaterial structures in multiple design scenarios: arbitrary geometrical shapes and sizes, choice of arbitrary materials, multi-layered environments, multiple-band and wide-band filters. The strength of these parametric macromodels lies in their ability to be reused in the optimization of multiple sets of specifications.

The results of the current analysis have been published in Ref. [1].

References

- [1] G. Antonini, M. D. Astorino, F. Ferranti, F. Frezza, and N. Tedeschi, "Efficient design of metamaterial absorbers using parametric macromodels," *Applied Computational Electromagnetics Society Journal*, vol. 33, no. 7, pp. 772–780, 2018.
- [2] Q. Wu, K. Zhang, and G. H. Yang, "Manipulation of electromagnetic waves based on new unique metamaterials: theory and applications," *ACES Journal*, vol. 12, pp. 977–989, December 2014.
- [3] O. Luukkonen, F. Costa, C. R. Simovski, A. Monorchio, and S. A. Tretyakov, "A thin electromagnetic absorber for wide incidence angles and both polarizations," *IEEE Trans. Antennas Propag.*, vol. 57, no. 10, pp. 3119–3125, 2009.
- [4] M. Diem, T. Koschny, and C. M. Soukoulis, "Wide-angle perfect absorber/thermal emitter in the terahertz regime," *Phys. Rev. B*, vol. 79, no. 3, p. 033101, 2009.
- [5] S. Ghosh, S. Bhattacharyya, D. Chaurasiya, and K. V. Srivastava, "Polarisation-insensitive and wide-angle multi-layer metamaterial absorber with variable bandwidths," *Electronics Letters*, vol. 51, no. 14, pp. 1050–1052, 2015.
- [6] H. Cheng, S. Chen, H. Yang, J. Li, X. An, C. Gu, and J. Tian, "A polarization insensitive and wide-angle dual-band nearly perfect absorber in the infrared regime," *J. Opt.*, vol. 14, no. 8, p. 085102, 2012.
- [7] N. I. Landy, C. Bingham, T. Tyler, N. Jokerst, D. R. Smith, and W. J. Padilla, "Design, theory, and measurement of a polarization-insensitive absorber for terahertz imaging," *Phys. Rev. B*, vol. 79, no. 12, p. 125104, 2009.
- [8] L. Lu, S. Qu, H. Ma, F. Yu, S. Xia, Z. Xu, and P. Bai, "A polarization-independent wide-angle dual directional absorption metamaterial absorber," *Prog. Electromagn. Res. M*, vol. 27, pp. 191–201, 2012.
- [9] D. Chaurasiya, S. Ghosh, S. Bhattacharyya, A. Bhattacharya, and K. V. Srivastava, "Compact multi-band polarisation-insensitive metamaterial absorber," *IET Microwaves, Antennas & Propagation*, vol. 10, pp. 94–101, 2016.
- [10] J. Sun, L. Liu, G. Dong, and J. Zhou, "An extremely broad band metamaterial absorber based on destructive interference," *Opt. Express*, vol. 19, no. 22, p. 21155, 2011.
- [11] S. Gu, J. P. Barrett, T. H. Hand, B. I. Popa, and S. A. Cummer, "A broadband low-reflection metamaterial absorber," *J. Appl. Phys.*, vol. 108, no. 6, p. 064913, 2010.
- [12] N. I. Landy, S. Sajuyigbe, J. J. Mock, D. R. Smith, and W. J. Padilla, "Perfect metamaterial absorber," *Phys. Rev. Lett.*, vol. 100, no. 20, p. 207402, 2008.
- [13] J. Grant, S. S. Y. Ma, L. B. Lok, A. Khalid, and D. R. S. Cumming, "Polarization insensitive terahertz metamaterial absorber," *Opt. Lett.*, vol. 36, no. 8, pp. 1524–1526, 2011.
- [14] G. Dayal and S. A. Ramakrishna, "Design of highly absorbing metamaterials for infrared frequencies," *Opt. Express*, vol. 20, no. 16, pp. 17503–17508, 2012.
- [15] N. Liu, M. Mesch, T. Weiss, M. Hentschel, and H. Giessen, "Infrared perfect absorber and its application as plasmonic sensor," *Nano Lett.*, vol. 10, no. 7, p. 2342, 2010.
- [16] X. Liu, T. Tyler, T. Starr, A. F. Starr, N. Jokerst, and W. J. Padilla, "Taming the blackbody with infrared metamaterials as selective thermal emitters," *Phys. Rev. Lett.*, vol. 107, no. 4, p. 045901, 2011.
- [17] M. Laroche, R. Carminati, and J. J. Greffet, "Near-field thermophotovoltaic energy conversion," *J. Appl. Phys.*, vol. 100, no. 6, p. 063704, 2006.
- [18] T. Maier and H. Bruckl, "Wavelength-tunable microbolometers with metamaterial absorbers," *Opt. Lett.*, vol. 34, no. 19, pp. 3012–3014, 2009.
- [19] R. L. Fante and M. T. McCormack, "Reflection properties of the Salisbury screen," *IEEE Trans. Antennas Propag.*, vol. 36, no. 10, pp. 1443–1454, 1988.
- [20] E. F. Knott and C. D. Lunden, "The two-sheet capacitive Jaumann absorber," *IEEE Trans. Antennas Propag.*, vol. 43, no. 11, pp. 1339–1343, 1995.

- [21] S. A. Tretyakov and S. I. Maslovski, "Thin absorbing structure for all incident angles based on the use of a high-impedance surface," *Microwave Opt. Technol. Lett.*, vol. 38, no. 3, pp. 175–178, 2003.
- [22] V. T. Pham, J. Park, D. L. Vu, H. Y. Zheng, J. Y. Rhee, K. Kim, and Y. P. Lee, "THz-metamaterial absorbers," *Adv. Nat. Sci. Nanosci. Nanotechnol.*, vol. 4, no. 1, p. 015001, 2013.
- [23] C. Debus and P. Bolivar, "Frequency selective surfaces for high sensitivity terahertz sensing," *Appl. Phys. Lett.*, vol. 91, no. 18, p. 184102, 2007.
- [24] C. S. Y. Ra'di and S. Tretyakov, "Thin perfect absorbers for electromagnetic waves: theory, design, and realization," *Phys. Rev. Appl.*, vol. 3, p. 037001, 2015.
- [25] B. A. Munk, *Frequency Selective Surfaces: Theory and Design*. Wiley, 2000.
- [26] M. D. Astorino, F. Frezza, and N. Tedeschi, "Broad-band terahertz metamaterial absorber with stacked electric ring resonators," *J. Electrom. Waves Appl.*, vol. 31, no. 7, pp. 727–739, 2017.
- [27] D.-H. Kwon, Z. Bayraktar, J. A. Bossard, D. H. Werner, and P. L. Werner, "Nature-inspired optimization of metamaterials," in *24th Annual Review of Progress in Applied Computational Electromagnetics*, April 2008.
- [28] S. Koziel, "Multi-fidelity optimization of microwave structures using response surface approximation and space mapping," *ACES Journal*, vol. 24, pp. 600–608, December 2009.
- [29] S. Koziel, J. Bandler, and Q. Cheng, "Robust trust-region space-mapping algorithms for microwave design optimization," *IEEE Transactions on Microwave Theory and Techniques*, vol. 58, pp. 2166–2174, August 2010.
- [30] S. Koziel and J. Bandler, "Fast design optimization of microwave structures using co-simulation-based tuning space mapping," *ACES Journal*, vol. 26, pp. 631–639, August 2011.
- [31] S. Koziel, "Space mapping: Performance, reliability, open problems and perspectives," in *2017 IEEE MTT-S International Microwave Symposium (IMS)*, pp. 1512–1514, June 2017.
- [32] S. Koziel and A. Bekasiewicz, "Reliable low-cost surrogate modeling and design optimisation of antennas using implicit space mapping with substrate segmentation," *IET Microwaves, Antennas and Propagation*, vol. 11, no. 14, pp. 2066–2070, 2017.
- [33] F. Ferranti, L. Knockaert, and T. Dhaene, "Parameterized S-parameter based macromodeling with guaranteed passivity," *IEEE Microw. Wireless Compon. Lett.*, vol. 19, pp. 608–610, October 2009.
- [34] P. Triverio, S. Grivet-Talocia, and M. S. Nakhla, "A parameterized macromodeling strategy with uniform stability test," *IEEE Transactions on Advanced Packaging*, vol. 32, pp. 205–215, February 2009.
- [35] F. Ferranti, L. Knockaert, and T. Dhaene, "Passivity-preserving parametric macromodeling by means of scaled and shifted state-space systems," *IEEE Transactions on Microwave Theory and Techniques*, vol. 59, pp. 2394–2403, October 2011.
- [36] E. R. Samuel, L. Knockaert, F. Ferranti, and T. Dhaene, "Guaranteed passive parameterized macromodeling by using Sylvester state-space realizations," *IEEE Transactions on Microwave Theory and Techniques*, vol. 61, pp. 1444–1454, April 2013.
- [37] M. Kabir and R. Khazaka, "Parametric macromodeling of high-speed modules from frequency-domain data using Loewner matrix based method," in *IEEE MTT-S International Microwave Symposium*, pp. 1–4, June 2013.
- [38] M. D. Astorino, F. Frezza, and N. Tedeschi, "Ultra-thin narrow-band, complementary narrow-band, and dual-band metamaterial absorbers for applications in the THz regime," *J. Appl. Phys.*, vol. 121, no. 6, p. 063103, 2017.

- [39] M. D. Astorino, R. Fastampa, F. Frezza, L. Maiolo, M. Marrani, M. Missori, M. Muzi, N. Tedeschi, and A. Veroli, “Polarization-maintaining reflection-mode THz time-domain spectroscopy of a polyimide based ultra-thin narrow-band meta-material absorber,” *Scientific Reports*, vol. 8, no. 1, p. 1985, 2018.
- [40] *COMSOL Multiphysics 4.4*.
- [41] B. Gustavsen, “Improving the pole relocating properties of vector fitting,” *IEEE Transactions on Power Delivery*, vol. 21, no. 3, pp. 1587–1592, 2006.
- [42] L. Ljung, *System Identification: Theory for the User (2nd Edition)*. Prentice Hall, 1999.
- [43] R. Pintelon and J. Schoukens, *System Identification: A Frequency Domain Approach*. Wiley-IEEE Press, 2012.
- [44] W. A. Weiser and S. E. Zarantonello, “A note on piecewise linear and multilinear table interpolation in many dimensions,” *Mathematics of Computation*, vol. 50, pp. 253–264, January 1988.
- [45] F. Ferranti, L. Knockaert, and T. Dhaene, “Guaranteed passive parameterized admittance-based macromodeling,” *IEEE Trans. Advanced Packaging*, vol. 33, pp. 623–629, August 2010.
- [46] J. De Caigny, J. Camino, and J. Swevers, “Interpolation-based modeling of MIMO LPV systems,” *IEEE Transactions on Control Systems Technology*, vol. 19, no. 1, pp. 46–63, 2011.
- [47] J. De Caigny, R. Pintelon, J. Camino, and J. Swevers, “Interpolated modeling of LPV systems,” *IEEE Transactions on Control Systems Technology*, vol. 22, pp. 2232–2246, November 2014.
- [48] M. D. Buhmann, *Radial Basis Functions*. New York, NY, USA: Cambridge University Press, 2003.
- [49] G. Liu and Y. Gu, *An Introduction to Meshfree Methods and Their Programming*. Springer, 2005.
- [50] G. R. Liu, *Meshfree methods: moving beyond the finite element method. Second Edition*. CRC Press, 2010.
- [51] F. Ferranti and Y. Rolain, “A local identification method for linear parameter-varying systems based on interpolation of state-space matrices and least-squares approximation,” *Mechanical Systems and Signal Processing*, vol. 82, pp. 478 – 489, 2017.
- [52] W.-L. Loh, “On Latin hypercube sampling,” *Ann. Statist.*, vol. 24, no. 5, pp. 2058–2080, 1996.
- [53] P. Brandimarte, *Low-Discrepancy Sequences*, pp. 379–401. John Wiley and Sons, Inc., 2014.
- [54] T. Hastie, R. Tibshirani, and J. Friedman, *The Elements of Statistical Learning: Data Mining, Inference, and Prediction, Second Edition (Springer Series in Statistics)*. Springer, 2009.

Polarization-Maintaining Reflection-mode THz Time-Domain Spectroscopy of a Polyimide Based Ultra-Thin Narrow-Band Metamaterial Absorber

This Chapter reports the design, the microfabrication and the experimental characterization of the ultra-thin narrow-band metamaterial absorber at terahertz frequencies, described in Chapter 5, Section 5.2. The metamaterial device is composed of a highly flexible polyimide spacer included between a top electric ring resonator with a four-fold rotational symmetry and a bottom ground plane that avoids misalignment problems. Its performance has been experimentally demonstrated by a custom polarization-maintaining reflection-mode terahertz time-domain spectroscopy system properly designed in order to reach a collimated configuration of the terahertz beam. The dependence of the spectral characteristics of this metamaterial absorber has been evaluated on the azimuthal angle under oblique incidence. The obtained absorbance levels are comprised between 67% and 74% at 1.092 THz and the polarization insensitivity has been verified in transverse electric polarization. This offers potential prospects in terahertz imaging, in terahertz stealth technology, in substance identification, and in non-planar applications. The proposed compact experimental setup can be applied to investigate arbitrary polarization-sensitive terahertz devices under oblique incidence, allowing for a wide reproducibility of the measurements.

The contents of this Chapter have been published in Ref. [1].

8.1 Introduction

Terahertz (THz) technology has recently received growing attention, enabling it to overcome the so-called “THz gap” thus connecting the fields of electronics and optics [2]. While the microwaves and the far-infrared frequency regions immediately below and above the THz band, respectively, have been extensively

investigated, the THz frequencies are still the aim of the research breakthroughs. An intense interaction between the disciplines of physics and engineering has made it possible to generate and detect broadband coherent THz radiation. In particular, THz Time-Domain Spectroscopy (THz-TDS) has matured into an extremely useful tool for characterizing THz devices, thanks to its non-destructive and non-invasive features [3–5]. The non-ionizing nature of the THz frequencies has promoted advanced applications in medical diagnoses and in material science, allowing it to identify different substances through their specific absorption patterns [6, 7]. THz devices have also been successfully applied in security detection [8–10], because non-conductive and non-polar materials, such as packaging, plastics, paper and ordinary clothes, show low absorption at these frequencies.

In this context, the THz regime represents a fertile area for the development of metamaterial absorbers (MMAs) [11–14], which are manmade devices designed to absorb specific bands of the incident electromagnetic radiation and generally constituted of periodic structures with sub-wavelength unit cells [15]. Their customizable optical characteristics [16–18] are not observed in their constituent materials, but they can be artificially manipulated by employing electromagnetic resonators. This resonant spectral feature is of particular interest at THz frequencies, where it is difficult to find natural materials with both narrow absorption bands and high absorption coefficients [19]. In addition, since the unit cell sizes necessary for the THz frequencies are of the order of tens of micrometers, they can be reproduced with high precision through micro-fabrication processes based on standard photolithographic techniques. This can be very useful in the development of various MMAs and applications, such as highly sensitive biochemical sensors [20], microbolometers of thermal detectors [21, 22], THz stealth technology [23], and THz imaging [24].

By exploiting the principle of scalability of these devices, once proved their feasibility, it is conceivable to extend their use even at higher frequencies where the tolerances required in manufacturing processes are more critical. A specific-designed MMA could be also dimensioned to operate over a wide range of frequencies spanning from microwave, THz, to the infrared (IR), and optical spectrum [25, 26].

In order to assess a benchmark for future MMAs development, it is fundamental to investigate the underlying physics on simple three-layer metal-dielectric-metal devices in which the interplay between the metallizations through the dielectric layer can be more easily studied as a function of incidence angle and polarization. In general, it is essential to maximize the losses and consequently the absorbance $A(\omega)$, where ω is the angular frequency, in narrow spectral bands. According to the relation $A(\omega) = 1 - R(\omega) - T(\omega)$ [27], this can be obtained

through the simultaneous minimization of the reflectance $R(\omega)$ by matching the impedance of the MMA to that of free space at a desired frequency, and of the transmittance $T(\omega)$ by employing a metallic ground plane. This achievement normally requires first a preliminary study in which the characteristics of the resonator are defined in connection with the material properties of the middle spacer; then followed by an optimization phase in which the geometrical features of the resonator and the thickness of the dielectric layer are adjusted for the best performance. Following the design phase, an accurate experimental characterization of MMA electromagnetic response is needed. This makes the THz spectroscopy fundamental both to demonstrate the functionality of the MMAs and to study their compliance with the design features.

With the aim of implementing a valid THz experimental setup for an MMA as described above, it is necessary to solve some significant problems. Due to the presence of a lower metallic ground plate which prevents transmission of THz radiation through the device, measurements should be conducted in reflection-mode. This configuration needs a higher number of THz optical components as compared to the more easily configurable transmission-mode setup [5]. The quality of the experimental results critically depends on alignment errors of THz optical components which might alter the measured signals due to differences in THz pulses path length and phase errors.

In this Chapter, I show how it is possible to realize and characterize at THz frequencies an ultra-thin ground-plane-backed MMA [28] with an extremely selective absorbance spectrum (see Section 8.2). This three-layer metal-dielectric-metal configuration has been chosen to simplify the fabrication processes and to avoid misalignment problems with respect to other more complex multi-layer configurations already published [24, 27]. This approach reduces the number of experimental degrees of freedom in the fabrication, allowing a more straightforward controllability of the prototype stage (see Section 8.3). The choice of polyimide, as the dielectric spacer, also takes into account its possible application as a flexible MMA, adaptable to non-planar surfaces. In Section 8.4, a specifically designed polarization-maintaining reflection-mode THz-TDS setup with innovative features is employed for the MMA electromagnetic characterization. The unit cell of the proposed MMA has been designed to exhibit a single resonance in the THz frequency range accessible to the custom reflection-mode THz-TDS setup, providing a well-recognizable experimental absorption signal particularly useful for comparison with numerical simulations (see Section 8.5). Furthermore, the wide reproducibility found in the measurements proves our THz-TDS setup to be potentially effective to accurately characterize arbitrary THz polarization-sensitive devices in reflection mode under oblique incidence (see Appendix B). In fact, in

the proposed reflection-mode THz-TDS system, only two identical plano-convex lenses and a custom aluminum prism reflector have been properly employed, thus avoiding the use of a complex set of parabolic mirrors to manipulate the THz optical path [3, 29, 30], potential source of disturbance for both polarization and propagation of THz radiation. In Section 8.6, the conclusions are drawn.

8.2 MMA description

The ultra-thin narrow-band MMA [28] is realized with a three-layer metal-dielectric-metal configuration consisting of a patterned Frequency-Selective Surface (FSS) [28, 31] inspired by Ref. [24], a highly flexible insulating polyimide spacer, and a metal ground plane on a silicon substrate. Polyimide PI-2611 from HD Microsystems [32] with nominal dielectric constant $\epsilon' = 2.9$, loss tangent $\tan \delta = 0.002$, and thickness of $5.4 \mu\text{m}$, has been chosen as middle dielectric layer for its high electrical and thermal stability, low refractive index, low absorption, and flexibility [33–41]. It is a well-established material within the micro-fabrication processes, and it is used in applications of electronics on plastic and in photonic devices [42, 43].

The upper Electric Ring Resonator (ERR) [24, 28, 31] (with optimized dimensions specified in Fig. 8.1(a)) and the lower ground plane with 100 nm thickness are both made of lossy gold in order to ensure chemical stability and a high electrical conductivity ($\sigma = 4.09 \times 10^7 \text{ S/m}$).

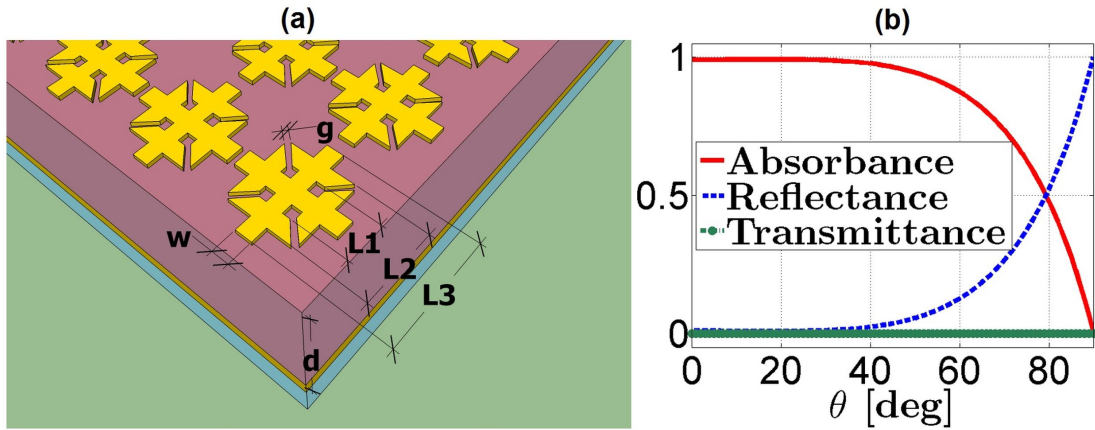


Figure 8.1: Schematic illustration of the ultra-thin narrow-band MMA and angular response in TE polarization. (a) Geometry of the narrow-band MMA with dimensions (in micrometer) $g = 7$, $w = 11$, $L1 = 26$, $L2 = 50$, $L3 = 72$, and $d = 5.4$. (b) Response as a function of the incidence angle θ at 1.09 THz in TE polarization with azimuthal angle $\varphi = 0^\circ$.

This ultra-thin MMA with unit cell of $80 \mu\text{m}$ periodicity presents a significant subwavelength thickness of about $\lambda_0/49$ at the absorbance frequency, where λ_0 is the free-space wavelength.

The proposed MMA was simulated by applying the Finite-Element Method (FEM), using the RF module of the commercial software package COMSOL Multiphysics. To this end, a single unit cell has been considered by applying Floquet periodic boundary conditions for the side boundaries perpendicular to the plane of the MMA to model a periodic structure. Perfectly Matched Layers (PMLs) are employed on the top and bottom of the unit cell to absorb the excited mode from the source port and any higher-order modes generated by the periodic MMA. Port boundary conditions are applied on the interior boundaries of the PMLs. For the excitation at the source port, an obliquely incident plane wave illumination with Transverse Electric (TE) polarization (i.e., the electric field is parallel to the ERR arm where $\varphi = 0^\circ$) and 1 W input power, constant over the THz band of interest, were used.

The materials choice in the metamaterial design is a key point for the energy dissipation: in order to reach the desired absorbance, one needs to select highly conductive metals and highly insulating dielectrics, i.e., materials with low losses in the working frequency band. By adopting these material characteristics and the optimized dimensions, I have reached in the simulations a near unity absorbance at 1.09 THz, supposing a plane wave impinging on the unit cell under 16° oblique incidence in TE polarization. These specific operating conditions have been implemented in the numerical simulations to take into account the restrictions imposed by the experimental setup. However, it has been shown in Ref. [28] how the proposed narrow-band MMA exhibits a wide angular response for both TE and Transverse Magnetic (TM) polarizations as the incidence angle θ varies (see Fig. 8.1(b)), even if the TE case exhibits the more critical working conditions. Indeed, under oblique incidence in TE polarization, the absorbance levels undergo a monotonic decrease with the increase of the incidence angle, while in TM polarization the resonance peaks maintain high absorbance levels even under 80° incidence.

8.3 Fabricated prototype

In order to manufacture the device, we adopted the top-down fabrication approach using standard microfabrication techniques. The MMA sample was fabricated on a high-resistivity $360\ \mu\text{m}$ -thick silicon substrate that also serves as a support for the structure. The manufacturing procedure consisted of five main fabrication steps: first (see Fig. 8.2(a)), on the silicon substrate cleaned with a buffered HF solution, a metal film was deposited by gun evaporator (10 nm of Cr adhesion layer and 100 nm of Au metal mirror); subsequently a $5.4\ \mu\text{m}$ -thick polyimide (PI-2611, HD Microsystems) middle layer was deposited onto the Au film by spin-coating and cured in vacuum oven at $250\ ^\circ\text{C}$ (see Fig. 8.2(b)). Then (see Fig. 8.2(c)-(d)), on the polyimide layer, the geometry of the unit cell, a

8. Polarization-Maintaining Reflection-mode THz-TDS of a 186 Polyimide Based Ultra-Thin Narrow-Band MMA

matrix consisting of $6 \text{ cm} \times 6 \text{ cm}$ of total active area (750×750 unit cells), was patterned with a UV-inverted resist (AZ 5214 E, MicroChemicals) using standard lithography process (Mask Aligner Karl Suss MA160); finally (see Fig. 8.2(e)), a second metal layer was evaporated (10 nm Cr adhesion layer and 100 nm of Au) obtaining the final structure after lift-off procedure in acetone (see Fig. 8.2(f)).

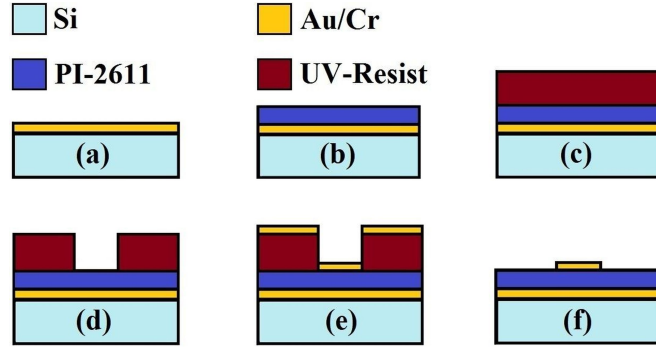


Figure 8.2: Schematic cross-sectional view of the fabrication process flow of a single unit cell. Steps of the fabrication process flow: (a) thermal evaporation of metal Au/Cr; (b) deposition of polyimide PI-2611; (c) deposition of UV-resist by spin-coating; (d) UV patterning process; (e) second thermal evaporation of metal Au/Cr; (f) removing of residual UV-resist by acetone.

In Fig. 8.3(a)-(b), the optical microscope images of the completed device are reported, while in Fig. 8.3(c)-(d), the Atomic Force Microscopy (AFM) inspection of the unit cell shows that we reached a good control in the process fabrication flow obtaining a good definition of the tips and a sharp vertical wall of the final metal film.

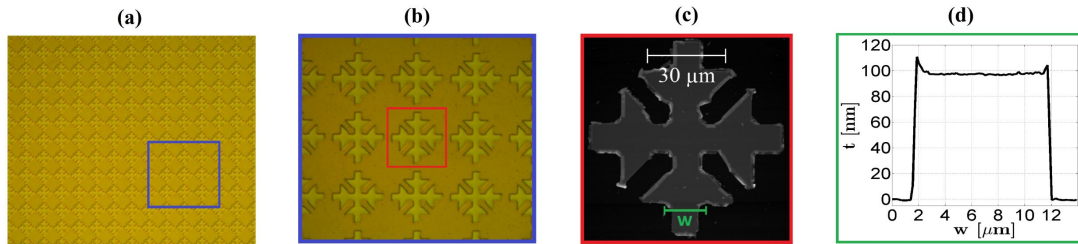


Figure 8.3: Optical microscope image illustrations and AFM inspection of the fabricated MMA. (a) Optical image of MMA large area; (b) optical image of ERRs details; (c) AFM inspection of a single unit cell; (d) AFM characterization of the arm width $w = 11 \mu\text{m}$ profile, where $t = 100 \text{ nm}$ is the metal thickness.

8.4 Experimental setup for polarization-maintaining reflection-mode THz-TDS

In order to characterize the electromagnetic behavior of the MMA in the THz range, a THz-TDS system in reflection mode has been devised (see Fig. 8.4(a) and Fig. 8.5 for more details). This setup is based on a standard Menlo Systems

(Germany) TERA K15 configuration [44–46] and it is designed to minimize the mobile optical and mechanical parts (mirrors, lenses, and mechanical mountings). This is to avoid alignment errors, which might result in differences in THz pulses path length and phase errors, altering the measured signals and making difficult the comparison with the theoretical predictions. Terahertz radiation is generated by photoconductive antennae that allow the optical to THz signal conversion [5]. The antennae are excited by a femtosecond fiber-coupled laser (Menlo Systems T-Light) with an emission wavelength of 1560 nm, a repetition frequency of 100 MHz, and pulse duration of nearly 90 fs. The remote control station of the THz-TDS system is constituted by an amplifier with the aim of amplifying the detected amplitude signal, an A/D converter and a PC for control and preliminary data processing (Fig. 8.4(a)).

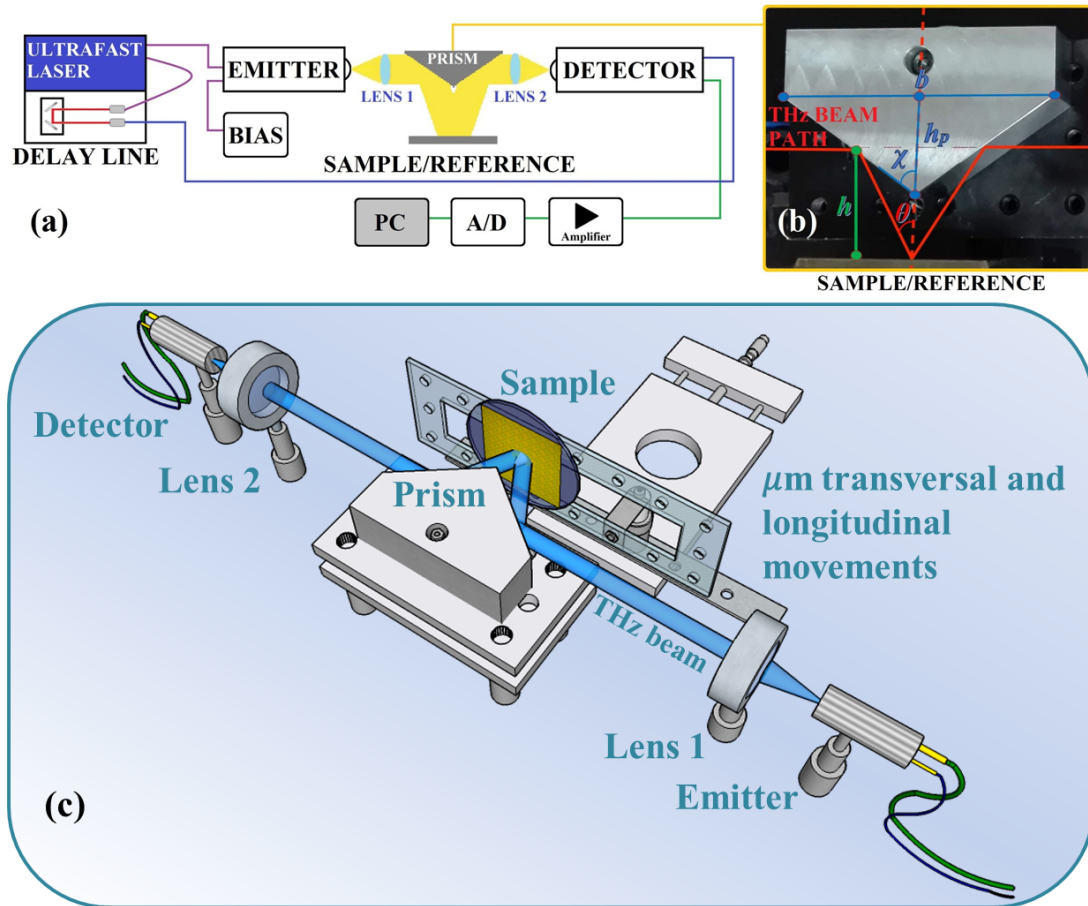


Figure 8.4: Sketch of the polarization-maintaining reflection-mode THz-TDS system and detail of the fabricated Al prism. (a) Experimental THz-TDS setup, (b) geometry of the aluminum prism with $\chi = 54.7^\circ$, $h_p = 19$ mm, $h = 38$ mm, and $b = 54$ mm, and (c) 3D representation of the THz beam line.

For the purpose of realizing the reflection configuration, the THz beam line of the system was designed by using a couple of HRFZ-Si plano-convex lenses with effective focal length $f = 25$ mm and a custom metallic aluminum prism

(Fig. 8.4(a)-(c)). The diverging THz radiation emitted by the emitter antenna is collected and collimated in a beam with a diameter of about 12 mm by means of the first lens (Lens 1 in Fig. 8.4(a)-(c)). Radiation collimated by Lens 1 impinges onto the prism and it is then reflected onto the sample (see Fig. 8.4(b)). Radiation reflected by the sample is reflected by the prism along the THz beam axis, while the second identical lens (Lens 2) permits the THz beam to be focused on the detector antenna. This realizes a reflection-mode collimated configuration in which the 12 mm diameter collimated beam of TE polarized THz wave impinges obliquely on the sample/reference with an angle θ of about 16° imposed by the prism geometry.

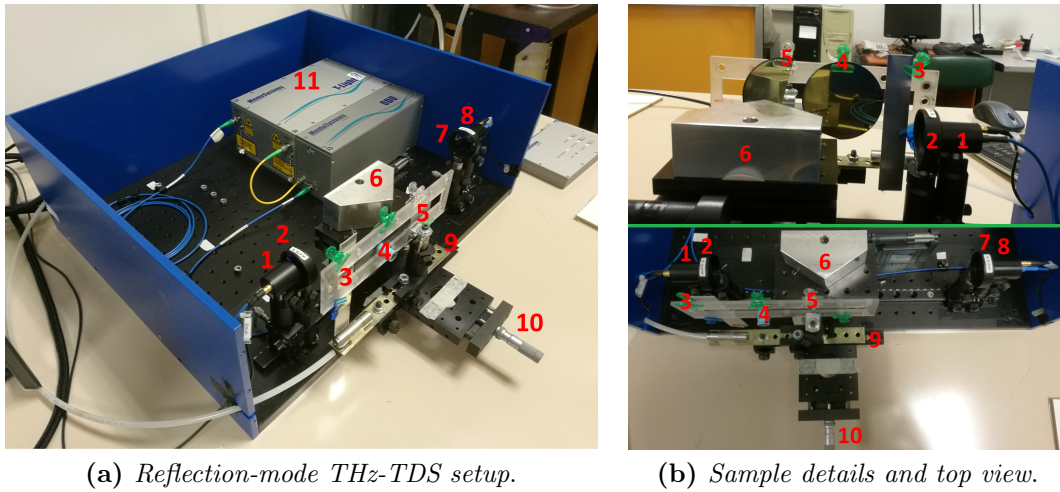


Figure 8.5: (a) Physical realization of the reflection-mode THz-TDS setup with (b) samples fixed on the perspex sample holder and THz wave path top view: (1) emitter antenna; (2) HRFZ-Si plano-convex lens (Lens 1); (3) aluminum reference sample; (4) MMA sample; (5) polyimide reference sample; (6) aluminum prism; (7) HRFZ-Si plano-convex lens (Lens 2); (8) detector antenna; (9) longitudinal movement; (10) micrometric transversal movement; (11) femtosecond laser source at 1560 nm emission wavelength and fiber coupled optical light path with delay line.

It is to be noted that the THz beam line of the reflection-mode THz-TDS system has been optimized employing only two identical plano-convex lenses and a custom aluminum prism reflector which determines the incidence and reflection angles on the MMA, thus maintaining the project requirements for a linearly polarized incident plane wave. Further, the choice of a compact setup in which the THz radiation interacts with a small number of components (two lenses and a metal prism) is functional to minimize disturbing effects for both the polarization and the propagation of THz beam, which are instead likely present when one or more parabolic mirrors are used to manipulate the THz optical path.

The aluminum prism shown in Fig. 8.4(b), has been properly designed to allow

the collimation of the THz beam on the sample following the derived relations:

$$\chi = \cot^{-1} \sqrt{1 - \frac{h_p}{h}}, \quad (8.1)$$

$$b = \frac{h_p}{\sqrt{1 - \frac{h_p}{h}}}, \quad (8.2)$$

where χ is the semi-angle of the lower vertex of the prism, h_p is its height, h is the distance between the axis of the incident THz beam on the prism and the sample surface, and b is the basis of the prism (see Section B.1 in Appendix B).

All the optical elements in the THz beam path were embedded in a dry nitrogen purged chamber at a relative humidity of about 4% in order to reduce the water vapor contribution, particularly present in the frequency band of interest. All spectroscopic measurements were performed at room temperature.

The MMA (sample) and a reference made of an aluminum sheet of 970 μm thickness were placed at about 36.5 mm from the lower vertex of the prism.

The electric field of the THz pulses propagating with the MMA sample and with the aluminum reference was measured. The THz pulses were averaged over 400 scans of the delay line with an overall acquisition time of 50 s and a delay line scan range of 100 ps. By applying the Fast Fourier Transform (FFT) to the acquired signals, the sample and reference THz electric field spectral amplitudes and phases were obtained as a function of frequency. The acquisition parameters of the THz setup determines the frequency spectrum resolution $\Delta f = 1/(N\Delta t) = 10.02$ GHz, being the time resolution of the THz pulses $\Delta t = 33.36$ fs and the measured data points $N = 2992$.

In the measurement setup, the correct placement of the surfaces of the MMA sample and of the aluminum reference at the same distance from the lower vertex of the aluminum prism is fundamental in order to avoid differences in THz pulses path length and phase error. For this reason, a specific sample holder allowing longitudinal and perpendicular micrometric displacement with respect to the lower vertex of the aluminum prism was employed. Finally, in order to obtain the complex spectral reflection S_{11} , i.e., the transfer function of the system which reports on the amplitude and phase changes due to absorbance and refraction of the MMA for a far-field characterization, I have divided the sample spectrum E_{sam} by the reference spectrum E_{ref} :

$$S_{11} = |S_{11}|e^{j\angle S_{11}} = \frac{|E_{sam}|}{|E_{ref}|}e^{j(\angle E_{sam} - \angle E_{ref})}. \quad (8.3)$$

The absorbance can be, therefore, obtained by: $A(\omega) = 1 - |S_{11}(\omega)|^2 = 1 - R(\omega)$,

where reflectance is defined as $R(\omega) = |S_{11}(\omega)|^2$. This because the THz waves cannot be transmitted through the Si substrate due to the lower gold ground plane thicker than the penetration depth and, consequently, the transmittance of the MMA $T(\omega) = |S_{21}(\omega)|^2$ is negligible.

8.5 Simulation and experimental results

One of the main aims of this work was to experimentally characterize the MMA in view of the optimizations of its performances under its more critical operating conditions, i.e., under oblique incidence in TE polarization [28]. In this case, the absorbance levels of the investigated MMA are typically lower, because the four-fold rotational symmetry [47, 48] of the resonator about the propagation axis cannot be fully exploited. Due to the presence of the lower metallic ground plate which prevents transmittance of the THz wave, we properly devised a compact polarization-maintaining THz-TDS setup in reflection-mode able to guarantee a collimated configuration of the THz beam for oblique incidence analysis in TE polarization as described in the previous Section.

Therefore the electromagnetic response of the ultra-thin MMA has been measured as a function of the azimuthal angle φ to verify the polarization insensitivity, rotating the sample of 0, 22.5, 45, 67.5, and 90 degrees with respect to the horizontal arm of the crossed-shaped ERR. As expected, thanks to the four-fold rotational symmetry of the MMA, the absorbance levels for the different values of φ are nearly equal and comprised between 67% and 74%, even under oblique incidence, as shown in Fig. 8.6(a) (see Figs. B.2-B.4 in Appendix B).

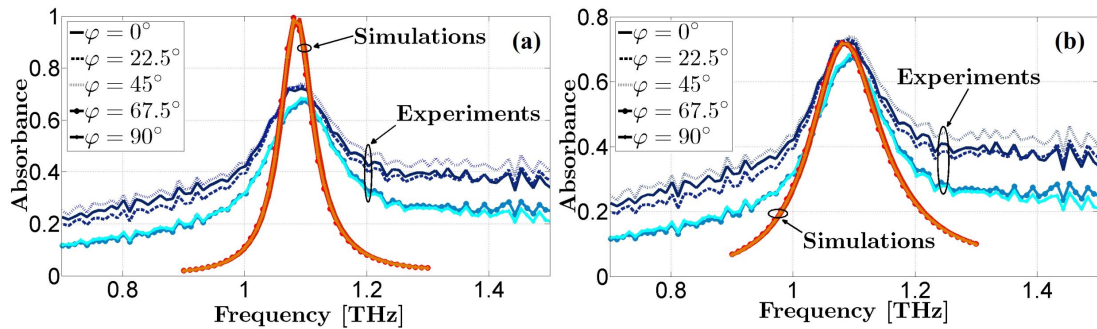


Figure 8.6: Comparison between simulated and experimental absorbance spectra as a function of the azimuthal angle φ with different polyimide loss tangent values under 16° oblique incidence in TE polarization. The simulations have been performed with the complex permittivity value (a) $\varepsilon_r = 2.9 - 0.0058j$ and with the estimated complex permittivity value (b) $\varepsilon_r = 2.9 - 0.25j$ for the polyimide layer.

The measured absorbance $A(\omega)$ differs from the near-unity value of the one simulated, and this discrepancy is mainly due to values of the material parameters used in the simulation for describing the MMA. A possible reason for the mismatch between the simulations and the measurements can be attributed to

higher Ohmic losses of the metal layers, being the electrical conductivity of thin Au films at THz frequencies much smaller than its bulk dc value [14, 49]. Relying on the published results in Ref. [49] and having performed the spectroscopic measurements at room temperature, I have considered a halved electrical conductivity $\sigma = 2 \times 10^7$ S/m for the 100 nm-thick metallizations in the full-wave simulations. However, this has produced only a slight reduction of the absorption level (considering an almost lossless polyimide dielectric layer) and a slight broadening of the bandwidth (see Fig. B.5 in Appendix B).

Instead, the dielectric losses of the polyimide spacer have been found to have a pronounced effect on the simulated results; indeed, the permittivity and loss tangent selected in the simulations were based on datasheet reported in Ref. [32]. In the literature, there are many published papers [34–39] in which the polyimide is treated as a dielectric with an a priori assumed permittivity value at THz frequencies. In the light of the foregoing considerations, I have determined a different value for the loss tangent of the polyimide, through parametric sweeps in order to match the measurements. I have found an estimated loss tangent $\tan \delta = 0.086$ to which corresponds a complex relative permittivity $\epsilon_r = 2.9 - 0.25j$ for the polyimide layer. Figure 8.6(b) shows the comparison between the simulations with the modified permittivity and the experiments which are now in a better agreement, with a remarkable resonance at about 1.092 THz.

8.6 Conclusions

An ultra-thin narrow-band MMA has been simulated and microfabricated in the THz regime: its performance has been experimentally characterized by using a custom collimated configuration reflection-mode THz-TDS.

The realization of the MMA needs five main fabrication steps with only one lithographic phase: because the bottom layer is a continuous metal film, no alignment between the metal layers is needed. Therefore, the fabrication process is noticeably simplified with respect to other available solutions, for example that presented in Ref. [24] which implies the control of misalignment errors between the two stacked crossed-shaped metallizations, resulting in lower production time and costs. In addition, the lower ground plane avoids the influence of the support Si substrate that produced in Ref. [24] uncertainty in the definition of the unit cell, as well as a not negligible asymmetry in the propagation direction due to the bianisotropy of the ERR design.

In order to experimentally characterize the MMA, a commercial Menlo Systems TERA K15 standard transmission configuration has been modified by inserting a fixed angle aluminum reflector in the collimated THz beam path. This permits the collimation of THz radiation on the sample/reference with a specific incidence angle, allowing investigating the MMA under oblique incidence. The

devised reflection-mode THz-TDS setup is polarization-maintaining because it does not use parabolic mirrors to manipulate the THz beam, allowing the characterization of polarization-sensitive devices and ensuring a wide reproducibility of the measurements.

The experimental results, carried out as a function of the azimuthal angle, have proved the high polarization insensitivity of the MMA even under 16° oblique incidence with absorbance levels comprised between 67% and 74% at 1.092 THz and a Full-Width-at-Half-Maximum (FWHM) of the absorption band of about 0.2 THz. The observed mismatch of the experimental FWHM with the full-wave simulations has been found to chiefly depend on the value of dielectric losses of the polyimide spacer. A good agreement with the experimental results has then been obtained by adjusting the value of the loss tangent of the polyimide spacer to $\tan \delta = 0.086$.

Furthermore, the proposed ultra-thin MMA has been realized with a highly flexible polyimide middle layer which expands its uses in non-planar applications. The MMA can be made actually flexible by spin-coating a further layer of polyimide on the Si substrate [40, 41], which represents only a mechanical support, not actively contributing to the absorption mechanism. The MMA can thus be regarded as a flexible metasurface which can be wrapped around non-planar surfaces and exploited to cover objects of considerable size.

These features make the device particularly suited for spectroscopic applications in several fields such as detection of explosive materials, THz imaging, electromagnetic cloaking, medical diagnoses, and spectrally selective security detection. The ultra-thin profile, the narrow spectral band of absorption and the polarization insensitivity, as well as the potential flexibility, open up also interesting prospects in the design of wearable THz MMAs.

The results of the current analysis have been published in Ref. [1].

References

- [1] M. D. Astorino, R. Fastampa, F. Frezza, L. Maiolo, M. Marrani, M. Missori, M. Muzi, N. Tedeschi, and A. Veroli, "Polarization-maintaining reflection-mode THz time-domain spectroscopy of a polyimide based ultra-thin narrow-band metamaterial absorber," *Scientific Reports*, vol. 8, no. 1, p. 1985, 2018.
- [2] J. M. Chamberlain, "Where optics meets electronics: recent progress in decreasing the terahertz gap," *Philosophical Transactions of the Royal Society of London A: Mathematical, Physical and Engineering Sciences*, vol. 362, no. 1815, pp. 199–213, 2004.
- [3] S. S. Dhillon, M. S. Vitiello, E. H. Linfield, A. G. Davies, M. C. Hoffmann, J. Booske, C. Paoloni, M. Gensch, P. Weightman, G. P. Williams, E. Castro-Camus, D. R. S. Cumming, F. Simoens, I. Escorcia-Carranza, J. Grant, S. Lucyszyn, M. Kuwata-Gonokami, K. Konishi, M. Koch, C. A. Schmuttenmaer, T. L. Cocker, R. Huber, A. G. Markelz, Z. D. Taylor, V. P. Wallace, J. A. Zeitler, J. Sibik, T. M. Korter, B. Ellison, S. Rea, P. Goldsmith, K. B. Cooper, R. Appleby, D. Pardo, P. G. Huggard, V. Krozer, H. Shams, M. Fice, C. Renaud, A. Seeds, A. Stöhr, M. Naftaly, N. Ridler, R. Clarke, J. E. Cunningham, and M. B. Johnston, "The 2017 terahertz science and technology roadmap," *Journal of Physics D: Applied Physics*, vol. 50, no. 4, p. 043001, 2017.
- [4] Y. Lee, *Principles of Terahertz Science and Technology*. Springer Science+Business Media, LLC, 2009.
- [5] P. U. Jepsen, D. G. Cooke, and M. Koch, "Terahertz spectroscopy and imaging—modern techniques and applications," *Laser & Photonics Reviews*, vol. 5, no. 1, pp. 124–166, 2011.
- [6] F. Huang, B. Schulkin, H. Altan, J. F. Federici, D. Gary, R. Barat, D. Zimdars, M. Chen, and D. Tanner, "Terahertz study of 1, 3, 5-trinitro-s-triazine by time-domain and Fourier transform infrared spectroscopy," *Applied Physics Letters*, vol. 85, no. 23, pp. 5535–5537, 2004.
- [7] B. Fischer, M. Hoffmann, H. Helm, G. Modjesch, and P. U. Jepsen, "Chemical recognition in terahertz time-domain spectroscopy and imaging," *Semiconductor Science and Technology*, vol. 20, no. 7, p. S246, 2005.
- [8] J. F. Federici, B. Schulkin, F. Huang, D. Gary, R. Barat, F. Oliveira, and D. Zimdars, "THz imaging and sensing for security applications—explosives, weapons and drugs," *Semiconductor Science and Technology*, vol. 20, no. 7, p. S266, 2005.
- [9] B. Ferguson, S. Wang, H. Zhong, D. Abbott, and X.-C. Zhang, "Powder detection with T-ray imaging," in *Proceedings of SPIE*, vol. 5070, pp. 7–16, Orlando, FL, USA, 2003.
- [10] R. Appleby and H. B. Wallace, "Standoff detection of weapons and contraband in the 100 GHz to 1 THz region," *IEEE Transactions on Antennas and Propagation*, vol. 55, no. 11, pp. 2944–2956, 2007.
- [11] C. M. Watts, X. Liu, and W. J. Padilla, "Metamaterial electromagnetic wave absorbers," *Advanced Materials*, vol. 24, no. 23, 2012.
- [12] C. Sabah, F. Dincer, M. Karaaslan, E. Unal, and O. Akgol, "Polarization-insensitive FSS-based perfect metamaterial absorbers for GHz and THz frequencies," *Radio Science*, vol. 49, no. 4, pp. 306–314, 2014.
- [13] Y. Ra'Di, C. Simovski, and S. Tretyakov, "Thin perfect absorbers for electromagnetic waves: theory, design, and realizations," *Physical Review Applied*, vol. 3, no. 3, p. 037001, 2015.
- [14] M. P. Hokmabadi, D. S. Wilbert, P. Kung, and S. M. Kim, "Design and analysis of perfect terahertz metamaterial absorber by a novel dynamic circuit model," *Optics Express*, vol. 21, no. 14, pp. 16455–16465, 2013.
- [15] C. Caloz and T. Itoh, *Electromagnetic metamaterials: transmission line theory and microwave applications*. John Wiley & Sons, 2005.
- [16] D. R. Smith, W. J. Padilla, D. Vier, S. C. Nemat-Nasser, and S. Schultz, "Composite medium with simultaneously negative permeability and permittivity," *Physical Review Letters*, vol. 84, no. 18, p. 4184, 2000.

- [17] V. G. Veselago, "The electrodynamics of substances with simultaneously negative values of ϵ and μ ," *Soviet Physics Uspekhi*, vol. 10, no. 4, p. 509, 1968.
- [18] R. A. Shelby, D. R. Smith, and S. Schultz, "Experimental verification of a negative index of refraction," *Science*, vol. 292, no. 5514, pp. 77–79, 2001.
- [19] H. Tao, W. J. Padilla, X. Zhang, and R. D. Averitt, "Recent progress in electromagnetic metamaterial devices for terahertz applications," *IEEE Journal of Selected Topics in Quantum Electronics*, vol. 17, no. 1, pp. 92–101, 2011.
- [20] X. Hu, G. Xu, L. Wen, H. Wang, Y. Zhao, Y. Zhang, D. R. Cumming, and Q. Chen, "Metamaterial absorber integrated microfluidic terahertz sensors," *Laser & Photonics Reviews*, vol. 10, no. 6, pp. 962–969, 2016.
- [21] T. Maier and H. Brückl, "Wavelength-tunable microbolometers with metamaterial absorbers," *Optics Letters*, vol. 34, no. 19, pp. 3012–3014, 2009.
- [22] H. Tao, N. I. Landy, C. M. Bingham, X. Zhang, R. D. Averitt, and W. J. Padilla, "A metamaterial absorber for the terahertz regime: Design, fabrication and characterization," *Optics Express*, vol. 16, no. 10, pp. 7181–7188, 2008.
- [23] K. Iwaszczuk, A. C. Strikwerda, K. Fan, X. Zhang, R. D. Averitt, and P. U. Jepsen, "Flexible metamaterial absorbers for stealth applications at terahertz frequencies," *Optics Express*, vol. 20, no. 1, pp. 635–643, 2012.
- [24] N. Landy, C. Bingham, T. Tyler, N. Jokerst, D. Smith, and W. Padilla, "Design, theory, and measurement of a polarization-insensitive absorber for terahertz imaging," *Physical Review B*, vol. 79, no. 12, p. 125104, 2009.
- [25] S. Zhang, W. Fan, N. Panoiu, K. Malloy, R. Osgood, and S. Brueck, "Experimental demonstration of near-infrared negative-index metamaterials," *Physical Review Letters*, vol. 95, no. 13, p. 137404, 2005.
- [26] B. Alam, A. Veroli, and A. Benedetti, "Analysis on vertical directional couplers with long range surface plasmons for multilayer optical routing," *Journal of Applied Physics*, vol. 120, no. 8, p. 083106, 2016.
- [27] N. I. Landy, S. Sajuyigbe, J. Mock, D. Smith, and W. Padilla, "Perfect metamaterial absorber," *Physical Review Letters*, vol. 100, no. 20, p. 207402, 2008.
- [28] M. D. Astorino, F. Frezza, and N. Tedeschi, "Ultra-thin narrow-band, complementary narrow-band, and dual-band metamaterial absorbers for applications in the THz regime," *Journal of Applied Physics*, vol. 121, no. 6, p. 063103, 2017.
- [29] M. Fu, X. Wang, S. Wang, Z. Xie, S. Feng, W. Sun, J. Ye, P. Han, and Y. Zhang, "Efficient terahertz modulator based on photoexcited graphene," *Optical Materials*, vol. 66, pp. 381–385, 2017.
- [30] A. Taschin, P. Bartolini, J. Tasseva, and R. Torre, "THz time-domain spectroscopic investigations of thin films," *Measurement*, 2017.
- [31] M. D. Astorino, F. Frezza, and N. Tedeschi, "Broad-band terahertz metamaterial absorber with stacked electric ring resonators," *Journal of Electromagnetic Waves and Applications*, vol. 31, no. 7, pp. 727–739, 2017.
- [32] HD MicroSystems, *Product Bulletin PI-2600 Series - Low Stress Applications*, September 2009.
- [33] Y. Yoo, J. Hwang, and Y. Lee, "Flexible perfect metamaterial absorbers for electromagnetic wave," *Journal of Electromagnetic Waves and Applications*, vol. 31, no. 7, pp. 663–715, 2017.
- [34] L. Huang, D. R. Chowdhury, S. Ramani, M. T. Reiten, S.-N. Luo, A. K. Azad, A. J. Taylor, and H.-T. Chen, "Impact of resonator geometry and its coupling with ground plane on ultrathin metamaterial perfect absorbers," *Applied Physics Letters*, vol. 101, no. 10, p. 101102, 2012.
- [35] W. Tan, C. Zhang, C. Li, X. Zhou, X. Jia, Z. Feng, J. Su, and B. Jin, "Selective coherent perfect absorption of subradiant mode in ultrathin bi-layer metamaterials via antisymmetric excitation," *Applied Physics Letters*, vol. 110, no. 18, p. 181111, 2017.

- [36] Y. Ishii, Y. Takida, Y. Kanamori, H. Minamide, and K. Hane, "Fabrication of metamaterial absorbers in THz region and evaluation of the absorption characteristics," *Electronics and Communications in Japan*, vol. 100, no. 4, pp. 15–24, 2017.
- [37] B.-X. Wang, G.-Z. Wang, and L.-L. Wang, "Design of a novel dual-band terahertz metamaterial absorber," *Plasmonics*, vol. 11, no. 2, pp. 523–530, 2016.
- [38] W. Pan, X. Yu, J. Zhang, and W. Zeng, "A broadband terahertz metamaterial absorber based on two circular split rings," *IEEE Journal of Quantum Electronics*, vol. 53, no. 1, pp. 1–6, 2017.
- [39] Y. Ma, Q. Chen, J. Grant, S. C. Saha, A. Khalid, and D. R. Cumming, "A terahertz polarization insensitive dual band metamaterial absorber," *Optics Letters*, vol. 36, no. 6, pp. 945–947, 2011.
- [40] J.-H. Kim, M. P. Hokmabadi, S. Balci, E. Rivera, D. Wilbert, P. Kung, and S. M. Kim, "Investigation of robust flexible conformal THz perfect metamaterial absorber," *Applied Physics A*, vol. 122, no. 4, p. 362, 2016.
- [41] M. P. Hokmabadi, E. Philip, E. Rivera, P. Kung, and S. M. Kim, "Plasmon-induced transparency by hybridizing concentric-twisted double split ring resonators," *Scientific Reports*, vol. 5, 2015.
- [42] A. Pecora, L. Maiolo, M. Cuscunà, D. Simeone, A. Minotti, L. Mariucci, and G. Fortunato, "Low-temperature polysilicon thin film transistors on polyimide substrates for electronics on plastic," *Solid-State Electronics*, vol. 52, no. 3, pp. 348–352, 2008.
- [43] L. Maiolo, A. Pecora, F. Maita, A. Minotti, E. Zampetti, S. Pantalei, A. Macagnano, A. Bearzotti, D. Ricci, and G. Fortunato, "Flexible sensing systems based on polysilicon thin film transistors technology," *Sensors and Actuators B: Chemical*, vol. 179, pp. 114–124, 2013.
- [44] R. Fastampa, L. Pilozzi, and M. Missori, "Cancellation of Fabry-Perot interference effects in terahertz time-domain spectroscopy of optically thin samples," *Phys. Rev. A*, vol. 95, p. 063831, 2017.
- [45] M. Peccianti, R. Fastampa, A. Mosca Conte, O. Pulci, C. Violante, J. Łojewska, M. Clerici, R. Morandotti, and M. Missori, "Terahertz absorption by cellulose: Application to ancient paper artifacts," *Phys. Rev. Appl*, vol. 7, p. 064019, 2017.
- [46] A. Ferraro, D. C. Zografopoulos, M. Missori, M. Peccianti, R. Caputo, and R. Beccherelli, "Flexible terahertz wire grid polarizer with high extinction ratio and low loss," *Opt. Lett.*, vol. 41, pp. 2009–2012, 2016.
- [47] J. Grant, Y. Ma, S. Saha, L. Lok, A. Khalid, and D. Cumming, "Polarization insensitive terahertz metamaterial absorber," *Optics Letters*, vol. 36, no. 8, pp. 1524–1526, 2011.
- [48] J. Grant, Y. Ma, S. Saha, A. Khalid, and D. R. Cumming, "Polarization insensitive, broadband terahertz metamaterial absorber," *Optics Letters*, vol. 36, no. 17, pp. 3476–3478, 2011.
- [49] N. Laman and D. Grischkowsky, "Terahertz conductivity of thin metal films," *Applied Physics Letters*, vol. 93, no. 5, p. 051105, 2008.

Transmission and Reflection Modes THz-TDS Characterization of Polyimide-based Metamaterial Devices

Experimental characterization results of highly flexible polyimide sheets with increasing thicknesses, and of ultra-thin THz metasurfaces are presented in this Chapter by using transmission-mode THz Time-Domain Spectroscopy (THz-TDS). An alternative reflection-mode THz-TDS setup has been employed to further analyze the angular electromagnetic behavior of the narrow-band metamaterial absorber described in Chapter 8. These polyimide-based metamaterial samples have demonstrated substantial environmental stability as well as high-performance repeatability.

9.1 Introduction

The rapidly developing research field of metamaterial devices, such as cloaks [1], concentrators [2] and absorbers [3], has paved the way for new fabrication strategies and more accurate material characterizations.

In this scenario, metasurfaces [4], i.e. two-dimensional metamaterials of sub-wavelength thickness in the wave propagation direction, have found many practical applications by enabling spatially varying electromagnetic/optical responses [5], waveform shaping [6], polarization conversion [7] and beam forming [8]. At terahertz frequencies, promising applications are in spatial light modulators [9], where metasurfaces act as flat compact platforms capable of giving rise to strong light-material interactions. The metasurface-based modulators reach an increase of the modulation speed extremely useful in imaging, light detection and ranging (LIDAR), remote sensing, security, and free-space communications [10]. Also, metasurfaces have potential applications in THz filters, transparent THz windows, and THz grid structures in THz switching devices [11–14].

9. Transmission and Reflection Modes THz-TDS Characterization of Polyimide-based Metamaterial Devices

Functional materials and flexible polymers can enhance the potentialities of THz metasurfaces in non-planar applications and multilayer devices, being able to be readily micro-fabricated with standard photolithography [15]. The use of highly flexible materials has offered substantial advantages for the realization of low loss frequency tunable metamaterial devices [16, 17]. This flexibility becomes instrumental in the overcoming of the intrinsic limits of Far Infrared Radiation (FIR) filters [18, 19] and Frequency Selective Surfaces (FSSs) [20], which are generally constituted of rigid metallic gratings, not easily adaptable to non-planar surfaces.

The versatility, efficiency, and customizability offered by metasurfaces can be additionally increased by patterning subwavelength metallic resonators, such as Electric Ring Resonators (ERRs), Split-Ring Resonators (SRRs) [21, 22] as well as a large number of elements in FSSs, which tailor the surface impedance and consequently the interface reflection/transmission. Metasurfaces can thus strongly manipulate the impinging electromagnetic waves, despite their ultra-thin thickness, and satisfy the increasing integration requests in electromagnetic/photonic systems [23].

In the design phase of metamaterial devices, it is essential to know the accurate values of the frequency-dependent complex dielectric functions of the materials in use. While for frequencies below 10 THz the metallic elements can still be described by a constant electric conductivity [24], the relative permittivity of dielectrics in the terahertz range generally presents higher losses [25–29]. These discrepancies can affect the simulation results obtained by commercial electromagnetic solvers with repercussions in terms of time and costs on the prototype stage. As an example, the performances of the FSSs printed on dielectric substrates depend strongly on the chosen materials, which affect the resonance frequencies and the reflection/transmission spectra [20].

The objective of this Chapter is to investigate the electromagnetic characteristics of polyimide at THz frequencies, even in critical environmental conditions, and to evaluate its effectiveness in the realization of ultra-thin metamaterial devices; to this purpose, various measurements have been operated and described in the following Sections. In Section 9.2, three polyimide PI-2611 sheets [30] of increasing thicknesses have been characterized by means of a transmission-mode THz-TDS setup, in order to obtain the complex refractive index in two case studies: heated at 100 °C and after heating; the details of the polyimide film fabrication are provided. In Section 9.3, the same measurement setup was employed for the characterization of a metasurface on a free-standing, flexible and ultra-thin polyimide substrate; also, the metasurface fabrication recipe is provided. In Section 9.4, the metamaterial absorber (MMA) [31, 32] has been angularly char-

acterized with a reflection-mode THz-TDS setup for incidence angles up to 45° . All the measurements considered here have been performed by using Transverse Electric (TE) linearly polarized THz beam impinging onto the sample/reference. Finally, in Section 9.5, the conclusions are drawn.

9.2 Transmission-mode THz-TDS for polyimide characterization

In order to provide more physical insight into the material properties of the polyimide (PI-2611, HD MicroSystems) previously used for the MMA prototype in Chapter 8, we have fabricated three films with different thicknesses of 32, 55 and $80 \mu\text{m}$.

A transmission-mode THz-TDS setup, based on a standard Menlo Systems (Germany) TERA K15 equipped with photoconductive antennas, was employed to extract the electromagnetic parameters of the ultra-flexible polyimide samples [33, 34]. With this configuration, which is sketched in Fig. 9.1, the transmission of the THz electric field can be measured for both the polyimide samples and the reference (simply air) at normal incidence.

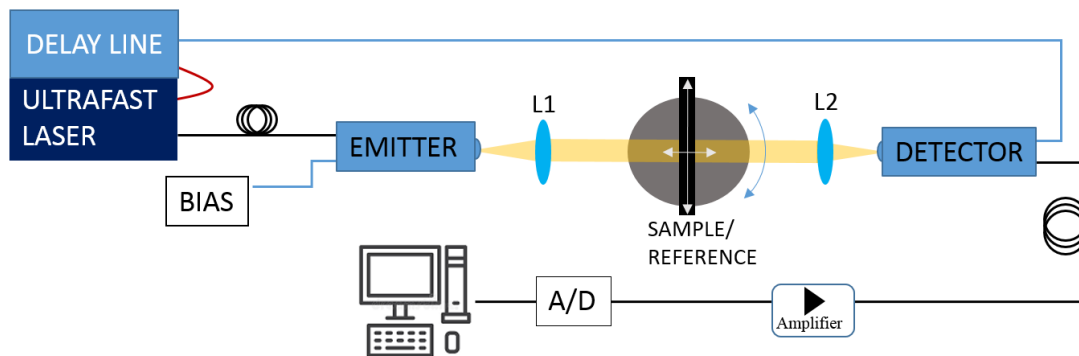


Figure 9.1: Sketch of the THz-TDS setup in transmission configuration.

As indicated by the arrows in Fig. 9.1, the angular measurements are obtained by means of a rotational stage that allows the rotation of the sample with respect to the incident beam line. The employment of two further micrometric movements, longitudinal and transversal, guarantees the correct placement of the samples' and references' surfaces, in order to prevent variations in THz pulses path length and phase error.

The THz beam line of the system was designed by using a couple of identical HRfZ-Si plano-convex lenses with effective focal length $f = 25 \text{ mm}$. The first lens (L1) collects the diverging THz radiation emitted by the emitter antenna and collimates a 12 mm diameter beam on the sample, which is significantly bigger than the THz beam dimension. The second lens (L2) collects the radiation transmitted by the sample and focuses it on the detector antenna. The THz-TDS

9. Transmission and Reflection Modes THz-TDS Characterization of 200 Polyimide-based Metamaterial Devices

is able to reveal the electric field of the THz pulses as a function of time. We acquired the transmitted signal by the samples and, by applying the Fast Fourier Transform (FFT), we have obtained THz electric field spectral amplitudes and phases as a function of frequency. For all acquisitions, the scan range was set to 100 ps; the data were collected with a time resolution of $\Delta t = 33.3$ fs and averaged over 800 waveforms. The acquisition parameters of the THz setup determines the frequency spectrum resolution $\Delta f = 1/(N\Delta t) = 10$ GHz, where the measured data points $N = 3000$.

In order to obtain the transfer function of the system, which provides the amplitude and phase changes due to absorbance and refraction of the samples, we have divided the electric field spectral amplitude of the sample $E_s(\omega)$ by that of the reference $E_{ref}(\omega)$. In the transmission-mode configuration, the reference spectra are obtained as the FFT of the signals transmitted by the empty space. Therefore, the frequency dependent complex transmittance parameter of the sample results:

$$S_{21} = |S_{21}|e^{j\angle S_{21}} = \frac{|E_{sam}|}{|E_{ref}|}e^{j(\angle E_{sam} - \angle E_{ref})}. \quad (9.1)$$

From the S_{21} -parameter, it is possible to extract the frequency dependent complex material parameters, by inverting numerically the Fresnel equations.

The measurements are performed in air at room temperature $T=25$ °C and relative humidity $RH = 30.1\%$.

For the purpose of investigating the potential contribution of the sample's water content on the polyimide losses, we have set two different series of measurements. For the first session of measurements ("dry" case), the three polyimide samples were measured immediately after being heated on a hot plate at 100 °C for five hours. For the second session of measurements ("wet" case), we waited two days after heating the samples on the hot plate to allow the natural sample's hydration.

Figure 9.2 represents the experimentally measured complex refractive index of the polyimide samples for each thickness and conditions (dry/wet).

Recalling the value of the refractive index $n = 1.70 - 0.07j$ (which corresponds to the relative permittivity $\varepsilon_r = 2.9 - 0.25j$) obtained from the parametric simulations in Chapter 8, we can deduce, from the THz-TDS measurements carried out on the three series of polyimide substrates, that the complex value of the refractive index assumes an almost frequency independent behavior in the range from 0.2 to 2.2 THz. More specifically, for each of the three sheets, the real part of the refractive index was about $Re[n] = 1.88$ at 1.09 THz. The imaginary part of the refractive index, instead, presents more variability in its amplitude rang-

ing from 0.012 up to 0.094 for the case of the heated 32 μm -thick layer. This can be due to imperfection in the polyimide substrate and to the influence of the structural chemical properties. However, there was no significant variation on the refractive index values between the dry and wet cases and with the increase of the thickness. Overall, with respect to the nominal value of the polyimide refractive index $n = 1.7029 - 0.0017j$, the polymer investigated here shows a higher imaginary part of n at terahertz frequencies; despite this, due to the high mechanical flexibility (see Fig. 9.3(d)), it is still an interesting and useful candidate material for THz metamaterial devices.

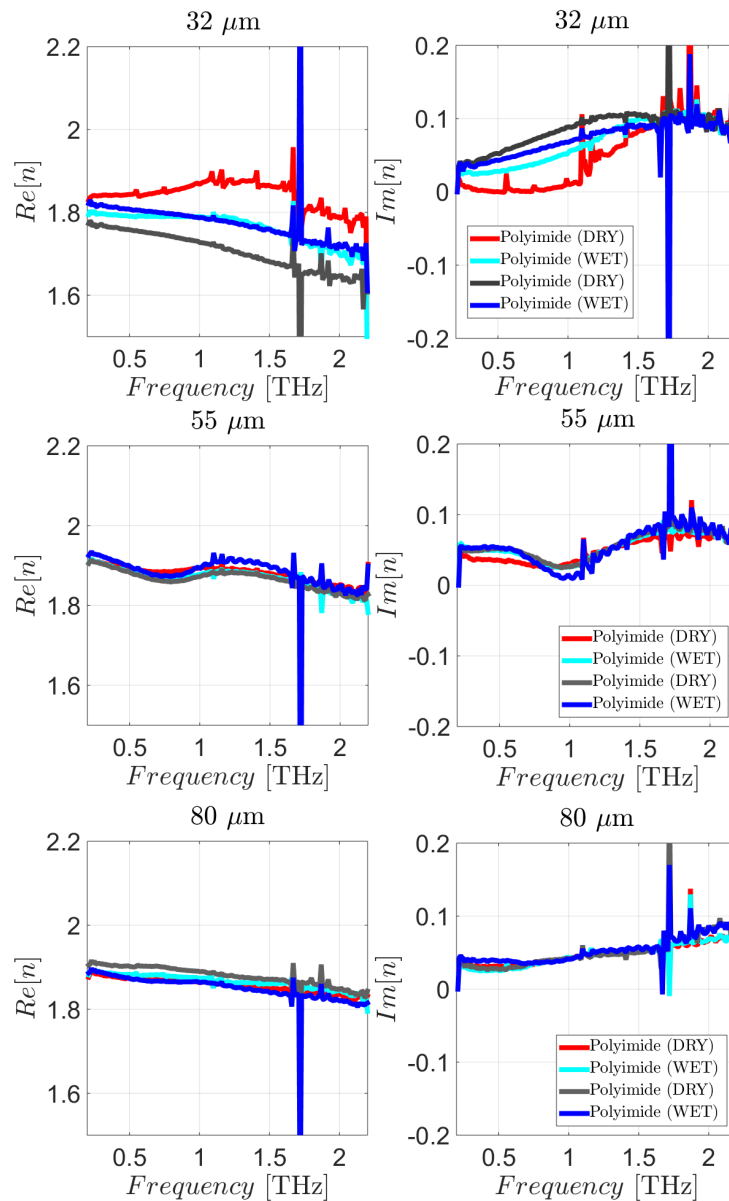


Figure 9.2: Real and imaginary parts of the refractive index for 32, 55, and 80 μm -thick polyimide sheets heated on the hot plate at 100 $^{\circ}\text{C}$ (dry case) and after heating (wet case). The presence of spikes at about 1.7 THz is due to the absorbance peaks of the water.

9. Transmission and Reflection Modes THz-TDS Characterization of Polyimide-based Metamaterial Devices

9.2.1 Polyimide film fabrication

Polyimide films, with increasing thickness up to $80\ \mu\text{m}$ (see Fig. 9.3), have been obtained by depositing multiple layers of PI-2611 through spin-coating technique. Starting from an oxidized silicon wafer, used as substrate, each layer was deposited at 2000 rpm and cured at $150\ ^\circ\text{C}$ on hot plate for 5 minutes, reaching a thickness of $8\ \mu\text{m}$ for each layer. Finally, the foil was cured at $250\ ^\circ\text{C}$ in oven and then mechanically released.

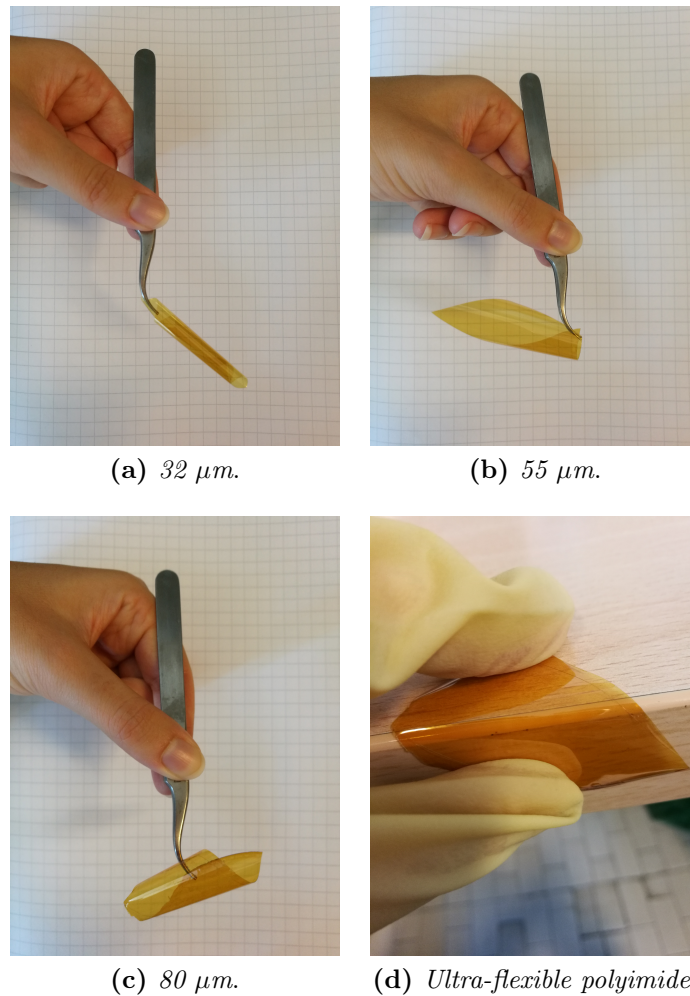


Figure 9.3: Fabricated ultra-flexible polyimide samples of increasing thicknesses of 32, 55, and $80\ \mu\text{m}$.

9.3 Transmission-mode THz-TDS measurements for metasurface characterization

With the aim to further exploit the extremely high flexibility of the previously characterized polyimide, we have fabricated two identical metasurface samples named S1 and S2 with the same ERR pattern of the metamaterial absorber investigated in Chapters 5-8 [31, 32]. This two-layer metasurface is composed of

an ERR top layer of 80 μm periodicity and a 5.4 μm -thick polyimide substrate (see fabrication details in Subsection 9.3.1).

The resonant ERRs on free-standing polyimide substrate have been characterized through the THz-TDS transmission-mode setup schematized in Fig. 9.1. The only difference in the physical implementation shown in Fig. 9.4, is the presence of a dry nitrogen purged chamber at a relative humidity of about 3.6% which embeds all the optical elements in the THz beam path; this reduces the water vapor contribution in the frequency band of interest.

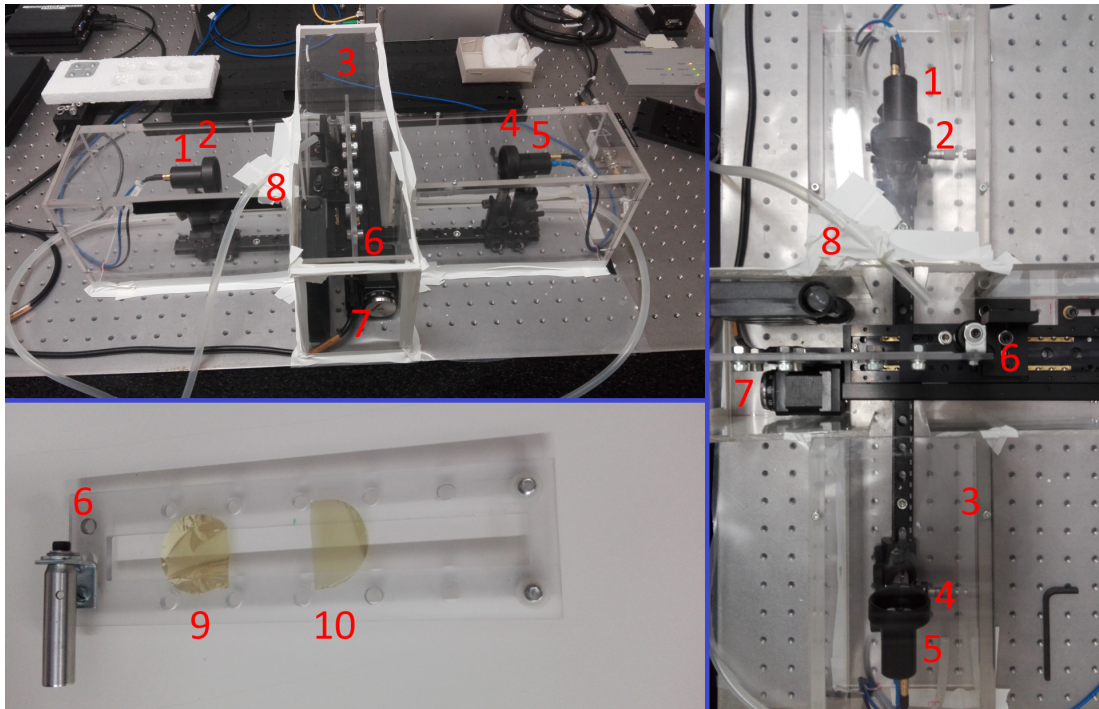


Figure 9.4: THz-TDS transmission mode setup details: (1) emitter antenna; (2) HRFZ-Si plano-convex lens L1; (3) dry nitrogen purged chamber; (4) HRFZ-Si plano-convex lens L2; (5) detector antenna; (6) perspex sample holder; (7) rotational stage and micrometric longitudinal and transversal movements; (8) small tube to flux nitrogen at about 10.2 l/s; (9) first metasurface sample (S1); (10) second metasurface sample (S2).

All the measurements were performed at the temperature of $T=26.4\text{ }^{\circ}\text{C}$ and repeated for three different series, by varying the regions illuminated by the incident THz beam on the samples S1 and S2 to verify the repeatability of the metasurface performances. Also, the position of the perspex sample holder has been translated to allow the THz ray to impinge on different air references in order to account for possible interference effects.

Figures 9.5-9.6 represent the experimentally determined relative electric permittivities and refractive indexes of the two metasurface samples. As we can notice, the electromagnetic responses are almost equal for both the metasurfaces, and the material parameters show a typical Lorentz-like resonant dispersion. The

frequency-dependent effective complex refractive index and relative permittivity are in good agreement with that of Nicolson-Ross-Weir (NRW) [35] algorithm as shown in Figs. 9.5-9.6. It should be noted that, being the measurements conducted at normal incidence, the electric and magnetic fields are in-plane with the metasurface. Therefore, being the magnetic field parallel to the ERR, there is no coupling to the magnetic response and only a pure electric resonant response is obtained. This means that the refractive index and relative permittivity provide a complete description of the electromagnetic behavior of the metasurfaces. In the implementation of the NRW algorithm, the permeability is thus correctly set to unity.

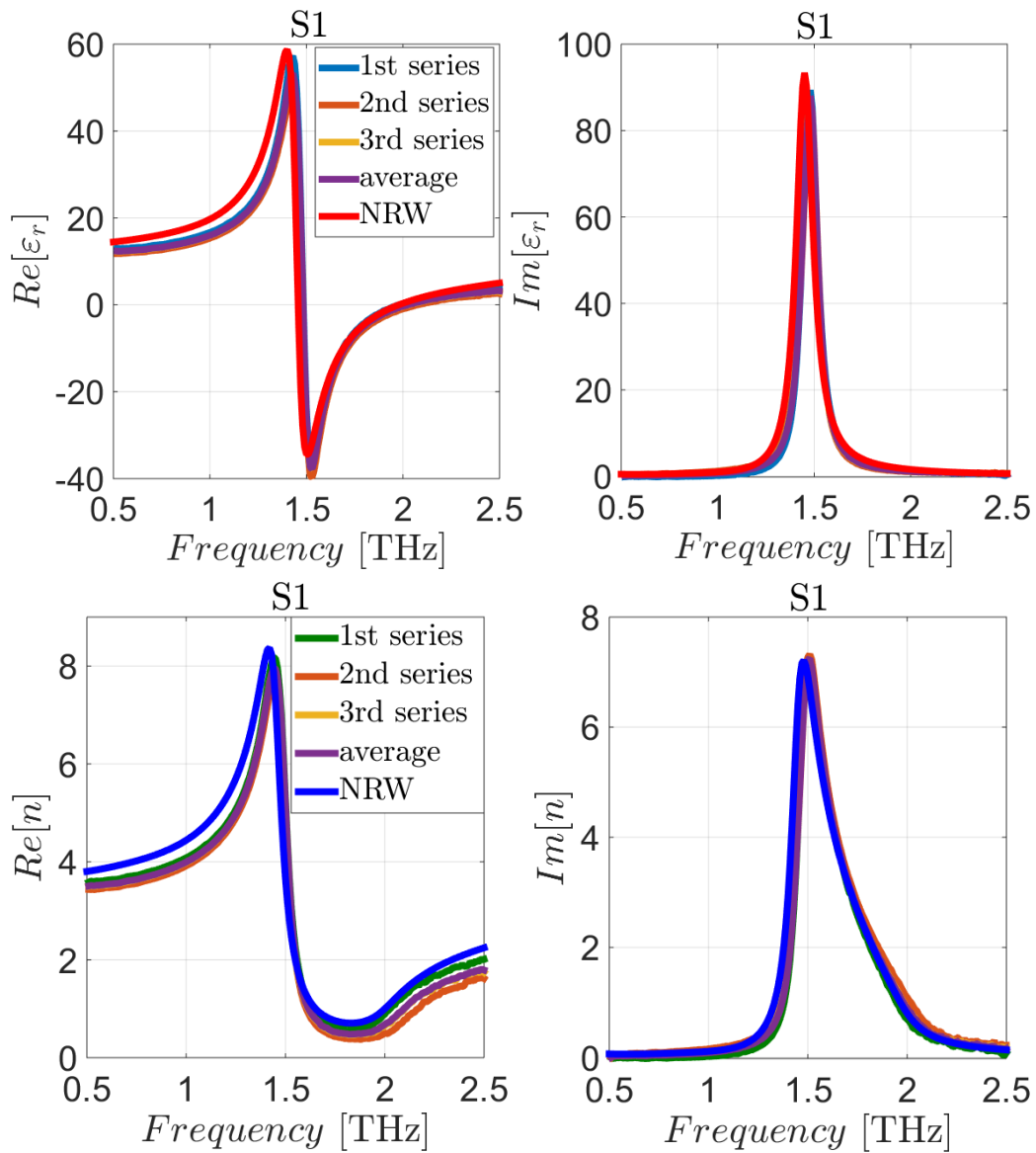


Figure 9.5: Measured complex relative permittivity and refractive index for the metasurface sample S1 for three different series of measurements, average value, and parameters extracted through the NRW algorithm.

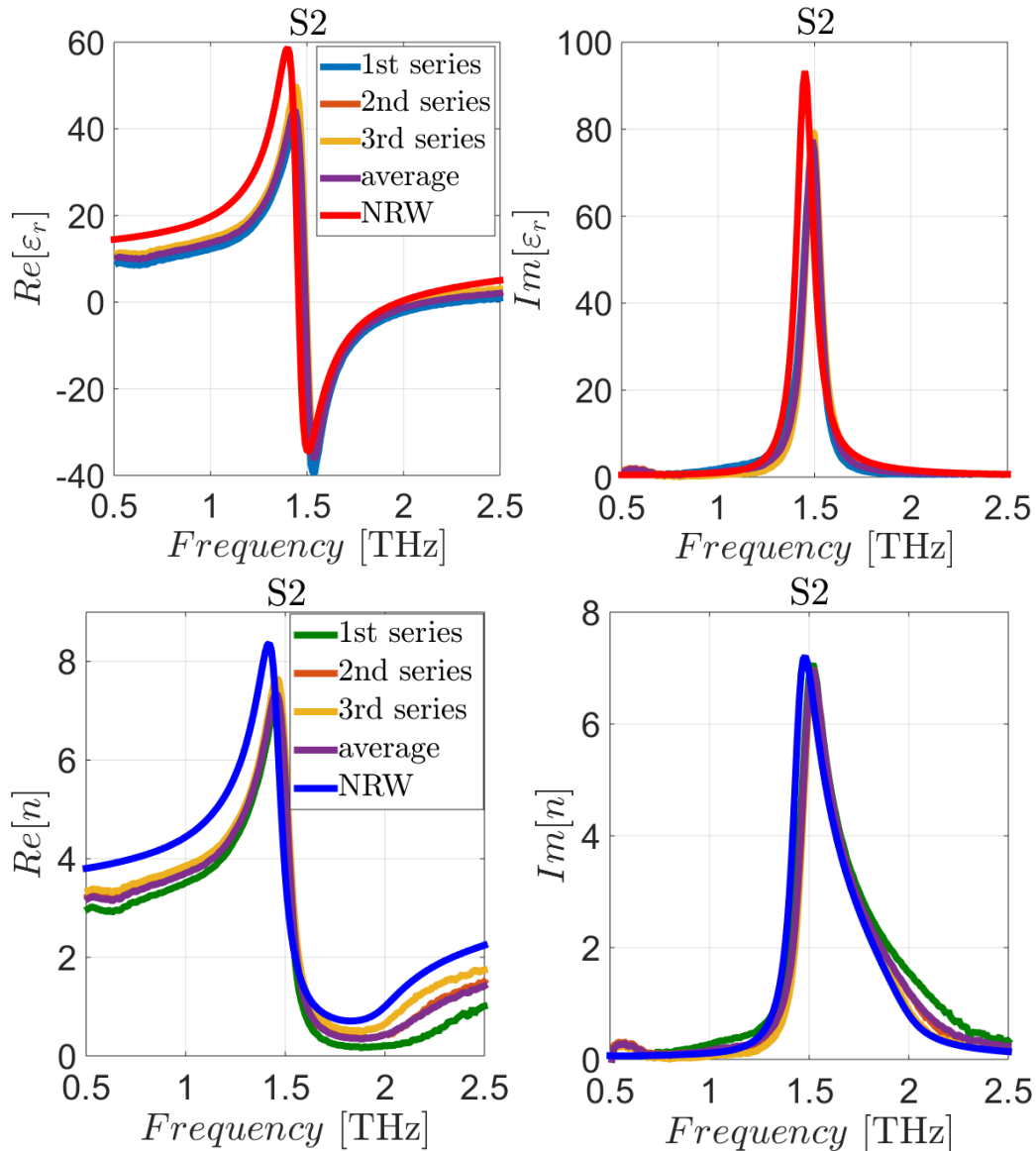


Figure 9.6: Measured complex relative permittivity and refractive index for the metasurface sample S2 for three different series of measurements, average value, and parameters extracted through the NRW algorithm.

The metasurfaces reveal a resonant dip in the transmittance $T(\omega)$ due to the purely electric resonant response, that is, in fact, characteristic of a Lorentz-like effective permittivity with resonant frequency $f_0 = 1.5$ THz, as described in Fig. 9.7. On the other hand, the off-resonance spectra show high values of the transmittance. Also, the transmittance spectra extracted from the experimental data are in agreement with the computationally simulated response of the finite element modeling of COMSOL Multiphysics.

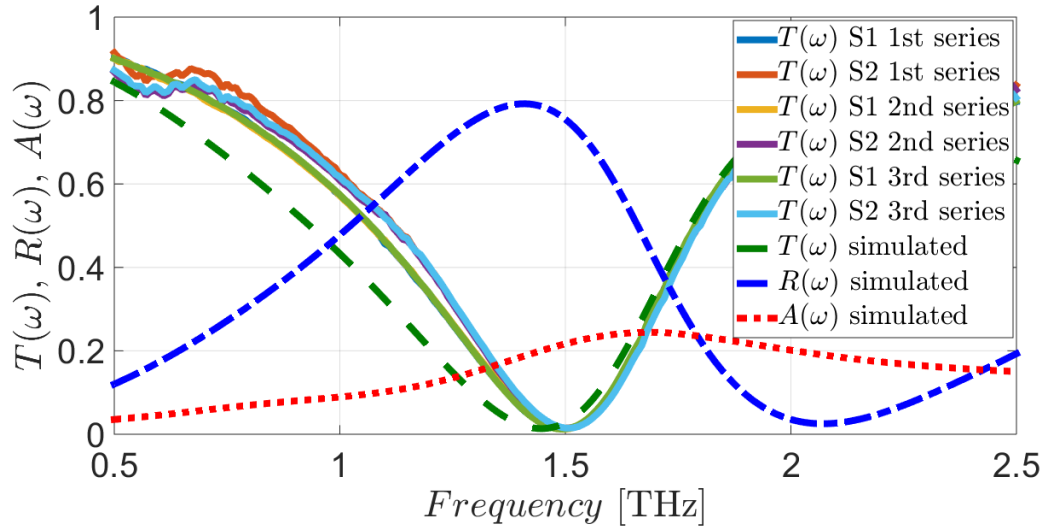


Figure 9.7: Simulated and measured transmittance spectra for the metasurface samples S1 and S2 for three different series of measurements.

9.3.1 Metasurface fabrication

To allow an easy handling of the device during the fabrication, the ultra-flexible polyimide film was deposited on an oxidized silicon wafer by spin-coating technique. The polyimide film was cured at 250 °C in a vacuum oven reaching a thickness of 5.4 μm . Then a metal layer of chromium and gold was evaporated on the surface (10 nm of Cr for an adhesion layer and 100 nm of Au) and lithographically patterned according to the geometry shown in Fig. 9.8. The device was realized with metal wet etching and resin removal. Finally, the flexible metasurface was shaped in foil of 5 cm \times 5 cm and mechanically detached from the rigid substrate (see Fig. 9.9).

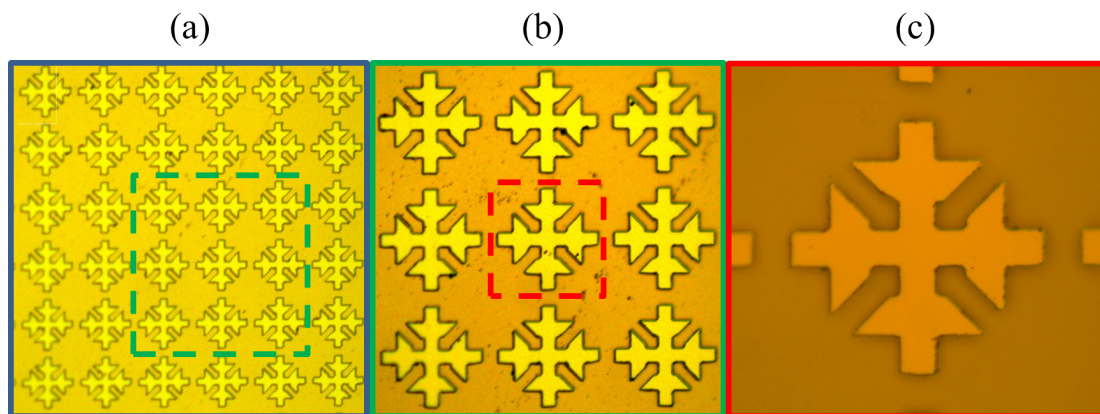


Figure 9.8: Optical microscope images of the fabricated metasurface: (a) Metasurface large area; (b) ERRs details; (c) higher-magnification of a single unit cell of 80 μm periodicity.



Figure 9.9: The ultra-flexible metasurface on its original rigid silicon substrate.

9.4 Reflection-mode THz-TDS measurements for oblique incidence characterization of the narrow-band MMA

In order to verify the incidence-angle insensitivity of the same ultra-thin narrow-band metamaterial absorber sample [32] investigated in Chapter 8, we have prepared an alternative THz-TDS reflection-mode configuration (see Fig. 9.10). This allowed us to validate the results achieved by the custom reflection-mode setup with the aluminum prism used in Chapter 8 under 16° oblique incidence in TE polarization, and to analyze the angular behavior also under 30 and 45 degrees.

As sketched in Fig. 9.10, the first lens (L1) collects the diverging THz radiation generated by the photoconductive antenna and collimates the linearly polarized THz beam onto the sample/reference to a diameter of about 12 mm, while the second lens (L2) collects the radiation reflected by the sample at a determined incidence angle θ and focuses it back to the photoconductive receiver (see also the inset in Fig. 9.10).

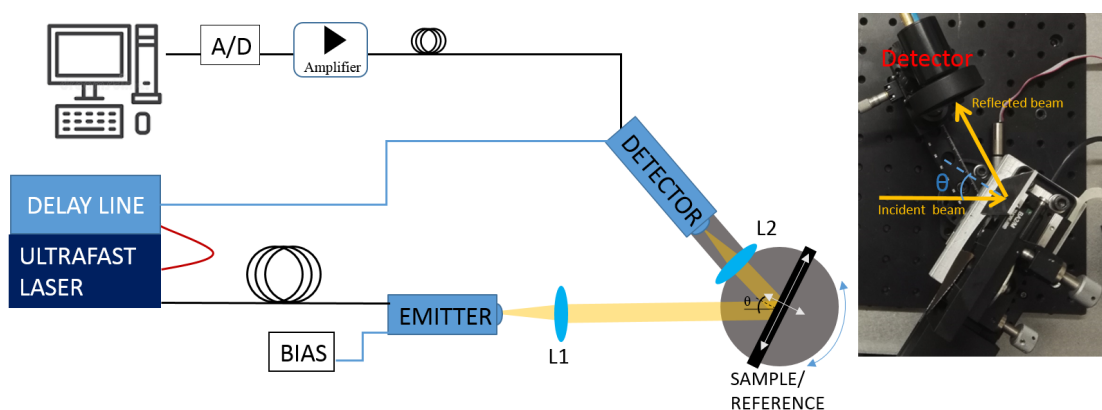


Figure 9.10: Sketch of the THz-TDS setup in reflection configuration and reflection geometry detail.

9. Transmission and Reflection Modes THz-TDS Characterization of Polyimide-based Metamaterial Devices

The physical implementation of the measurement setup is illustrated in Fig. 9.11, where are also shown all the mechanical freedom degrees and the additional holders, which are necessary for the precise alignment of the optical elements along the THz path as well as the longitudinal/transversal movements. In particular,

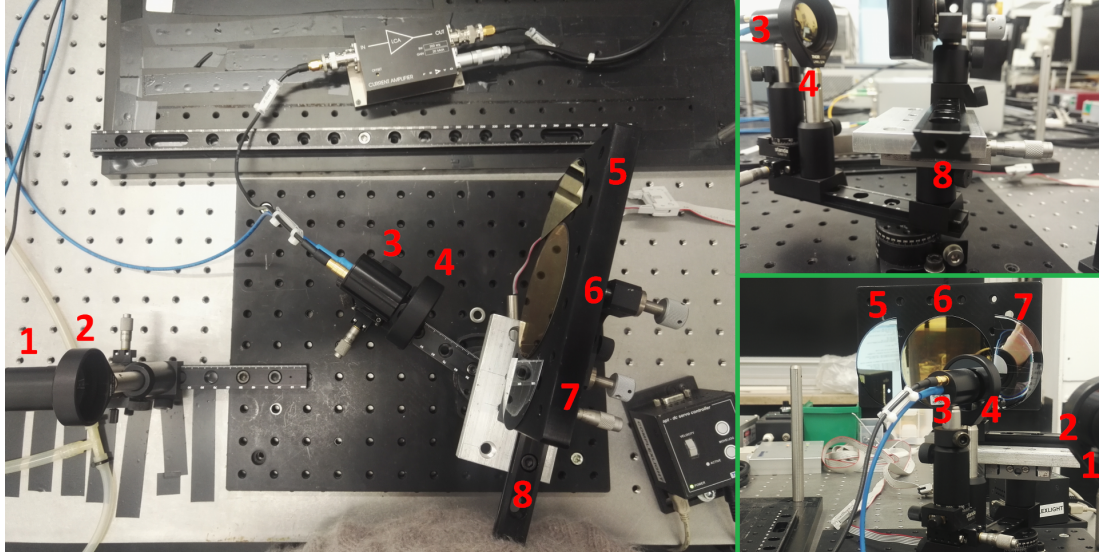


Figure 9.11: THz-TDS reflection setup details: (1) emitter antenna; (2) HRFZ-Si plano-convex lens L1; (3) detector antenna; (4) HRFZ-Si plano-convex lens L2; (5) aluminum reference sample; (6) metamaterial absorber sample; (7) polyimide reference sample; (8) sample holder with its rotational stage and micrometric longitudinal and transversal movements.

here the rotational stage, with its micrometric precision, allows to accurately direct the THz radiation at a desired incidence angle θ towards the receiving antenna.

Figure 9.12 describes the experimentally measured absorbance spectra at different incidence angles obtained by dividing the electric field spectral amplitude of the metamaterial absorber by that of the aluminum reference. The measurements at 16° incidence have been conducted at the temperature of $T=25.4^\circ\text{C}$ and Relative Humidity $\text{RH}=15.8\%$, while the ones at 30° and 45° have been performed at $T=25.8^\circ\text{C}$ and $\text{RH}=40.7\%$. We can observe that the absorbance values are in good agreement with those obtained in Chapter 8 and that, with the increase of the incidence angle, only a slight shift of the resonance frequency is present, as expected in TE polarization. Figure 9.12 exemplifies the average value of the angular-dependent absorbance spectra with a global resonance frequency at $f = 1.09\text{ THz}$ and a peak value of 62%.

In Chapter 8, the silicon substrate made the MMA a rigid device. In order to realize a flexible MMA, it is needed to add a further polyimide layer between the lower ground plane and the bare silicon substrate; the MMA is thus transferred from the rigid Si substrate, used as a sacrificial wafer, onto a flexible polyimide

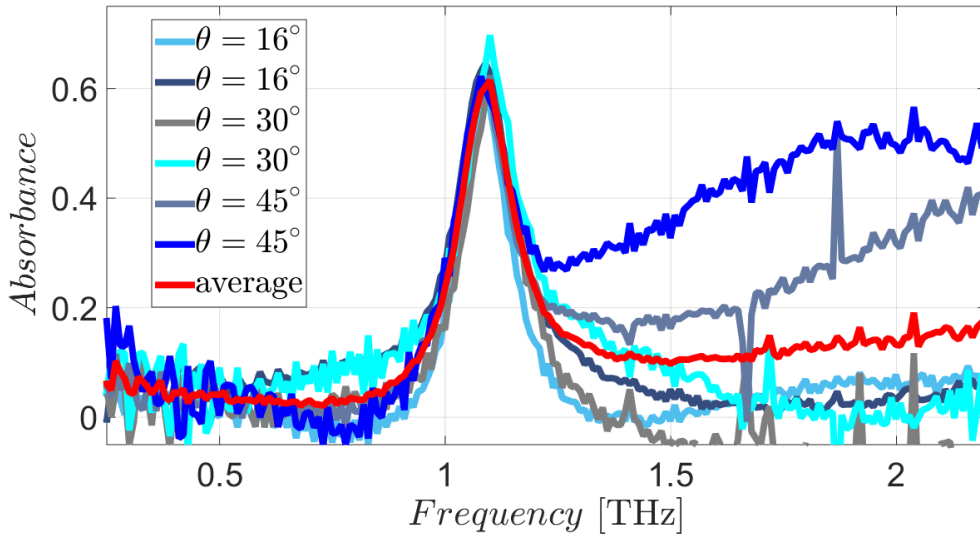


Figure 9.12: Absorbance spectra as a function of the incidence angle $\theta = 16^\circ, 30^\circ, 45^\circ$ in TE polarization.

film (allowing to fabricate the metamaterial elements independently of the chosen substrate). It is to be noted that this structural modification does not influence the electromagnetic response, since the lower ground plane prevents THz transmission.

9.5 Conclusions

In this Chapter, three sets of measurements have been performed to investigate the electromagnetic features of polyimide-based metamaterial devices at THz frequencies.

In the first experimental group, our goal was to characterize ultra-flexible polyimide films with various thicknesses under different environmental conditions, in particular high temperatures and humidity. The polyimide samples have been heated in order to evaluate possible physical variations due to the humidity content; this has allowed to prove that the water vapor contribution does not influence appreciably the polyimide loss tangent in the various study cases.

In the second experimental group, we have designed, fabricated, and characterized a freestanding THz metasurface on an ultra-thin and highly flexible polyimide substrate. From the measured data, we have extracted a typical Lorentz-like resonant dispersion behavior for the effective relative permittivity, mainly due to the electric response of the ERRs; the material parameters retrieved with the NRW algorithm and the full-wave FEM-based simulations are both in good agreement with the spectral experimental results.

In the third experimental group, our aim has been to prove the substantial angular-independence of the absorbance spectra of the MMA, previously measured with the custom THz-TDS setup in Chapter 8, at incidence angles up to

9. Transmission and Reflection Modes THz-TDS Characterization of Polyimide-based Metamaterial Devices

45°. As expected, being the THz beam TE polarized, the absorbance resonant values undergo only a slight frequency shift around 1.09 THz for increasing incidence angles, with an average absorbance peak value of 62%.

All the measurements have been conducted by using THz-TDS: for the first two experimental groups, we have prepared a transmission-mode setup, while for the third experimental group we have exploited a reflection-mode setup. More specifically, the metasurface characterization has required a dry nitrogen purged chamber in order to reduce the water vapor effect particularly present at the expected resonant frequency.

As demonstrated in this Chapter, because of the high stability of material parameters, polyimide-based metasurface and metamaterial absorber are of potential interest and practical use in the realization of functional THz elements and multilayer electromagnetic devices, such as angular-independent surfaces, terahertz switches/modulators and controllable metasurfaces, capable of operating as non-planar ultra-thin films thanks to the intrinsic flexibility.

References

- [1] D. Schurig, J. Mock, B. Justice, S. A. Cummer, J. B. Pendry, A. Starr, and D. Smith, "Metamaterial electromagnetic cloak at microwave frequencies," *Science*, vol. 314, no. 5801, pp. 977–980, 2006.
- [2] J. Yang, M. Huang, C. Yang, Z. Xiao, and J. Peng, "Metamaterial electromagnetic concentrators with arbitrary geometries," *Optics Express*, vol. 17, no. 22, pp. 19656–19661, 2009.
- [3] N. Landy, S. Sajuyigbe, J. Mock, D. Smith, and W. Padilla, "Perfect metamaterial absorber," *Physical Review Letters*, vol. 100, no. 20, p. 207402, 2008.
- [4] H.-T. Chen, A. J. Taylor, and N. Yu, "A review of metasurfaces: physics and applications," *Reports on Progress in Physics*, vol. 79, no. 7, p. 076401, 2016.
- [5] A. V. Kildishev, A. Boltasseva, and V. M. Shalaev, "Planar photonics with metasurfaces," *Science*, vol. 339, no. 6125, p. 1232009, 2013.
- [6] S. Keren-Zur, O. Avayu, L. Michaeli, and T. Ellenbogen, "Nonlinear beam shaping with plasmonic metasurfaces," *ACS Photonics*, vol. 3, no. 1, pp. 117–123, 2015.
- [7] A. C. Strikwerda, K. Fan, H. Tao, D. V. Pilon, X. Zhang, and R. D. Averitt, "Comparison of birefringent electric split-ring resonator and meanderline structures as quarter-wave plates at terahertz frequencies," *Optics Express*, vol. 17, no. 1, pp. 136–149, 2009.
- [8] S. Pandi, C. A. Balanis, and C. R. Birtcher, "Design of scalar impedance holographic metasurfaces for antenna beam formation with desired polarization," *IEEE Trans. Antennas Propag.*, vol. 63, no. 7, pp. 3016–3024, 2015.
- [9] W. L. Chan, H.-T. Chen, A. J. Taylor, I. Brener, M. J. Cich, and D. M. Mittleman, "A spatial light modulator for terahertz beams," *Applied Physics Letters*, vol. 94, no. 21, p. 213511, 2009.
- [10] C. L. Holloway, E. F. Kuester, J. A. Gordon, J. O'Hara, J. Booth, and D. R. Smith, "An overview of the theory and applications of metasurfaces: The two-dimensional equivalents of metamaterials," *IEEE Antennas and Propagation Magazine*, vol. 54, no. 2, pp. 10–35, 2012.
- [11] Y. Fan, N.-H. Shen, T. Koschny, and C. M. Soukoulis, "Tunable terahertz metasurface with graphene cut-wires," *ACS Photonics*, vol. 2, no. 1, pp. 151–156, 2015.
- [12] D. Wang, L. Zhang, Y. Gu, M. Mehmood, Y. Gong, A. Srivastava, L. Jian, T. Venkatesan, C.-W. Qiu, and M. Hong, "Switchable ultrathin quarter-wave plate in terahertz using active phase-change metasurface," *Scientific Reports*, vol. 5, p. 15020, 2015.
- [13] Y. Yang, I. I. Kravchenko, D. P. Briggs, and J. Valentine, "All-dielectric metasurface analogue of electromagnetically induced transparency," *Nature Communications*, vol. 5, p. 5753, 2014.
- [14] W. B. Lu, J. L. Liu, J. Zhang, J. Wang, and Z. G. Liu, "Polarization-independent transparency window induced by complementary graphene metasurfaces," *Journal of Physics D: Applied Physics*, vol. 50, no. 1, p. 015106, 2016.
- [15] H. Tao, A. Strikwerda, K. Fan, C. Bingham, W. Padilla, X. Zhang, and R. Averitt, "Terahertz metamaterials on free-standing highly-flexible polyimide substrates," *Journal of Physics D: Applied Physics*, vol. 41, no. 23, p. 232004, 2008.
- [16] R. Melik, E. Unal, N. Kosku Perkgoz, C. Puttlitz, and H. V. Demir, "Flexible metamaterials for wireless strain sensing," *Applied Physics Letters*, vol. 95, no. 18, p. 181105, 2009.
- [17] K. Iwaszczuk, A. C. Strikwerda, K. Fan, X. Zhang, R. D. Averitt, and P. U. Jepsen, "Flexible metamaterial absorbers for stealth applications at terahertz frequencies," *Optics Express*, vol. 20, no. 1, pp. 635–643, 2012.
- [18] R. Ulrich, "Far-infrared properties of metallic mesh and its complementary structure," *Infrared Physics*, vol. 7, no. 1, pp. 37–55, 1967.
- [19] R. Ulrich, "Interference filters for the far infrared," *Applied Optics*, vol. 7, no. 10, pp. 1987–1996, 1968.

- [20] B. A. Munk, *Frequency selective surfaces: theory and design*. John Wiley & Sons, 2005.
- [21] J. B. Pendry, A. J. Holden, D. J. Robbins, and W. Stewart, "Magnetism from conductors and enhanced nonlinear phenomena," *IEEE Transactions on Microwave Theory and Techniques*, vol. 47, no. 11, pp. 2075–2084, 1999.
- [22] H.-T. Chen, J. F. O'Hara, A. J. Taylor, R. D. Averitt, C. Highstrete, M. Lee, and W. J. Padilla, "Complementary planar terahertz metamaterials," *Optics Express*, vol. 15, no. 3, pp. 1084–1095, 2007.
- [23] C. E. Gutiérrez, L. Pallucchini, and E. Stachura, "General refraction problems with phase discontinuities on nonflat metasurfaces," *JOSA A*, vol. 34, no. 7, pp. 1160–1172, 2017.
- [24] N. Laman and D. Grischkowsky, "Terahertz conductivity of thin metal films," *Applied Physics Letters*, vol. 93, no. 5, p. 051105, 2008.
- [25] P. D. Cunningham, N. N. Valdes, F. A. Vallejo, L. M. Hayden, B. Polishak, X.-H. Zhou, J. Luo, A. K.-Y. Jen, J. C. Williams, and R. J. Twieg, "Broadband terahertz characterization of the refractive index and absorption of some important polymeric and organic electro-optic materials," *Journal of Applied Physics*, vol. 109, no. 4, pp. 043505–043505, 2011.
- [26] L. Duvillaret, F. Garet, and J.-L. Coutaz, "Highly precise determination of optical constants and sample thickness in terahertz time-domain spectroscopy," *Applied Optics*, vol. 38, no. 2, pp. 409–415, 1999.
- [27] L. Duvillaret, F. Garet, and J.-L. Coutaz, "A reliable method for extraction of material parameters in terahertz time-domain spectroscopy," *IEEE Journal of Selected Topics in Quantum Electronics*, vol. 2, no. 3, pp. 739–746, 1996.
- [28] T. D. Dorney, R. G. Baraniuk, and D. M. Mittleman, "Material parameter estimation with terahertz time-domain spectroscopy," *JOSA A*, vol. 18, no. 7, pp. 1562–1571, 2001.
- [29] M. Scheller, C. Jansen, and M. Koch, "Analyzing sub-100- μm samples with transmission terahertz time domain spectroscopy," *Optics Communications*, vol. 282, no. 7, pp. 1304–1306, 2009.
- [30] HD MicroSystems, *Product Bulletin PI-2600 Series - Low Stress Applications*, September 2009.
- [31] M. D. Astorino, F. Frezza, and N. Tedeschi, "Ultra-thin narrow-band, complementary narrow-band, and dual-band metamaterial absorbers for applications in the THz regime," *Journal of Applied Physics*, vol. 121, no. 6, p. 063103, 2017.
- [32] M. D. Astorino, R. Fastampa, F. Frezza, L. Maiolo, M. Marrani, M. Missori, M. Muzi, N. Tedeschi, and A. Veroli, "Polarization-maintaining reflection-mode THz time-domain spectroscopy of a polyimide based ultra-thin narrow-band metamaterial absorber," *Scientific Reports*, vol. 8, no. 1, p. 1985, 2018.
- [33] R. Fastampa, L. Pilozzi, and M. Missori, "Cancellation of Fabry-Perot interference effects in terahertz time-domain spectroscopy of optically thin samples," *Phys. Rev. A*, vol. 95, p. 063831, 2017.
- [34] P. U. Jepsen, D. G. Cooke, and M. Koch, "Terahertz spectroscopy and imaging—modern techniques and applications," *Laser & Photonics Reviews*, vol. 5, no. 1, pp. 124–166, 2011.
- [35] O. Luukkonen, S. I. Maslovski, and S. A. Tretyakov, "A stepwise Nicolson–Ross–Weir-based material parameter extraction method," *IEEE Antennas and Wireless Propagation Letters*, vol. 10, pp. 1295–1298, 2011.

Finite Element Analysis of Scatterers with Discontinuous Impedance Boundary Conditions

In this Chapter, I present finite element scattering analysis of a composite sphere with strongly discontinuous surface impedance parameters: the upper hemisphere is made of Perfect Electric Conductor (PEC), while the lower hemisphere is a Perfect Magnetic Conductor (PMC). The electromagnetic response of this PEC-PMC sphere is investigated through its bistatic radar cross section and surface electric current distributions under different excitations, comparing the results obtained by applying conventional PEC/PMC boundary conditions with the Impedance Boundary Conditions (IBCs). The PEC-PMC sphere has revealed an unexpected and strongly anisotropic scattering behavior. The axial and transversal polarizabilities of the object are computed through numerical Finite Element Method (FEM) simulations, by setting a proper two-dimensional axial symmetry electrostatic domain and providing an alternative resolution model using infinite elements in order to improve the solution convergence. Both simulation domains can be applied to analyze arbitrary rotationally symmetric scatterers.

The results collected in this Chapter have contributed to the conference paper published in Ref. [1].

10.1 Introduction

The theoretical analysis of spherical shape is of particular interest in the electromagnetic field, especially in perspective of possible applications (cloaking, metamaterial inclusions, and lenses) [2–6]. The sphere is an element widely occurring in nature, due to its ability of reducing the surface energy of the objects (fullerenes, spherical crystals, and rain droplets) [7–10]. While homogeneous and isotropic spheres are more easily examinable, there are spherical shapes more complex that pose a greater challenge. These can be constituted for example

by several concentric layers, known in the literature as Radially Uniaxial (RU) spheres [11, 12]. The locally anisotropic material responds differently to the electric field component tangential to the surface of the spherical layers and to the radial component, showing distinct electromagnetic properties, described by means of a dyadic representation of the relative permittivity in spherical coordinates.

The concept of RU sphere can be further generalized to include spherical objects with two different tangential components of the permittivity, giving rise to the so-called systropic sphere [13, 14]. The term systropic derives from the Greek word *συστροφική* (twist) and refers to a material with the axis of anisotropy defined in a spherical reference system. Its electric response is more complex than the one of the RU sphere, due to the different symmetry properties. In particular, the RU sphere is spherically symmetric, while the systropic sphere, being rotationally symmetric with respect to the axis of anisotropy, causes the polarizability to divide into two components depending on the electric field polarization, parallel or transverse to the axis of symmetry. Assuming a static and uniform excitation field, the electrical response of the systropic sphere can be expressed in terms of a dipole field in the far-region of the sphere. The factor of proportionality between the electric excitation field and the dipole moment corresponding to the dipole field is the polarizability of the scatterer [10].

From the point of view of electrostatics, Lorenz-Mie analysis [9] is usually applied to study the interaction of electromagnetic waves with spherical scatterers, by expanding the incident and scattered fields in vector multipole functions. Then, in order to get the unknown expansion coefficients, these expansions are matched via interface condition on the surface of the sphere.

In this Chapter, I analyze scattering by non-penetrable objects with strongly discontinuous surface impedance parameters in which the electric and magnetic fields have to satisfy certain boundary conditions (see Section 10.2). More specifically, in Section 10.3, the electromagnetic response of a PEC-PMC sphere has been investigated, revealing a marked anisotropic scattering behavior. In Section 10.4, the calculation methodologies for the axial polarizability are provided. These were initially applied to a PEC sphere and a PMC sphere to verify the validity of the simulation setup. However, this 2D axial symmetry electrostatic domain simulation provides a slowly convergence solution for the PEC-PMC sphere study case. In order to overcome this inconvenience, in Section 10.5, an alternative solution using infinite elements is suggested to obtain a better convergence of the axial polarizability results. Finally, in Section 10.6, the conclusions are drawn, and in Appendix C the axial and transversal polarizabilities for the prolate and oblate PEC ellipsoids and double PEC spheres (touching and intersecting), are computed through 2D axial symmetry electrostatic FEM-based simulations.

10.2 Impedance boundary conditions

In the analysis of the interaction between electromagnetic radiation and complex materials, there are few geometries and structures that can be solved in closed form. Numerical simulations and computational approach are needed in most practical situations, especially in connection with complex structures such as metamaterials and systropic spheres. In the following, I present numerical simulation results obtained through a FEM-based commercial software (COM-SOL Multiphysics) in order to solve response of electromagnetic scatterers. In the case of non-penetrable objects, the scattering interaction takes place at the surface and will be characterized by boundary conditions. Well-known examples of boundary conditions are the PEC and PMC. These can be seen as special cases of the IBC [15, 16] which imposes a linear relation between the time-harmonic electric (\mathbf{E}_t) and magnetic (\mathbf{H}_t) fields tangential to the boundary surface of the scatterer.

In general, the IBC can be expressed in the following form [17–19]:

$$\mathbf{E}_t = \overline{\overline{Z}}_s \cdot \mathbf{n} \times \mathbf{H}, \quad (10.1)$$

where \mathbf{n} is the outer normal unit vector, the subscript t denotes component tangential to the surface ($\mathbf{n} \cdot \mathbf{E}_t = 0$) and $\overline{\overline{Z}}_s$ is the 2D surface impedance dyadic. This equation can be interpreted as 2D extension of Ohm's law, through the substitution of the tangential magnetic field with the effective surface current density $\mathbf{J}_s = \mathbf{n} \times \mathbf{H}$.

As already mentioned, there are some special cases of the IBCs:

- Isotropic impedance boundary $\overline{\overline{Z}}_s = Z_s \overline{\overline{I}}$;
- Perfect electric conductor (PEC) $\overline{\overline{Z}}_s = 0$;
- Perfect magnetic conductor (PMC) $\overline{\overline{Z}}_s^{-1} = 0$;
- Perfect electromagnetic conductor (PEMC) $\overline{\overline{Z}}_s = Z_s \mathbf{n} \times \overline{\overline{I}}$,

where $\overline{\overline{I}}$ is the unit dyadic.

In the following Sections, I will restrict the analysis into the subclass of isotropic and reciprocal impedance surfaces, for which the impedance dyadic is a multiple of the unit dyadic.

The isotropic IBC can be written as

$$\mathbf{E}_t = Z_s \mathbf{n} \times \eta_0 \mathbf{H}_t, \quad (10.2)$$

where η_0 is the free-space wave impedance.

If the surface impedance $Z_s = R_s + jX_s$ is purely imaginary ($Z_s = jX_s$), the surface is lossless. A passive (dissipative or lossy) surface has positive real part $R_s > 0$, while a negative real part $R_s < 0$ corresponds to a gain and active surface.

10.2.1 IBC implemented in COMSOL Multiphysics

In COMSOL Multiphysics, the IBC is used at boundaries where the field is known to penetrate only a short distance outside the boundary. This penetration is approximated by a boundary condition to avoid the need to include another domain in the model; in fact, the material properties are set only for the domain outside the boundary and not inside. The IBC implemented in the multiphysics simulation software reads:

$$\sqrt{\frac{\mu_0\mu_r}{\varepsilon_c}}\mathbf{n} \times \mathbf{H} + \mathbf{E} - (\mathbf{n} \cdot \mathbf{E})\mathbf{n} = (\mathbf{n} \cdot \mathbf{E}_s)\mathbf{n} - \mathbf{E}_s, \quad (10.3)$$

where ε_c is the complex electric permittivity $\varepsilon_c = \varepsilon_0\varepsilon_r - j\frac{\sigma}{\omega}$, with ε_0 being the free-space permittivity, ε_r the relative permittivity, σ the electric conductivity, ω the angular frequency, and \mathbf{E}_s the source electric field ($\mathbf{E}_s = 0$).

From the comparison with the isotropic IBC in Eq. (10.2), it is possible to infer $Z_s = jX_s = \sqrt{\frac{\mu_r}{\varepsilon_r}}$.

10.3 PEC-PMC sphere

In this Section, I have simulated inhomogeneous objects immersed in free space and illuminated by an incident plane wave ($\mathbf{E}_i, \mathbf{H}_i$). FEM techniques require a defined region for analysis, therefore the free-space domain is truncated by a Perfectly Matched Layer (PML) and far-field calculations are done on the inner boundary of the PML domain. As a first example, I analyze the electromagnetic response of a composite scatterer whose surface impedance has very strong discontinuity. More specifically, I have set a strong discontinuity between the two hemispheres imposing PEC on the upper hemisphere and PMC on the lower hemisphere, obtaining a PEC-PMC sphere. The only necessary geometrical parameter of the scatterer is its size parameter $x = 2\pi r/\lambda = kr = 0.1$, where k is the wave number.

I assumed a sphere of radius $r = 1$ m at the frequency $f = c/\lambda = 4.77$ MHz. The surface impedance of the upper hemisphere is Z_{s1} and that of the lower hemisphere is Z_{s2} , as shown in the detail of Fig. 10.1.

The bistatic Radar Cross Sections (RCS) of the PEC-PMC sphere for both E-plane and H-plane under different excitations are shown in Figs. 10.2(a)-10.5(a) in logarithmic scale $bRCS = 10 \log(emw.bRCS3D)$ [dBsm]. The bistatic variable $emw.bRCS3D$ (where emw represents the label used in COMSOL Multiphysics

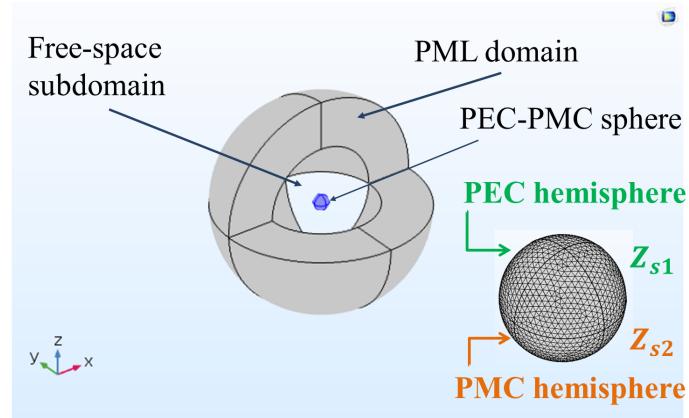


Figure 10.1: PEC-PMC sphere and the simulation domain.

in the Radio Frequency module to indicate “electromagnetic waves”) describes the RCS measured through a transmitter and a receiver that are located separately. The E-plane (H-plane) contains the electric field vector (magnetic field vector) and the direction of maximum radiation. In particular, for a vertically polarized antenna, the E-plane coincides with the elevation plane, while for a horizontally polarized antenna, the E-plane coincides with the azimuthal plane.

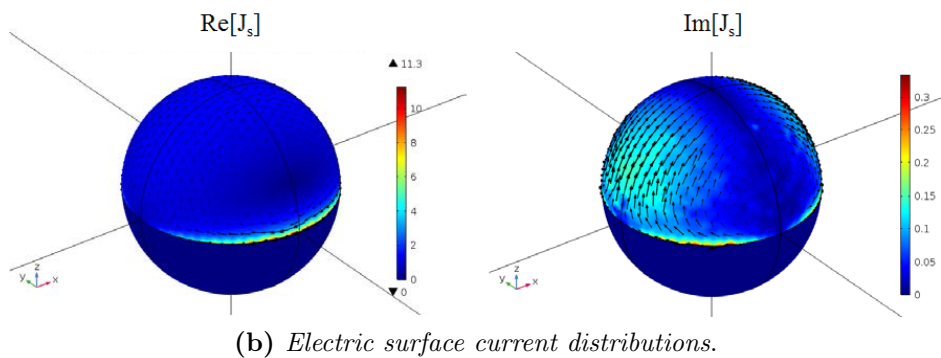
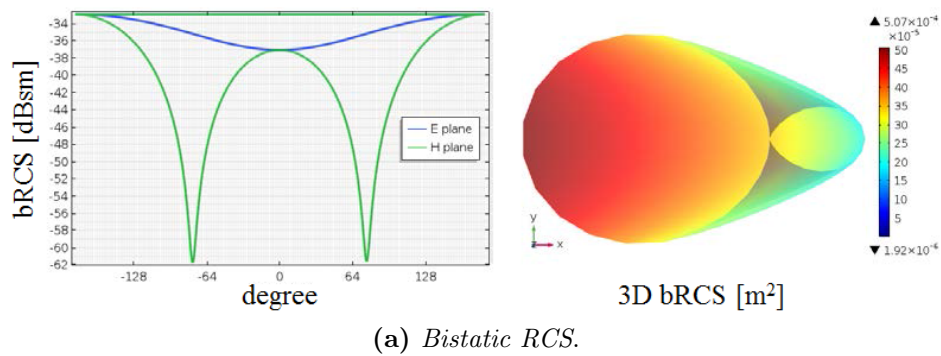
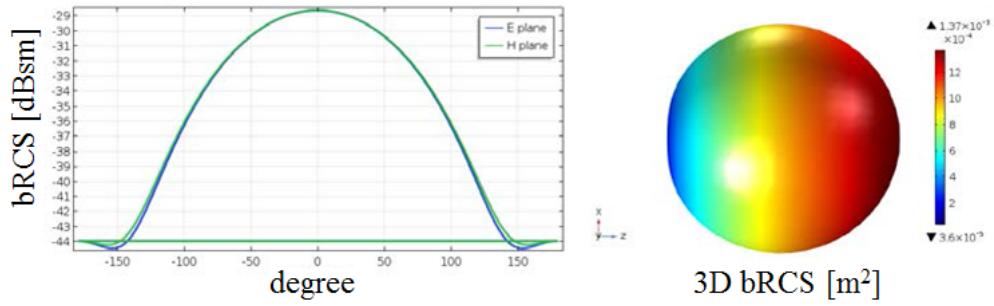
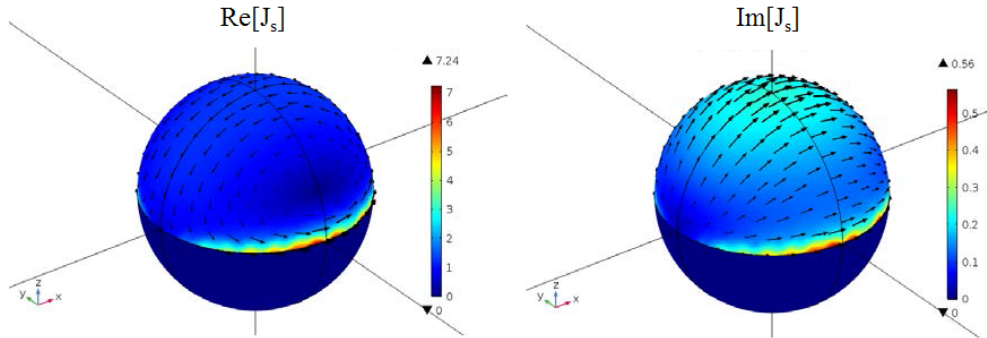


Figure 10.2: (a) Bistatic RCS and (b) real/imaginary parts of the electric current distribution on the PEC-PMC sphere in E-plane and H-plane for (E_z, k_x) excitation.

The electric surface current distributions of the PEC-PMC sphere with different excitations are illustrated in Figs. 10.2(b)-10.5(b). It can be observed that the currents cannot flow across the discontinuous interface of PEC and PMC.

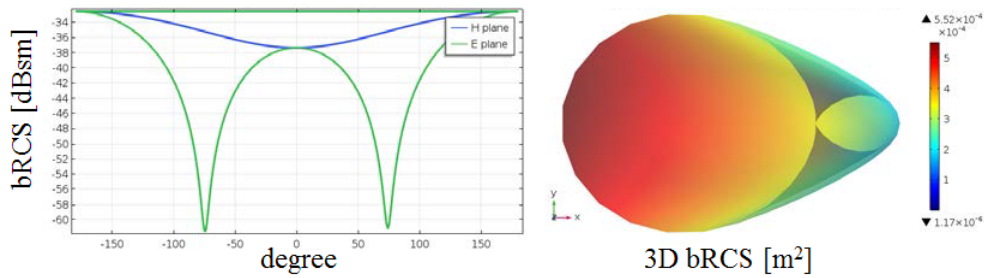


(a) Bistatic RCS.

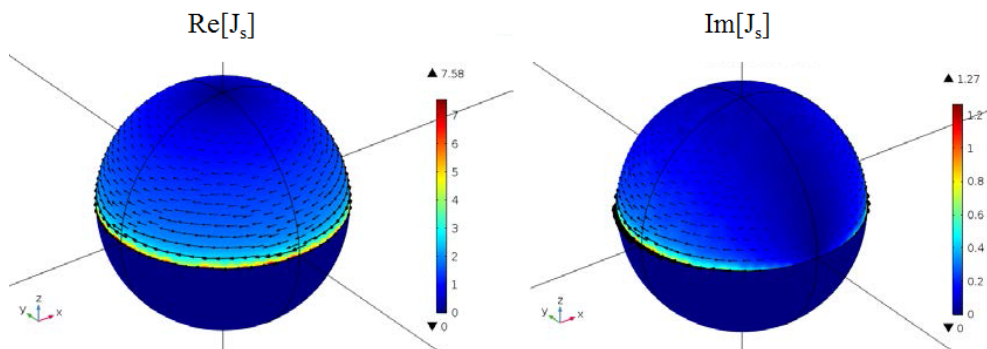


(b) Electric surface current distributions.

Figure 10.3: (a) Bistatic RCS and (b) real/imaginary parts of the electric current distribution on the PEC-PMC sphere in E-plane and H-plane for (E_x, k_z) excitation.

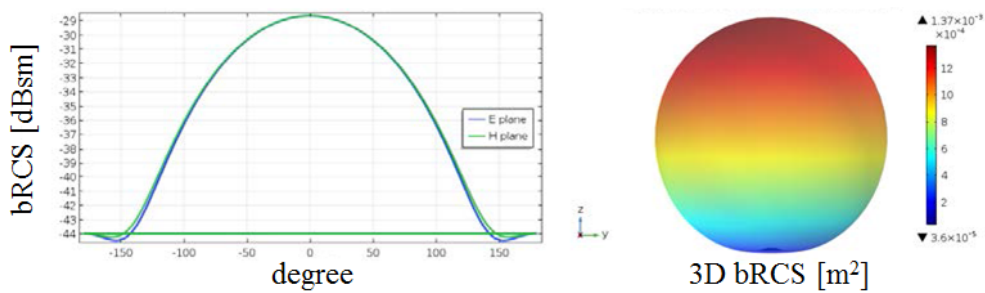


(a) Bistatic RCS.

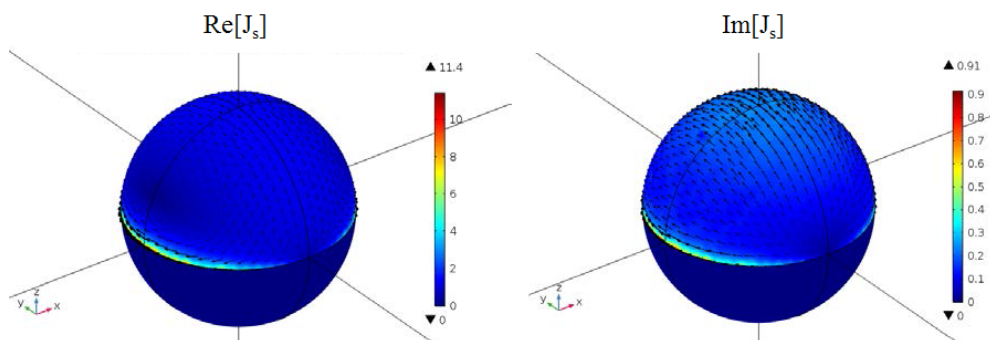


(b) Electric surface current distributions.

Figure 10.4: (a) Bistatic RCS and (b) real/imaginary parts of the electric current distribution on the PEC-PMC sphere in E-plane and H-plane for (E_y, k_x) excitation.

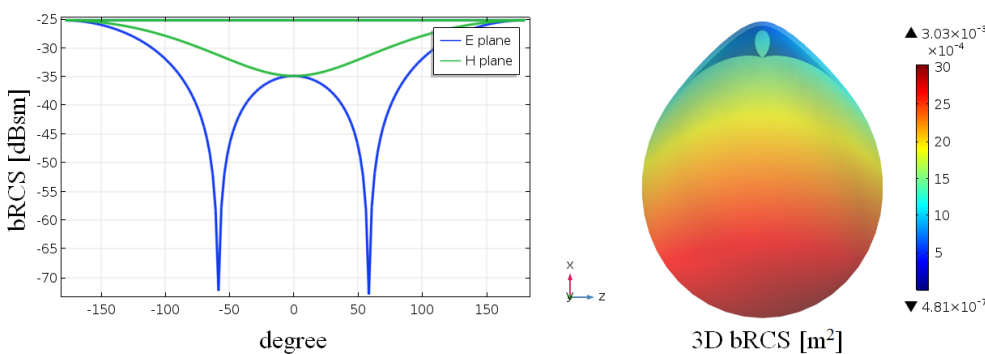


(a) *Bistatic RCS.*

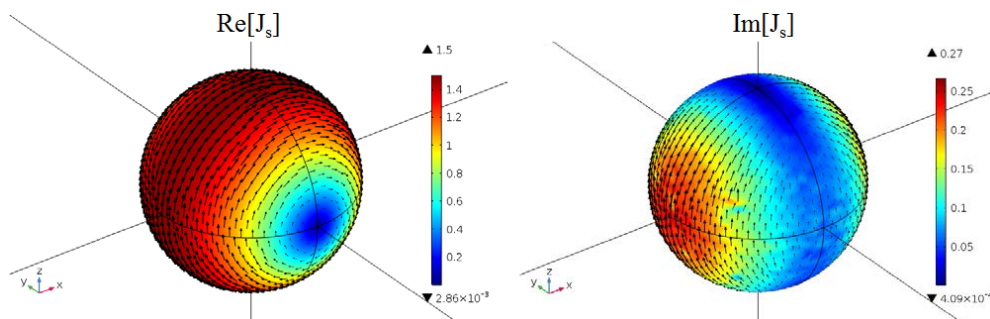


(b) *Electric surface current distributions.*

Figure 10.5: (a) Bistatic RCS and (b) real/imaginary parts of the electric current distribution on the PEC-PMC sphere in E-plane and H-plane for (E_y, k_z) excitation.



(a) *Bistatic RCS.*



(b) *Electric surface current distributions.*

Figure 10.6: (a) Bistatic RCS and (b) real/imaginary parts of the electric current distribution on the PEC sphere in E-plane and H-plane for (E_z, k_x) excitation.

It should be noticed that the directions of the currents on the interface are always parallel to the boundary under different excitations.

The sharp discontinuity in the surface impedance forces the currents to flow separately in the two hemispheres and form electric and magnetic dipoles in both regions. The interplay of these dipoles makes the far-field scattering of the PEC-PMC sphere to be drastically different from that of a homogeneous PEC sphere (see Fig. 10.6). For example, a longitudinally incident wave will be scattered with very large front-to-back ratio.

10.3.1 IBC PEC-PMC sphere

In order to study the electromagnetic behavior of IBC spheres, I have tested again the case of a PEC-PMC sphere (size parameter $x = 0.1$), this time with IBCs and the following two possible choices for the material parameters:

1. $\mu_{r1} = 10^{-10}$, $\mu_{r2} = 10^{10}$, $\varepsilon_{r1,2} = 1$, $\sigma = 0$ S/m;
2. $\varepsilon_{r1} = 10^{10}$, $\varepsilon_{r2} = 10^{-10}$, $\mu_{r1,2} = 1$, $\sigma = 0$ S/m,

where μ_{ri} and ε_{ri} refer to the relative permeability and permittivity of the upper hemisphere ($i = 1$) and lower hemisphere ($i = 2$), respectively. A strong discontinuity between the two hemispheres has been reached by imposing an upper $Z_{s1} = 10^{-5}$ and a lower $Z_{s2} = 10^5$. The upper hemisphere can be regarded as PEC and the lower hemisphere as PMC, making this an IBC PEC-PMC sphere [1].

The resulting real and imaginary parts of the surface electric current distribution on the IBC PEC-PMC sphere for (E_z, k_x) excitation are illustrated in Fig. 10.7.

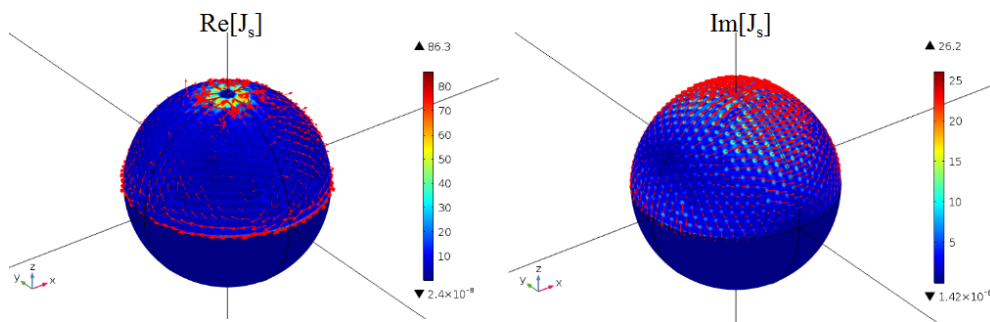


Figure 10.7: Real and imaginary parts of the electric current distribution on the IBC PEC-PMC sphere for (E_z, k_x) excitation.

The corresponding bistatic RCS in both E-plane and H-plane is shown in Fig. 10.8.

As can be seen from the previous results, which were obtained by using PEC and PMC boundary conditions (see Fig. 10.2), in this case we have different surface electric current distributions due to the specific material parameters assigned

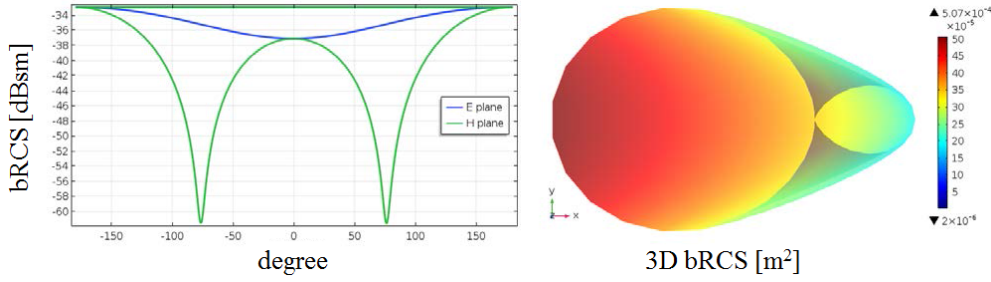


Figure 10.8: Bistatic RCS of the IBC PEC-PMC sphere in E-plane and H-plane for (E_z, k_x) excitation.

to the boundaries. Indeed, we are simulating distinct scatterers characterized through surface impedances, but with the same bistatic RCS responses (see Fig. 10.8).

10.4 2D axial symmetry electrostatic simulation for axial polarizability analysis

In this Section, a primary electric field $\mathbf{E}_p = \mathbf{E}_0 \mathbf{u}_z$ is assumed, from which the primary potential is $\phi_p = -E_0 z = -E_0 r \cos \theta$. As stated in Section 2.10, the main component of the secondary electric field, due to the polarization of the object, is the dipolar one. The polarized object can, therefore, be approximated using an electric dipole. The induced dipole moment \mathbf{p} can be determined by comparing the dipolar term of the series expansion of the potential function with the potential function of an electric dipole, which is of the form:

$$\phi_s = \frac{\mathbf{p} \cdot \mathbf{u}_z}{4\pi\epsilon_0 r^2} = \frac{p \cos \theta}{4\pi\epsilon_0 r^2}, \quad (10.4)$$

being the dipole z -directed in the axial case and the object immersed in free-space.

The total potential ϕ , which has to satisfy the Laplace equation $\nabla^2 \phi = 0$, is the sum of the primary and secondary potentials $\phi = \phi_p + \phi_s$. If we consider a spherical domain of radius R (see Fig. 10.9) and we calculate the derivative of the total potential with respect to the r -coordinate, we obtain:

$$\begin{aligned} \frac{\partial \phi}{\partial r} &= \frac{\partial}{\partial r}(\phi_p + \phi_s) = \frac{\partial}{\partial r}(-E_0 r \cos \theta + \frac{p \cos \theta}{4\pi\epsilon_0 r^2}) \\ &= -E_0 \cos \theta - \frac{p \cos \theta}{2\pi\epsilon_0 r^3} = \frac{\phi_p}{r} - \frac{2}{r}\phi_s = \frac{3}{r}\phi_p - \frac{2}{r}\phi. \end{aligned} \quad (10.5)$$

This expression, applied on the external spherical boundary $r=R$, assumes the form:

$$\frac{\partial \phi}{\partial n} + \frac{2}{R}\phi = \frac{3}{R}\phi_p, \quad (10.6)$$

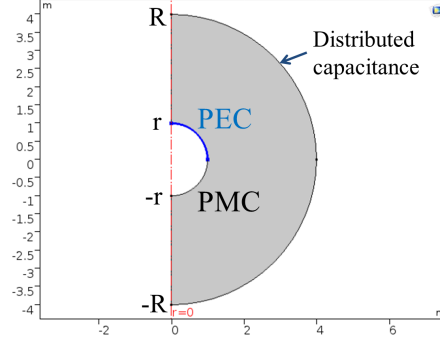


Figure 10.9: 2D axial symmetry electrostatic COMSOL Multiphysics simulation.

where n represents the outer normal direction to the boundary.

In order to implement this boundary condition in COMSOL Multiphysics, a distributed capacitance has been used. This option node adds a distributed capacitance boundary condition according to the following equations for exterior boundaries and interior boundaries, respectively:

$$-\mathbf{n} \cdot \mathbf{D} = \varepsilon_0 \varepsilon_r \frac{V_{ref} - V}{d_s}, \quad (10.7)$$

$$-\mathbf{n} \cdot (\mathbf{D}_1 - \mathbf{D}_2) = \varepsilon_0 \varepsilon_r \frac{V_{ref} - V}{d_s}. \quad (10.8)$$

The distributed capacitance expression can be rewritten in this form:

$$\frac{\partial V}{\partial n} + \frac{1}{d_s} V = \frac{V_{ref}}{d_s}, \quad (10.9)$$

showing a parallelism with Eq. (10.6) through the following parameter substitutions:

$$\begin{aligned} V &= \phi, \\ d_s &= \frac{R}{2}, \\ V_{ref} &= -\frac{3}{2} E_0 z. \end{aligned} \quad (10.10)$$

At this point, the dipole moment p and the electric polarizability α can be computed upon evaluating the integral:

$$\begin{aligned} I &= \iint_{r=R} \phi_s \cos \theta \, dS = \int_0^{2\pi} \int_0^\pi \frac{p \cos \theta}{4\pi \varepsilon_0 R^2} \cos \theta R^2 \sin \theta \, d\theta \, d\phi \\ &= \frac{p}{2\varepsilon_0} \int_0^\pi (\cos \theta)^2 \sin \theta \, d\theta = \frac{p}{3\varepsilon_0}, \end{aligned} \quad (10.11)$$

from which $p = 3\varepsilon_0 I$.

The axial polarizability, normalized with respect to the volume V_r of the r -sphere, can be thus calculated through the line integration:

$$\alpha_z = \frac{p}{\epsilon_0 E_0 V_r} = \frac{3\epsilon_0 I}{\epsilon_0 E_0 \frac{4}{3}\pi r^3} = \frac{9}{4\pi r^3 E_0} I = \frac{9}{4\pi r^3 E_0} \int_{r=R} (V + E_0 z) \frac{z}{R} 2\pi r dc. \tag{10.12}$$

In order to check the validity of this simulation approach, I have initially considered two basic examples: a PEC sphere and a PMC sphere of radius $r = 1$ m. To this end, I have used the AC/DC module of COMSOL Multiphysics, by setting electrostatic 2D axial symmetry simulations.

10.4.1 Axial polarizability of a PEC sphere

Figure 10.10 represents the simulation domain set in COMSOL and the computed normalized axial polarizability as a function of the external radius R. As can be noticed, α_z converges to the analytical value 3 with almost 6 digits accuracy.

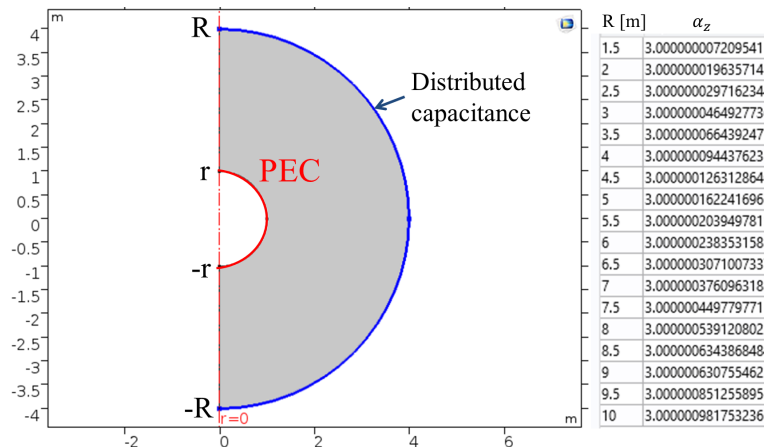


Figure 10.10: Axial polarizability of a PEC sphere.

Figure 10.11 shows the electric potential and the electric field of the PEC sphere when R=10 m.

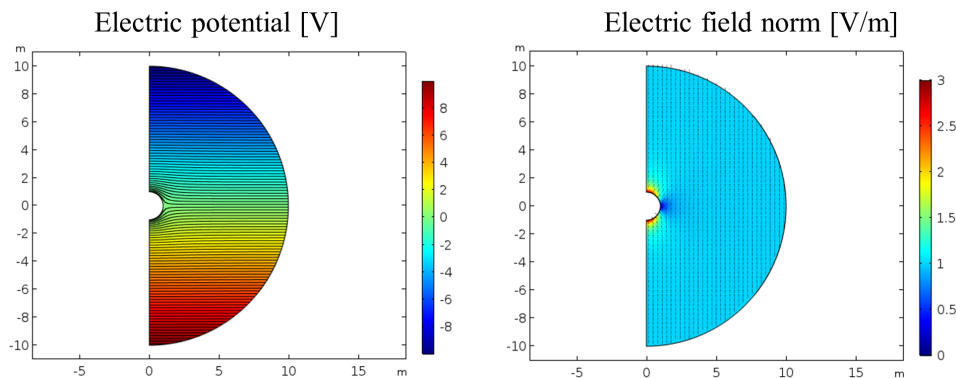


Figure 10.11: Electric potential and electric field of a PEC sphere.

10.4.2 Axial polarizability of a PMC sphere

Figure 10.12 illustrates the computed normalized axial polarizability as a function of the external radius R of a PMC sphere. In this case, α_z converges to the analytical value -1.5 with almost 6 digits accuracy. Figure 10.13 shows the electric potential and the electric field when $R=10$ m.

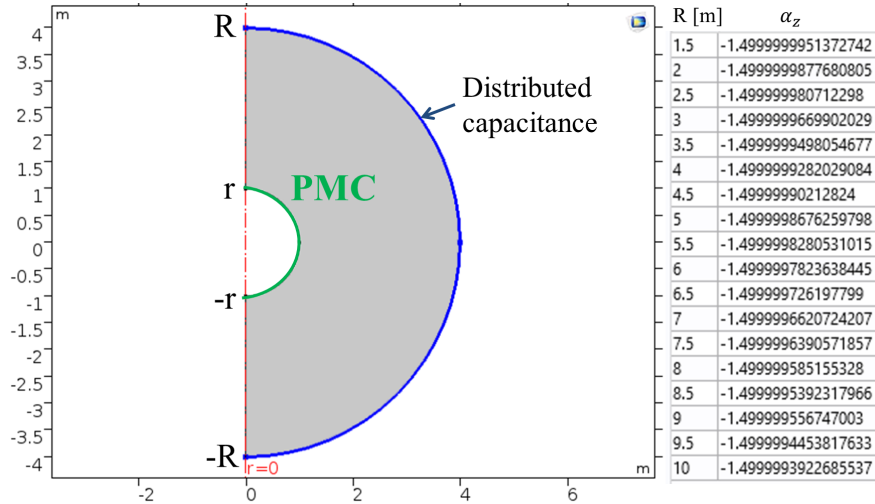


Figure 10.12: Axial polarizability of a PMC sphere.

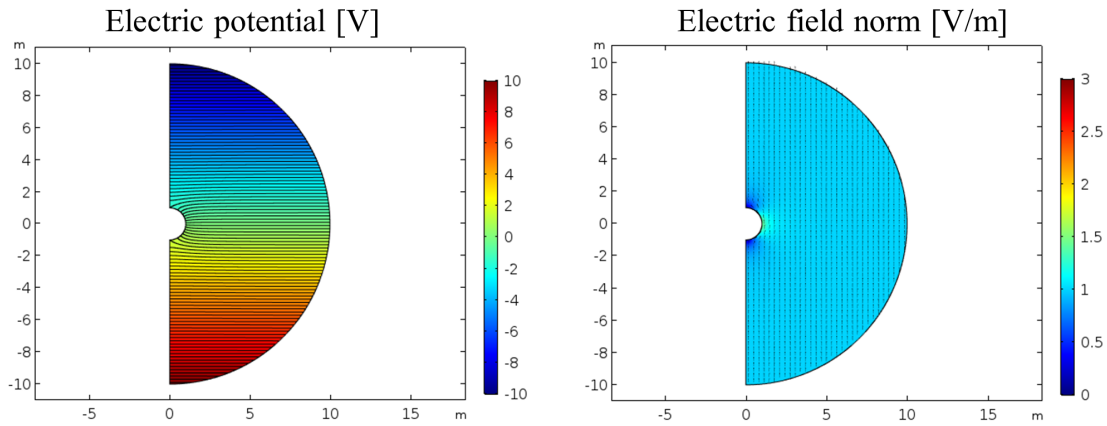


Figure 10.13: Electric potential and electric field of a PMC sphere.

Other numerical examples will be proposed in Appendix C for the following study cases: axial and transversal polarizabilities of PEC oblate and prolate spheroids, and two touching and intersecting PEC spheres.

10.4.3 Axial polarizability of a PEC-PMC sphere

At this point, I have analyzed the PEC-PMC sphere, applying the same simulation domain used so far. As can be seen from Fig. 10.14, the normalized axial polarizability converges slowly with the increase of the radius R . For this reason, another simulation domain setup has been implemented in order to improve the convergence of the solutions (see Section 10.5).

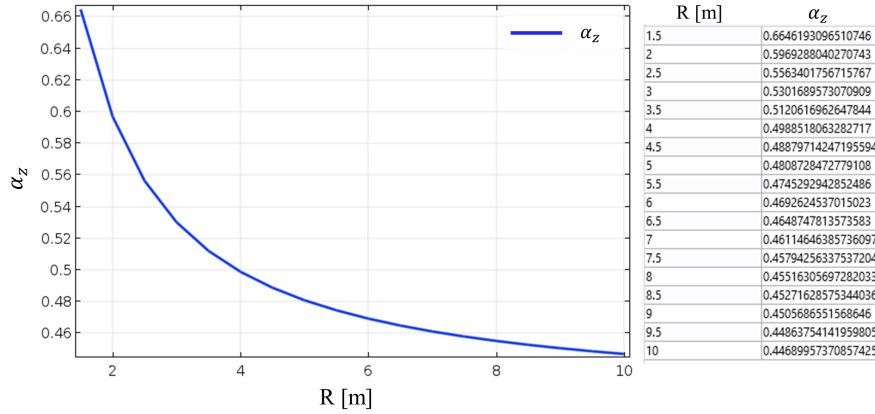


Figure 10.14: Axial polarizability of a PEC-PMC sphere as a function of the radius.

10.5 Alternative solution using infinite elements

In the previous resolution of the electrostatic problem, in COMSOL Multiphysics the total potential ϕ was the unknown. In this alternative version, the COMSOL unknown will be the secondary potential ϕ_s .

We recall the expression of the total potential:

$$\phi = \phi_p + \phi_s, \quad (10.13)$$

where ϕ_p was the primary potential.

The object of analysis is composed of a PEC hemisphere and a PMC hemisphere, so we need to apply different boundary conditions for the potential on the two boundaries:

$$\phi = 0 \longrightarrow V = E_0 z \quad \text{for the PEC hemisphere,} \quad (10.14)$$

$$\frac{\partial \phi}{\partial n} = 0 \longrightarrow \frac{\partial V}{\partial n} = \frac{\partial E_0 z}{\partial n} = E_0 \frac{\partial z}{\partial r} = \frac{E_0 z}{r} \quad \text{for the PMC hemisphere,} \quad (10.15)$$

being $z = r \cos \theta$.

In COMSOL, the PEC boundary can be realized with the electric potential option, while the PMC boundary can be obtained with the surface charge density $\rho_s = -\frac{\epsilon_0 E_0 z}{\sqrt{r^2 + z^2}}$.

Ultimately, an outer infinite element domain backed by a ground has been added. This applies a rational coordinate scaling to the external layer surrounding the physical region of interest where the Laplace equation is solved. The finite element can thus be stretched in the radial direction, so that boundary conditions

on the outside of the infinite element layer are effectively applied at a very large distance from the region of interest (see Fig. 10.15(a)).

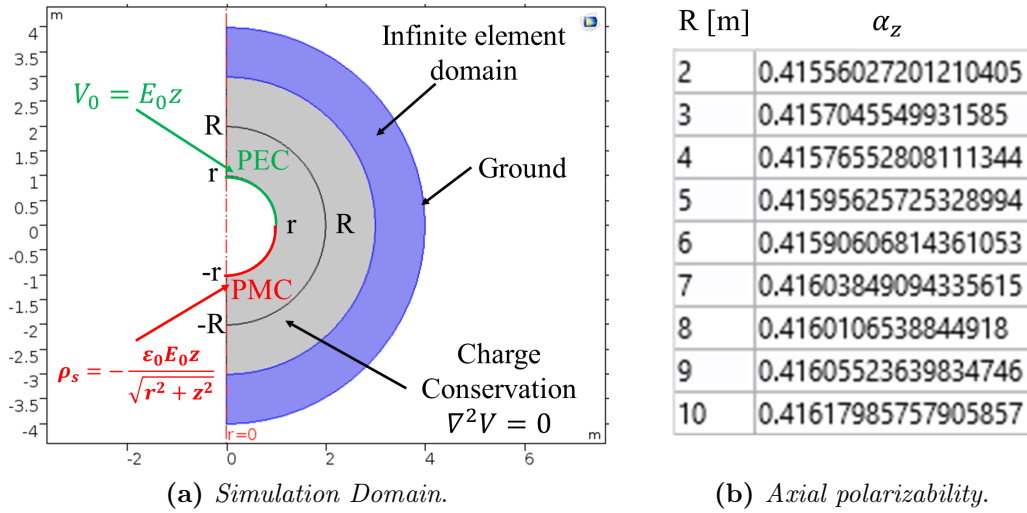


Figure 10.15: (a) 2D axial symmetry simulation domain for computing the (b) axial polarizability of a PEC-PMC sphere with the alternative resolution.

The normalized axial polarizability is then calculated through the line integral $\alpha_z = \frac{3}{\epsilon_0 Volume} \int V \frac{z}{R} 2\pi r dc$, giving the results displayed in Fig. 10.15(b); with an increasingly refined mesh α_z converges to the value $0.415 \approx \frac{1}{2\zeta(3)}$, where ζ is the Riemann Zeta function.

Through the same simulation setup, with the implementation in the three-dimensional case as shown in Fig. 10.16, it is also possible to calculate the normalized transversal polarizability through the integral $\alpha_t = \frac{3}{\epsilon_0 Volume} \iint_{R-sphere} V \frac{x}{R} dS$, supposing the electric field polarized along the x -axis. The obtained transversal polarizability reaches the value $\alpha_t \approx 1.57 \approx \frac{\pi}{2}$.

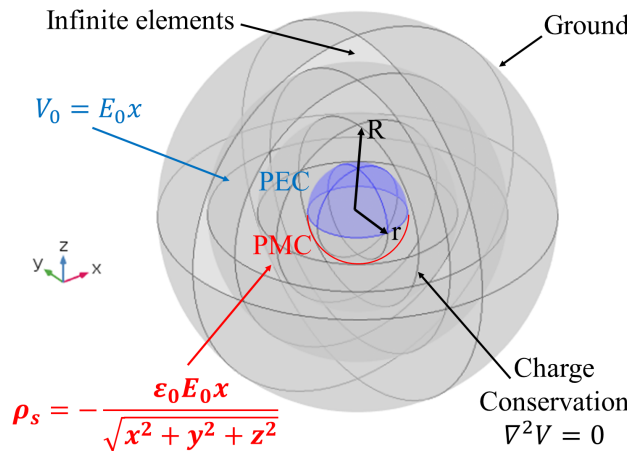


Figure 10.16: 3D simulation domain for computing the transversal polarizability of a PEC-PMC sphere with the alternative resolution.

10.6 Conclusions

In this Chapter, I have operated finite element analyses on the scattering properties of objects defined through proper impedance boundary conditions.

I have considered scatterers with strongly discontinuous IBCs, such as the IBC PEC-PMC sphere, by showing the bistatic RCS behavior and the surface electric current distributions. These currents flow separately in the two hemispheres due to the sharp discontinuity in the surface impedance, determining electric and magnetic dipoles whose interplay gives rise to a far-field scattering totally different from that of a homogeneous PEC (or PMC) sphere. Indeed, a longitudinally incident wave is scattered with very large front-to-back ratio.

An informative parameter in the scattering analysis is represented by the polarizability, which is a measure of the object to become dipolarized. Since the analytical calculations of the axial polarizability parameter are difficult for complex structures such as the PEC-PMC sphere, I have set a custom 2D axial symmetry electrostatic simulation domain, validating it through some canonical geometries: PEC and PMC spheres, prolate and oblate PEC ellipsoids, and touching/intersecting double PEC spheres (see Appendix C).

The convergence of the simulated axial polarizability solution has been further improved by adopting an alternative 2D setup based on the infinite elements, while the transversal polarizability has been retrieved in a 3D space domain.

In general, starting from a single sphere with polarizability $\alpha = 3$, it has been observed that for the transversal case $\alpha_t < \alpha$, while for the axial case $\alpha_z > \alpha$. For example, the case of two touching spheres (the analysis is expanded in Appendix C) can be assimilated to the case of an elongated scatterer as the prolate spheroid, for which the axial polarizability is larger and the transversal one is smaller with respect to a sphere of the same size.

These simulation setups can be applied to investigate arbitrary rotationally symmetric scatterers with various geometrical shapes.

The results presented in this Chapter have contributed to the conference paper in Ref. [1] made in collaboration with the Department of Electronics and Nanoengineering of the Aalto University.

References

- [1] B. B. Kong, P. Ylä-Oijala, M. D. Astorino, H. Wallén, and A. Sihvola, "Analysis of scatterers with discontinuous impedance boundary condition using surface-integral equation method," in *12th International Congress on Artificial Materials for Novel Wave Phenomena - Metamaterials 2018*, pp. 225–227, IEEE, 2018.
- [2] J. B. Pendry, D. Schurig, and D. R. Smith, "Controlling electromagnetic fields," *Science*, vol. 312, no. 5781, pp. 1780–1782, 2006.
- [3] H. Chen, B.-I. Wu, B. Zhang, and J. A. Kong, "Electromagnetic wave interactions with a metamaterial cloak," *Physical Review Letters*, vol. 99, no. 6, p. 063903, 2007.
- [4] H. Kettunen, H. Wallén, and A. Sihvola, "Cloaking and magnifying using radial anisotropy," *Journal of Applied Physics*, vol. 114, no. 4, p. 044110, 2013.
- [5] A. Alù and N. Engheta, "Polarizabilities and effective parameters for collections of spherical nanoparticles formed by pairs of concentric double-negative, single-negative, and/ or double-positive metamaterial layers," *Journal of Applied Physics*, vol. 97, no. 9, p. 094310, 2005.
- [6] Y. Koike, Y. Sumi, and Y. Ohtsuka, "Spherical gradient-index sphere lens," *Applied Optics*, vol. 25, no. 19, pp. 3356–3363, 1986.
- [7] S. Iijima, "Direct observation of the tetrahedral bonding in graphitized carbon black by high resolution electron microscopy," *Journal of Crystal Growth*, vol. 50, no. 3, pp. 675–683, 1980.
- [8] R. Ruppin, "Thermal fluctuations and Raman scattering in small spherical crystals," *Journal of Physics C: Solid State Physics*, vol. 8, no. 12, p. 1969, 1975.
- [9] C. F. Bohren and D. R. Huffman, *Absorption and scattering of light by small particles*. John Wiley & Sons, 2008.
- [10] A. H. Sihvola, *Electromagnetic mixing formulas and applications*. No. 47, IET, 1999.
- [11] H. Wallén, H. Kettunen, and A. Sihvola, "Singularities or emergent losses in radially uniaxial spheres," in *Electromagnetic Theory (EMTS), Proceedings of 2013 URSI International Symposium on*, pp. 388–390, IEEE, 2013.
- [12] K.-L. Wong and H.-T. Chen, "Electromagnetic scattering by a uniaxially anisotropic sphere," in *IEE Proceedings H (Microwaves, Antennas and Propagation)*, vol. 139, pp. 314–318, IET, 1992.
- [13] T. Rimpiläinen, M. Pitkonen, H. Wallén, H. Kettunen, and A. Sihvola, "General systropy in spherical scatterers," *IEEE Transactions on Antennas and Propagation*, vol. 62, no. 1, pp. 327–333, 2014.
- [14] T. Rimpiläinen, H. Wallén, H. Kettunen, and A. Sihvola, "Electrical response of systropic sphere," *IEEE Transactions on Antennas and Propagation*, vol. 60, no. 11, pp. 5348–5355, 2012.
- [15] D. J. Hoppe, *Impedance boundary conditions in electromagnetics*. CRC Press, 1995.
- [16] S. V. Yuferev and N. Ida, *Surface impedance boundary conditions: a comprehensive approach*. CRC press, 2009.
- [17] H. Wallén, I. V. Lindell, and A. Sihvola, "Mixed-impedance boundary conditions," *IEEE Transactions on Antennas and Propagation*, vol. 59, no. 5, pp. 1580–1586, 2011.
- [18] I. V. Lindell and A. Sihvola, "Electromagnetic wave reflection from boundaries defined by general linear and local conditions," *IEEE Transactions on Antennas and Propagation*, vol. 65, no. 9, pp. 4656–4663, 2017.
- [19] I. V. Lindell and A. H. Sihvola, "Electromagnetic boundaries with PEC/PMC equivalence," *Progress In Electromagnetics Research*, vol. 61, pp. 119–123, 2016.

Conclusions

Equivalent-circuit models, metamaterials, terahertz frequencies, and THz time-domain spectroscopy measurements represent challenging developing research fields, which have greatly attracted scientific interest thanks to their promising and not yet fully explored applications. These encompass many branches of applied physics, optics, and engineering with potential uses in bio-sensing, imaging, security, photo-detecting, and wireless communications.

The aims of this PhD thesis were multiple: the development of equivalent-circuit networks for modeling the electromagnetic behavior of stacked 2D apertures in metallic films; the design and numerical study of metamaterial absorbers with different spectral responses; the deviser of parametric macromodels for optimization of metamaterial devices; the design, fabrication and characterization of metamaterial flexible structures; the setting of efficient simulation domains for polarizability retrieval. I have extensively worked in all research phases including design, numerical analysis and experimental measurements, with a lower extent in the fabrication processes.

In order to provide the fundamentals of this study, in Chapter 2 I have focused on basic concepts such as electromagnetic wave propagation, Fresnel equations, Floquet's theorem, metamaterials, homogenization algorithm, transmission line theory, fabrication methods, THz-TDS, and polarizability.

In Chapter 3, after reviewing the current state-of-the-art literature, I have described equivalent-circuit networks for the modeling of the scattering properties of strip/slit gratings and 2D arrays of FSS/complementary FSS in layered dielectric environments. Both the case of lossy and lossless grounded dielectric slab has been implemented in the model. This systematic approach is based on the transmission-line theory and the Floquet-mode decomposition of the electromagnetic fields around the scattering elements. The electromagnetic behavior is synthesized with both low-order and high-order circuit elements, which consider

explicitly the propagative modes through the relevant transmission-line sections; global lumped elements accounted for the evanescent modes. In particular, the contribution of high-order modes has been represented by inductance and capacitance. For all the circuit elements, fully-analytical expressions have been derived; in addition, a semi-analytical EC representation has been provided for more complex shaped unit cell elements. The validity of the EC models has been tested for TE and TM polarizations, at oblique incidence and over a broad frequency range, by comparing the results with full-wave FEM-based simulations. These EC models not only significantly reduce the computational time and memory, but they also provide a physical insight into the understanding of the electromagnetic performance and a useful tool in the design phase.

In Chapter 4, I have expanded the 2D equivalent circuit models described in Chapter 3 to deal with stacked periodic slot-based FSSs of arbitrary geometry. I have first analyzed a pair of different and aligned FSSs, retrieving a Π topology. Then, the resulting network for each pair of closely coupled FSSs can be cascaded to obtain the spectral features of the whole device. The derived Π network overcomes the intrinsic limits of the even/odd excitation approach and is able to reproduce the scattering behavior over a broad spectral range, from the quasi-static regime to the first grating lobe appearance. The proposed equivalent circuit is thus able to account for the high-order mode interaction between two consecutive stacked arrays and for the frequency-dependent response due to the lowest-order propagating modes. The interest in analyzing the transmission and reflection spectra of stacked 2D arrays is increased by the further degrees of freedom with respect to the single array case in the design phase; in fact, the electromagnetic response of a single array can be suitably changed by stacking an arbitrary number of arrays, enabling a wide variety of applications in many branches of applied physics and engineering. The versatility of this circuit model has been proven after analyzing various types of stacked structures and comparing with FEM-based simulations; the results have shown a negligible numerical effort in terms of CPU time and memory resources. Moreover, this equivalent circuit model can be applied to investigate also other complex electromagnetic phenomena such as Wood's anomalies, extraordinary transmission through arrays of subwavelength apertures, electromagnetic-induced transparency, and negative refractive index media. The results contained in this Chapter have been published in Ref. [1].

In Chapter 5, I have designed and demonstrated ultra-thin narrow-band, complementary narrow-band, and dual-band metamaterial absorbers (MMAs) through FEM-based simulations in the THz range for both Transverse Electric (TE) and Transverse Magnetic (TM) polarizations in the general case of oblique

incidence. The narrow-band devices are formed by a periodic arrangement of metallic Electric Ring Resonators (ERRs) over a grounded dielectric slab, while the dual-band structure is composed of two stacked resonant elements embedded in dielectrics backed by a ground plane. All the devices reach near-unity absorbance levels and relative Full Width at Half-Maximum (FWHM) absorption bandwidths about 8%. The performances have been investigated in the case of lossy/lossless dielectric and metallic materials, proving the prevalence of Ohmic losses in the absorbance mechanism. I have applied the Nicolson-Ross-Weir (NRW) algorithm to extract the effective electromagnetic parameters, which exhibited a typical Lorentz-like dispersion response, while the interference theory results have shown a good agreement with the coupled-model results. The analysis presented in this Chapter has been published in Refs. [2, 6, 7].

In Chapter 6, by properly stacking and scaling three ERRs with the same geometry of Chapter 5 in a dielectric grounded slab, I have devised an ultra-thin broad-band metamaterial absorber with an absorption bandwidth greater than 300 GHz at a center resonant frequency of 1 THz. The device has shown wide angular performances for both polarizations for incidence angles up to 80°. By applying the homogenization theory, I have extracted the effective wave impedance and electric permittivity; the former presented a nearly perfectly matching with the free-space impedance at the three resonant peaks, while the latter displayed high values mainly due to the quasi-infinite permittivity of the ground plane. The theoretical grounded-slab model has been validated by analyzing the decoupled system, despite the multi-layer nature of the structure. This work has been published in Ref. [3].

In Chapter 7, we have introduced efficient parametric macromodels for the optimization of metamaterial-based devices in various electromagnetic scenarios. In particular, we have applied this procedure to the narrow-band MMA described in Chapter 5 (see Refs. [2, 5, 6]) handling with a six-dimensional design space, which takes into account the main geometrical sizes of the unit cell. The model was constructed by using quasi-random sampling, radial basis functions and polynomial functions. The validity has been successfully demonstrated by investigating three study cases of MMAs resonating at different frequencies with a noticeable speeding of the design flow compared to commercial electromagnetic solvers. This analysis has been published in Ref. [4].

In Chapter 8, we have designed, microfabricated and experimentally characterized the narrow-band MMA analyzed in Chapter 5 (see Refs. [2, 4, 6]), after adopting as dielectric middle layer an ultra-flexible polyimide spacer in place of the previously used rigid BCB middle layer. The goal of this work was to devise a compact reflection-mode THz-TDS setup capable of maintaining both the po-

larization and the collimation of the beam. This has been reached by inserting a custom aluminum prism along the THz path, properly optimized to allow oblique incidence investigations. The post-processing of the measurements has revealed a resonance at 1.09 THz with an absorbance mean value of 70%. We have ascribed the lack of near-unity absorbance mainly to the higher polyimide losses at THz frequencies by performing parametric simulations on the dielectric loss tangent values. These results have been published in Ref. [5].

In Chapter 9, we have conducted three THz-TDS experiments in both transmission and reflection modes with multiple objectives. Our first goal was to characterize polyimide samples of different thicknesses and subjected to heating at 100 °C, in order to evaluate the water vapor contribution on the losses. We have found negligible variations on the imaginary part of the electric permittivity for all the samples; this validates the use of polyimide in critical environmental conditions. The second group of experiments was aimed at investigating the material properties of the designed and fabricated metasurfaces on free-standing polyimide substrates. The measured data have shown a typical Lorentzian dispersion behavior in accordance with the NRW results and the full-wave simulations. In the third measurement, the theoretical angular insensitivity of the metamaterial absorber (the same investigated in Chapter 8) has been experimentally verified for incidence angles up to 45° by adopting an alternative reflection-mode THz-TDS setup.

In Chapter 10, I have conducted finite-element analysis on a spherical scatterer, a PEC-PMC sphere, with strongly discontinuous impedance boundary conditions. Through numerical simulations on the bistatic radar cross section and surface current distributions, I have shown how the sharp discontinuity in the surface impedance forces the currents to flow separately in the two hemispheres, giving rise to electric and magnetic dipoles. The interplay of these dipoles makes the far-field scattering of the PEC-PMC sphere to be drastically different from that of a homogeneous PEC (or PMC) particle; for example, a longitudinally incident wave is scattered with very large (15 dB) front-to-back ratio. Due to the difficulties related to the analytical calculations of the polarizability parameter, I have set a specific 2D axial symmetry electrostatic simulation domain for retrieving the axial polarizability, by checking for some known study cases. In order to improve the convergence of the solutions for the PEC-PMC object, an alternative simulation setup has been devised by using infinite elements, obtaining approximated normalized axial polarizability values. The transversal polarizability has been evaluated by extending the 2D simulation domain to the 3D space. This procedure can be applied to analyze rotationally symmetric scatterers with various geometrical shapes as shown in Appendix C. The results of this analysis have

contributed to the conference paper in Ref. [9].

The multifaceted aspects of the projects presented in this PhD thesis have required me to collaborate with various Institutions, for both design tasks and fabrication/measurements purposes: *Institute for Microelectronics and Microsystems* CNR-IMM of Rome for fabrication of polyimide-based samples; *Research Center for Nanotechnologies Applied to Engineering* (CNIS, Sapienza) for access to Atomic Force Microscopy (AFM); *Institute for Complex Systems* CNR-ISC and *Physics Department* (Sapienza) for THz-TDS measurements; *Department of Industrial and Information Engineering and Economics* (University of L'Aquila Electromagnetic Compatibility Research Laboratory, UAq EMC Laboratory), and *Microwave Department Institut Mines-Télécom Atlantique* (CNRS UMR 6285 Lab-STICC, Brest, France) for parametric macromodel development; *Department of Electronics and Nanoengineering*, Aalto University (School of Electrical Engineering, Espoo, Finland) for inclusion in the electromagnetic research group activities of Professor Ari Sihvola and for logistic support; *Department of Information Engineering, Electronics and Telecommunications* (DIET, Sapienza) and *Department of Basic and Applied Sciences for Engineering* (SBAI, Sapienza) for software licenses and doctoral funds.

The topics covered in this thesis have a wider range of applications than the specific cases presented, as the methods I have developed can be applied to study also other types of devices and/or other frequency spectra (including microwaves and optics). The equivalent-circuit models and parametric macromodels devised here, thanks to their versatility, can be successfully used for the optimization of various classes of metamaterial devices; these methods require an initial analytical complexity for the setup of the analysis, but on the long run the efforts are largely amortized, as they allow to reduce the computational costs with a significant speed-up of the design flow. What I found particularly interesting and enjoyable was to follow the development of the devices also during the physical realization and the characterization, other than the design and post-processing phases; this allowed me not only to confirm the effectiveness of the proposed methods, but also to accrue a global view of the systems and some “craftsmanship”. I believe that the synergistic cooperation of the multiple analytical, numerical and experimental aspects, as shown in this thesis, could streamline the burden of work, which would otherwise be overwhelming.

Overall, while some milestones in THz technology have been reached in recent years, research is currently very active in this field; as new functionalities are demonstrated, it will be possible to evaluate the real potentiality of THz to impact our world.

11.1 Author's bibliography

Publications

- [1] **M. D. Astorino**, F. Frezza, and N. Tedeschi, "Equivalent-circuit model for stacked slot-based 2D periodic arrays of arbitrary geometry for broadband analysis," *Journal of Applied Physics*, vol. 123, no. 10, p. 103106, 2018.
- [2] **M. D. Astorino**, F. Frezza, and N. Tedeschi, "Ultra-thin narrow-band, complementary narrow-band, and dual-band metamaterial absorbers for applications in the THz regime," *Journal of Applied Physics*, vol. 121, no. 6, p. 063103, 2017.
- [3] **M. D. Astorino**, F. Frezza, and N. Tedeschi, "Broad-band terahertz metamaterial absorber with stacked electric ring resonators," *Journal of Electromagnetic Waves and Applications*, vol. 31, no. 7, pp. 727–739, 2017.
- [4] G. Antonini, **M. D. Astorino**, F. Ferranti, F. Frezza, and N. Tedeschi, "Efficient design of metamaterial absorbers using parametric macromodels," *Applied Computational Electromagnetics Society Journal*, vol. 33, no. 7, pp. 772-780, 2018.
- [5] **M. D. Astorino**, R. Fastampa, F. Frezza, L. Maiolo, M. Marrani, M. Missori, M. Muzi, N. Tedeschi, and A. Veroli, "Polarization-maintaining reflection-mode THz time-domain spectroscopy of a polyimide based ultra-thin narrow-band metamaterial absorber," *Scientific Reports*, vol. 8, no. 1, p. 1985, 2018.

Proceedings

- [6] **M. D. Astorino**, F. Frezza, and N. Tedeschi, "Narrow-band and dual-band metamaterial absorbers in the THz regime," in *URSI International Symposium on Electromagnetic Theory (EMTS 2016)*, pp. 34–37, IEEE, Espoo, Finland, 2016.
- [7] **M. D. Astorino** and N. Tedeschi, "Design and analysis of an ultra-thin dual-band metamaterial absorber for THz applications," in *XXI Riunione Nazionale di Elettromagnetismo (RiNEm)*, 2016.
- [8] E. Sassolini, N. Tedeschi, M. Khalid, E. Lia, **M. D. Astorino**, and F. Frezza, "A simple wide-angle metamaterial absorber," in *XXI Riunione Nazionale di Elettromagnetismo (RiNEm)*, 2016.
- [9] B. B. Kong, P. Ylä-Oijala, **M. D. Astorino**, H. Wallén, and A. Sihvola, "Analysis of scatterers with discontinuous impedance boundary condition using surface-integral equation method," in *12th International Congress on Artificial Materials for Novel Wave Phenomena - Metamaterials 2018*, pp. 225-227, IEEE, Espoo, Finland, 2018.

APPENDIX A

Supplementary Information: Equivalent-Circuit Model for Stacked Slot-based 2D Periodic Arrays of Arbitrary Geometry for Broadband Analysis

A.1 Equivalent circuit model for a single periodic slot-based FSS embedded within two arbitrary dielectric half-spaces

Exploiting the periodicity (P_x and P_y along the transverse directions) of the 2D slot-based metallic surface on the plane $z = 0$ as depicted in Fig. A.1, the transverse electric field, for an obliquely incident TM wave, can be expanded in Floquet series [A1, A2]:

$$\begin{aligned} \mathbf{E}(x, y) = & (1 + R)e^{-jk_t x} \hat{\mathbf{x}} + \sum_{nm, m \neq 0} \mathbf{E}_{nm}^{TE} e^{-j(k_{xn}x + k_{ym}y)} \\ & + \sum_{(n,m) \neq (0,0)} \mathbf{E}_{nm}^{TM} e^{-j(k_{xn}x + k_{ym}y)}, \end{aligned} \quad (\text{A.1})$$

where R is the reflection coefficient, $k_{xn} = k_t + k_n = k_0 \sin \theta + 2\pi n/P_x$, and $k_{ym} = k_m = 2\pi m/P_y$, with k_0 being the free-space wavenumber and θ being the incidence angle. The TE_{n0} harmonics cannot be excited by the TM_{00} polarized impinging plane wave due to the boundary conditions. These allow to reduce the periodic structure to the analysis of a single unit-cell with PMCs parallel to the xz -plane and Floquet periodic boundary conditions parallel to the yz -plane.

The Floquet harmonics \mathbf{E}_{nm}^{TE} and \mathbf{E}_{nm}^{TM} read:

$$\mathbf{E}_{nm}^{TE} = E_{nm}^{TE} \frac{k_{ym} \hat{\mathbf{x}} - k_{xn} \hat{\mathbf{y}}}{\sqrt{k_{xn}^2 + k_{ym}^2}}, \quad (\text{A.2})$$

$$\mathbf{E}_{nm}^{TM} = E_{nm}^{TM} \frac{k_{xn}\hat{\mathbf{x}} + k_{ym}\hat{\mathbf{y}}}{\sqrt{k_{xn}^2 + k_{ym}^2}}. \quad (\text{A.3})$$

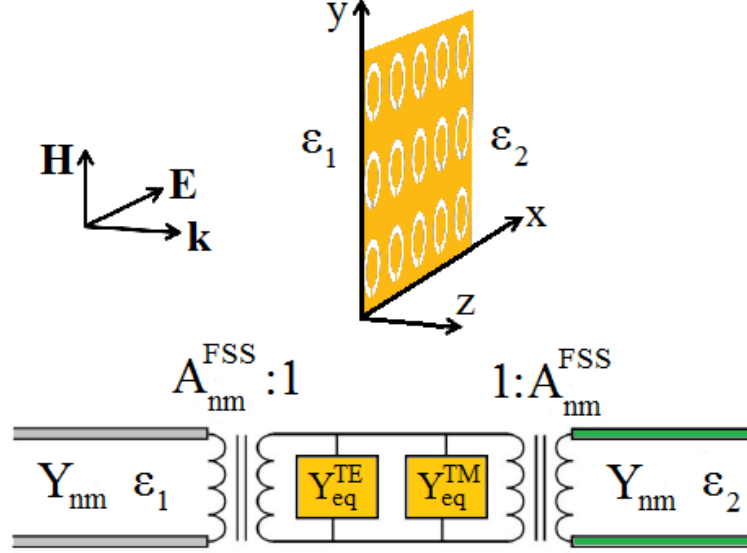


Figure A.1: EC for a single periodic slot-based FSS embedded between two different dielectric half-spaces of relative permittivity ε_1 and ε_2 , respectively. The equivalent admittance $Y_{eq} = Y_{eq}^{TE} + Y_{eq}^{TM}$ takes into account the contribution of the parallel-connected transmission lines corresponding to all the TE and TM harmonics through the relevant transformer turn ratios A_{nm}^{FSS} .

The expansions of the transverse magnetic field on the FSS planes $z = 0^-$ and $z = 0^+$ are given, respectively, by:

$$\begin{aligned} \mathbf{H}^{(1)}(x, y) &= Y_{00}^{TM(1)}(1 - R)e^{-jk_t x} \hat{\mathbf{y}} + \sum_{(n,m) \neq (0,0)} \mathbf{H}_{nm}^{TM(1)} e^{-j(k_n x + k_y y)} \\ &+ \sum_{nm, m \neq 0} \mathbf{H}_{nm}^{TE(1)} e^{-j(k_n x + k_y y)}, \end{aligned} \quad (\text{A.4})$$

$$\begin{aligned} \mathbf{H}^{(2)}(x, y) &= Y_{00}^{TM(2)}(1 + R)e^{-jk_t x} \hat{\mathbf{y}} + \sum_{(n,m) \neq (0,0)} \mathbf{H}_{nm}^{TM(2)} e^{-j(k_n x + k_y y)} \\ &+ \sum_{nm, m \neq 0} \mathbf{H}_{nm}^{TE(2)} e^{-j(k_n x + k_y y)}, \end{aligned} \quad (\text{A.5})$$

where

$$\mathbf{H}_{nm}^{(i)} = \mp Y_{nm}^{(i)} (\hat{\mathbf{z}} \times \mathbf{E}_{nm}), \quad (\text{A.6})$$

the signs \mp corresponding to the left medium ($i = 1$) and the right medium ($i = 2$), respectively.

More specifically, the transverse wave admittances of the nm -th harmonic in

the i -th medium result for TE and TM polarizations [A3]:

$$Y_{nm}^{TE,(i)} = \frac{\beta_{nm}^{(i)}}{\omega\mu_0}, \quad (\text{A.7})$$

$$Y_{nm}^{TM,(i)} = \frac{\omega\varepsilon_i}{\beta_{nm}^{(i)}}, \quad (\text{A.8})$$

where $\beta_{nm}^{(i)} = \sqrt{\omega^2\varepsilon_i\mu_0 - k_{xn}^2 - k_{ym}^2}$ is the propagation wavenumber along the z -direction, ω is the angular frequency, μ_0 is the free-space permeability, and $\varepsilon_i = \varepsilon_0\varepsilon_{r,i}$ is the complex permittivity of the i -th medium.

The tangential aperture electric field on the complementary FSS can be approximated as follows:

$$\mathbf{E}_s(x, y; \omega) = A(\omega)\mathbf{e}_s(x, y), \quad (\text{A.9})$$

where $A(\omega)$ represents a frequency-dependent complex amplitude and $\mathbf{e}_s(x, y)$ is the spatial invariant profile of the aperture field in the operating frequency band. The assumption of a frequency-independent aperture field profile has been found valid in a wide band, even inside the grating-lobe regime, as long as the considered complex geometries are single resonant. Analytical expressions for the spatial profile $\mathbf{e}_s(x, y)$ are only known in closed form for canonical geometries [A4], giving rise to a fully analytical circuit model. However, in order to consider arbitrary complex aperture shapes, the spatial profile can be extracted from a single low-frequency full-wave simulation of the free-standing periodic array under test, without further significant computational costs.

The expansion coefficients of the tangential aperture electric field are expressed, in terms of the reflection coefficient R , by:

$$E_{nm}^{TE} = (1 + R) \frac{I_{ex}k_{ym} - I_{ey}k_{xn}}{I_e\sqrt{k_{xn}^2 + k_{ym}^2}}, \quad (\text{A.10})$$

$$E_{nm}^{TM} = (1 + R) \frac{I_{ex}k_{xn} + I_{ey}k_{ym}}{I_e\sqrt{k_{xn}^2 + k_{ym}^2}}, \quad (\text{A.11})$$

being the Fourier transforms of the aperture (ap) field:

$$I_e = \iint_{ap} \mathbf{e}_s(x, y) \cdot \hat{\mathbf{x}} e^{jk_x x} dx dy, \quad (\text{A.12})$$

$$I_{ex} = \iint_{ap} \mathbf{e}_s(x, y) \cdot \hat{\mathbf{x}} e^{jk_x x} e^{jk_n x} e^{jk_m y} dx dy, \quad (\text{A.13})$$

$$I_{ey} = \iint_{ap} \mathbf{e}_s(x, y) \cdot \hat{\mathbf{y}} e^{jk_x x} e^{jk_n x} e^{jk_m y} dx dy. \quad (\text{A.14})$$

The equivalent admittance Y_{eq} in Eq. (4.1) has been obtained from the integral equation for the continuity condition of the Poynting vector through the aperture:

$$\iint_{ap} \left[\mathbf{E}_s^* \times (\mathbf{H}^{(2)} - \mathbf{H}^{(1)}) \right] \cdot \hat{\mathbf{z}} dx dy = 0, \quad (\text{A.15})$$

where the reflection coefficient for the dominant TM_{00} harmonic reads:

$$R = S_{11} = \frac{(Y_{00}^{TM(1)} - Y_{00}^{TM(2)}) - Y_{eq}}{(Y_{00}^{TM(1)} + Y_{00}^{TM(2)}) + Y_{eq}}. \quad (\text{A.16})$$

A.2 References

- [A1] C. Wan and J. A. Encinar, "Efficient computation of generalized scattering matrix for analyzing multilayered periodic structures," *IEEE Transactions on Antennas and Propagation*, vol. 43, no. 11, pp. 1233–1242, 1995.
- [A2] M. Garcia-Vigueras, F. Mesa, F. Medina, R. Rodriguez-Berral, and J. L. Gomez-Tornero, "Simplified circuit model for arrays of metallic dipoles sandwiched between dielectric slabs under arbitrary incidence," *IEEE Transactions on Antennas and Propagation*, vol. 60, no. 10, pp. 4637–4649, 2012.
- [A3] N. Marcuvitz, *Waveguide Handbook* (McGraw-Hill, 1951).
- [A4] S. R. Rengarajan, "Choice of basis functions for accurate characterization of infinite array of microstrip reflectarray elements," *IEEE Antennas and Wireless Propagation Letters*, vol. 4, no. 1, pp. 47–50, 2005.

Supplementary Information: Custom Reflection-Mode THz-TDS

B.1 Aluminum prism geometry

As represented in Fig. B.1, we consider an incident Gaussian beam on a triangular section prism. We call V the lower vertex of the prism, \overline{VH} its height,

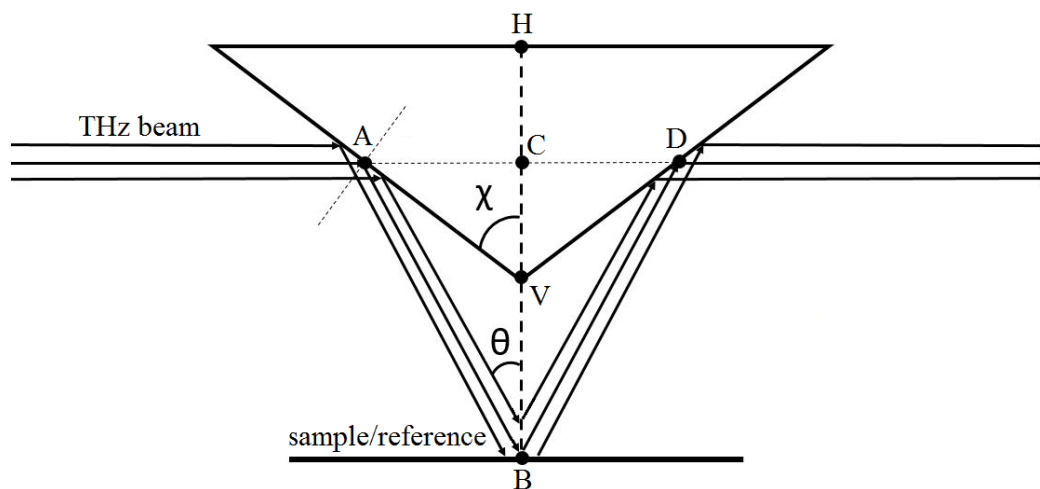


Figure B.1: Aluminum prism geometry.

C the midpoint of \overline{VH} , A and D the projections of C on the two sides of the prism in the directions of the transmitting and receiving antennas, respectively. We call $\widehat{AVC} = \chi$ the semi-angle of the prism. We suppose a horizontal propagating beam (perpendicular to \overline{VH}) that, with its center, impinges on point A . By construction, the incidence angle will be equal to χ and the beam will be totally reflected towards the sample/reference that we suppose to be horizontal. Therefore, we aim at determining the relationship between the semi-angle of the prism and the distance between the center of the prism and the sample/reference,

\overline{BC} , so that the incidence on the sample/reference occurs at point B , projection of the vertex V of the prism on the sample/reference. For simplicity, let's say: $h_p = \overline{VH}$, $b = \overline{AD}$ and $h = \overline{BC}$.

We see that $\widehat{BAV} = \pi/2 - \chi$ and $\widehat{AVB} = \pi - \chi$, from which the incidence angle on the sample/reference is $\theta = 2\chi - \pi/2$. At this point, we notice that the semi-angle of the prism must be $\chi > \pi/4$ to ensure that the beam reflected by the prism had a horizontal component as the horizontal beam. In order to determine the distance between prism and sample/reference, we considered AVC triangle:

$$\tan \chi = \frac{b}{h_p}, \quad (\text{B.1})$$

while from ABC triangle:

$$\tan \theta = \frac{b}{2h}. \quad (\text{B.2})$$

From the two previous equations, we obtain:

$$\tan \theta = \frac{h_p \tan \chi}{2h}. \quad (\text{B.3})$$

We have thus determined the relationship between the height and the semi-angle of the prism, h_p and χ , and the distance between the center of the prism and the sample, h :

$$h = \frac{h_p \tan \chi}{2 \tan \theta} = -\frac{h_p \tan \chi}{2 \cot(2\chi)} = \frac{h_p \tan \chi}{1 - \cot^2 \chi} \cot \chi = \frac{h_p}{1 - \cot^2 \chi}. \quad (\text{B.4})$$

From Eq. (B.4), it is possible to obtain:

$$\cot \chi = \sqrt{1 - \frac{h_p}{h}}, \quad (\text{B.5})$$

$$b = \frac{h_p}{\sqrt{1 - \frac{h_p}{h}}}. \quad (\text{B.6})$$

B.2 Experimental absorbance spectra under 16° oblique incidence in TE polarization as a function of the azimuthal angle φ .

In order to demonstrate the reproducibility of the spectral data measured by means of the polarization-maintaining reflection-mode THz Time-Domain Spectroscopy (THz-TDS) system, we reported the absorbance spectra obtained under 16° oblique incidence in Transverse Electric (TE) polarization for different azimuthal angles φ of 0, 22.5, 45, 67.5, and 90 degrees.

All spectroscopic measurements were performed at room temperature and at a Relative Humidity (RH) between 3.5% and 4.7%, to reduce the water vapor contribution particularly present in the frequency band of interest.

Figures B.2-B.4 show the comparison between two different absorbance spectra $A(\omega)$ measured at specific values of RH, temperature, and azimuthal angle, illustrating the reproducibility of the measurements. It should be noted that all the plots shown in Figs. B.2-B.4 represent the absorbance spectra obtained by applying the Fast Fourier Transform (FFT) to the acquired signals in the time-domain. The small differences that are present on the tails of the absorbance spectra are due to slight variations of the baseline. These do not significantly alter the relevant physical information that is contained in the position, amplitude, and shape of the absorbance peaks.

Bearing in mind that a THz-TDS setup operating in reflection-mode has considerable criticality compared to the more easily configurable transmission-mode setup [B1], we have reached a noticeable quality of the measurements. This is allowed by the adopted reflection-mode THz-TDS configuration, properly designed with the smallest number of mobile optical and mechanical parts (mirrors, lenses, and mechanical mountings), to avoid alignment errors. These might result in differences in THz pulses path length and phase errors, thus altering the measured signals and making difficult the comparison with the theoretical predictions.

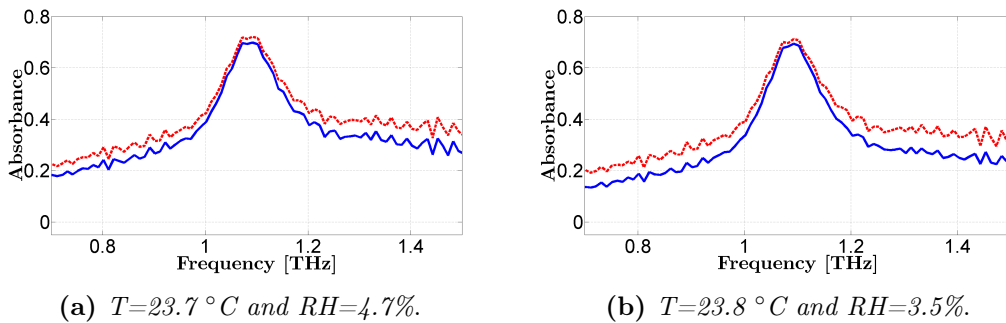


Figure B.2: Experimental absorbance spectra under 16° oblique incidence in TE polarization with azimuthal angle $\varphi = 0^\circ$.

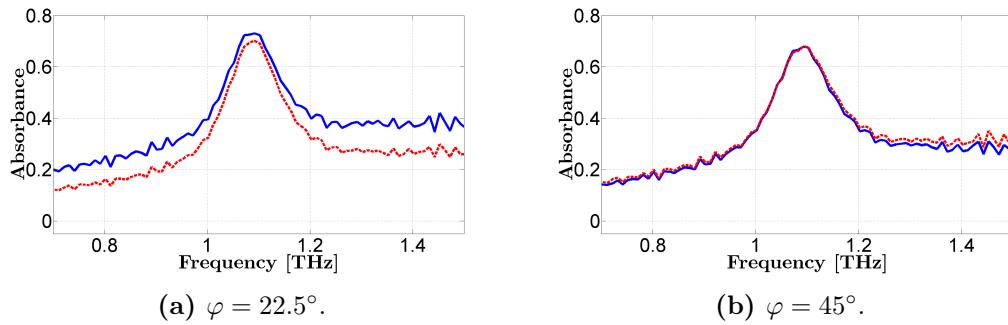


Figure B.3: Experimental absorbance spectra under 16° oblique incidence in TE polarization. The measurements have been performed at (a) 23.6°C and $\text{RH}=4.2\%$ and at (b) 23.7°C and $\text{RH}=4.0\%$

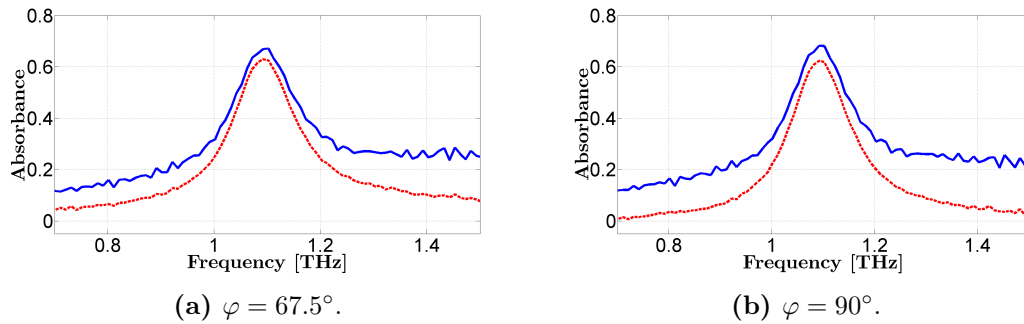


Figure B.4: Experimental absorbance spectra under 16° oblique incidence in TE polarization. The measurements have been performed at (a) 23.7°C and $\text{RH}=3.8\%$ and at (b) 23.8°C and $\text{RH}=3.6\%$

B.3 Effect of higher Ohmic losses of the metal layers at THz frequencies.

In order to analyze the discrepancy between the measured and simulated absorbance spectra, we have considered the effect of lower conductivity of gold at THz frequencies. In particular, in Ref. [B2], the conductivities of thin Al, Au, and Ag films measured via their transmission at THz frequencies, have been found much smaller than their bulk dc values, especially in the case of the thinner films and Al films. More specifically, the conductivity of 85 nm and 150 nm-thick Au films has been measured at 77 and 295 K. At the temperature of 295 K, the conductivity of 85 nm-thick Au film results of 1.5×10^7 S/m, while for a 150 nm-thick Au film is of 3.1×10^7 S/m. Since we performed the spectroscopic measurements at room temperature (see Figs. B.2-B.4), in the full-wave simulations, we initially considered an electrical conductivity of 4.09×10^7 S/m for the 100 nm-thick metallizations, corresponding to the Au bulk conductivity dc value. We have then tested the effect of higher Ohmic losses on the absorbance behavior

through parametric simulations as a function of the electrical conductivity σ .

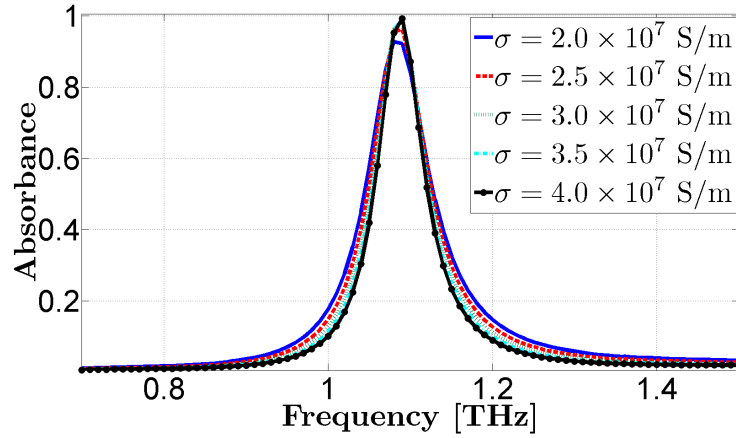


Figure B.5: Effect of higher Ohmic losses of the metal layers under 16° oblique incidence in TE polarization. Absorbance spectra as a function of the electrical conductivity σ of the 100 nm-thick metal layers, with a relative permittivity $\varepsilon_r = 2.9 - 0.0058j$ for the polyimide spacer.

In Fig. B.5, it is highlighted how a halving of the electrical conductivity ($\sigma = 2 \times 10^7$ S/m) produces only a slight reduction of the absorption level and a slight broadening of the bandwidth when considering an almost lossless polyimide dielectric layer with a relative permittivity $\varepsilon_r = 2.9 - 0.0058j$ under 16° oblique incidence in TE polarization. Consequently, the dielectric losses of the polyimide spacer represent the main reason for the mismatch with the measurements.

B.4 References

- [B1] P. U. Jepsen, D. G. Cooke, and M. Koch, “Terahertz spectroscopy and imaging—modern techniques and applications,” *Laser & Photonics Rev.*, vol. 5, no. 1, pp. 124–166, 2011.
- [B2] N. Laman and D. Grischkowsky, “Terahertz conductivity of thin metal films,” *Appl. Phys. Lett.*, vol. 93, no. 5, p. 051105, 2008.

APPENDIX C

Normalized Axial and Transversal Polarizabilities

C.1 Normalized polarizabilities of ellipsoids

Let us expand the discussion from Chapter 10, by changing the spherical form to ellipsoid [C1]. The dipole moment of these geometries can be written in a closed form, because the internal field of a homogeneous ellipsoid in a constant electric field is also constant. The amplitude of this field is linear to the external field and it is possible to find its dependence on the permittivity of the ellipsoid and on the depolarization factor [C2], a particular shape parameter. If we defined r_x, r_y, r_z the three orthogonal semi-axes of an ellipsoid, the depolarization factor in the x -direction is:

$$N_x = \frac{r_x r_y r_z}{2} \int_0^\infty \frac{1}{(s + r_x^2) \sqrt{((s + r_x^2)(s + r_y^2)(s + r_z^2))}} ds, \quad (\text{C.1})$$

where the other depolarization factors N_y (N_z) can be obtained by interchanging r_y and r_x (r_z and r_x) in the above integral.

These three depolarization factors have to satisfy:

$$N_x + N_y + N_z = 1, \quad (\text{C.2})$$

from which it is immediate to note that a sphere has three equal depolarization factors of $1/3$. Being the spherical symmetry broken, the polarizabilities are different for different directions. In general, the normalized polarizabilities in the x, y, z -directions read:

$$\alpha_{n,x(y,z)} = \frac{\varepsilon_r - 1}{1 + N_{x(y,z)}(\varepsilon_r - 1)}. \quad (\text{C.3})$$

In particular, I am interested to analyze the case of PEC prolate and oblate

spheroids in which the relative permittivity $\varepsilon_r \rightarrow \infty$. Therefore, the normalized axial polarizabilities are equal to $\alpha_{n,x(y,z)} = 1/N_{x(y,z)}$.

C.1.1 PEC prolate spheroid

Axial polarizability As a first example, I consider a PEC prolate spheroid with axis ratio 2:1, as shown in Fig. C.1, with semi-axes $r_x = r_y = r/2$ and $r_z = r = 1$ m.

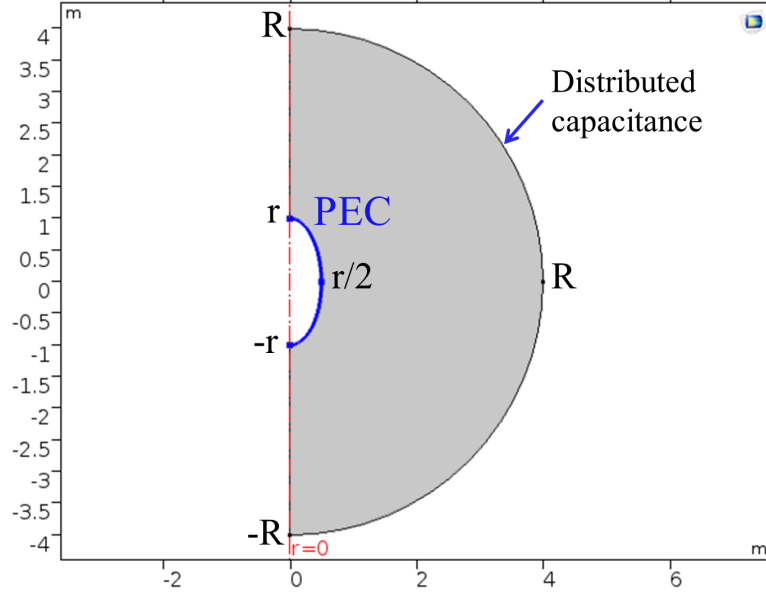


Figure C.1: Geometry of the PEC prolate spheroid.

The eccentricity of the prolate spheroid and its volume V_{ps} are respectively:

$$e = \sqrt{1 - \left(\frac{r_x}{r_z}\right)^2} = \frac{\sqrt{3}}{2}, \quad (\text{C.4})$$

$$V_{ps} = \frac{4}{3}\pi r_x r_y r_z = \frac{4}{3}\pi \frac{r^3}{4} = \pi \frac{r^3}{3}. \quad (\text{C.5})$$

The depolarization factors result:

$$N_z = \frac{1 - e^2}{2e^3} \left(\ln \frac{1 + e}{1 - e} - 2e \right) \approx 0.1736, \quad (\text{C.6})$$

$$N_x = N_y = \frac{1}{2}(1 - N_z) \approx 0.4132, \quad (\text{C.7})$$

from which the analytical normalized axial polarizability is $\alpha_{z,norm} = \frac{1}{N_z} \approx 5.7604$.

By using the previously described 2D axial symmetry electrostatic simulation in COMSOL and implementing the line integral $\alpha_z = \frac{3}{E_0 V_{ps}} \int (V + E_0 z) \frac{z}{R} 2\pi r dc$, I obtained an axial polarizability very close to the analytical result (see Fig. C.2).

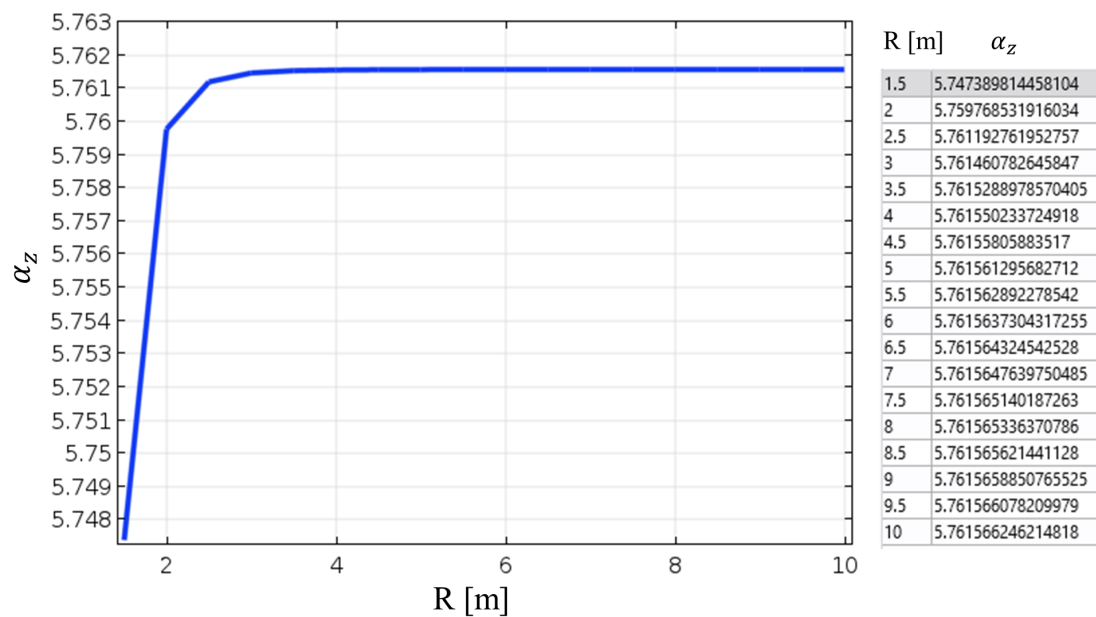


Figure C.2: Axial polarizability of a PEC prolate spheroid as a function of the radius.

Transversal polarizability In order to retrieve the transversal polarizability of this PEC prolate spheroid, I have set a 3D electrostatic simulation, computing this time the surface integral $\alpha_t = \frac{3}{E_0 V_{ps}} \iint (V + E_0 x) \frac{x}{R} dS$, as shown in Fig. C.3. From the analytical solution, the normalized transversal polarizability should be equal to $\alpha_{t,norm} = \frac{1}{N_x} \approx 2.4201$; therefore, the simulated results represent a good approximation.

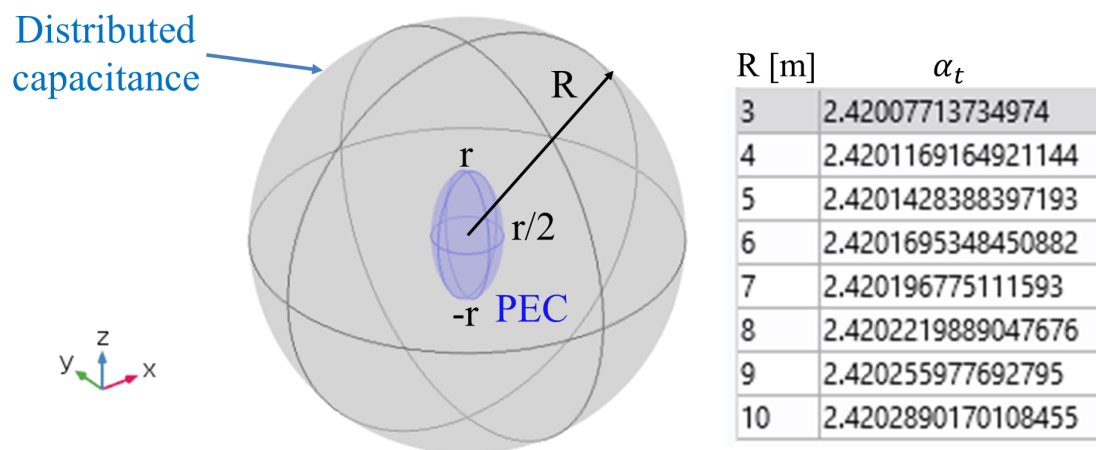


Figure C.3: 3D geometry of the PEC prolate spheroid and its transversal polarizability.

C.1.2 PEC oblate spheroid

Axial polarizability As a further example, I have considered a PEC oblate spheroid with axis ratio 2:1, as shown in Fig. C.4, with semi-axes $r_x = r_y = r = 1$ m and $r_z = r/2$.

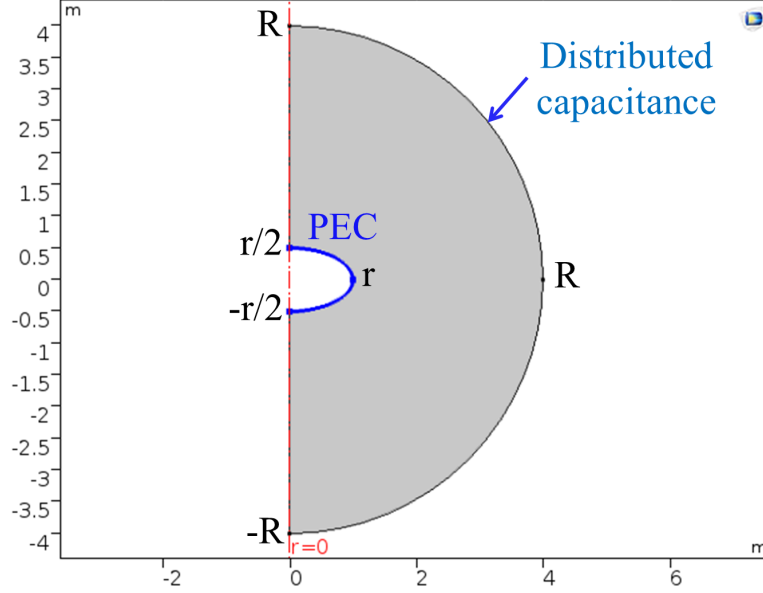


Figure C.4: Geometry of the PEC oblate spheroid.

The eccentricity of the oblate spheroid and its volume V_{os} are respectively:

$$e = \sqrt{\left(\frac{r_x}{r_z}\right)^2 - 1} = \sqrt{3}, \quad (\text{C.8})$$

$$V_{os} = \frac{4}{3}\pi r_x r_y r_z = \frac{4}{3}\pi \frac{r^3}{2} = \frac{2}{3}\pi r^3. \quad (\text{C.9})$$

The depolarization factors result:

$$N_z = \frac{1 + e^2}{e^3}(e - \tan^{-1} e) \approx 0.5272, \quad (\text{C.10})$$

$$N_x = N_y = \frac{1}{2}(1 - N_z) \approx 0.2364, \quad (\text{C.11})$$

from which the analytical normalized axial polarizability is $\alpha_{z,norm} = \frac{1}{N_z} \approx 1.8968$.

By using the previously described 2D axial symmetry electrostatic simulation in COMSOL Multiphysics and implementing the line integral $\alpha_z = \frac{3}{E_0 V_{os}} \int (V + E_0 z) \frac{z}{R} 2\pi r dc$, I have been able to obtain an axial polarizability very close to the analytical result (see Fig. C.5).

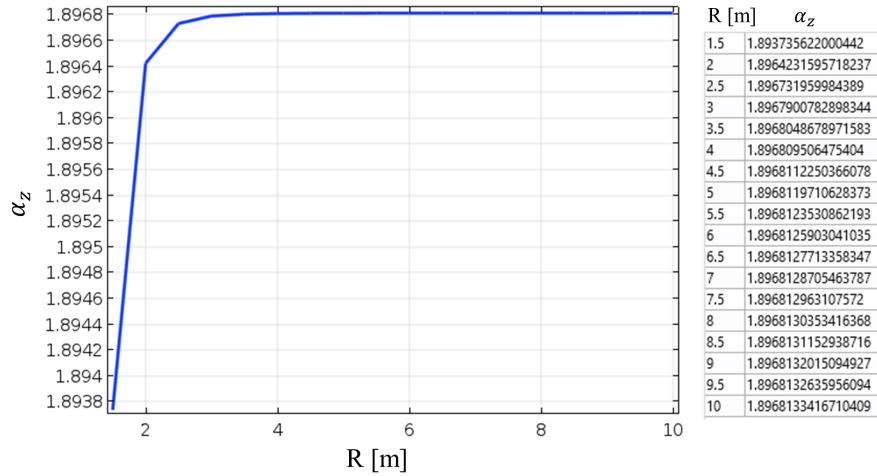


Figure C.5: Axial polarizability of a PEC oblate spheroid as a function of the radius.

Transversal polarizability In order to retrieve the transversal polarizability of this PEC oblate spheroid, I have set a 3D electrostatic simulation, computing this time the surface integral $\alpha_t = \frac{3}{E_0 V_{os}} \iint (V + E_0 x) \frac{x}{R} dS$, as shown in Fig. C.6. From the analytical solution, the normalized transversal polarizability should be equal to $\alpha_{t,norm} = \frac{1}{N_x} \approx 4.2301$.

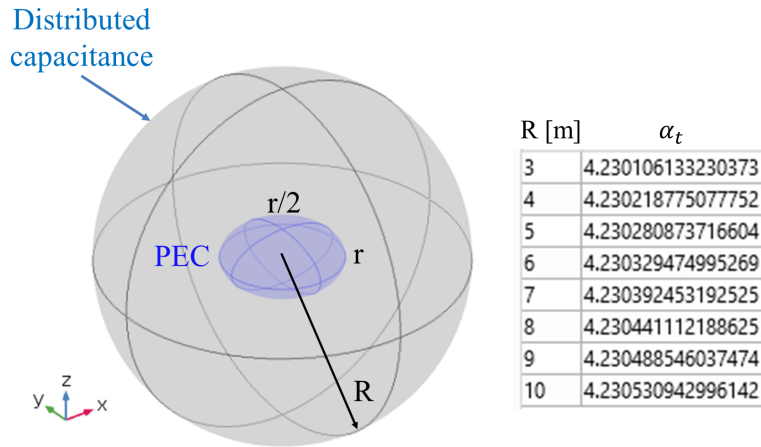


Figure C.6: 3D geometry of the PEC oblate spheroid and its transversal polarizability.

C.2 Normalized polarizabilities of double sphere

The concept of doublet of spheres [C3] is very useful in the modeling of random nanomaterials. As we know, being the sphere an equilibrium shape, when in a mixture it gets into the vicinity of another sphere the interaction forces may be very strong. Therefore, the doublet of spheres can be regarded as a single polarizing object. In particular, if two spheres become so closely in contact, they can merge into a cluster. Such a doublet can be described with one geometrical parameter: the distance between the center points C_a of the spheres $L = 2d$ divided by their radius a (see Fig. C.7). The value $L/a = 2$ divides the range into

the two cases whether the doublet is clustered or separated. Again, this object is rotationally symmetric and needs to be described by two polarizabilities, axial and transversal.

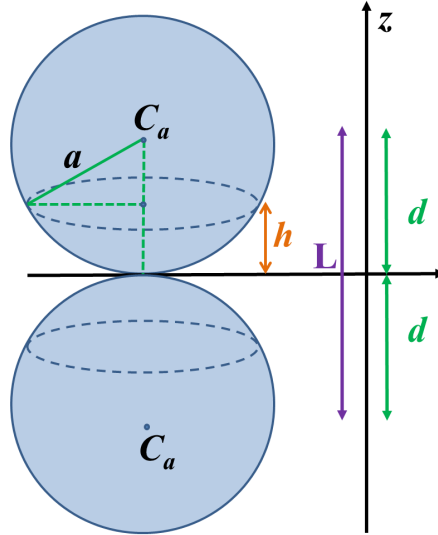


Figure C.7: Double sphere geometry.

C.2.1 Two touching PEC spheres

I have first analyzed the case of two touching PEC spheres ($L/a = 2$), computing the normalized axial polarizability through the line integral $\alpha_z = \frac{3}{E_0 V_{ds}} \int (V + E_0 z) \frac{z}{R} 2\pi r dc$, where the volume of the double sphere is $V_{ds} = 2(4\pi a^3)/3$ as shown in Fig. C.8. The obtained results as a function of the radius R are in good agreement with the analytical result in Ref. [C3] $\alpha_{z,norm} = 6\zeta(3) \approx 7.21234$, where ζ represents the Riemann Zeta function.

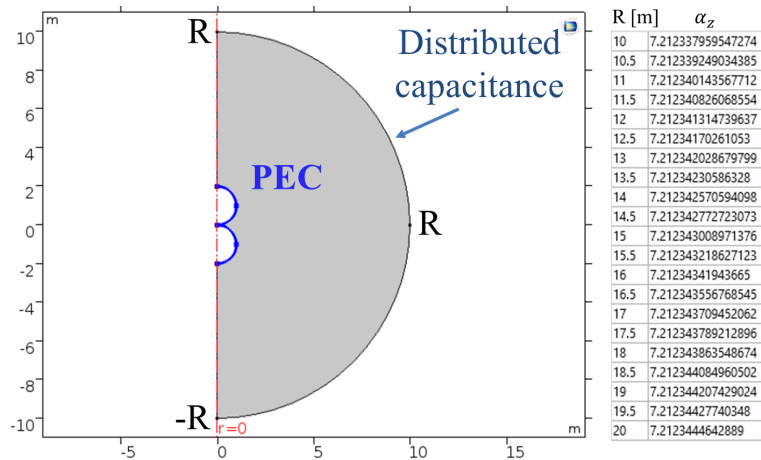


Figure C.8: Geometry of the two touching PEC spheres and the axial polarizability.

C.2.2 Two intersecting PEC spheres

In order to simulate the case of two intersecting spheres [C4], we have to pay attention to the computation of the volume of the merged geometry. For clarity, I report the expression of the volume of a spherical cap (see Fig. C.9).

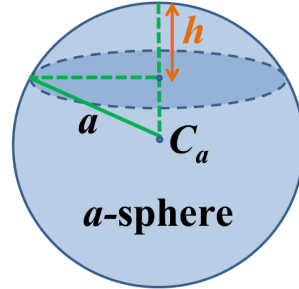


Figure C.9: Spherical cap.

In this case, the height of the cap is $h = a/2$, from which the spherical cap volume results:

$$V_{cap} = \frac{\pi h^2}{3}(3a - h) = \frac{5}{24}\pi a^3. \quad (C.12)$$

The volume of the spherical cap subtracted from the volume of the a -sphere is:

$$V_a = \frac{4\pi a^3}{3} - \frac{5}{24}\pi a^3 = \frac{9}{8}\pi a^3. \quad (C.13)$$

The total volume of the two intersecting spheres is given by:

$$V_{tot} = 2V_a = \frac{9}{4}\pi a^3. \quad (C.14)$$

The resulting geometry of the two merged spheres is shown in Fig. C.10 with the computed axial polarizability in the case $L/a = 1$. The result converges to the analytical value shown in Ref. [C3].

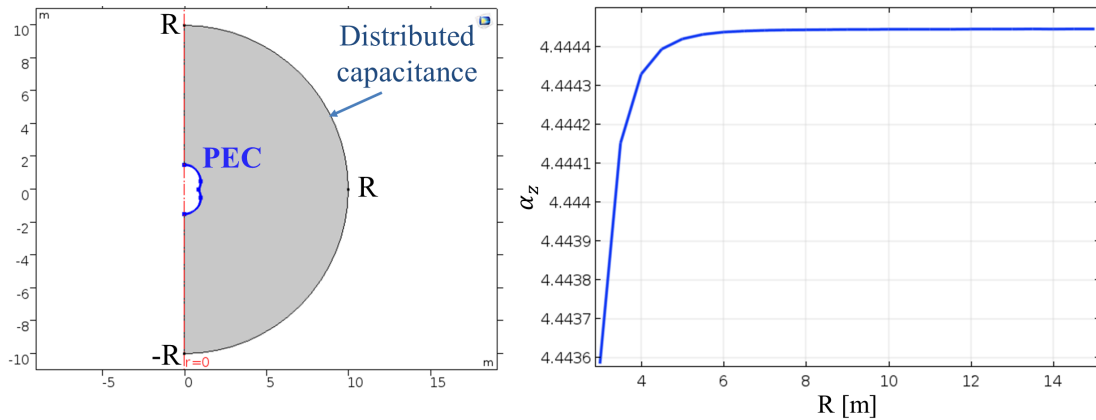


Figure C.10: Two intersecting PEC spheres $L/a = 1$ and computed axial polarizability.

Orthogonal symmetric PEC spheres Then, I have considered the case of two orthogonal symmetric PEC spheres with $L/a = \sqrt{2}$. In general, two spheres are orthogonal when the square of the distance L of their centers is equal to the sum of the squares of their radii a . The height of the spherical cap is in this case $h = (1 - \sqrt{2}/2)a \approx 0.2929a$ (see Fig. C.9). The spherical cap volume results:

$$V_{cap} = \frac{\pi h^2}{3}(3a - h) = 0.2323 \frac{\pi a^3}{3}. \quad (\text{C.15})$$

The volume of the spherical cap subtracted from the volume of the a -sphere is:

$$V_a = \frac{4\pi a^3}{3} - 0.2323 \frac{\pi a^3}{3} = 3.7677 \frac{\pi a^3}{3}. \quad (\text{C.16})$$

The total volume of the two intersecting spheres is given by:

$$V_{tot} = 2V_a = 7.5354 \frac{\pi a^3}{3} \approx 1.884 \frac{4\pi a^3}{3}. \quad (\text{C.17})$$

I can then compute the normalized axial polarizability through a line integration, obtaining the results plot in Fig. C.11 as a function of the radius R , that converge to the analytical value in Ref. [C3].

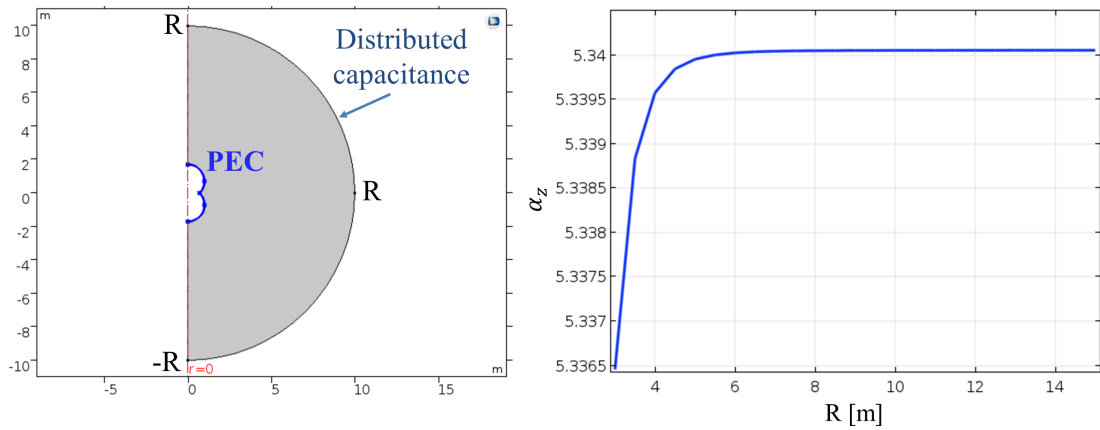


Figure C.11: Two intersecting orthogonal PEC spheres $L/a = \sqrt{2}$ and computed axial polarizability.

Intersecting PEC spheres Finally, I have considered the case of two intersecting PEC spheres in the range $0 \leq L/a \leq 2$. The limit values $L/a = 0$ and $L/a = 2$ correspond to a single PEC sphere of radius a and to two touching PEC spheres, respectively. I calculated the total volume of the merged spheres through a volume integral implemented in COMSOL Multiphysics, retrieving the normalized axial polarizability shown in Fig. C.12, which well agrees with the results in Ref. [C3].

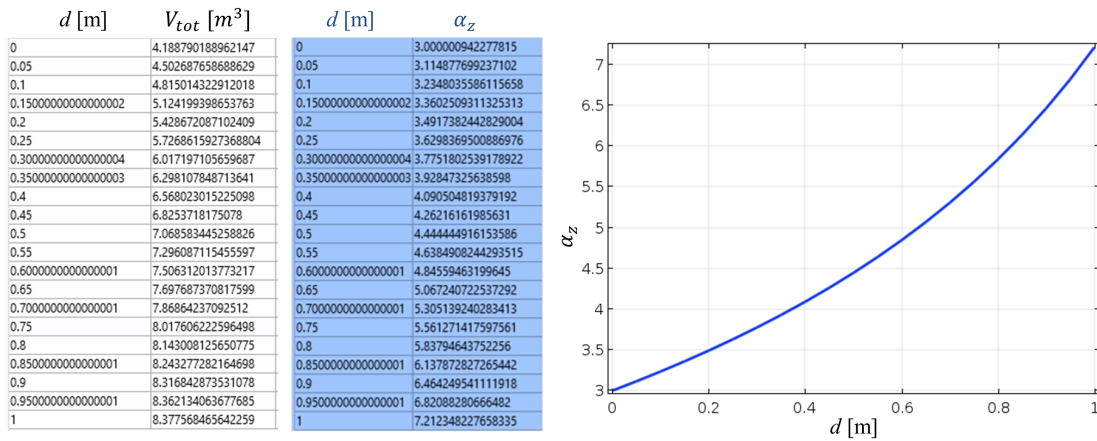


Figure C.12: Volume and axial polarizability of two intersecting PEC spheres as a function of d .

C.3 References

- [C1] A. Sihvola, “Dielectric polarization and particle shape effects,” *Journal of Nanomaterials*, vol. 2007, pp. 1-9, 2007.
- [C2] A. Sihvola, *Electromagnetic mixing formulas and applications*, IET, 1999.
- [C3] H. Wallén and A. Sihvola, “Polarizability of conducting sphere-doublets using series of images,” *Journal of Applied Physics*, vol. 96, no. 4, pp. 2330-2335, 2004.
- [C4] I. V. Lindell, K. H. Wallén, and A. Sihvola, “Electrostatic image theory for two intersecting conducting spheres,” *Journal of Electromagnetic Waves and Applications*, vol. 17, no. 11, pp. 1643–1660, 2003.